Observing Ultra-Low Surface Brightness Objects In a Bright Sky Environment

Anna Skrinnik

A Thesis Submitted to
The Faculty of Graduate Studies
in Partial Fulfillment of The Requirements
For The Degree of
Master of Science

Graduate Program in Physics and Astronomy
York University, Toronto, Ontario

September 2024

© Anna Skrinnik, 2024

"Time and place are nothing. Constructs of a feeble mortal mind attempting to categorize and understand the world around it. If you were one of the fortunate few, you would one day understand and accept this. However, you are not and you will not."
Dyus, *The Elder Scrolls IV: Oblivion*

Abstract

An array of n identical lenses operating in tandem acts as an optical system that has an effective focal ratio that is faster than that of an individual lens by a factor of $\sqrt{\mathrm{n}}$. Hence, arrays of lenses with small focal ratios have opened doors to imaging ultra-low surface brightness objects. Such an optical system, when coupled to narrow-band line filters, offers the opportunity to isolate emission from targets while suppressing light from other sources, such as the sky. Additionally, this optical system offers the opportunity to observe the targets through multiple line filters simultaneously. In this work, we report on the development of a fast focal ratio system consisting of two Canon $400\,\mathrm{mm}\ \mathrm{f}/2.8$ lenses coupled with astronomy grade CCD cameras to observe ultra-low surface brightness objects in the light of Hα and [OI]. The system was used to search for missing gas around a dwarf spheroidal satellite of the Andromeda Galaxy M31 and to locate the transition zones of nebulae. Additionally, we report on the results of observation, the processes and algorithms that were developed for the analysis of the data, and the results provided by the analysis. Our array of two lenses was successfully used to observe ultra-low surface brightness objects in the severely light polluted environment of Toronto through a line and a continuum filter simultaneously.

Contents

List of Tables

List of Figures

Chapter 1
Introduction

1.1 Overview and Motivations

In an attempt to locate the gas evacuated from dwarf spheroidal galaxies (dSphs) and identify the transition zones in the nebulae of the Milky Way we have developed an observational apparatus that is capable of observing faint extended structures from relatively bright ground-based sites.

1.1.1 Gas-Poor Dwarfs

The first objective was to locate the missing gas of Andromeda XVIII (henceforth, And XVIII) – one of the dwarf spheroidal satellites of the Andromeda Galaxy (henceforth, M31). The dwarf spheroidal galaxies have lost most, if not all, of their gas (Ivkovich & McCall, 2019), and And XVIII is no exception. There are several proposed processes of gas removal that can be grouped into two categories – internal processes and external processes.

1.1.1.1 External Processes

The external processes remove gas from a dwarf galaxy via interactions with other galaxies and the intergalactic medium. These processes include ram pressure stripping, tidal stripping and dynamical harassment.

In the case of ram pressure stripping, the dwarf's gas gets peeled away by the drag caused by moving through the intergalactic medium (IGM), such as the halo of a massive galaxy or the intra-cluster medium (Golden, 2022). For the gas to get removed by ram pressure stripping, the column densities of the dwarf and the IGM must be at least equal (Blitz & Robishaw, 2000). Since the IGM is normally rarefied, the favourable conditions for ram pressure stripping occur mostly in the vicinity of other galaxies, where the IGM is saturated by

the galactic haloes and intra-cluster medium.

In the case of tidal stripping, if a small dwarf galaxy is orbiting a relatively massive galaxy it can lose its gas to the tidal pull of its large neighbour. For that to happen, the large galaxy must sufficiently outweigh the dwarf galaxy, and be situated close enough for the tidal pull to strip away the dwarf's gas.

In the case of dynamical harassment, a dwarf galaxy loses its gas as it moves through a galaxy cluster. The dwarf's gas gets heated by the gravitational encounters with other galaxies, and gets pulled towards them due to gravity. For a dwarf galaxy to lose its gas to dynamical harassment, it needs to belong to a dense cluster and hence be closely situated to other galaxies.

While external processes can explain the presence of close companion gas-poor dwarfs, it fails to explain the existence of relatively isolated and gas-poor dwarfs. Therefore, for an isolated dwarf such as And XVIII, the internal processes must be the dominant cause of gas loss.

1.1.1.2 Internal Processes

Internal processes such as photoionization, supernovae and star formation occur within the galaxy, and can also be the reason behind the removal of gas from a dwarf galaxy.

Photoionization is a process in which the gaseous matter within the dwarf galaxy gets ionized by absorbing sufficiently energetic photons, typically produced by hot and young stars. Ionization causes an increase in the temperature of the gas, and eventually, the thermal energy of the gas overcomes the galaxy's gravitational pull. Consequently, the gas photoevaporates by escaping the dwarf's gravitational pull due to its particles obtaining an average speed greater than or equal to the escape velocity.

In the case of star formation, the gas is not missing from the galaxy – instead it gets converted into stars that still reside within the galaxy. The stellar winds associated with the birth and subsequent evolution of stars could also

potentially contribute to the evacuation of gas from the galaxy in the case of a particularly violent starburst. However, it has been shown by Ivkovich & McCall (2019) that dSphs have not converted all of their gas into stars, yet they have a large portion of their gas missing. Additionally, Ferrara & Tolstoy (2000) showed that for supernovae and starburst winds alone to remove the gas from a dwarf galaxy, the dwarf must have a very low mass, which fails to explain the existence of more massive isolated gas-poor dwarfs. In summary, external processes, converting gas into stars, and a total blowout of gas by starbursts and supernovae fail to explain the lack of gas in relatively isolated dSphs. Therefore, either photoionization or a combination of photoionization and supernovae-driven winds must be the dominant mechanisms of gas removal.

Some of the gas evacuated from gas-poor dwarfs might still be ionized, and thus can be located in the vicinity of the dwarf. While ionized gas itself is invisible, the recombinations of electrons with hydrogen ions are accompanied with the release of photons of different energies. Among them is emission at $\lambda = 656.3\,\mathrm{nm}$, which is commonly referred to as Hα. Therefore, it may be possible to locate the missing gas by observing the vicinity of a gas-poor dwarf, such as And XVIII, in Hα.

1.1.2 Transition Zones of Nebulae

The second objective was to observe forbidden line emissions of neutral oxygen [OI] in the nebulae of the Milky Way galaxy. Emission nebulae are clouds of dust and gas that get ionized by ultraviolet radiation provided by hot O and B type stars that reside within or near the nebulae. The emission nebulae can be categorized into two types – density-bounded or ionization-bounded. An emission nebula is said to be density-bounded if the ionizing radiation is sufficient to ionize all gas surrounding the source of the UV photons. Alternatively, the luminosity of UV photons may be insufficient to ionize the entirety of the gas,

in which case the nebula is said to be ionization-bounded. In the case of an ionization-bounded nebula, when the source of ionizing photons turns on, the surrounding gas is bombarded with ionizing photons and the rate of ionizations prevails over the rate of recombinations to the excited states. Hence the ionization front advances. The ionization front will continue advancing until the rate of recombinations to excited states becomes equivalent to the rate of ionization of gas. At that point the source of UV photons will "run out of steam" and the proportion of ionized-to-neutral gas quickly diminishes from almost fully ionized to neutral, as there are no ionizing radiation photons left to maintain the ionization of the gas. The region over which the ionization fraction of gas drops off is referred to as the transition zone, and together with the inner ionized region it comprises the so called the Strömgren Sphere. A more detailed discussion of the Strömgren Sphere and its transition zones can be found in Section 1.3.

Nebulae are comprised of hydrogen, helium and metals, such as iron, silicon, carbon, neon, and oxygen, etc. Of a particular interest is the behaviour of oxygen. In the transition zones of nebulae, collisions between oxygen ions and neutral hydrogen atoms can lead to charge exchange reactions. In charge exchange, a transfer of an electron from a neutral hydrogen atom to an ionized oxygen atom results in the addition of neutral oxygen and ionized hydrogen atoms. The collisional excitation of neutral oxygen from the ground state to ^1D state can then lead to the transition of an electron to the $^3P_2$ and $^3P_1$ ground states. These transitions result in the production of an [OI] photon with $\lambda = 636.3\,\mathrm{nm}$, or $\lambda = 630.0\,\mathrm{nm}$ respectively. Charge exchange reactions become dominant in the transition zones of nebulae due to a higher amount of neutral hydrogen; however, in the inner layers of the Strömgren Sphere they can seldom occur because hydrogen is mostly ionized. Outside of the Strömgren Sphere, beyond the transition zone, all gas is neutral and too cold to collisionally excite [OI] emission. Thus, the line emission of neutral oxygen

enhanced by charge exchange in the transition zone can serve as a diagnostic tool to determine the location of the transition zones of photoionized nebulae.

1.1.3 Apparatus and Synopsis

Gas ejected from dSphs and [OI] in photoionized nebulae both have very low surface brightnesses. This means that a special apparatus and a specific set of techniques must be involved if one wishes to observe them.

The development of the Dragonfly Telephoto Array (Abraham & van Dokkum, 2014) opened a door to imaging extended ultra-low surface brightness objects. The “Dragonfly’s eye” formed from an array of fast telephoto lenses created a very fast optical system by maximizing the light-gathering power and keeping the focal length constant. Creating such a composite "Dragonfly’s eye" provides the means to observe ultra-low surface brightness objects due to the system’s fast effective focal ratio. Additionally, it offers the opportunity of observing an object in multiple filters simultaneously, which lays the foundation of the research described in this work.

In this work, we employed Dragonfly’s design of a fast optical system by building the Quick Array of Isolating Lenses (QUAIL) from two Canon EF $400\,\mathrm{mm}$ $\mathrm{f}/2.8$ L IS II USM telephoto lenses coupled to Diffraction Limited SBIG Aluma 3200 CCD Cameras. The goal was to observe ultra-low surface brightness targets, such as the photo-evaporated gas of And XVIII and the transition zones of nebulae, through line and continuum filters simultaneously, which would allow us to subtract the continuum from line emission precisely. To do that, one of the lenses was equipped with the continuum filter and the second lens was used to observe line emission. The line filter in the second lens could be conveniently switched from Hα to [OI] and vice versa using a slide-in filter holder.

1.2 Dwarf Galaxies

"Galaxies are like people. The better you get to know them the more peculiar they often seem to become."

van den Bergh, Sidney, *Galaxy Morphology and Classification*

1.2.1 Definition of Dwarf Galaxy

There exists a plethora of galaxies with different shapes and sizes, from magnificent grand-design giant spiral galaxies, such as Messier 81 (Bode's Galaxy), to small, dim and featureless dwarf elliptical galaxies, such as Messier 32. The bulk of this work focuses on exploring the space around dwarf galaxies, so it is useful to define what a dwarf galaxy is.

As the name suggests, dwarf galaxies are characterized by their low total mass of $10^7 \leq \mathrm{M_{gal}}\ (\mathrm{M_\odot}) \leq 10^9$, low luminosity of $10^5 \leq \mathrm{L_{gal}}\ (\mathrm{L_\odot}) \leq 10^7$, and their small size of typically only a few kiloparsecs across. Dwarf galaxies also have several different morphologies, which include dwarf elliptical galaxies (dEs), dwarf spheroidal galaxies (dSphs), dwarf irregular galaxies (dIs) and blue compact dwarfs (BCDs) (Swinburne University of Technology, 2022). Following Ivkovich & McCall (2019), we define dwarf galaxies as pressure-supported galaxies with velocity dispersions of $30\ \mathrm{km/s}$ or less.

In a pressure-supported galaxy, the random motion of its baryonic matter is the primary source of support against the gravitational collapse. Baryonic matter is what makes up all of the visible matter in the galaxy, which includes stars, gas, dust, etc. Dark matter, on the other hand, is invisible as it does not interact electromagnetically. Velocity dispersion is a measure of the range of baryonic velocities – the higher the velocity dispersion, the larger the amplitude of random motions. The only way to observe dark matter is through

gravitational interactions.

Dwarf galaxies can be further categorized into gas-rich and gas-poor dwarfs, which are also referred to as late-type dwarfs (LTDs) and early-type dwarfs (ETDs), respectively. The gas-rich galaxies are comprised of dIs and BCDs. The gas-poor galaxies comprise dSphs and dEs. Similarities in structure suggest that dSphs used to be dIs that somehow failed to retain their gas (Ivkovich & McCall, 2019; Kormendy, 2014).

1.2.2 The Fundamental Plane and The Potential Plane

When one ponders the properties of a star, such as its temperature or luminosity, they can refer to the Hertzsprung-Russell diagram (H-R diagram). The H-R diagram has several variations where its abscissa can have surface temperature, colour or spectral class; meanwhile the ordinate can have the star's luminosity or absolute magnitude (the apparent magnitude that a star would have if it were $10\ \mathrm{pc}$ away). It is often plotted with two sets of complimentary axes, such as in Figure 1.1. This allows an astronomer to relate and deduce a star's properties from its other parameters – for instance a star's spectral class can be used to find its surface temperature. Similarly, there exist several relationships that can help an astronomer learn something

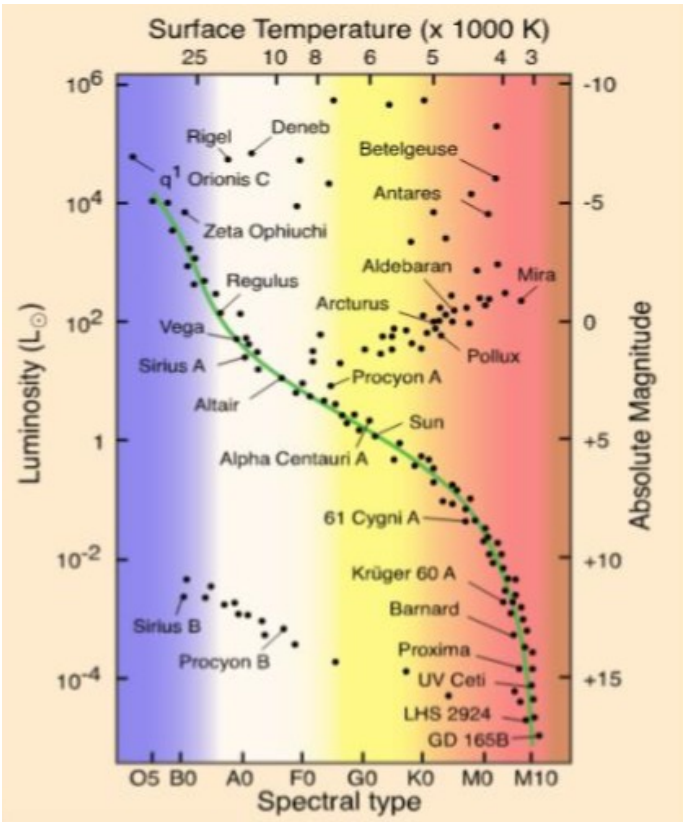

Figure 1.1: An example of the Hertzsprung-Russell diagram. The H-R diagram allows one to use its two sets of abscissa and ordinates to infer certain properties of a star. (Learn the Sky LLC, 2022)

about a galaxy. For instance, the Tully-Fisher Relation describes the relationship between a spiral galaxy's luminosity and the asymptotic rotational velocity (Tully & Fisher, 1977; McGaugh et al., 2000). The Faber-Jackson Relation defines the relationship between an elliptical galaxy's luminosity and its central stellar velocity dispersion. However, it was noticed by Djorgovski & Davis (1987) that the Faber-Jackson Relation has a significant scatter that cannot be be explained solely by the errors in measurements. The investigation of the source of this scatter led to the establishment of the relationship between the radius, the velocity dispersion and the surface brightness of a galaxy called the Fundamental Plane (Djorgovski & Davis, 1987; Bender et al., 1992). Although the Fundamental Plane is normally defined for giant elliptical galaxies, similar 3-space relationships have been derived for Dwarf Galaxies, such as the Fundamental Manifold, Fundamental Curve and Fundamental Line (Zaritsky et al., 2006; Ivkovich & McCall, 2019, & references therein.) Essentially, all of them describe the relationship between velocity dispersion, radius, and surface brightness. Of particular interest is the Fundamental Plane for dwarfs called the Potential Plane, which was developed by McCall et al. (2012).

1.2.3 The Establishment of The Potential Plane for Dwarfs

The Potential Plane serves as an important basis for the discussion of dSphs and their properties. In this section, the process that led to the discovery and establishment of the Potential Plane for dwarfs will be briefly outlined.

Using $\mathrm{K_s}$ images of 34 dIs, Vaduvescu et al. (2005) have determined that the best function that fits the surface brightness profiles in both the core and the outer regions of dIs is the hyperbolic secant function:

$$I_s(r) = \frac{2I_{0,s}}{e^{\frac{r}{r_{0,s}}} + e^{-\frac{r}{r_{0,s}}}} \tag{1.1}$$

where r is the distance from centre of the galaxy along the semimajor axis, $I_s(r)$ is the fitted intensity at distance r, $I_{0,s} = I_s(r = 0)$ is the central intensity, and $r_{0,s}$ is the scale length of the fitted sech profile (Vaduvescu et al., 2005). Having established how best to quantify the luminous properties of LTDs, Vaduvescu et al. (2005) proposed a relationship between luminosity and internal motions akin to the Tully-Fisher relation. Unfortunately, it displayed a weak relationship with a large amount of scatter which could not be attributed to observational errors alone. Thus, it was investigated whether the large residuals could be attributed to the variations in the central surface brightness μ_0 or the scale length r_0. It was then discovered that the large residuals were related to the variations in the central surface brightness μ_0. Motions are characterized by the logarithm of the velocity dispersions $\log(W_{20})$, defined by:

$$W_{20} = (8\ln(5))^{1/2}\sigma_{los} \tag{1.2}$$

where σ_{los} is the line-of-sight velocity dispersion that was derived from the width of the HI line at 20% of its peak. Thus, the Fundamental Plane for dIs was established:

$$M_S = (-4.27 \pm 0.61)\log(W_{20}) + (0.70 \pm 0.09)\mu_0 - (22.08 \pm 2.40) \tag{1.3}$$

where μ_0 is the central surface brightness, and M_S is the absolute sech magnitude in K_s (Vaduvescu et al., 2005).

An attempt was then made to improve the fit to the Fundamental Plane with an expanded number of LTDs, including BCDs (McCall et al., 2012). BCDs have surface brightness profiles that were fitted by superimposing a Gaussian profile on top of a sech profile (Vaduvescu & McCall, 2006). Unfortunately, the fit to a larger sample of dwarfs failed to reduce the scatter. Attempting to correct for tilt and attributing some of the motion to rotation did not ameliorate the fit. The desire to reduce the scatter motivated the idea to fit baryonic

masses with a linear combination of the logarithm of the velocity dispersion and the central surface brightness, resulting in the so-called baryonic plane. This significantly improved the fit, albeit it failed to reduce the scatter to acceptable levels. However, while the baryonic plane itself was not an ideal fit, it gave rise to the idea of fitting the baryonic potential to reduce the scatter (McCall et al., 2012). To define the baryonic potential, McCall et al. (2012) referred to the Virial Theorem. The Virial Theorem is used to relate the kinetic energy E_k of baryonic matter to its gravitational potential energy E_p for a system in equilibrium, such as a galaxy:

$$2E_k + E_p = 0 \tag{1.4}$$

For pressure-supported galaxies the kinetic energy E_k is

$$E_k \propto \frac{1}{2} M\sigma^2 \tag{1.5}$$

where M is the mass of the galaxy and σ is the velocity dispersion of baryonic matter in the galaxy. The potential energy can be approximated as

$$E_p \propto -\frac{GM^2}{r_0} \tag{1.6}$$

where r_0 is a measure of the size of the galaxy, such as the scale length. Substituting Equations 1.5 and 1.6 into Equation 1.4 and rearranging

$$\frac{GM}{r_0} \propto \sigma^2 \tag{1.7}$$

The left-hand side of Equation 1.7 is referred to as the potential which can be defined as The mass, size, and motions, are quantified via the properties of baryonic matter, which include the luminosity, velocity dispersion, and scale

length.

$$P = \frac{GM_{bar}}{r_0} \propto W_{20}^2 \tag{1.8}$$

Fitting the baryonic potential yielded

$$\log(P) = (5.559 \pm 0.011) + (1.760 \pm 0.058)(\log(W_{20}) - 1.8) \tag{1.9}$$

This relationship still had a significant amount of scatter. Thus, following earlier work, the surface brightness μ_0 was introduced as a second parameter:

$$\begin{aligned}\log(P) = (5.578 \pm 0.011) \\ + (1.101 \pm 0.065)(\log(W_{20}) - 1.8) + (-0.208 \pm 0.012)(\mu_0 - 20)\end{aligned} \tag{1.10}$$

This fit was a drastic improvement from the previous one, as it reduced the scatter from $0.24\,\mathrm{dex}$ to $0.12\,\mathrm{dex}$. In an attempt to further improve the fit, it was decided to use the surface brightness corrected for the tilt. The face-on surface brightness can be written as

$$\mu_0^{i=0} = \mu_0 - 2.5\log(q) \tag{1.11}$$

where $q = b/a$ is the ratio of the semi-major to semi-minor axes of the galaxy. The fit of the baryonic potential using the face-on surface brightness yielded a significant reduction to the amount of scatter, resulting in the Potential Plane for Dwarfs being established. It is parameterized as follows:

$$\begin{aligned}\log(P) = (5.720 \pm 0.065) \\ + (1.134 \pm 0.080)(\log(W_{20}) - 1.8) + (-0.198 \pm 0.018)(\mu_0^{i=0} - 20)\end{aligned} \tag{1.12}$$

1.2.4 Dwarf Spheroidals and The Potential Plane

Prior to examining the details of processes of gas loss, it is important to establish the benchmark for the baryonic potential at or below which dSphs are known to have lost a substantial portion of their gas. It is also important to discuss how much gas was lost and the implications of the aforementioned gas loss for dSphs. The lion's share of the theoretical basis of this work was established by Ivkovich & McCall (2019), a review of which is provided here. This section will also establish the amount of gas lost by dSphs and discuss the so-called "critical potential" at which dSphs start to deviate from the Potential Plane.

Ivkovich & McCall (2019) found that dSphs systematically deviate from the Potential Plane defined by LTDs, and hence require a different relationship to describe them. The deviation is represented in Figure 1.2, where the observed baryonic potential $\log(P^{obs})$ is plotted against the predicted baryonic potential $\log(P^{pre})$ defined by Equation 1.12. Here, the observed baryonic potential $\log(P^{obs})$ is derived from observational data, and is defined as

$$P^{obs} = \frac{M_{bar}}{r_0} \tag{1.13}$$

The baryonic mass M_{bar} is comprised of the stellar component M_{str} and the gaseous component M_{gas}

$$M_{bar} = M_{str} + M_{gas} \tag{1.14}$$

The stellar mass M_{str} was obtained by using Equation 1.15 which is defined in terms of the surface photometry of the dSph in K_s, sech surface brightness profile defined in Equation 1.1, and the stellar mass-to-light ratio derived by McCall et al. (2012) $\Upsilon_{str,K_s} = 0.88 \pm 0.20$:

$$M_{str} = \Upsilon_{str,K_s} L_s \tag{1.15}$$

The ETDs are known to lack gas, so the mass of the gaseous component $M_{gas} = 0$.

Ivkovich & McCall (2019) showed that there exists a critical potential (dashed vertical line in Figure 1.2) below which dwarfs fail to retain their gas:

$$\log(P^{pre}_{crit}) = 5.74 \pm 0.19 \quad (\mathrm{M}_{\odot}/\mathrm{pc}) \tag{1.16}$$

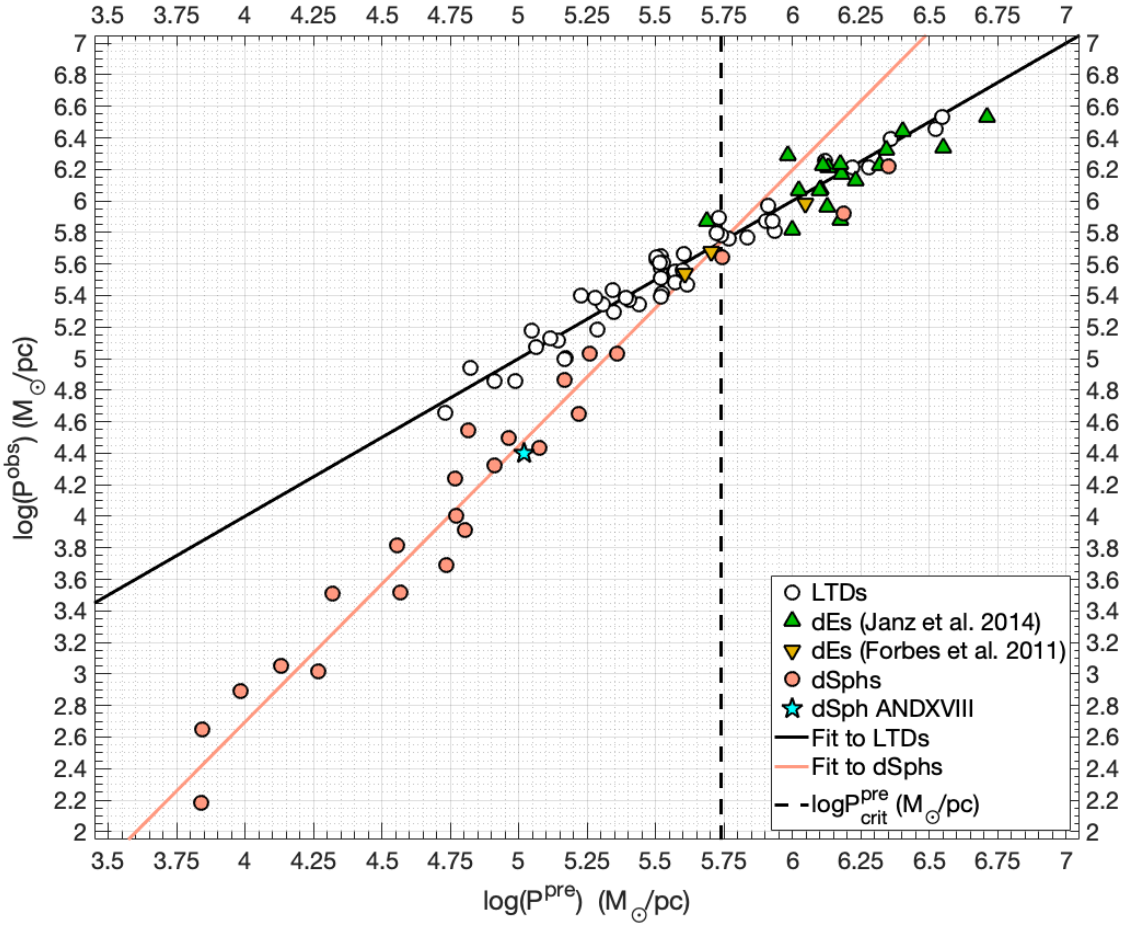

Figure 1.2: The plot of the Potential Plane as defined by McCall et al. (2012) and Ivkovich & McCall (2019). The LTDs define the Potential Plane and are marked with open black circles; dEs are marked with green triangles and dSphs are salmon-coloured; our target dSph And XVIII is plotted as a cyan star. The plot is reproduced using the data from Figure 3 in Ivkovich & McCall (2019), with 3σ confidence boundaries for Potential Plane fit to LTDs omitted. Details about And XVIII can be found in Section 3.4.

The offset of dSphs below the Potential Plane described by LTDs was attributed to M_{bar} being underestimated due to the absence of gaseous content. Ivkovich & McCall (2019) deduced that the only way that dSphs could have lost their gas was through photoevaporation due to the heating of the gas by

hot O-type stars.

1.2.5 Overview of Potential Processes of Gas Loss

There are several processes that can be held accountable for driving the gas out of dwarf spheroidal galaxies. In the following section the processes by which dwarf galaxies could have lost their gas will be described.

1.2.5.1 Ram Pressure Stripping

As a galaxy moves through the intergalactic medium it can experience "drag" which can cause it to shed its gas and dust. If a dwarf galaxy orbits a massive galaxy within a certain radius the gas will get peeled off by the hot gas located in the halo of its massive neighbour (Blitz & Robishaw, 2000). However, this will only happen if the dwarf galaxy is small and does not have sufficient gravity to retain most of its gas. Moreover, it needs to be close enough to its massive galactic neighbour to be passing through its halo (Blitz & Robishaw, 2000).

Blitz & Robishaw (2000) conducted a study on the relationship between HI gas reservoirs of 21 dSphs and dIs in the Local Group. They noticed that some dSphs may have large reservoirs of HI gas located at large distances from their centres, while some dSphs lack these reservoirs entirely. In an attempt to elucidate the source of this difference, they plotted the mass of the HI gas of dwarfs versus the distance to the nearest massive neighbour – M31 or the Milky Way Galaxy. The plot, taken directly from Blitz & Robishaw (2000) can be seen in Figure 1.3. The plot revealed that there is a sharp decline if the dwarf galaxy is located within $250\,\mathrm{kpc}$ of another galaxy. It was noted that dSphs tend to be positioned closer to their massive neighbours than dIs, which could indicate that the sharp cutoff could be a consequence of a morphological difference.

Kormendy (2014), van den Bergh (1994), and Lin & Faber (1983) suggested that dSphs are a result of ram-pressure stripping of lenticular and irregular galaxies. This conclusion was based on the star formation histories of dwarf companions of the Local Group (van den Bergh, 1994). van den Bergh (1994) showed that dwarf satellites that are close companions (with Galactocentric distance $\mathrm{R_{gc}} < 85\ \mathrm{kpc}$ of their massive neighbours) are moving through the thicker part of the intergalactic medium and were found to predominantly have a spheroidal morphology.

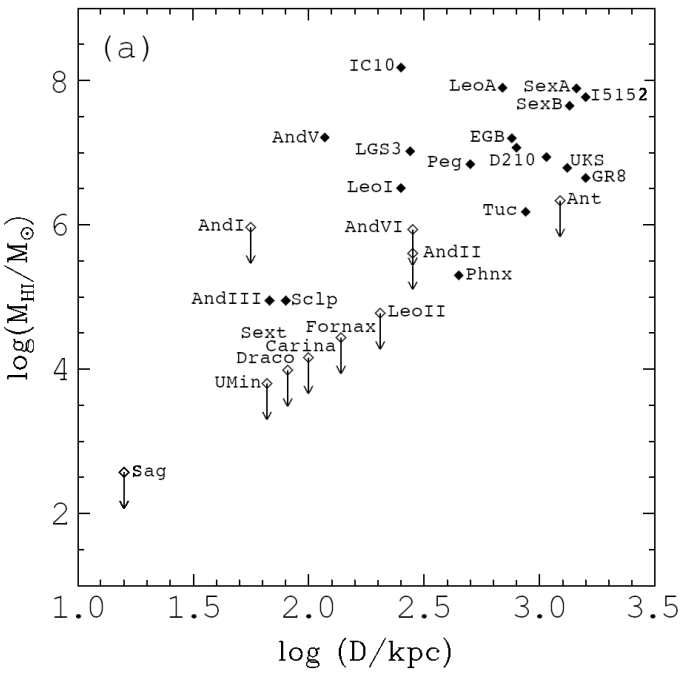

Figure 1.3: HI masses of the Local Group dwarfs plotted against the distance to the centre of the nearest massive neighbour (either M31 or the Milky Way). The plot is taken directly from Blitz & Robishaw (2000).

Dwarf satellites located at intermediate distances from their massive neighbours $89 \leq \mathrm{R_{gc}\ (kpc)} \leq 277$, such as Carina, Fornax and Leo I commonly have spheroidal or irregular morphology (van den Bergh, 1994). Dwarf satellites that are distant companions with Galactocentric distances $\mathrm{R_{gc}} \geq 390\ \mathrm{kpc}$ have irregular morphology. This suggests that the distance at which the dwarf satellite orbits its companion affects its morphology and its gas content, and hence suggests that the dSphs that are near massive neighbours are former dwarf irregulars that lost their gas. However, this was ruled out on the account of dSphs existing beyond the $250\ \mathrm{kpc}$ cutoff distance (Blitz & Robishaw, 2000).

Of course, for distant companion dwarfs in highly elliptical orbits the gas could have been ram pressure stripped while the dwarf was moving through the host galaxy's halo near the pericenter. However, this fails to explain why the Large Magellanic Cloud with a pericentre of $\mathrm{r_p} = 47\ \mathrm{kpc}$ (Lux et al., 2010)

is gas rich, while the dSphs such as Fornax and Leo I with pericentres of $r_p \sim 110\,\mathrm{kpc}$ (Lux et al., 2010) and $r_p \sim 90\,\mathrm{kpc}$ (Sohn et al., 2013) respectively are gas poor. Additionally, it does not explain the existence of dSphs like And XVIII that have not yet passed near the pericenter (Makarova et al., 2017). Moreover, if the gas was stripped away, it would produce emissions in HI and would have been detected by now (Grcevich & Putman, 2009), but attempts at detecting the aforementioned gas have thus far not succeeded.

1.2.5.2 Tidal Stripping

If a dwarf galaxy with a shallow potential well moves close to a galaxy with a large potential well, then its weakly bound gas can be gravitationally pulled away. As the small galaxy is orbiting its massive neighbour, its mass experiences a tidal gravitational acceleration – a pull towards its massive neighbour. If this tidal acceleration overpowers the gravitational force of the dwarf galaxy, then the loosely-bound mass will be torn away by the gravity of the massive neighbour (Blitz & Robishaw, 2000). Blitz & Robishaw (2000) showed that tidal stripping could play a role in the removal of gas from dSphs, but it cannot be solely accountable for the total evacuation of gas from a dSph within the $250\,\mathrm{kpc}$ cutoff, as ram pressure stripping becomes the dominant force of gas removal. It is important to note that the removal of gas via tidal stripping predicts the presence of extra-tidal stars. Extra-tidal stars are the stars that are found outside of the tidal radius of their former host, such as a galaxy or a stellar cluster. However, no extra-tidal stars have been located in the vicinity of dSphs. This points towards the conclusion that the absence of gas in dSphs is not the result of tidal stripping.

1.2.5.3 Dynamical Harassment

A galaxy in a cluster can be distorted by gravitational forces from surrounding bodies, such as other galaxies. As the galaxy is "flying" in its orbit in the cluster, the gas located in its disk gets heated by high-speed gravitational en-

counters. The heating and the gravitational pull can lead to a loss of a portion of the gas, as well as a change in morphology and its ability to form stars. However, this only applies to dwarfs in dense clusters, and cannot explain gas loss for isolated dwarfs, such as And XVIII (Kormendy, 2014; Makarova et al., 2017).

1.2.5.4 Star Formation and Supernovae Winds

It has been shown by Ivkovich & McCall (2019) that while the dSphs might have been efficient at converting their gas to stars, they have not been $100\,\%$ efficient at doing so. Moreover, Ivkovich & McCall (2019) showed that the efficiency of converting gas to stars decreases with a weakening of the potential. Therefore, gas being "tucked away" into stars cannot by itself explain the loss of gas (Ivkovich & McCall, 2019).

It was proposed by Dekel & Silk (1986) that dSphs lose their gas during the first wave of star formation as a result of supernovae and starburst-driven winds. However, it has been shown by Ferrara & Tolstoy (2000) that supernovae and starbursts alone cannot be held entirely accountable for gas removal. For these processes to completely remove the gas from a dwarf galaxy, the dwarf must be very tiny, with total mass $\mathrm{M} \leq 5 \times 10^6\ \mathrm{M}_\odot$ (Ferrara & Tolstoy, 2000). Of all the galaxies under study by Ivkovich & McCall (2019), only Canes Venatici II, Leo IV and Coma Berenices match that criteria. The rest might have lost a portion of their baryonic mass to a combination of processes, but not due to supernovae and star formation alone.

Alternatively, dwarf galaxies could have lost their gas immediately after the universe's first wave of star formation due to UV heating during the reionization epoch (Ricotti & Gnedin, 2005). Ivkovich & McCall (2019) showed that most dSphs in their sample lost more than a half of their baryonic mass. For a galaxy to remain gravitationally bound after losing most of its baryons, it needs to be dark-matter dominant. Indeed, the velocity dispersions of dSphs

reveal that dSphs are mostly comprised of dark matter (Ivkovich & McCall, 2019).

If the dark matter halo (an envelope of dark matter enclosing the galaxy) of a dwarf galaxy is sufficiently small, then it cannot accrete gas from an intergalactic medium heated by background UV radiation. That implies that these gas-poor dwarf galaxies would be "galactic fossils" from the re-ionization era (Gnedin & Kravtsov, 2006). However, early UV heating cannot explain the lack of gas in galaxies that have exhibited star formation episodes after the re-ionization epoch, such as And XVIII (Makarova et al., 2017; Karachentsev & Kaisina, 2013).

1.2.5.5 Photoevaporation

The UV radiation of O-type stars can photo-evaporate the surrounding gas over time. These stars will ionize the gas and heat it to a point that the thermal velocity becomes comparable to the escape velocity from the galaxy's gravitational pull, allowing it to escape.

Ivkovich & McCall (2019) showed that there exists a critical potential P_{crit}^{pre} below which the gas can achieve the escape velocity by being photoionized by hot O-type stars. The trend for dSphs intersects the Potential Plane at $\log(P_{crit}^{pre}) = 5.74 \pm 0.19$ $\mathrm{M}_{\odot}/\mathrm{pc}$, which occurs at an absolute magnitude in K_s of about -17.5 corresponding the escape velocity of $v_{esc} = 50 \pm 8$ $\mathrm{km/s}$. Monatomic gas expands into a vacuum at three times the speed of sound in gas at a given temperature. To reach the critical velocity it has to get heated to a temperature of $T = 13,000 \pm 4,000$ K, which is a characteristic temperature of a low-metallicity HII gas ionized by UV radiation emanating from a collection of hot O-Type stars (Ivkovich & McCall, 2019). The ionizing radiation produced by a starburst can be sufficient to ionize the bulk of gas, thereby raising it to a temperature at which the gas can escape the galaxy. It has been shown in Section 1.2.5.4 that starbursts and supernovae driven winds cannot be held solely responsible for

the evacuation of the gas from dwarf galaxies. However, photoevaporation by the overall ionizing radiation field produced by the hot O-type stars produced in a starburst can be held accountable for the removal of gas.

1.3 Neutral Oxygen in Photoionized Nebulae

Prior to delving into the specifics of line emission of neutral oxygen and hydrogen it is necessary to establish the theoretical basis and a certain intuition about how photoionized nebulae work. This section will be dedicated to a qualitative discussion of the formation of the Strömgren Sphere, ionization fronts and charge exchange in the transition zone.

1.3.1 Formation of The Strömgren Sphere

Consider a sphere of neutral atomic hydrogen gas of radius R_T as shown in Figure 1.4a. Suddenly, a source of ionizing radiation is introduced at its geometric centre. The source of radiation is emitting Q photons per second, with photon energy $h\nu \geq 13.6$ eV, where h is Plank's constant and ν is the frequency of emitted radiation.

The emitted photons will ionize and heat the gas in the immediate vicinity, creating a sphere of ionized gas surrounded by neutral gas. This sphere will contain a mix of hydrogen ions and electrons, which have a probability to recombine and create a neutral atom. The total rate of recombinations into all states r_T is governed by the density of hydrogen ions N_p and density of electrons N_e and a recombination coefficient $\alpha_A(T)$.

The recombination coefficient $\alpha_A(T)$ describes the probability of recombination to every energy level of hydrogen, while $\alpha_B(T)$ describes the probability of recombination to the excited states, and $\alpha_1(T)$ to the ground state.

The relationship between the recombination coefficients to various states can be written as

$$\alpha_A(T) = \alpha_B(T) + \alpha_1(T) \quad \mathrm{cm^3\,s^{-1}} \tag{1.17}$$

The total rate of recombination into every energy level per unit volume can be written as

$$r_T = N_e N_p \alpha_A(T) \quad \mathrm{cm^{-3}\,s^{-1}} \tag{1.18}$$

which includes the recombinations to the ground level that release a photon capable of ionizing gas.

The ionized sphere will expand in radius until the rate of recombinations of gas into excited levels throughout the volume of the sphere becomes equivalent to that of the rate of ionization:

$$Q = \frac{4\pi}{3} N_p N_e \alpha_B(T) R_S^3 \tag{1.19}$$

Rearranging Equation 1.19 yields the radius of the Strömgren Sphere:

$$R_S = \left(\frac{3Q}{4\pi N_e N_p \alpha_B(T)} \right)^{\frac{1}{3}} \tag{1.20}$$

Upon reaching $R = R_S < R_T$, the advance of the ionization front halts due to the combined effects of recombina-

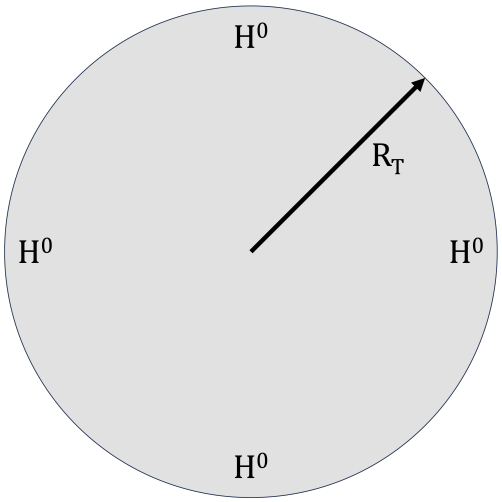

(a) A sphere of neutral hydrogen gas of radius R_T.

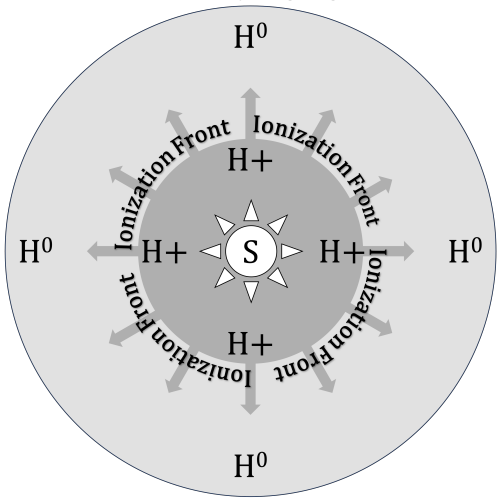

(b) A source of ionizing radiation S is introduced to the centre of the sphere. It ionizes the gas in its immediate vicinity, and the ionization front expands.

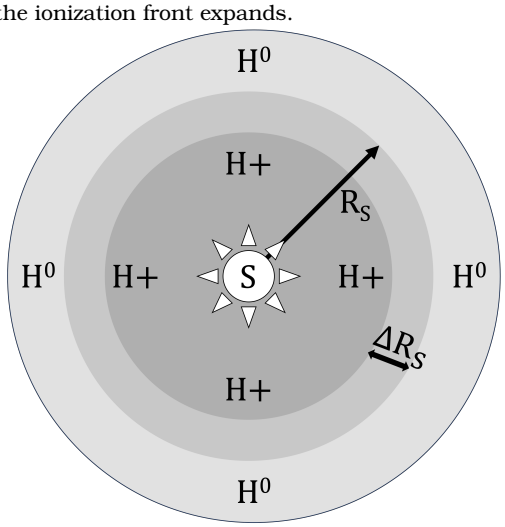

(c) The advance of the ionization front is halted by the recombinations to excited states, and Strömgren Sphere of radius R_S is formed. The ionization drops to zero over the transition zone ΔR_S.

Figure 1.4: Evolution of the Strömgren Sphere.

tions to excited levels and geometric dilution. The radius of the Strömgren Sphere therefore marks the outer edge of the ionization front, past which the ionizing radiation field is no longer present. A nebula that roughly follows the form of the Strömgren Sphere is said to be ionization-bounded. There are no ionizing photons that make it past $R = R_S$, since the last photons are absorbed by the gas over a distance of one absorption length ΔR_S

$$\Delta R_S = \frac{1}{A_0 N_H} \tag{1.21}$$

where A_0 is the photoionization cross-section of hydrogen, and N_H is the number density of hydrogen in all states. The region ΔR_S is called the transition zone and it is located within the Strömgren Sphere.

1.3.2 Neutral Oxygen Emission in The Transition Zone

For a perfectly spherical Strömgren Sphere, the inner part of the transition zone is located at distance $R_{S,i} = R_S - \Delta R_S$ from the source of ionizing radiation. The outer region of the transition zone is located at $R_{S,o} = R_S$. The inner radius of the transition zone $R_{S,i}$ marks the location where almost all of the gas is ionized, while the outer radius of the transition zone $R_{S,o}$ marks the location at which the ionizing photons are depleted and the hydrogen gas is almost completely neutral. Transition zones can also occur at the edges of neutral density enhancements (clumps) embedded within the ionized region.

The transition zone of the Strömgren Sphere is a unique region where both neutral and ionized species of hydrogen are abundant. This is due to the fact that in the transition zone, the ionization fraction of atoms for which the ionization potential is similar to that of hydrogen $E \sim 13.6$ eV goes from almost completely ionized to almost completely neutral. This mixture facilitates the augmentation of certain spectral lines via the process of charge exchange,

which enhances the abundance of neutral metal atoms through interactions between singly ionized counterparts and neutral hydrogen atoms. Of a particular interest is charge exchange between ionized oxygen and neutral hydrogen:

$$\mathrm{O}^{+}(^{4}\mathrm{S}) + \mathrm{H}^{0}(^{2}\mathrm{S}) \longrightarrow \mathrm{O}^{0}(^{3}\mathrm{P}) + \mathrm{H}^{+} \tag{1.22}$$

In this reaction, a singly ionized oxygen $\mathrm{O}^{+}(^{4}\mathrm{S})$ gets converted into a neutral oxygen atom $\mathrm{O}^{0}(^{3}\mathrm{P})$ by taking an electron from H^{0}, which turns H^{0} into a hydrogen ion H^{+}. Ionization potentials for O and H are extremely similar, with the ionization potential of $\mathrm{O}^{0}(^{3}\mathrm{P})$ being $E_O = 13.62\ \mathrm{eV}$ and the ionization potential of $\mathrm{H}^{0}(^{2}\mathrm{S})$ being $E_H = 13.59\ \mathrm{eV}$. Thus, the probability of a charge exchange reaction is high. Even though the inverse reaction also transpires, the net effect is to boost the abundance of O^{0} in the transition zone. Excitation of O^{0} atoms by collisions with free electrons followed by cascades to the ground state leads to forbidden emission lines. Charge exchange reactions further enhance the strength of these lines by increasing the abundance of O^{0}.

$$\mathrm{O}^{0}(^{3}\mathrm{P}) + \mathrm{H}^{+} \longrightarrow \mathrm{O}^{+}(^{4}\mathrm{S}) + \mathrm{H}^{0}(^{2}\mathrm{S}) \tag{1.23}$$

Because two charge exchange reactions given by Equation 1.22 and Equation 1.23 are found exclusively in the transition zones of nebulae, the [OI] emissions can be used for identifying whether the nebula is density-bounded or ionization-bounded. Additionally, the [OI] emissions can be used to determine the location of the transition zones of ionization-bounded nebulae.

1.4 Observing Ultra-Low Surface Brightness Objects

"A thousand eyes

Open inside

To grant me sight to see the end"

Miracle of Sound, *A Thousand Eyes*

1.4.1 Principles and Basics

When observing faint extended objects, the optical system must be optimized to meet several criteria. Firstly, it is imperative to ensure that the field of view is sufficient to accommodate the size of the extended object. Secondly, the low surface brightness of the objects necessitates that the rate of detection of photons is maximized.

1.4.2 Field of View

One of the most important things to consider when observing an extended object is the field of view. If the field of view is too small, it will be impossible to encompass the entirety of the extended object in a single image. This can be ameliorated by constructing a mosaic image. Alternatively, one can use an observational apparatus with a large field of view. The equation of the field of view can be written as:

$$FOV = 2\arctan\left(\frac{h}{2L}\right) \tag{1.24}$$

where h is the size of the sensor, and L is the focal length of the lens. In our case, gas can be ejected to a substantial distance away from the dSphs, and some of the angular diameters of the nebulae can also be quite large.

Therefore, it is necessary to maximize the field of view. This can be done by selecting CCD cameras with large sensors and/or by employing lenses with short focal lengths. However, L cannot be so short that the required angular resolution is not achieved.

1.4.3 Optimizing The Optical System

1.4.3.1 Rate of Detection of Photons Φ

The rate of detection Φ of photons per pixel is given in Abraham & van Dokkum (2014) as:

$$\Phi = a\left(\frac{D}{L}\right)^2 \int \frac{E(\lambda)S_\lambda(\lambda)}{hc} e^{-k(\lambda)\sec(Z)} d\lambda \tag{1.25}$$

where a is the area of the pixel, D is the aperture diameter of the optical system, L is the focal length of the optical system, λ is the wavelength at which the observations are conducted, Z is the zenith angle, $k(\lambda)$ is the extinction coefficient of the atmosphere, $\sec(Z)$ is the airmass of the object, $S_\lambda(\lambda)$ is the intrinsic surface brightness of the object at wavelength of observation λ, and $E(\lambda)$ is the efficiency of the system. (Abraham & van Dokkum, 2014).

1.4.4 The Optimization Problem

Given $S_\lambda(\lambda)$, $\sec(Z)$ and $k(\lambda)$, and a wavelength of observation λ, there are several possible ways to maximize Φ. In what will follow, the possible methods of increasing the rate of detection of photons Φ, along with their challenges and limitations are discussed.

1.4.4.1 Increase Pixel Size

Since the rate of detection of photons Φ and the field of view are both directly proportional to the area of the pixel a, one might consider using a CCD camera with bigger pixels. However, it is not difficult to imagine that the angular

resolution will start to deteriorate with an increasing pixel size, if the other parameters are held constant. While resolution is not necessarily of paramount importance when imaging extended objects, it is useful to be able to reliably recognize small-scale features in an image. Fortunately, if the background is dominated by the signal from the sky, increasing the signal per pixel can be done without adding instrumental noise by binning the pixels. Here, binning the pixels means adding the signal from each pixel in a group of $\mathrm{N} \times \mathrm{M}$ pixels, and attributing the sum to one pixel of size $(\mathrm{h} \cdot \mathrm{N}) \times (\mathrm{h} \cdot \mathrm{M})$, where h is the side length of a square pixel. One might consider making a gargantuan CCD with huge pixels. However, to keep the angular field of view the same, the focal length L would have to be increased to compensate, negating the advantage to Φ. Moreover, a giant CCD will eventually become unwieldy and costly to operate.

1.4.4.2 Optimize Efficiency $E(\lambda)$

Another way to improve Φ is to increase the efficiency of the system $E(\lambda)$. The efficiency of the system depends on the transmission of the filter $t(\lambda)$, the quantum efficiency $QE(\lambda)$ of the CCD chip as a function of wavelength, and the optical properties of the lens. However, the current technologies used to manufacture the CCD cameras, the optical interference filters, and the lens coatings, already ensure a high level of efficiency.

CCD detectors in modern science-grade cameras already have high quantum efficiencies. The SBIG cameras that are typically used for research at York University have quantum efficiencies as high as $78\% - 93\%$ (Diffraction Limited, 2024b). One way to increase the signal-to-noise ratio is to decrease the amount of dark current on the CCD. The dark current is generated by the thermal excitation of electrons and its effect can be minimized by cooling down the CCD to very low temperatures.

The ideal CCD temperature will depend on the specifications of the cool-

ing system and the CCD, and might vary based on a number of other factors. First, there is a limit on the minimum achievable CCD temperature, which stems from the architecture of the cooling system. For instance, the cooling system of SBIG CCD cameras can cool the CCDs down to $50\,^{\circ}\mathrm{C}$ below the ambient temperature. Another consideration when choosing an ideal CCD temperature is the efficiency of the cooling system. Attempting to cool the CCD past a certain temperature might take an inordinate amount of time. The advantage in having a very cold CCD may not justify the time it took to achieve that CCD temperature, especially if the cooling time reduced the observing time. Additionally, the fluctuations in the ambient temperature throughout the night of observation might cause the cooling system to adjust the temperature of the CCD accordingly. If the ambient temperature rises while the cooling system is working at maximum capacity the cooling system will attempt to keep the CCD at the same temperature, causing images to be taken at varying temperatures. The difference in temperatures at which the images were taken might slightly complicate the analysis in the best case, and introduce artifacts to the data in the worst case. Optimal minimization of the dark current is an additional consideration to keep in mind when choosing the CCD temperature. If the dark current is sufficiently reduced at a certain CCD temperature, the advantage in attempting to achieve a lower temperature might be insignificant.

One might consider maximizing the efficiency of the system by creating a more efficient lens. Approximately 5% of incident light reflects back at the lens-air boundary, if no anti-reflection coating is applied to the lens' surface. However, this has been masterfully tackled by the new generation of Canon lenses, which utilize nano-fabricated anti-reflection coatings as well as standard multi-layer anti-reflection coatings. The multi-layer anti-reflection coating is a series of thin films with different indices of refraction, such as magnesium fluoride ($\mathrm{MgF_2}$), or silicon monoxide (SiO). For destructive interference, the thickness of a layer is a quarter of the wavelength of light to be suppressed.

To provide a smoother transition between refractive indices of air and glass and thereby reduce the reflectivity further, Canon also utilizes what they refer to as Subwavelength Structure Coating. This coating is comprised of a grid of cones $220\ \mathrm{nm}$ in height made of aluminum oxide (Al_2O_3). It can reduce the reflected light to 0.01% of the incident light (Canon Science Lab: Lens Coatings).

While commercially available narrow-band filters have an outstanding 90% or higher transmission at wavelengths of interest, there is still room for improvement. To detect faint objects, one must prevent light at unwanted wavelengths from impinging on the CCD. To do so, the optical system can be equipped with filters that can entirely block out wide chunks of the unwanted parts of the spectrum. Such filters are called blocker filters or blockers. As a crude example, if one wanted to observe an object in Hα, one would want to equip the system with a blocker that only transmits wavelengths between $600\ \mathrm{nm}$ and $700\ \mathrm{nm}$. The blocker maximizes the detection of photons emanating at the wavelengths of interest from the target, thereby increasing the efficiency of the system.

To further optimize the optical system for observing the sources of line emission, a narrow-band filter can be inserted between the blocker and the CCD. These filters transmit a highly restricted range of wavelengths centred around the wavelength of interest, thus maximizing observation efficiency. The narrower the filter, the less light of unwanted wavelengths will impinge upon the detector. Blocking out all but the desired range of wavelengths significantly reduces the light from unwanted sources that might otherwise overwhelm the signal from the target.

However, unduly restricting the range of transmitted wavelengths will limit the range of target velocities and potentially reduce the number of observable targets to an unsatisfying amount. Balance between the range of target velocities and the transmission width of the optical system must be considered when designing and procuring components for the observational apparatus.

1.4.4.3 Reduce the Focal Ratio

The rate of photon detection Φ is inversely proportional to the square of the focal ratio, also referred to as the f-number:

$$f/\# = \frac{L}{D} \tag{1.26}$$

Intuitively, we want to increase the aperture D. However, increasing the aperture for a given focal length quickly becomes prohibitively expensive, and the lens becomes physically heavier.

It might seem to be more productive to reduce the focal ratio by reducing the focal length L, because the field of view and the rate of photon detections are both inversely proportional to L. However, there are limitations to how short the focal length can be for a single lens. To craft a lens with a short focal length, one must make its optics with higher curvature, which becomes increasingly difficult to craft precisely. Clearly, there is a finite amount of improvement that can be done with a single lens. A way forward is then to construct an array of lenses that have the same focal lengths and increase the total aperture by expanding the array.

1.4.4.4 A Way Forward: Multiplexing and Dragonfly

Prior to describing the apparatus that pertains to this thesis, it is necessary to describe the Dragonfly Telephoto Array, which was the inspiration for the QUAIL project. Dragonfly was developed by Abraham & van Dokkum (2014) to seek ultra-low surface brightness candidates for the missing substructures and missing satellites of galaxies. It consisted originally of an array of eight Canon $400\ \mathrm{mm}\ \mathrm{f}/2.8$ L IS II USM telephoto lenses coupled to high quality STF-8300M CCD cameras manufactured by the Santa Barbara Instrument Group (SBIG). Observations were made using broad-band SDSS *g* and *r* filters. This system was successfully used to observe extended structures with

surface brightness as faint as $\mu_{\rm B} = 30$ mag arcsec^{-2} (Abraham & van Dokkum, 2014).

An array of lenses is better for detecting faint extended sources than a single lens. This is due to the fact that for an array of lenses the effective aperture is:

$$D_{total} = D\sqrt{N} \tag{1.27}$$

where N is the number of identical lenses in the array. Substituting this into Equation 1.25 we get the improved rate of photon collection:

$$\Phi = a\,N \left(\frac{D}{L}\right)^2 \int \frac{\lambda\, E(\lambda) S_\lambda(\lambda)}{hc} e^{-k(\lambda)\sec(Z)} d\lambda \tag{1.28}$$

Even though the effective diameter of the optical system grows with N, the focal length remains as that of each lens. Thus, the effective f-number becomes faster, and the detected flux grows.

1.5 Purpose of the Thesis

The commonalities of finding the missing gas of And XVIII and locating the transition zones of nebulae are faintness and size. The purpose of this project is a proof of concept to demonstrate that with the appropriate filters and a few telephoto lenses one can detect and observe ultra-faint extended emissions despite sky brightnesses similar to that of Toronto.

Chapter 2

Apparatus

2.1 QUAIL Hardware

As introduced in Section 1.4, our approach to observing faint extended objects was to assemble a small array of fast lenses, each equipped with a narrow-band filter. In this section, the instrument called QUAIL (Quick Array of Isolating Lenses) is described in detail.

A diagram containing a breakdown of QUAIL's overall setup can be seen in Figure 2.1. All components mentioned in the figure, with the exception of the mechanical connectors and filter holders, are discussed in detail in Sections 2.1.1, 2.1.2 , 2.1.4, and 2.1.5.

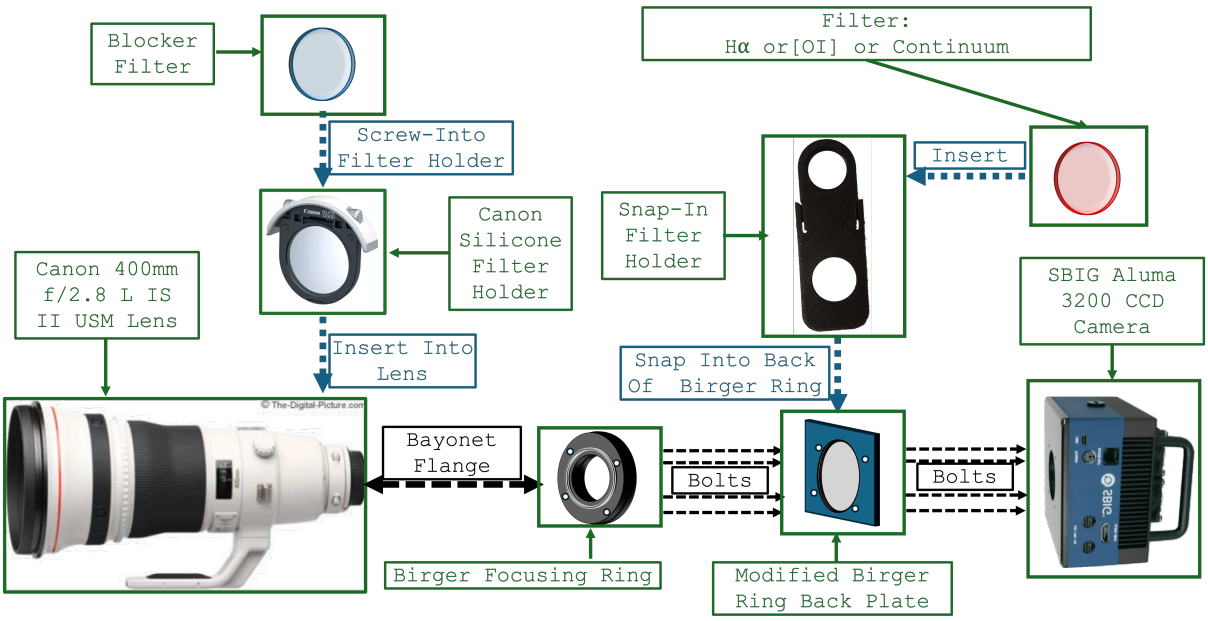

Figure 2.1: A diagram of QUAIL's setup, depicting the connections and positions of QUAIL's components. The blocker filters get screwed into the Canon filter holders, which get inserted into the lens. The narrow-band filters (either Hα, [OI] or Continuum) get inserted into the plastic snap-in filter holder. The snap-in filter holder then gets snapped into the modified Birger ring back plate. The Birger focusing ring, and its modified backplate with the snap-in filter holder get fastened to the face-plate of the SBIG Aluma 3200 camera by a set of 4 long bolts. These components then get attached to the lens via the bayonet flanges located on the back-end of the lens and the front-end of the Birger focusing ring.

2.1.1 Lenses

At the time of observation, the apparatus was comprised of two Canon $400\,\mathrm{mm}\ \mathrm{f}/2.8$ super telephoto lenses with $142.9\,\mathrm{mm}$ aperture diameters. The effective aperture diameter of the system is $\mathrm{D} = 202.1\,\mathrm{mm}$, and the effective focal ratio is $\mathrm{f}/\# = 1.98$ if identical filters are employed with each lens. The Canon lenses utilize Ultra Sonic Motors (USM) for focusing and nano-structure anti-reflection coating technology, coupled with the standard multi-layer anti-reflection coatings. QUAIL was configured to be expandable to four lenses. Once done, this would enable observation of two emission lines and associated continuum simultaneously.

2.1.2 Focusing Rings

The lenses are subject to contraction and expansion due to changes in the ambient temperature, which negatively affect the stability of focus. This was ameliorated using focusing rings from Birger Engineering that would control the Ultra Sonic Motors (USM) to ensure that the images stay crisp throughout the night.

The Birger focusing rings are attached to the Canon lenses, allowing one to adjust the focus remotely from the control computer. The focusing rings have $20,000$ digital motor steps, each corresponding to $3.15\ \mu\mathrm{m}$ of focus motion. The rings coupled with Canon's USM focusing allowed for frictionless, precise and nearly instantaneous adjustments in focus.

2.1.3 Thermometer

The focus of the Canon lenses varied with ambient temperature. To maximize the efficiency of our observations, we needed to map out the relationship between the ambient temperature and the position of Birger rings' digital motor at the which the optical system was focused. To precisely monitor the

temperature in the vicinity of QUAIL a Bluetooth-compatible thermometer was obtained from SensorPush. It was attached to the top of the QUAIL buckets which can be seen in Figure 2.6. The readings provided by the SensorPush Smart Sensor were obtained and recorded using control software installed on the control computer. The sensor was capable of recording the temperature, humidity and the barometric pressure at one minute increments. This allowed us to record the focus setpoints under different weather conditions and to devise appropriate predictive focusing functions.

2.1.4 CCD Cameras

Two Diffraction Limited Aluma 3200 Cameras were chosen for their high quantum efficiency (QE $\geq 80\%$ at $550 \leq \lambda\ (\mathrm{nm}) \leq 670$; see Figure 2.2), their large pixel arrays of 2184×1472 square pixels, with pixel width of $6.8\ \mu\mathrm{m}$, and pixel angular scale $\sim 3.5\ \mathrm{arcsec/pixel}$. The resulting field of view was $2.13^{\mathrm{o}} \times 1.43^{\mathrm{o}}$ when used with the Canon lenses (Golden, 2022; Semiconductor Components Industries, LLC, 2018).

Each camera employs a Kodak-3200 CCD with a 16-bit analog-to-digital (A/D) converter which allows for a fast readout. A diagram of the KAF-3200 CCD can be seen in Figure 2.3 and its parameters are listed in Table 2.1. The chip is equipped with four regions marked as 34 Dark, 34 Dark line and 4 Dark line in Figure 2.3. These regions will be referred to as the overscan areas. They are comprised of pixels that are shielded from incoming light, which makes them useful for monitoring the bias level and dark current of the array. It should be noted that the 2 lines of dark pixels located in the immediate vicinity of active pixels may get exposed to light, and hence might serve as a poor indicator of the amount of bias and dark current (Semiconductor Components Industries, LLC, 2018).

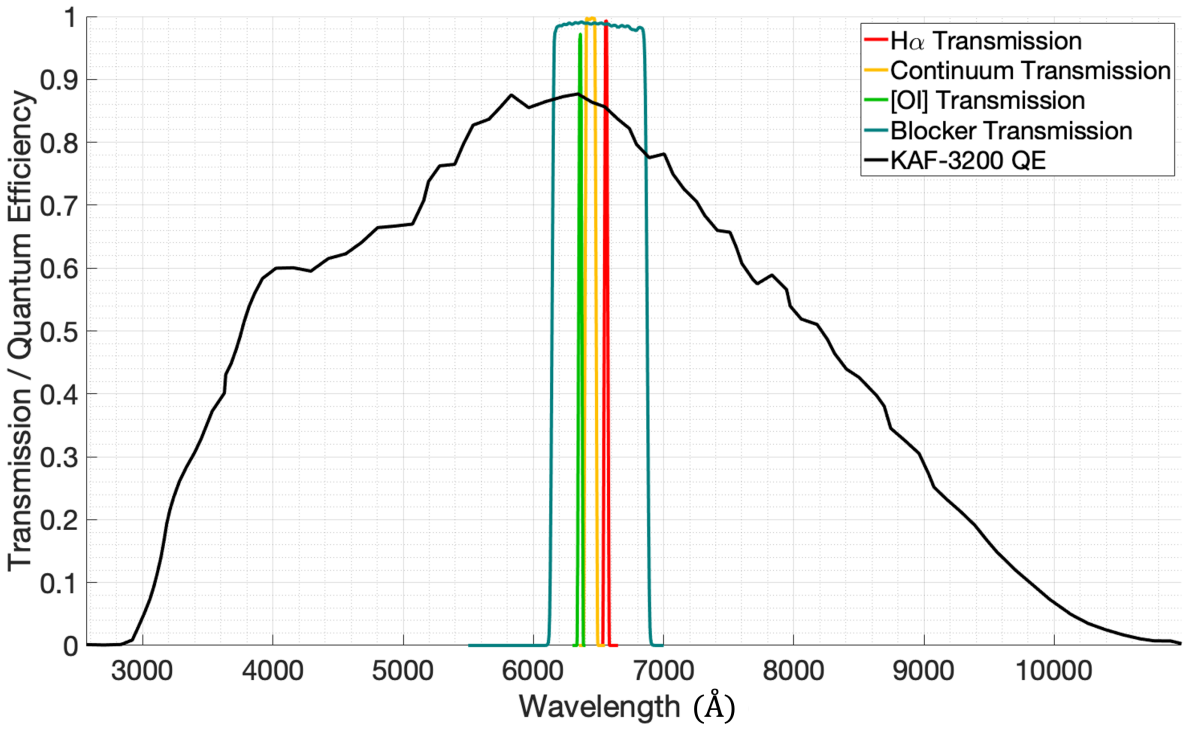

Figure 2.2: Quantum Efficiency of KAF-3200 plotted with Transmission Curves of our Hα, [OI], Continuum and Blocker Filters.

The CCD allows for 1×1, 2×2 and 3×3 on-chip binning, as well as Fast and Low-Noise pixel digitization modes. The Fast mode allows one to digitize the data from the CCD at $4\ \mathrm{MPix/s}$ with a readout noise of $\pm 11.6\ \mathrm{e^-}$, while the Low-Noise readout mode allows one to read the data at $1\ \mathrm{MPix/s}$ with a readout noise of $\pm 10\ \mathrm{e^-}$.

The cameras are equipped with a three-stage thermoelectric cooler which is capable of cooling the CCDs to $50\,^{\circ}\mathrm{C}$ below the ambient temperature. This enables the minimization of the thermal noise, commonly referred to as the dark current (Semiconductor Components Industries, LLC, 2018).

With the overscan regions included, the total number of pixels amounts to 2267×1510 pixels. The chip is read out from top to bottom, one 2267 pixels long line at a time. According to the KAF-3200 manual (Semiconductor Components Industries, LLC, 2018), the readout time of the chip follows the formula

$$t_{r_C} = 1510 * t_{line} \tag{2.1}$$

where t_{line} is the time it takes to read out one horizontal line of pixels, and 1510

is the number of vertical pixel lines.

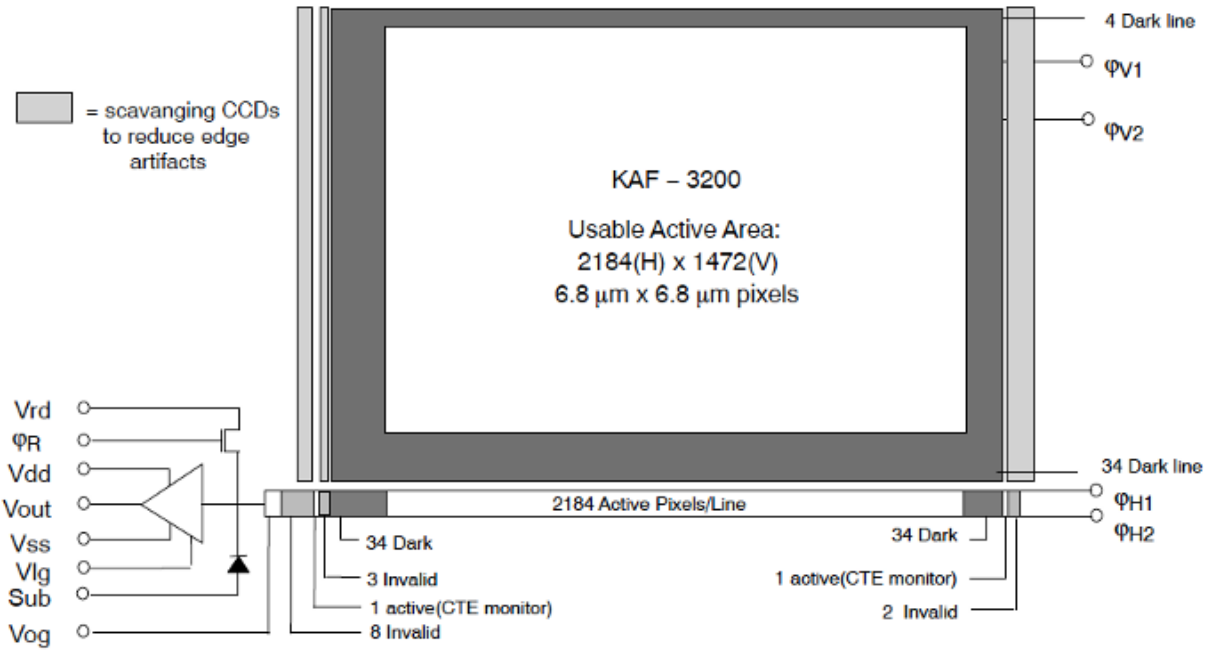

Figure 2.3: Diagram of KAF-3200 CCD Chip.(Semiconductor Components Industries, LLC, 2018)

Only the Low-Noise pixel digitization mode was utilized during observing, and every image was taken with its overscan area. Using the digitization rate of pixels in Low-Noise mode and the total number of pixels, the time it takes to digitize data is $\mathrm{t_D} = 3.42\ \mathrm{s}$. The total readout time can be calculated using

$$t_{readout} = t_{r_C} + t_D \tag{2.2}$$

which yields $3.67 \leq t_{readout}\ (\mathrm{s}) \leq 3.79$.

The camera is equipped with a USB 2.0 readout port, which has a data transfer rate of $480\ \mathrm{Mbit/s}$ (Wikipedia contributors, 2023). The camera uses 16-bit unsigned integers to represent the number of counts stored in each pixel, which means that the total amount of data in an image is $\mathrm{D_T} = 16 \times 1510 \times 2267 = 54.8\ \mathrm{Mbit}$. Therefore, the time it takes to transfer the data from the camera into the USB cable through the USB 2.0 port is $\mathrm{t_{USB}} = 0.114\ \mathrm{s}$. The Thunderbolt-3 ports located on the Mac Mini has a data transfer speed of $40\ \mathrm{Gbits/s}$ (Wikipedia contributors, 2024), so it takes $\mathrm{t_{Th}} = 1.37\ \mathrm{ms}$ to transfer

the data through it. Therefore, the data digitization time is the dominant source of delay in transferring the data to the computer. The total time it takes to transfer the data from the CCD to the computer can be calculated using

$$t_{DT} = t_{readout} + t_{USB} + t_{Th} \tag{2.3}$$

which yields $3.79 \leq \mathrm{t_{DT}\ (s)} \leq 3.91$.

Parameter	Typical Value	Unit
Total Number Pixels	2267×1510	pix^2
Total Number of Active Pixels	2184×1472	pix^2
Pixel Size	6.8×6.8	μm
Optical Fill Factor	100	%
Full-Well Capacity	$55,000$	e^-
Gain	0.41	e^-/ADU
Pixel Digitization Speed	Fast: 4; Low-Noise: 1	MPix/s
Readout Noise	Fast: ± 11.6; Low-Noise: ± 10	e^-
$QE(\lambda)$ with Microlenses (Blue, Green, Red)	$55, 70, 80$	%
Maximum Data Rate	15	MHz
Dark Current (25 °C, Accumulation Mode)	< 7	$\mathrm{pA/cm}^2$
Dark Current Doubling Rate	6	°C
Readout Time for 1 Line	$167.2 \leq t_{line} \leq 242.6$	μs

Table 2.1: KAF-3200 CCD Chip Specifications (Semiconductor Components Industries, LLC, 2018)

2.1.5 Filters

Two narrow-band line filters, a continuum filter and two blocker filters were purchased from Chroma Technology Corporation. The line filters for Hα and neutral oxygen [OI] are 2.8 nm wide at 50% of the peak transmission; the continuum filter is 8.6 nm wide and allows for precise subtraction of continuum admitted by the line filters (Chroma Technology Corporation & M. McCall, personal communication). The plot of filter transmission curves can be seen in

Figure 2.4.

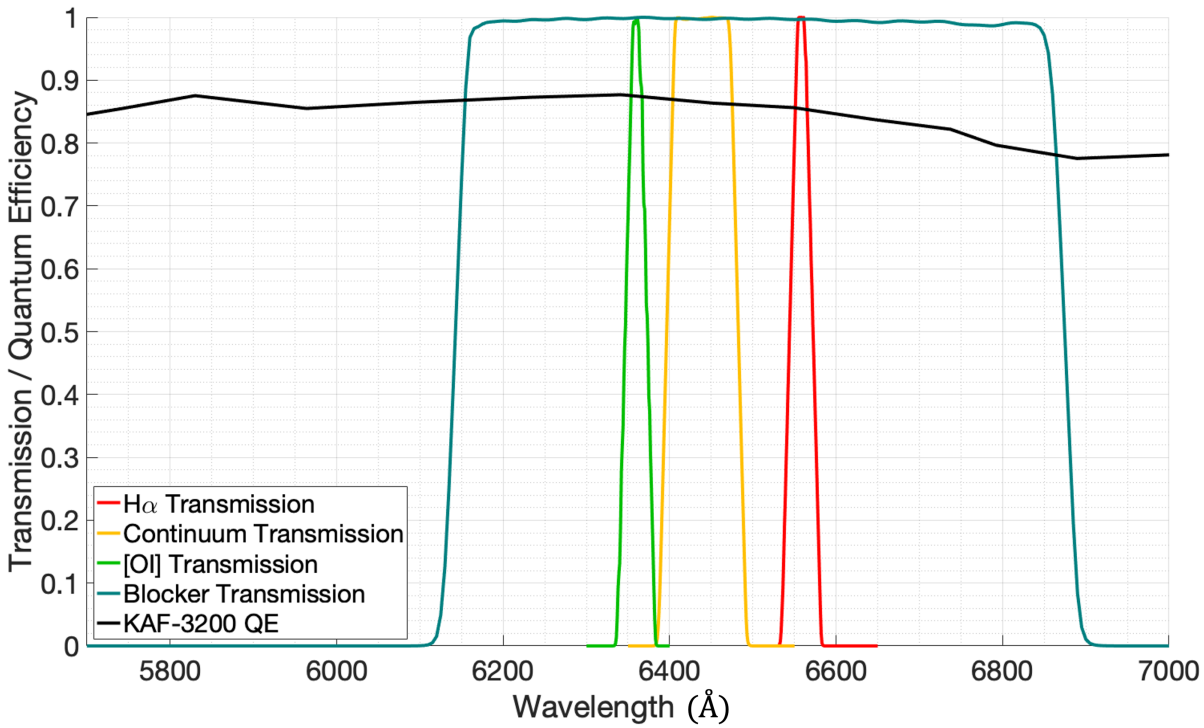

Figure 2.4: Transmission curves of Continuum, [OI], H-Alpha and Blocker filters are plotted together with Quantum Efficiency of KAF-3200 CCD chip. Transmission curves of filters are normalized to be unity at peak.

The central wavelengths of the line filters were chosen to optimize detection of emission from And XVIII and target nebulae. The central wavelength of the [OI] filter was adopted to pass the [OI] emission at $\lambda = 636.3$ nm rather than the stronger [OI] emission at $\lambda = 630.0$ nm to avoid any chance of contamination by emission from [S III] $\lambda = 631.2$ nm. The filter widths were minimized as much as the technology allowed for the f/2.8 beam coming from the Canon lenses. The continuum filter was designed to be free of contamination from night sky emission, yet close in wavelength to both the Hα and [OI] filters. Proximity to the line filters was necessary to enable accurate subtraction of the continuum background in line images. The larger width ensured that background subtraction could be accomplished without significantly degrading the noise

in the line images. The background outside of each transmission window was suppressed by a factor of 10^5 with the aid of a blocker filter colinearly inserted into the beam. The diagram of QUAIL's optics can be seen in Figure 2.1. In addition, these filters perform excellently regardless of the ambient temperature: their central wavelengths shift only by 0.003 nm per $1\,^{\circ}\mathrm{C}$ degree change in temperature.

The manufacturer provided the transmission curves for the filters in an $\mathrm{f}/2.8$ beam. The plots of the transmission curves can be seen in Figures 2.4 and 2.2, and filter properties are listed in Table 2.2. The provided transmission curves for the Hα and Continuum filters were normalized by the manufacturer such that their peak transmissions were 100%. The transmission curve for the [OI] filter was not normalized and had a peak transmission of 97%. The manufacturer stated that we should expect the Hα and Continuum filters to have a peak transmission that is at 95% or higher.

Filter	Peak Location (nm)	FWHM (nm)
Hα	655.9	2.81
Continuum	645.2	8.60
[OI]	636.0	2.62
Blocker	$614.3 \leq \lambda \leq 687.4$	73.2

Table 2.2: Properties of filters used by QUAIL. The blocker filter's peak is represented here as the wavelengths λ at which the blocker filter's normalized transmission is ~ 1.

2.1.6 Computer Interface

To control the observational apparatus and ensure a fast readout of data, we obtained a Mac Mini computer. Mac Mini has four Thunderbolt ports, which

allowed for fast transfer of data and hence minimized delays associated with communication to the observational apparatus and data download. The Mac Mini was configured with a fast 3.2 GHz Intel Core i7 Processor, 32 Gb of RAM and a 1 Tb SSD, which allowed for fast saving and processing of astronomical data. A diagram of the connections can be seen in Figure 2.5.

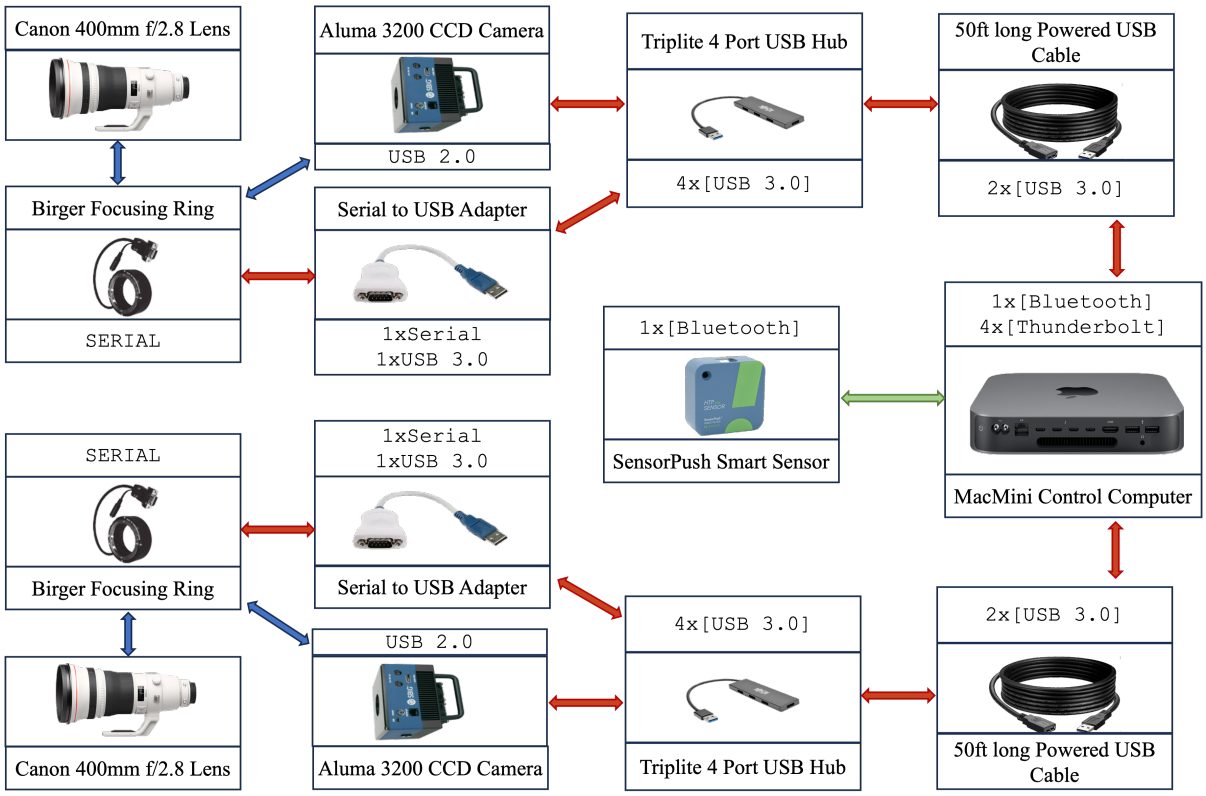

Figure 2.5: Diagram of the QUAIL setup. Red arrows represent a cable connection, blue arrows represent mechanical connections and the green arrow represents connection via Bluetooth. Images obtained from Diffraction Limited (2024a), SensorPush (2024), The Digital Picture (2024), Cheeku Technologies (2024), Apple Inc. (2024), Eaton (2024), Future Technology Devices International Limited (2024)

2.1.7 Backup Hard Drive Array

A QNAP hard drive array was employed to back up and store data obtained from QUAIL to ensure data integrity and alleviate the load on the Mac Mini's SSD. The array was composed of four 4 Gb hard drives configured to run as

RAID 6. In this configuration, up to two drives could fail without loss of data.

2.2 Observatory Hardware

QUAIL was mounted on the side of the $60\,\mathrm{cm}$ telescope of the Allan I. Carswell Astronomical Observatory. In this section, the observatory's hardware devices, layout, connections and relationships of the devices will be described. Some of the devices discussed in this section have now (in 2023) been retired, and are no longer being used to operate the dome or the telescope. These devices include all but the $60\,\mathrm{cm}$ telescope itself. Nevertheless, they were used to operate the $60\,\mathrm{cm}$ telescope and were in charge of QUAIL's pointing, so it is necessary to discuss them in order to bring clarity to their interactions later in this work.

2.2.1 The $60\,\mathrm{cm}$ Telescope

The $60\,\mathrm{cm}$ telescope in the Allan I Carswell Astronomical Observatory was used for pointing and guiding QUAIL. QUAIL was mounted onto the $60\,\mathrm{cm}$ Telescope using two of the four octagonal buckets as shown in Figure 2.6.

The telescope is capable of tracking and pointing with a high degree of precision in both Right Ascension (henceforth, α) and Declination (henceforth, δ). However, its range of motions in α is limited, as moving the telescope too far East or West could damage the telescope, the guider-scope, the SBIG camera used for regular research, its cables or its motors.

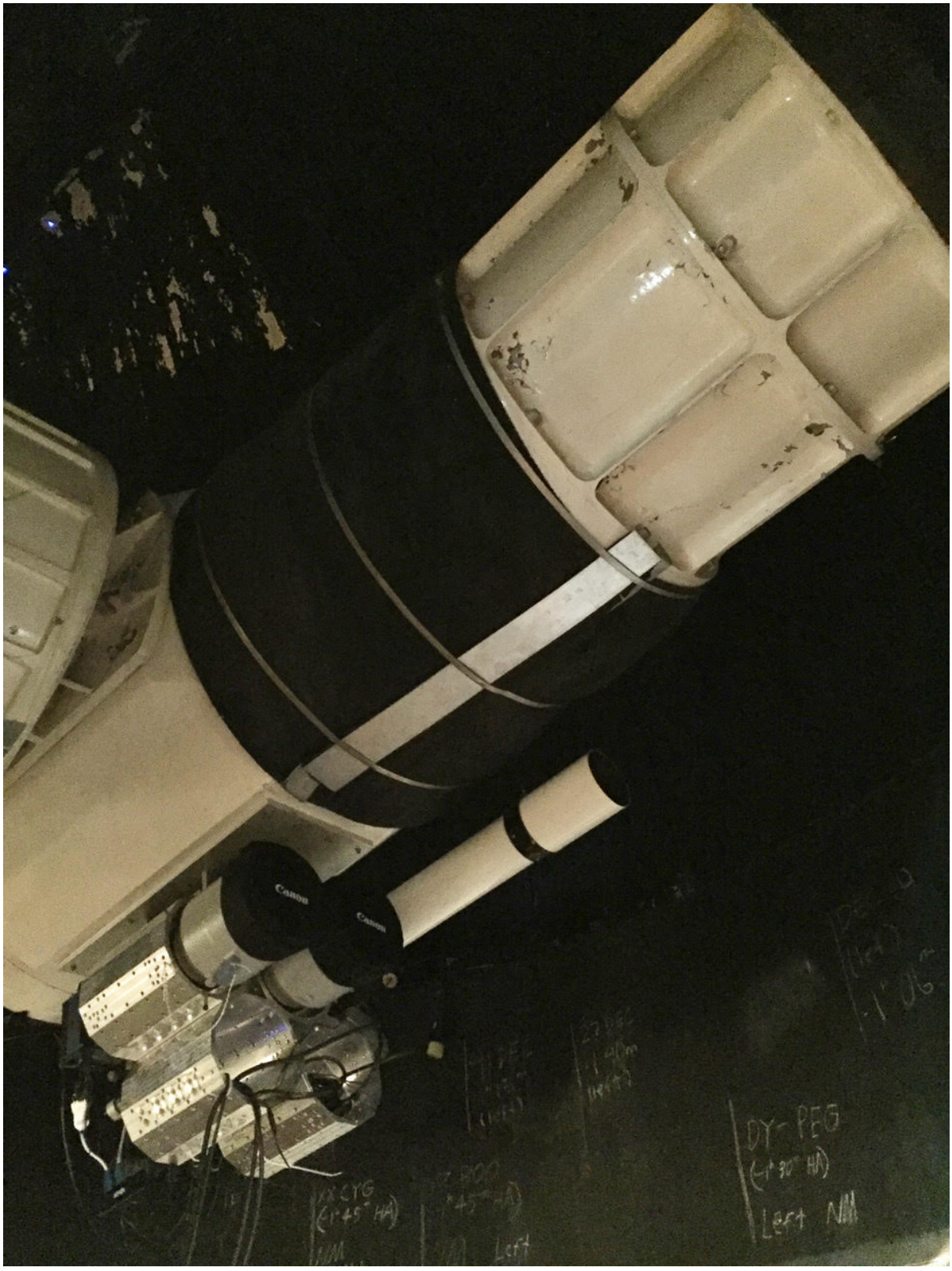

Figure 2.6: Photo of the 60 cm telescope inside of the Allan I. Carswell Astronomical Observatory at York University. The two Canon Lenses are mounted underneath the 60 cm telescope inside aluminum buckets. Image taken by Marshall McCall.

The motion range in the East-West direction is limited to hour angles

$-02^{\mathrm{h}} \leq \mathrm{H.A.} \leq +05^{\mathrm{h}}$, where H.A. is the hour angle. A cartoon of the telescope's range of motion is shown in Figures 2.7a and 2.7b.

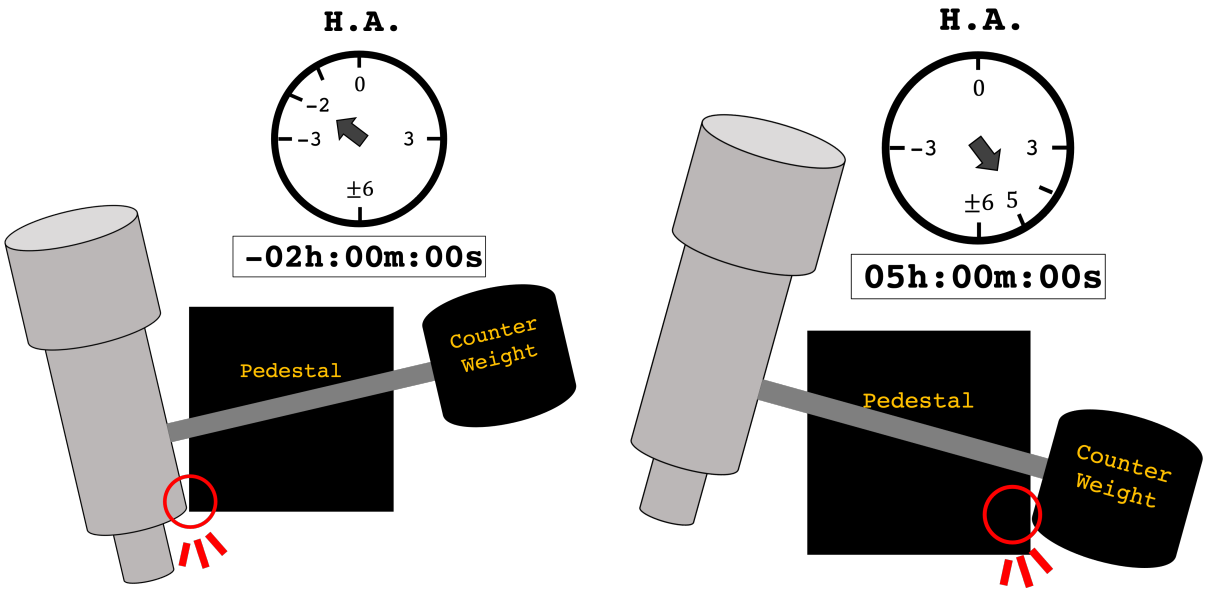

(a) If the telescope were to be pointed too far East its rear end would bump into the pedestal and damage the telescope.

(b) If the telescope were to be pointed too far West its counterweight end would bump into the pedestal and damage the telescope's α Motor.

Figure 2.7: The limits of the 60 cm Telescope.

The motion range in the North-South direction is also limited. The motion South is limited by the floor of the telescope – moving too far South will make the telescope hit the floor. Theoretically, the range of motion of the telescope North is also only limited by the floor of the observatory. However, in both cases there is little merit in pointing the telescope farther South than $\delta \leq +20^{\circ}$, or farther North than $\delta \geq +90^{\circ}$. In both cases, the field of view of the 60 cm telescope and QUAIL will be blocked by the dome wall to the South or the Life Science Building to the North. A picture of the 60 cm telescope and the dome can be seen in Figure 2.8.

Figure 2.8: Photo of the $60\,\mathrm{cm}$ telescope inside of the Allan I. Carswell Astronomical Observatory at York University. The two Canon Lenses are mounted underneath the $60\,\mathrm{cm}$ telescope inside aluminum buckets. The dome's shutter door (horizontal) can be seen under the telescope's front-end. In this position, the telescope is parked at $\mathrm{H.A.} = 0^{\mathrm{o}}$ and $\delta = +20^{\mathrm{o}}$.

2.2.2 Telescope Motors

The $60\,\mathrm{cm}$ telescope is equipped with two stepping motors – one for moving the telescope in α (henceforth, the α motor), and another one responsible for moving the telescope in δ (henceforth, the δ motor). The α motor has over twelve million steps to allow for smooth and seamless target tracking, as well as precision pointing. The δ motor has fewer encoder steps – just over seven million. Because there is no need to point the telescope directly downwards, the motor can have fewer steps while maintaining the same versatility and precision.

2.2.3 Argo Navis

The $60\,\mathrm{cm}$ telescope's motors are equipped with optical encoders that can be related to the shift in the telescope's pointing in α and δ. This is done via a device called Argo Navis, which is connected to the telescope through Dome

Tracker. The Dome Tracker is an in-house program that was developed by Matthew Cutone, Jesse Rogerson and Richard Bloch from 2008 to 2014 for the purposes of controlling the 60 cm telescope.

A detailed discussion of the Dome Tracker and its functionality can be found in Section 2.3.5.

The Argo Navis is an external device manufactured by Wildcard Innovations. Its purpose is to provide the relationship between the steps of the encoder motors of the telescope and the coordinates of the sky to which the telescope points. The number of steps traversed by the stepper motors is passed by the Argo Navis to Dome Tracker, which in turn converts them into α and δ using a conversion factor. Argo Navis also contains information about coordinates of well-known stars. Sometimes, the 60 cm telescope would lose its connection to Argo Navis, its motors, or both in the case of a particularly bad malfunction. The position of the stepper motors reported to Argo Navis could then be wrong (if the connection was lost, but the telescope got moved), which could lead to pointing the telescope in the wrong direction at best, or damaging to the telescope system at worst, as shown in Figures 2.7a

Figure 2.9: A picture of the Argo Navis device retrieved from Wildcard Innovations (2019).

and 2.7b. In such an occurrence, the telescope would be moved using The Handpaddle (discussed in Section 2.2.4) to point at a well-known star. Then, Argo Navis would be "told" that the telescope is currently pointing at that star to re-synchronize it with the sky.

2.2.4 The Handpaddle

The Handpaddle is a rudimentary "joystick" that was used to control the 60 cm telescope. A labeled photograph of The Handpaddle can be seen in Figure 2.10. It has four buttons that allow an observer to control the telescope's motion – East, West, South, North – and two buttons that control the telescope's focus. The Handpaddle is also equipped with a slider for the telescope's speed regulation and a dial for regulating the focus. The Handpaddle was mostly used to manually point the telescope using a guider scope in circumstances when the telescope lost connection to the Argo Navis and "forgot" where it was pointing. The Handpaddle was also the only device capable of focusing the 60 cm telescope's optics, as its electronic pin-out did not allow the focusing to be done from software.

2.2.5 Altair

A Windows computer named Altair was used to control the 60 cm telescope. It was responsible for tracking, driving to targets, and rotating the dome, via a program called Dome Tracker, which will be discussed in Section 2.3.5.

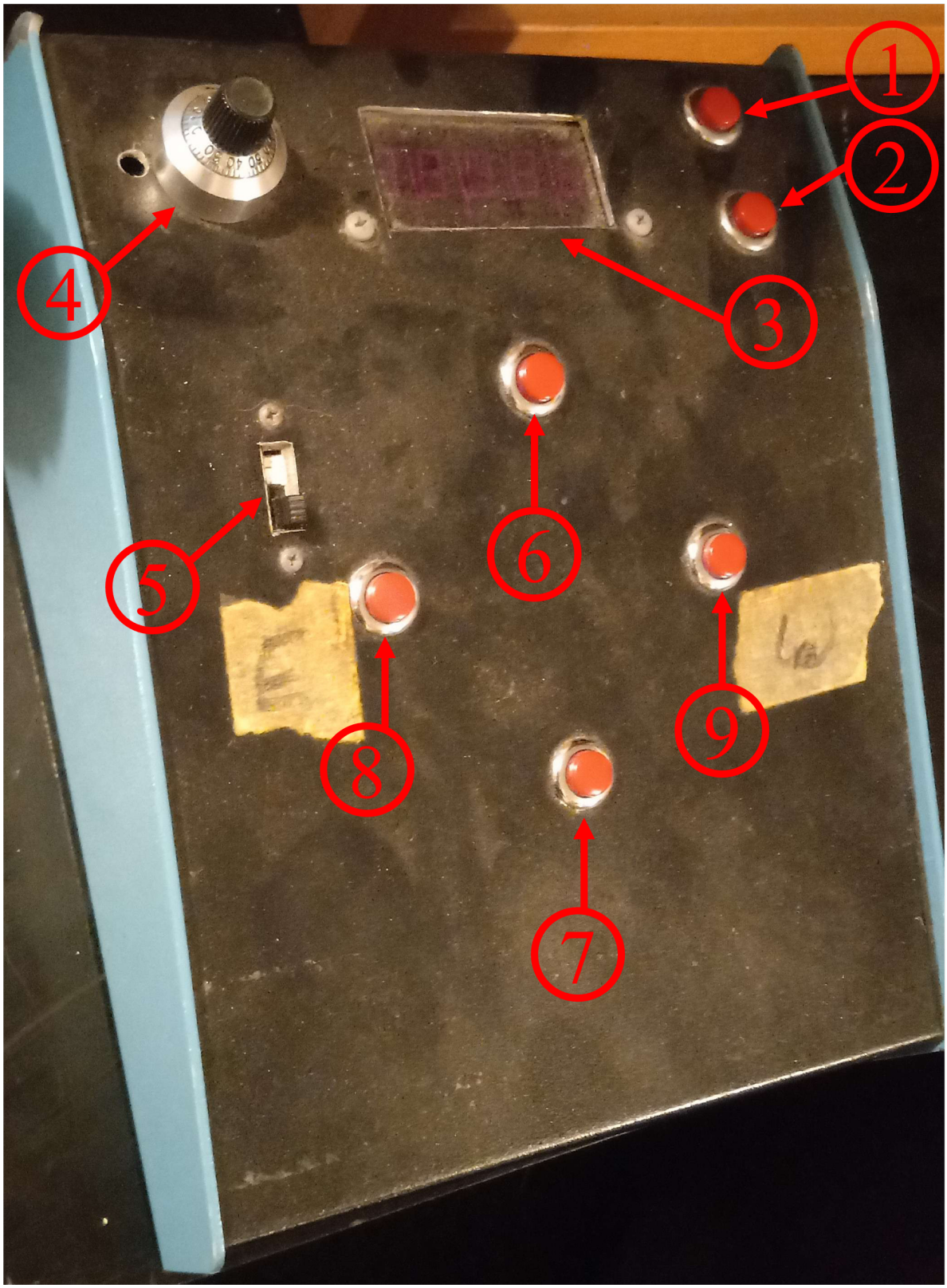

Figure 2.10: A labeled photograph of The Handpaddle. The labels pertain to the following functions of The Handpaddle: 1) Increase Focus Setpoint (Focus In); 2) Decrease Focus Setpoint (Focus Out); 3) Focus Setpoint Display; 4) Focus Speed Regulation Dial; 5) Telescope Motion Speed Regulation (Fast, Medium, Slow); 6) Move Telescope North; 7) Move Telescope South; 8) Move Telescope East; 9) Move Telescope West.

2.2.6 Dome Control Panel

The Dome Control Panel was comprised of an Arduino Mega circuit board and four (physical) buttons that could be used to control the dome's functions. It was mounted on the East side of the $60\,\mathrm{cm}$ telescope's pedestal. The Arduino circuit board had a custom pin-out and control software. The software was interfaced such that the Arduino board could be polled by Dome Tracker, while allowing simultaneous control of the dome via the physical buttons from within the observatory dome. The four physical buttons were Open Shutter, Close Shutter, Rotate Clockwise and Rotate Counterclockwise. An identical set of digital buttons existed in the Dome Tracker GUI. The dome's motors had stepper motors that reported the number of steps traversed to Dome Tracker. However, unlike the telescope's motors, the dome motor was much more primitive. The dome only had one sensor, and it had to come in contact with a matching sensor mounted to the wall of the observatory for the dome to register as being at the zero-point of rotation. Therefore, in order to operate the dome remotely, sometimes several minutes worth of rotation had to be done for the dome's stepper motors to find their zero-point before the dome could rotate to match the shutter position with the telescope's position.

2.2.7 Autoguiding Camera

The $60\,\mathrm{cm}$ telescope is permanently equipped with an SBIG STXL-6303-3 CCD Camera that is used regularly for variable star research. However, when QUAIL observations were occurring, this camera was used for refining the

pointing of the telescope at the target and for autoguiding. The autoguiding routine was developed in order to mitigate the telescope's imperfect tracking due to a previously damaged α motor shaft and poor telescope balance. However, due to the time constraints the routine was never perfected and was not utilized for observations.

The autoguiding SBIG CCD camera has 1536×1023 square pixels, each 9.0 μm wide. The camera is compatible with a wide variety of operating software, such as SkyX, which provides a convenient and stable way of operating it. The camera is also provided with drivers written by the manufacturer, which allows it to be operated by custom software.

2.3 Software

2.3.1 CCD Application Programming Interface

Despite their claims, Diffraction Limited failed to provide the software capable of controlling the SBIG Aluma 3200 cameras from Mac and Linux operating systems. This type of control software is generally referred to as an Application Programming Interface (API), and its purpose lies in allowing the used to issue commands to the cameras. To combat our inability to control the cameras, we developed our own API capable of utilizing most of the available camera functions. Our API (hitherto, SBIG API) is written in C++, and is capable of simultaneous control of an unlimited number of cameras. The code has been tested using only two cameras thus far.

A Python-based Graphical User Interface (GUI) was used to allow the user

to communicate to the SBIG API by issuing commands via the terminal. Every $100\ \mathrm{ms}$ the SBIG API checked whether a new command appeared in the terminal, and then executed any found commands. The result of executing a command was then posted back into the terminal, where it would be read out and used by the GUI to inform the user of the current status of the camera. A detailed description of the Python-based GUI can be found in Section 2.3.4. The SBIG API and the GUI developed to control QUAIL are open-source and can be found on GitHub (Anna Skrinnik, 2024). The SBIG API is capable of the following:

★ Controlling CCD Temperature: This includes enabling and disabling the cooling module of the camera, monitoring the current CCD temperature and heat sink power, and cooling the CCD down to a user-specified setpoint.

★ Regulating Shutter Functions: This allows the user to choose whether to capture images with a closed shutter (necessary for bias and dark frames), or with an open shutter (to observe targets).

★ Regulating Exposure and CCD Readout Settings: This allows the user to specify the following parameters:

1. The length of exposure. The minimum exposure time is $0.1\ \mathrm{s}$, and exposure times can be incremented in $0.1\ \mathrm{s}$ intervals.
2. Utilization of on-chip binning during the exposure. Available on-chip binning modes are 1×1, 2×2, 3×3.
3. Toggle between Fast and Low-Noise readout modes.

4. Toggle between reading out the masked regions of the CCD (overscan), or not reading out the overscan.

★ Choose to perform a Residual Bulk Image (RBI) Preflash before taking an exposure. This includes regulating the preflash length and the number of RBI post-flash readouts. The RBI Preflash exists to prevent the trapping of electrons in the charge traps. Charge traps are defects on the CCD detector which can capture charge carriers, such as electrons, but are not always cleared out during readout. This can create ghost images of bright objects on successive exposures and undermine the precision of observation. Depending on the detector, to prevent the formation of ghost images, RBI preflash would be performed before each exposure. During the preflash, the CCD gets filled with a uniform light, in our case by the IR LEDs installed in the cameras. This light fills the electron traps and prevents them from capturing electrons during the exposure. To remove the electrons sedimented on the CCD by the RBI preflash, the camera would perform Post-RBI flushes after each RBI exposure. While the RBI Preflash capability was implemented as a part of our software, it was never tested or utilized, as no formation of ghost images ever occurred during our observations.

★ Reporting the camera's status and any existing errors at $100\ \mathrm{ms}$ intervals.

★ Regulating the camera's fan speed and toggling an external status LED on and off.

★ Saving the images in FITS format with appropriate headers to a user-specified folder on the hard disk of the control computer.

★ Terminating (aborting) an ongoing exposure.

2.3.2 Birger Focusing Ring API

Birger focusing rings arrived with their own proprietary software, which made troubleshooting and operating them very easy. The Birger Ring software package also included drivers written in C. To operate the Birger Rings from the Python-based GUI we utilized an API written by Roberto Abraham (Roberto Abraham, 2012), which allowed the Birger Rings to be controlled from the terminal. This made it possible for the Birger Rings API to be integrated into the QUAIL Control Software identically to the SBIG API, which significantly streamlined the software development process.

2.3.3 SensorPush Temperature Sensor Software

In order to calculate the optimal CCD temperature and estimate the ideal focus setting for the focusing rings, we needed to be able to measure the temperature near the lenses and cameras quickly, digitally and remotely. To do so, we recorded the temperatures reported by the SensorPush digital thermometer into the headers of our images. The temperature readings were obtained by establishing a connection between the QUAIL software and the web-based application programming interface of the SensorPush thermometer.

2.3.4 QUAIL Graphical User Interface

To control the functions of the CCDs and Birger rings quickly, conveniently and automatically, a Python-based QUAIL GUI was developed. It allows the

user to regulate and monitor the functions of the Birger focusing rings and CCD cameras by clicking buttons and entering parameters, as opposed to a slow, inconvenient and often non-intuitive command-line interface. Moreover, the GUI offers the opportunity to use automated scripts that allow one to take series of exposures and automatically focus. The GUI also kept track of the ambient temperature by communicating with the SensorPush Bluetooth thermometer. The GUI has the option to save the name of the target of observation, its coordinates, and the calculated Local Mean Sidereal Time, Altitude and Azimuth into the header of the FITS file. Upon saving an image to the hard disk, the GUI displayed the image on a built-in IRAF-compatible interface. This allowed the user to utilize IRAF's `imexamine` function to check the focus, pointing and overall quality of images. A comprehensive list of QUAIL's GUI functions can be seen below, and is supplemented with a screenshot of QUAIL's GUI, which can be viewed in Figure 2.11.

Figure 2.11: A screenshot of QUAIL's Graphical User Interface.

★ Find and connect to all CCD cameras: On start of the program, the QUAIL GUI finds all devices that are compatible with the SBIG drivers and attempts to establish a connection with each. In the case of a successful connection to at least one device, it enables control of this device. In the case that no devices were found, all buttons remain disabled with the exception of the "Close" button. This allows the user to check the connection to its cameras and restart the software without damaging the camera.

★ Find and connect to all Birger focusing rings: On start of the program, the QUAIL GUI retrieves the serial numbers of all connected Birger focusing rings and assigns them to the pertinent CCD cameras.

★ Monitor Status of the Cameras: This automated software function requests all cameras to report the states of their various components every $100\ \mathrm{ms}$, and displays the results on the QUAIL's GUI for the user to see. Each camera is requested to provide the following information:

1. Current CCD temperature.
2. Heat sink power usage (how much the cooling system is exerted to maintain the current CCD temperature). This can vary from 0%, when the CCD is not being cooled, to 100% when the camera's cooling system is actively bringing the CCD to a specified temperature.
3. External fan speed. The choice of speeds are high, medium, low and off.
4. Shutter status. The shutter can be either open or closed. The minimum possible exposure length is $0.1\ \mathrm{s}$, which forces the speed of the shutter to be such that it can open and close within that time limit.

5. Exposure status. The possibilities are: preparing for exposure, exposing, and ending exposure.
6. Readout status. The possibilities are: preparing for readout, performing the readout, ending the readout and saving an image to the hard disk.

★ Regulate Cooling Control of the Cameras: This allows the user to cool the CCD down to the desired temperature, or to shut down the cooling module and allow the CCD to thermalize with the environment.

★ Regulate the Exposure Settings: This allows the user to communicate the settings mentioned in Section 2.3.1 to the CCD driver by using a GUI. Due to the large number of settings, entering these commands by hand is unwieldy and prone to error, so interfacing it through a GUI safeguards against human error and allows for remote and automated observing.

★ Monitor Exposure Progress and Taking Series: This allows the user to set the CCD cameras to take multiple identical exposures one after another, and to monitor the number of exposures taken, the number of exposures that are left, and whether or not there is an ongoing exposure. This also allows the user to start or abort exposures on all cameras simultaneously.

★ Examine Most Recent Image: The GUI is capable of displaying the most recent images right after they have been saved on the hard disk. This allows the observer to check whether the pointing of the telescope is satisfactory, or whether the dome is in the way. The GUI is capable of utilizing IRAF's `imexamine` capabilities using Python's PyRAF library. This offers the opportunity to measure the Moffat FWHM of a star, and the total signal (in counts) found

within the Moffat FWHM radius of a star. This allows the user to check the focus of each lens in a convenient and expeditious manner.

★ Control Birger Focusing Rings: This allows the user to control the focus of each lens remotely by inputting the desired setpoint.

2.3.5 New Dome Tracker

The Old Dome tracker was developed by Matthew Cutone, Jesse Rogerson and Richard Bloch from 2008 to 2014. It is a monumental and sophisticated program that was used to conduct observations using the $60\,\mathrm{cm}$ telescope and its dome for many years. QUAIL introduced a need for the $60\,\mathrm{cm}$ telescope to autoguide, and the pandemic necessitated the fine-tuning of the remote control of the observatory's systems. It was decided to upgrade The Old Dome Tracker to The New Dome Tracker by implementing additional control functions to the existing software. The New Dome Tracker is an open-source Python-based application which is available on GitHub (Anna Skrinnik, 2024).

To bring some clarity into the functions of Old Dome Tracker and New Dome Tracker, it is necessary to discuss these systems and provide some supplementary diagrams. Both programs do the following:

★ Move the telescope in α and δ at five different speed settings.

★ Set the telescope to track a celestial object by moving continuously in small increments of α.

★ Connect to the Argo Navis device and retrieve the telescope's pointing coordinates.

★ Allow the telescope to be controlled by the Handpaddle.

★ Monitor the telescope's α, δ and $\mathrm{H.A.}$.

★ Open and close the dome's shutter.

★ Rotate the dome clockwise or counter-clockwise.

★ Enable dome macros to schedule incremental rotations of the dome. This allows the dome's open shutter to follow the telescope, such that the dome does not block the field of view during observations.

★ Perform scheduled shutdown functions. Both programs would close the dome's shutter, stop the telescope's tracking motion, rotate the dome to a parked position, and drive the telescope to a parked position. The parked position of the dome was such that its solar panel would be pointed South, to allow the dome battery to recharge during the day. The telescope's parked position is located at $\mathrm{H.A.} = 0^{\mathrm{h}}$ and $\delta = -20^{\mathrm{o}}$.

As previously mentioned, New Dome Tracker was developed to extend the functions of Old Dome Tracker. The additional functions would mitigate the difference in pointing and field of view of QUAIL, and included a new autoguiding module, which would allow for the performance of corrections for tracking errors in real time. Additionally, New Dome Tracker was equipped with several new modules to ameliorate the difficulty in observing remotely during the pandemic. One of the modules was a Drive-To routine that automatically pointed the telescope to a given set of coordinates and rotated the dome until the position of the dome's shutter matched that of the $60\,\mathrm{cm}$ telescope. All features, with the exception of autoguiding were tested and utilized during the

observation period. The New Dome Tracker was specifically made with a dark red and black colour palette to minimize the light pollution that the screen will provide in the observatory, and to make it easier on the eyes of the astronomer.

Figure 2.12: A screenshot of the New Dome Tracker GUI

New Dome Tracker also had the capability of controlling the SBIG STXL-6303-3 camera (Autoguiding Camera), which was necessary for the autoguiding routine. New Dome Tracker could control the following functions of the Autoguiding Camera:

★ Connect and disconnect from the camera.

★ Poll camera status.

★ Control camera's cooling functions. This included retrieving the current

CCD temperature, cooling to a user-specified setpoint, and cessation of cooling.

★ Open and close the shutter.

★ Start an exposure with user-specified parameters.

★ Abort an exposure.

2.4 Hardware Performance

Due to a meagre number of clear nights during Fall 2021, and limited availability of the $60\,\mathrm{cm}$ telescope due to the pandemic and frequent malfunctions of the dome and the $60\,\mathrm{cm}$ telescope, it was decided that bias and dark frames would be taken only if the circumstances allowed. This was feasible because the bias of each image could be deduced from the generous overscan regions. Also, the dependence of the dark current on the CCD temperature (mentioned in Semiconductor Components Industries, LLC (2018)) and exposure length could be predicted from analysis of dark images of varying durations over a range of CCD temperatures.

For the sake of convenience of distinguishing between the two optical systems, the cameras were christened as Harlequin and Bobwhite, after species of quail.

Harlequin proved to behave as expected when it came to cooling. It cooled down to $\sim 50\,^{\circ}\mathrm{C}$ below ambient temperature quickly, and without overworking the electronic cooler. Bobwhite, on the other hand, exhibited poor cooling capabilities – it was unable to cool to temperatures colder than $-36\,^{\circ}\mathrm{C}$ below the ambient temperature. Furthermore, it took a very long time to cool down

and its electronic cooler was working at 100% of its power all of the time, thus raising the heat sink temperature to a rather high value.

(a) A photo of the Harlequin Quail retrieved from Wikipedia.

(b) A photo of the Bobwhite Quail retrieved from Wikipedia.

Figure 2.13: Pictures of the Harlequin and the Bobwhite Quail.

Due to the poor cooling capabilities of Bobwhite, it was decided that Harlequin would be responsible for taking all of the images using line filters, while Bobwhite would be used to take images through the continuum filter. Bobwhite's warmer CCD would introduce a higher dark current into images, which would hinder the detection of faint line emission.

Another issue with the Bobwhite camera was a variable focus across the field of view. The objects on the left-hand side of an image would remain crisp until approximately the middle of the image. Then, the focus gradually degraded as one moved closer to the right-hand side of the image. The upper-right corner of the image was particularly affected by this problem which was caused by a malfunction of Bobwhite's cooling system. Thus, removal of stars was a lot trickier on images taken using Bobwhite, so we nicknamed the top-right corner of the continuum images "The Corner of Dread". Because continuum images were taken simultaneously with all line images regardless of the

line filter, a vast amount of continuum data was accumulated, which made it possible to quantify and mitigate any persistent artifacts.

The decision to restrict Bobwhite to continuum observations proved to be a wise one, as many artifacts related to temperature and focusing were found in continuum data. If these artifacts plagued our line images, observing goals would have been compromised. The artifacts and their subtraction will be discussed in detail in Sections 6.1, 6.2 and 6.3.

2.5 Software Bugs, Hardware Malfunctions, and How We Handled Them

With the introduction of additional features to the functionality of the $60\,\mathrm{cm}$ telescope and its peripherals, the software became a lot more complicated. In addition to communicating with the $60\,\mathrm{cm}$ telescope, the dome, Argo Navis, and the Handpaddle, New Dome Tracker had to also control the Autoguiding Camera for autoguiding to work. Moreover, a new routine had to be implemented so that the dome would track the telescope position in such a way that QUAIL's field of view wouldn't be blocked by the dome's wall.

Originally, we planned to entirely automate the functions of the $60\,\mathrm{cm}$ telescope and the dome to accommodate the demands of social distancing. However, due to frequent power failures in the observatory, multiple failures of the dome motors, and several floods, some of the new features were never perfected. As mentioned previously, the autoguiding routine was never perfected, as it would require dedicating multiple clear nights to testing and debugging,

which we could not afford due to constraints of the weather and the pandemic. Because the $60\,\mathrm{cm}$ telescope would only track reliably (i.e., to within one pixel of QUAIL's cameras) for approximately four minutes, we resorted to restricting QUAIL exposures to $240\,\mathrm{s}$. The issue with the pointing of the dome shutter was never fully resolved either, due to frequent malfunctions of the dome motors. As a result, several exposures taken with QUAIL had to be rejected during the analysis.

Another set of issues arose from the absence of drivers for the CCD Cameras. The manufacturer failed to provide any drivers or software other than a header file that listed the capabilities of the CCD Cameras and an "example" file that connected to a camera and took a $0.1\,\mathrm{s}$ light frame exposure. Needless to say, this code hardly utilized any of the capabilities of the CCD camera, let alone the minimal capabilities that are necessary for any scientific endeavour (such as shutter control, or cooling the CCD). Due to the necessity to operate several cameras at once, take series of images with a substantial number of user requirements, monitor the CCD temperatures, and save the images to the hard drive, the control software for the CCD cameras had to be developed from the ground up.

The CCD cameras had one additional problem – Bobwhite's cooling system had a defect that caused it to be inefficient at cooling down its CCD. The defect would cause the cooling system to take a long time to cool down its CCD to the desired temperature. Additionally, Bobwhite could never cool its CCD to temperatures lower than $\sim 28\,^{\circ}\mathrm{C}$ below the ambient temperature. Unfortunately, at the time we could not send the camera to the manufacturer to get repaired

due to the constraints of the pandemic. Instead, we developed a procedure that would allow us to cool Bobwhite's CCD down in a reliable manner. The details of the procedure can be found in Section 4.1.

Additionally, the observing efficiency was further reduced by unfortunate delays caused by the software. As mentioned in Section 2.1.4, the time it takes to transfer the data to the computer is $t_{DT} = 3.85 \pm 0.06$ s. There also existed a software-related delay arising from the need to convert the raw 16-bit data into a FITS image and write it on the SSD. The time required to save a FITS image is $t_f = 2.18 \pm 0.11$ s. This value was obtained by measuring the delay between the time at which the readout of data was completed, and the time at which the data was saved into a FITS image, for 30 images of different exposure lengths with both cameras. Both cameras showed a similar delay regardless of the length of exposure or temperature of the CCD. The shortest exposure length achievable by our cameras was set by the manufacturer to 0.1 s, which would sometimes be used when taking twilight flat-field images. Thus, the total time to take the shortest possible image was $t_T = 6.03 \pm 0.12$ s, which significantly lowered the number of flat-field images that could be obtained during twilight.

The software and download speed related delays caused an additional problem. We aimed to capture the line and continuum images simultaneously for precise subtraction of the continuum from the line image. However, there were minor variations in the time required to download and save images. These variations most likely stem from the variation in the overall time needed to transfer image data from the camera to the computer t_T. At the beginning of the observation night, the time differences between the line and the continuum images

were typically insignificant. However, over the night of observations, these slight variations accumulated, resulting in a noticeable delay between the line and the continuum images. Additionally, sometimes the Mac Mini lost connection to one or both of the Birger rings or cameras. The images that were taken when the connection loss occurred were deleted, as they would lack the overscan regions and image headers.

Finally, the apparatus would occasionally shift positions, resulting in the stars in the image appearing as peanut-shaped smears. The jolt is attributed to the combined effects of the telescope's α motor shaft being damaged, which would cause the $60\,\mathrm{cm}$ telescope to jump over several steps of the stepper motor, and to the shifting of the lenses' components as the telescope passes over the meridian. Normally, this jolt only happened one or two times during a night of observations, so it did not drastically reduce the amount of data taken. The affected images were rejected from the analysis.

Chapter 3
Sample Selection

3.1 Sample Selection for Nebulae

For our study of transition zones, the selected nebulae had to satisfy the following criteria:

★ Be visible during the night in the Northern Hemisphere during Spring and Fall for a reasonable period of time. Due to the constraints of the $60\,\mathrm{cm}$ telescope, this narrowed the α range of observational targets to approximately $19^{\mathrm{h}} \leq \alpha \leq 03^{\mathrm{h}}$ during the Fall semester, as the $60\,\mathrm{cm}$ telescope can only achieve H.A. positions within the range of $-2^{\mathrm{h}} \leq \mathrm{H.A.} \leq 5^{\mathrm{h}}$. The targets also had to be located such that their $\delta \geq +10^{\mathrm{o}}$ to avoid being blocked by the wall of the dome as shown in Figure 2.8.

★ Be photoionized. Such nebulae, like HII regions or planetary nebulae, may have transition zones that can be traced via [OI] emission. Emission in Hα assists in ascertaining the shape of any ionized volume and the location of the transition zone.

★ Be large enough to appear as a source of extended emission on an image. Nebulae were constrained to be no smaller than $\sim 1'(\approx 17\ \mathrm{pix})$ across, for it to appear as an extended object.

The list of target nebulae to be observed in the Fall and their properties can be found in Table 3.1.

Fall Nebulae Observing Targets				
Target Name	NGC 6888 Crescent Nebula	M27 Dumbbell Nebula	NGC 281 PacMan Nebula	IC 5146 Cocoon Nebula
α (J2000)	$20^{\mathrm{h}}12^{\mathrm{m}}07.0^{\mathrm{s}}$	$19^{\mathrm{h}}59^{\mathrm{m}}36.4^{\mathrm{s}}$	$00^{\mathrm{h}}52^{\mathrm{m}}25.1^{\mathrm{s}}$	$21^{\mathrm{h}}53^{\mathrm{m}}29.3^{\mathrm{s}}$
δ (J2000)	$+38^{\mathrm{d}}21^{\mathrm{m}}18^{\mathrm{s}}$	$+22^{\mathrm{d}}43^{\mathrm{m}}16^{\mathrm{s}}$	$+56^{\mathrm{d}}33^{\mathrm{m}}54^{\mathrm{s}}$	$+47^{\mathrm{d}}14^{\mathrm{m}}46^{\mathrm{s}}$
Galactic Longitude (^{o})	75.4765	060.8361	123.0678	094.3820
Galactic Latitude (^{o})	+02.4250	−03.6963	−06.3065	−05.5204
$V_\odot$ (km/s)	−25.5	−42.0	−33.7	−5.50
$\lambda_{H\alpha}$ (nm)	656.33	656.37	656.35	656.29
$\lambda_{[OI]}$ (nm)	636.45	636.49	636.47	636.41
Type	HIIRegion	PlanetaryNebula	HIIRegion	HIIRegion
Size ($'\times'$)	20×10	8.0×5.7	35×30	10×10

Table 3.1: Sample of nebulae available to be observed during Fall.

3.2 Sample Selection for Calibration Targets

To properly relate the signal (in counts) collected by QUAIL to fluxes, it is imperative to include targets with well-known fluxes. The fluxes determined with QUAIL can be checked and scaled (if necessary) by observing a target for which the flux has been independently measured and published. This can be done for line and continuum filters. For instance, Hα flux of an HII region obtained with QUAIL can be compared to the Hα flux of that region provided in a publication, and QUAIL's flux value can be scaled until the expected flux value is met. Alternatively, the flux per wavelength $F(\lambda)$ of a standard star can be used together with the transmission curve of a filter $t(\lambda)$ and the raw signal from an image taken with QUAIL to relate the raw signal from an image to the flux in $\mathrm{erg\ s^{-1}\,cm^{-2}\,pixel^{-1}}$. Ideally, the fluxes of calibration targets are available for all filters used by the observational apparatus, and all fluxes can be cali-

brated. However, in the absence of published data one can utilize the relative scaling of filters to relate the flux in one spectral line to another. A detailed discussion of calibration of sources can be found in Section 6.6.

To obtain the relationship of signal to flux we have observed a standard star HD 217086. This star has a spectral type O5 was chosen as a calibration target due to its proximity to the rest of the observation targets, and due to having flux-calibrated spectra provided by Massey et al. (1988) and Carrasco et al. (2020). To further calibrate the flux, we observed the HII regions of the Triangulum Galaxy M33. The Triangulum Galaxy is located close to the rest of the targets. Many studies of the HII regions of M33 have been done, and Hα fluxes of more than fifty HII regions have been published. Among these studies are the publications by Relaño & Kennicutt (2009), Lee & Lee (2014) and Hodge et al. (1999), which allowed us to compare QUAIL's fluxes to published values for over thirty HII regions. The detailed list of calibration targets can be seen in Table 3.2.

Fall Calibration Targets		
Target Name	HD 217086 O5 Type Star	M33 Triangulum Galaxy
α (J2000)	$22^{h}56^{m}47.2^{s}$	$01^{h}33^{m}50.9^{s}$
δ (J2000)	$+62^{d}43^{m}38^{s}$	$+30^{d}39^{m}36^{s}$
Galactic Longitude (^{o})	110.2206	1133.6102
Galactic Latitude (^{o})	+02.7198	−31.3307
$V_{\odot}$ (km/s)	−16.20	−179.2
$\lambda_{H\alpha}$ (nm)	656.24	656.28
$\lambda_{[OI]}$ (nm)	635.96	636.00

Table 3.2: Sample of calibration targets available to be observed during Fall.

3.3 Sample Selection for Dwarf Spheroidal Galaxies

Galaxies to be observed using QUAIL were selected by Golden (2022). Golden (2022) selected nine dSphs from Karachentsev's Updated Nearby Galaxy Catalog (Karachentsev et al., 2013) that fit the following criteria:

★ They are sufficiently faint: The candidate galaxies had to have absolute magnitudes in the K_s fainter than $M_{K_s} = -17.5$. This would ensure that they lie below $\log(P_{crit}^{pre})$ and hence should have expelled their gas.

★ They are sufficiently far away from other galaxies: If a dSph is too close to its neighbours, there is a chance that it lost its gas via external processes. To ensure that the galaxy is sufficiently isolated, the Tidal Index was used. The Tidal Index Θ of a galaxy is defined in Karachentsev et al. (2013) as:

$$\Theta = max\left[\log\left(\frac{M_n}{D_{in}^3}\right)\right] + C \tag{3.1}$$

where M_n is the mass of its most significant neighbour and D_{in} is the distance to the most significant neighbour, also referred to as the Main Disturber. The constant $C = -10.96$ is chosen such that a galaxy with $\Theta < 0$ can be considered to be an isolated galaxy and a galaxy with $\Theta > 0$ can be considered to be a member of a galaxy group (Karachentsev et al., 2013). In our case, the Main Disturbers were M31 for Fall targets, and the Milky Way Galaxy for Spring targets. An ideal candidate for our observation would have $\Theta \leq 0$. However, a lack of potential targets that satisfied this criterion necessitated the relaxation

of the Tidal Index requirement. Hence, dSphs with $\Theta \leq 2$ were considered. A diagram of Fall dSph targets and their relative distances from M31 can be seen in Figure 3.1.

★ Their heliocentric velocities are known: The heliocentric velocity places a constraint on how much the line emission will be shifted by the Doppler effect. The heliocentric velocity of the target has to be known *a priori* in order to design a filter that would accommodate the velocity shift of its emission line.

★ That there would be no Hα emission from the Milky Way at the wavelength of emission from the target dSph: Golden (2022) ensured that the velocity shift of Hα emission associated with target galaxies made it distinguishable from any weak Hα emission that might be associated with the Milky Way's clouds of neutral hydrogen moving along the line of sight.

★ They are visible in the Northern Hemisphere during Fall or Spring.

Lists of potential dSph targets have been transcribed from Golden (2022) and can be seen in Tables 3.3 and 3.4. Unfortunately, the Spring targets could not be observed due to pandemic-related constraints. For our observations, we chose to focus on And XVIII due to the fact that it has the smallest Tidal Index (0.4) and due to it being situated high in the sky with $\delta = +45^{\circ}$.

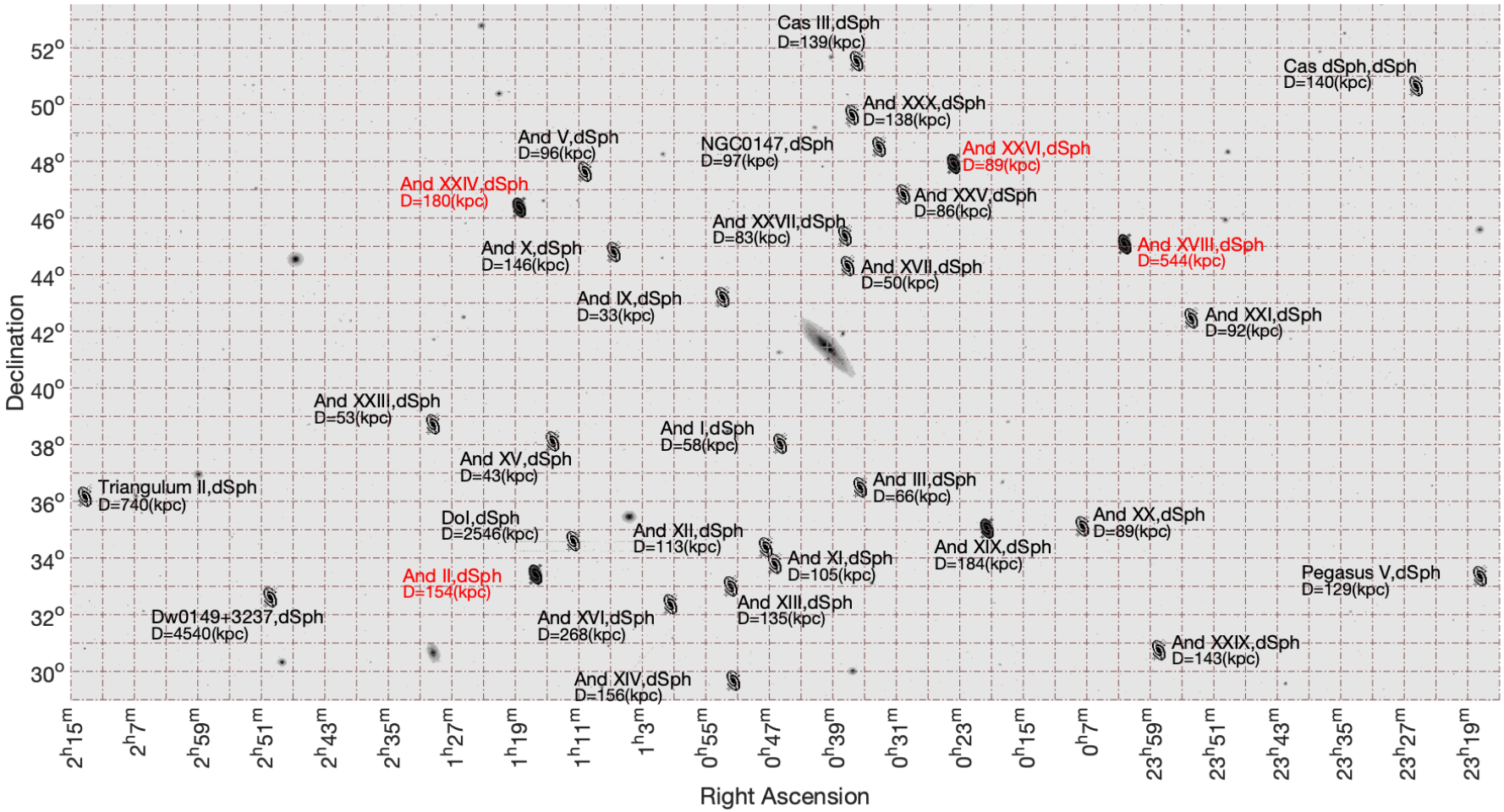

Figure 3.1: M31 is shown with its dSph satellites, and the Triangulum Galaxy M33. Galaxy names, types and their distance from M31 is displayed for all dSph satellites of M31. Galaxies with names written in red are our potential observation targets for the Fall semester.

Fall dSph Observing Targets					
Target Name	And II	And XVIII	And XIX	And XVI	And XXIV
α (J2000)	$01^h16^m29.8^s$	$00^h02^m14.5^s$	$00^h19^m32.1^s$	$00^h59^m29.8^s$	$01^h18^m30.0^s$
δ (J2000)	$+33^d25^m09^s$	$+45^d05^m20^s$	$+35^d02^m37^s$	$+32^d22^m36^s$	$+46^d21^m58^s$
Galactic Longitude (^{o})	128.9186	113.8879	115.5824	124.9059	127.7893
Galactic Latitude (^{o})	-29.1611	-16.9171	-27.3724	-30.4641	-16.2502
$V_\odot$ (km/s)	-194.0	-332.0	-111.0	-385.0	-128.0
$\lambda_{H\alpha}$ (nm)	655.86	655.55	656.04	655.44	656.00
M_K	-12.3	-12.2	-11.4	-11.3	-10.1
Tidal Index	2.0	0.4	1.9	1.5	1.9
Distance (Mpc)	0.65	1.36	0.93	0.52	0.6

Table 3.3: Sample of dSphs available to be observed during Fall (Golden, 2022).

Spring dSph Observing Targets				
Target Name	Leo I	Leo II	CVn I	CVn II
α (J2000)	$10^h08^m26.9^s$	$11^h13^m29.2^s$	$13^h28^m03.5^s$	$12^h57^m10.0^s$
δ (J2000)	$+12^d18^m29^s$	$+22^d09^m17^s$	$+35^d33^m21^s$	$+34^d19^m14^s$
Galactic Longitude (^{o})	225.9858	220.1693	74.3056	113.578
Galactic Latitude (^{o})	49.1124	67.2313	79.8229	82.7031
$V_\odot$ (km/s)	282.5	78	30.9	-128.9
$\lambda_{H\alpha}$ (nm)	656.9	656.45	656.35	656
M_K	-14.1	-12.2	-11	-7.2
Tidal Index	1.4	1.6	1.5	2.0
Distance (Mpc)	0.25	0.21	0.22	0.16

Table 3.4: Sample of dSphs available to be observed during Spring (Golden, 2022).

3.4 And XVIII and The Potential Plane

3.4.1 And XVIII Predicted Potential

Our target dSphs And XVIII was not included in the sample of dSphs modelled by Ivkovich & McCall (2019). Therefore, it is imperative to calculate And

XVIII's Observed Potential P^{obs} and the Predicted Potential P^{pre} and place it on the Potential Plane to estimate the mass and location of its missing gas. The works of Makarova et al. (2017) and Tollerud et al. (2012) provide the parameters for And XVIII needed to calculate its location on the Potential Plane. The stellar mass M_{str} provided by Makarova et al. (2017) was estimated from a detailed analysis of a colour-magnitude diagram of stars within And XVIII. These values are listed in Table 3.5.

Parameters of And XVIII				
Parameter	Symbol	Value	Units	Reference
Total Stellar Mass	M_{str}	$(4.2 \pm 0.3) \times 10^6$	$M_\odot$	1
Distance	d_{pc}	$1.33^{+0.06}_{-0.09}$	Mpc	1
Central Surface Brightness in V	$\mu_{0,exp,V}$	23.96 ± 0.02	$\frac{\text{mag}}{\text{arcsec}^2}$	1
Velocity Dispersion	σ_{los}	9.7 ± 2.3	km/s	2
Exponential Scale Length	$r_{0,exp,V}$	26.2 ± 0.4	arcsec	1
Axial Ratio	$q = b/a$	0.99		1
References:	1: (Makarova et al., 2017); 2: (Tollerud et al., 2012)			

Table 3.5: Published Parameters of And XVIII.

Makarova et al. (2017) used an exponential function to model the surface brightness profile of And XVIII. Meanwhile, the Potential Plane and the Critical Potential P^{pre}_{crit} were found by fitting the surface brightness profiles of dwarfs in K_s with a sech function. This was done because the sech function was optimal at describing the flat cores and exponential wings of dSphs and dIs. Therefore, to place And XVIII with respect to the Potential Plane it is necessary to fit its surface brightness with a sech function.

To do so, the data in Figure 6 in Makarova et al. (2017) was digitized and fit with a sech function. The data of choice are the surface brightness in

Johnson-Cousins V-band. The stellar contamination from the Milky Way was previously accounted for by Makarova et al. (2017).

The sech surface brightness profile has the form

$$I_s(r) = \frac{2I_{0,s}}{e^{\frac{r}{r_{0,s}}} + e^{-\frac{r}{r_{0,s}}}} \tag{1.1}$$

where I_s is the fitted sech intensity at distance r from the dwarf's centre, $I_{0,s}$ is the central intensity of the sech fit, and $r_{0,s}$ is the scale length of the sech fit. The sech fit to the data yielded an unsatisfying result, so a superposition of a sech and a Gaussian surface brightness profiles were used to fit the data. It should be noted that some dSphs in Ivkovich & McCall (2019) were also fitted with a superposition of sech and Gaussian surface brightness profiles. The Gaussian surface brightness profile can be written as

$$I_G = I_{0,G} e^{-\frac{1}{2}\left(\frac{r}{r_{0,G}}\right)^2} \tag{3.2}$$

The model that was used can be written as

$$I_T = I_s + I_G \tag{3.3}$$

The parameters of fitted surface brightness profiles can be seen in Table 3.6 and the plot of the fits can be seen in Figure 3.2.

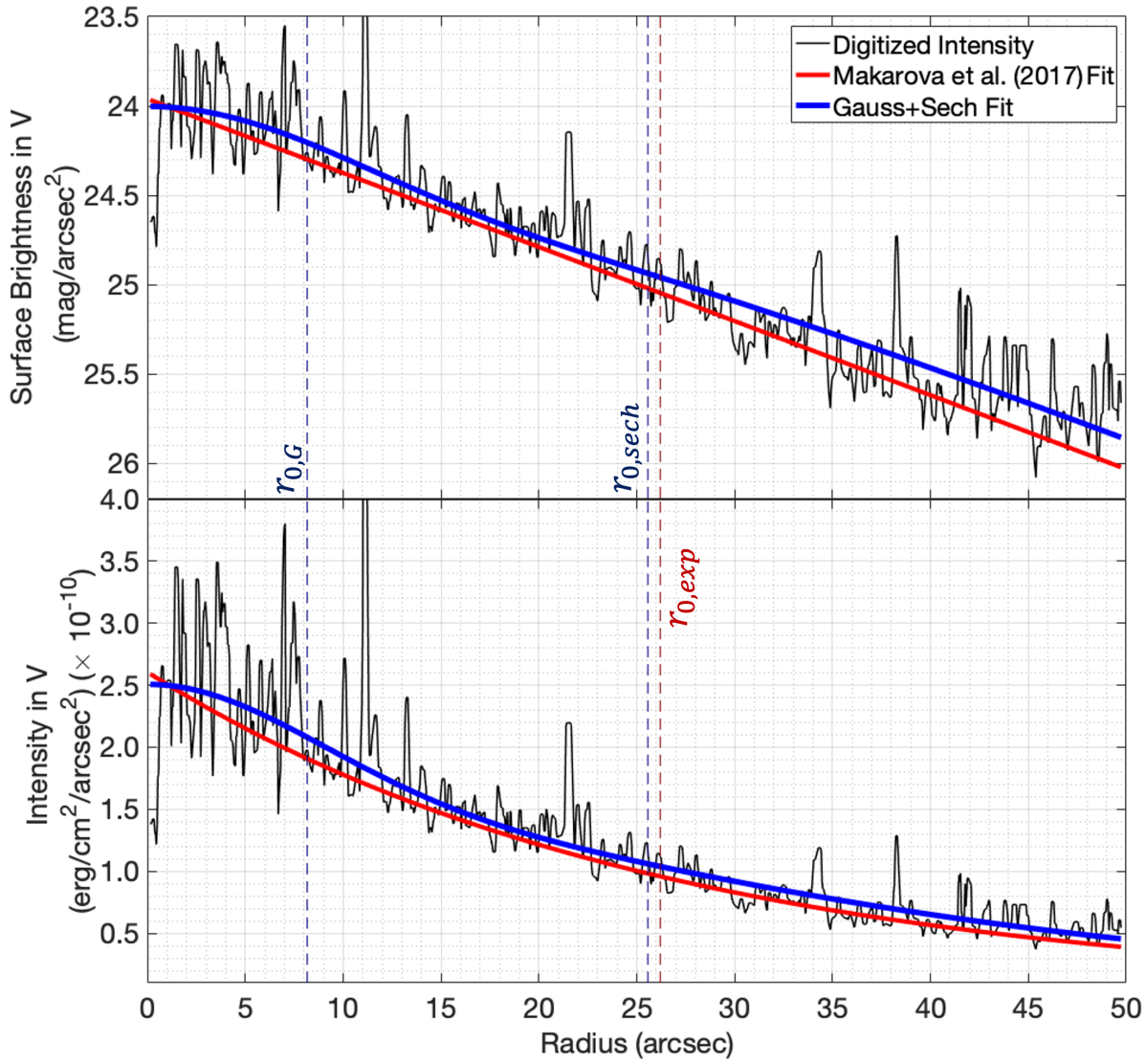

Figure 3.2: Sech and Exponential Fits to the Intensity and Surface Brightness in V for And XVIII. The digitized data is plotted in black. Exponential fit provided by (Makarova et al., 2017) is plotted in red. In the legend entry "Gauss+Sech Fit", the word "Gauss" stands for Gaussian, and the superimposed Gaussian+Sech Fit is plotted in blue. The vertical lines marked with $r_{0,G}$, $r_{0,sech}$ and $r_{0,exp}$ show the positions of the scale lengths of the Gaussian, Sech and Exponential profiles respectively.

We can convert the central surface brightness of the sech profile using the mean $V - K_s$ colour provided for dSphs in Ivkovich & McCall (2019), which is $V - K_s = 2.49 \pm 0.27$. Thus, the central surface brightness μ_{0,K_s} is

$$\mu_{0,K_s} = 21.98 \pm 0.28 \quad \text{mag arcsec}^{-2} \tag{3.4}$$

Parameters of And XVIII's Surface Brightness Profiles			
	Exponential Profile	Sech Profile	Gaussian Profile
Central Intensity I_0 $(\mathrm{erg\,cm^{-2}\,arcsec^{-2}}) \times 10^{-10}$	$I_{0,exp} = 2.61 \pm 0.12$	$I_{0,s} = 1.63 \pm 0.10$	$I_{0,G} = 0.88 \pm 0.09$
Scale Length r_0 (arcsec)	$r_{0,exp} = 26.2 \pm 0.4$	$r_{0,s} = 25.56 \pm 1.45$	$r_{0,G} = 8.16 \pm 0.77$
Central Sufrace Brightness μ_0 $(\mathrm{mag\,arcsec^{-2}})$	$\mu_{0,exp} = 23.96 \pm 0.02$	$\mu_{0,S} = 24.47 \pm 0.07$	$\mu_{0,G} = 25.14 \pm 0.12$

Table 3.6: Parameters of And XVIII's Fitted Surface Brightness Profiles.

To determine the placement of And XVIII with respect to the Potential Plane the central surface brightness needs to be corrected to face-on. This can be done using Equation 1.11, which assumes an oblate spheroidal geometry and axial ratio provided in Table 3.5:

$$\mu^{i=0}_{0,S,K_s} = \mu_{0,K_s} - 2.5\log(q) = 21.99 \pm 0.28 \quad \mathrm{mag\,arcsec^{-2}} \tag{3.5}$$

Here q is the ratio of the semi-minor to the semi-major axis of the isophotes.

Using Equation (1) from Ivkovich & McCall (2019) and the measured line-of-sight velocity dispersion σ_{los} of stars given in Table 3.5, we can calculate the corresponding 20% width that HI emission would have if it were present:

$$W_{20} = (8\ln(5))^{1/2}\sigma_{los} = 34.8 \pm 8.2 \quad \mathrm{km/s} \tag{3.6}$$

Taking the logarithm yields $\log(W_{20}) = 1.54 \pm 0.10$.

Using Equation 1.12 and the values obtained for $\mu^{i=0}_{0,K_s}$ and $\log(W_{20})$ we can calculate the Predicted Potential for And XVIII. One might note that the left-hand side of Equation 1.12 is labeled as $\log(P^{obs})$, while we are calculating $\log(P^{pre})$. This is because $P^{obs} = P^{pre}$ for dSphs that lie on the Potential Plane.

However, we are yet to determine whether And XVIII lies on the Potential Plane, and the calculation using Equation 1.12 is done to determine its predicted position on the Potential Plane.

$$\log(P^{pre}) = 5.02 \pm 0.71 \quad \mathrm{M}_{\odot}/\mathrm{pc} \tag{3.7}$$

This is below $P^{pre}_{crit} = 5.74 \pm 0.19\ \mathrm{M}_{\odot}/\mathrm{pc}$ listed in Ivkovich & McCall (2019), which is the value below which the relationship between P^{obs} and P^{pre} for dSphs diverges from the Potential Plane.

3.4.2 And XVIII Observed Potential

The baryonic mass is given by Equation 3.8:

$$M_{bar} = M_{gas} + M_{str} \tag{3.8}$$

where M_{gas} is the mass of gas in the galaxy and M_{str} is the stellar mass of the galaxy. Because we are operating under the assumption that dSphs have lost all of their gas, the baryonic mass of the galaxy becomes equivalent to its stellar mass. Therefore, the above equation becomes $M_{bar} = M_{str}$. The stellar mass of And XVIII is provided by (Makarova et al., 2017) and can be seen in Table 3.5. The value of $r_{0,s}$ needs to be converted into parsecs using

$$r_{0,s,pc} = d_{pc} \tan(r_{0,s}) = 165^{+17}_{-20} \quad \mathrm{pc} \tag{3.9}$$

where d_{pc} is the distance in parsecs. Substituting the result of Equation 3.9 and the stellar mass provided by Makarova et al. (2017) into equation 1.13

yields

$$P^{obs} = \frac{M_{str}}{r_{0,s,pc}} = 2.54^{+0.56}_{-0.40} \times 10^4 \quad \mathrm{M}_\odot/\mathrm{pc} \tag{3.10}$$

Taking the logarithm of the result of Equation 3.10 yields

$$\log\left(P^{obs}\right) = 4.40^{+0.09}_{-0.08} \quad \mathrm{M}_\odot/\mathrm{pc} \tag{3.11}$$

Based on $\log(P^{obs})$ and $\log(P^{pre})$ the location of And XVIII relative to the Potential Plane is displayed in Figure 1.2.

3.4.3 Mass of Lost Gas

In this section we will use the results obtained in Sections 3.4.1 and 3.4.2 to estimate the mass of gas that was lost by And XVIII. Knowing P^{pre}, we can calculate the total amount of baryonic mass that And XVIII had before it lost its gas. Multiplying $\log(P^{pre})$ by the sech scale length yields the baryonic mass in solar masses prior to gas loss:

$$\log(M_{bar}) = 7.24^{+1.79}_{-0.35} \quad \mathrm{M}_\odot \tag{3.12}$$

Subtracting the stellar mass from the upper and lower limits of the baryonic mass yields the lower and upper caps on the amount of gas mass that was lost by And XVIII:

$$\log(M_{gas}) = 7.12^{+1.79}_{-0.35} \quad \mathrm{M}_\odot \tag{3.13}$$

3.4.4 Location of Missing Gas

In this section an estimate of the whereabouts of And XVIII's missing gas will be provided.

According to Makarova et al. (2017), there was a burst of star formation that happened $12 - 14$ Gyr ago, and more star formation activity $1.5 - 8$ Gyr ago. That means that there was still gas left in And XVIII after the first burst of star formation, or some of the gas that got ejected by the first wave of star formation fell back into the galaxy. We can use the lower and upper caps on the occurrence of star formation activity to estimate the location of the gas, and hence whether its edge remains inside of our field of view. If the ejection was isotropic, there would be gas on near and far sides within the field no matter how big the nebula has become.

However, the gas wouldn't be simply flying away from the dSph at the escape velocity. Since the total mass of dSphs is dominated by dark matter, the dSph will continue to project its gravitational force, despite the loss of gas (Ivkovich & McCall, 2019). Therefore, the gas will be gradually decelerating. We will approximate that at the time of the photoevaporation t_0, the average location of the gas was at $r_0 = r_{1/2}$ where $r_{1/2}$ is the half-light radius (i.e. radius of the volume containing half of the light) from the centre of the galaxy. We will approximate that the gas took the form of a thin spherical shell. The acceleration of the shell of gas can be written using Newton's second law

$$a\hat{r} = -\frac{GM}{r^2}\hat{r} \tag{3.14}$$

where M is the dynamical mass M_{dyn} of the dSph, a is the acceleration due to the gravity, and r is the distance from the gas to the centre of dSph, and $\hat{r}$ is the radial direction pointing outward from the centre of the dSph. Because the expansion of the spherical shell will have a spherical symmetry, we are going to omit the $\hat{r}$ notation to avoid redundancy. We will assume that the gas radially expands due to photoevaporation, while decelerating due to the gravitational pull of the dwarf. Velocity as a function of time t can then be written as

$$v(t) = v_0 + at \tag{3.15}$$

where v_0 is the initial escape velocity. Substituting the acceleration yields

$$v = v_0 - \frac{GM}{r^2}t \tag{3.16}$$

The position can be written as

$$r = r_0 + vt + \frac{1}{2}at^2 \tag{3.17}$$

Substituting Equations 3.14 and 3.16 into Equation 3.17 yields

$$r = r_0 + v_0 t - \frac{GM}{r^2}t^2 - \frac{GM}{2r^2}t^2 \tag{3.18}$$

This can be further simplified to yield

$$r^3 - r^2(r_0 + v_0 t) + \frac{3GM}{2}t^2 = 0 \tag{3.19}$$

The radius of the expanded shell r can be calculated by finding the roots of this equation.

The positions are going to be calculated using two possible choices for the initial velocity v_0. The first choice for v_0 stems from the escape velocity defined by the dynamical mass of the galaxy. The second choice of v_0 is the velocity at which the photoionized gas expands into a vacuum. These two choices for the initial velocity v_0 define the two scenarios for which the position of gas will be computed. For both scenarios, r_0 is defined as the half-light radius $r_{1/2}$, and M is the dynamical mass of the galaxy M_{dyn}.

From Ivkovich & McCall (2019), the dynamical mass of the galaxy can then be calculated using

$$M_{dyn} = 6G^{-1}\sigma_{los}^2 r_{1/2} = 6G^{-1}\sigma_{los}^2 r_{0,s}\left[\frac{r_{eff}}{r_{0,s}}\right]\left[\frac{r_{1/2}}{r_{eff}}\right] \tag{3.20}$$

where r_{eff} is the radius of the isophote encompassing half of the light, $r_{0,s}$ is the scale length of the sech profile, σ_{los} is the line-of-sight velocity dispersion given in Table 3.5, and G is the gravitational constant. The relationship between the effective radius r_{eff} and half-light radius $r_{1/2}$ can be estimated using Equation (24) given in Ivkovich & McCall (2019):

$$\frac{r_{eff}}{r_{1/2}} = \frac{3}{4} \tag{3.21}$$

Similarly, the ratio of the effective radius r_{eff} and the scale length of the sech profile $r_{0,s}$ is provided in Ivkovich & McCall (2019):

$$\frac{r_{eff}}{r_{0,s}} = 1.80584 \tag{3.22}$$

Expressing the half-light radius in terms of the sech scale length yields:

$$r_{1/2} = \frac{4}{3}\,1.80584\,r_{0,s} \tag{3.23}$$

The initial velocity v_0 for the first scenario is the escape velocity, which can be calculated using Equation (30) from Ivkovich & McCall (2019):

$$v_{esc} = \left[\frac{GM_{dyn}}{r_{1/2}}\right]^{1/2} \tag{3.24}$$

For the second scenario, the escape velocity for the photoevaporated gas is $v_{esc,p} = 50 \pm 8$ km/s for all galaxies with $P^{pre} \leq P^{pre}_{crit}$ (Ivkovich & McCall, 2019). This escape velocity is governed by the expansion rate of photoionized gas into vacuum, for which the typical temperature of photoionized gas is $T = 13,000 \pm 4,000$ K.

Equation 3.19 was used to calculate the distances traveled by the exiled gas from the centre of the dSph, depending on its initial escape velocity and the time it had to travel. These values are listed in Table 3.7. The values of the escape velocity v_{esc}, dynamical mass M_{dyn}, and the half-light radius $r_{1/2}$ used to calculate the lower and upper bounds on distance r and angular radius θ are listed in horizontal rows of Table 3.7.

Estimated Locations and Angular Sizes of Photoevaporated Gas												
			Classical					Photoevaporation				
				$t = 1.5\,(Gyr)$		$t = 8\,(Gyr)$			$t = 1.5\,(Gyr)$		$t = 8\,(Gyr)$	
	M_{dyn} ($\times 10^{37}$) (kg)	$r_{1/2}$ ($\times 10^{18}$) (m)	$v_{esc,c}$ ($\times 10^{3}$) (m/s)	r ($\times 10^{20}$) (m)	θ (^{o})	r ($\times 10^{20}$) (m)	θ (^{o})	$v_{esc,p}$ ($\times 10^{3}$) (m/s)	r ($\times 10^{20}$) (m)	θ (^{o})	r ($\times 10^{20}$) (m)	θ (^{o})
Lower	18	10.73	16	6.9	0.9	40	5.3	42	20	2.6	106	14
Middle	10	12.22	23.8	11	1.6	60	8.3	50	24	3.3	126	17
Upper	5.0	13.48	32.9	16	2.3	83	12	58	27	4.1	146	21

Table 3.7: Possible locations of missing gas of And XVIII depending on the escape velocity and the time of star formation episode.

Our field of view is $2.13^o \times 1.43^o$ in horizontal and vertical directions respectively; the diagonal field of view is 2.56^o. This means that any gaseous envelope associated with the gas expelled by star formation activity 8 Gyr ago would have expanded to a size exceeding the field of view of QUAIL.

Chapter 4
Observational Procedure

In the following section the observational procedures, the reasoning behind them, their shortcomings, and possible future improvements are outlined in order of execution.

4.1 One Hour Before Twilight: Cooling Down The CCDs

The observational procedure began with cooling the Harlequin and Bobwhite CCDs. The CCDs would normally be set to cool down one hour before twilight to ensure that they reached a uniform and stable temperature by twilight, which is when the flat-field images of the twilight sky needed to be taken.

Theoretically, the cooling systems are capable of cooling the CCDs down to $T_{CCD} = -50\,^{\circ}\mathrm{C}$, where T_{CCD} is the temperature of the CCD below the ambient temperature. However, we chose to cool down the CCDs down to $T_{CCD} = -30\,^{\circ}\mathrm{C}$ and $T_{CCD} \sim -25\,^{\circ}\mathrm{C}$ for Harlequin and Bobwhite respectively. This decision was influenced by the following reasons. Firstly, the CCDs took several hours to cool down to $T_{CCD} = -50\,^{\circ}\mathrm{C}$, so waiting for them to reach that temperature would reduce the time spent observing. Secondly, the attempts to cool down to $T_{CCD} = -50\,^{\circ}\mathrm{C}$ resulted in an unstable CCD temperature as T_{CCD} would continue to perpetually fluctuate between $-50 \leq T_{CCD}\,(^{\circ}\mathrm{C}) \leq -48$. Moreover, the cooling system was working at 100% of its power to maintain the $T_{CCD} \sim -50\,^{\circ}\mathrm{C}$,

which indicated that the cooling system would not stabilize.

Additionally, we were apprehensive about having the cameras' cooling system operate at 100% of its power for several hours, as we feared it would strain the cooling system and eventually cause damage to it.

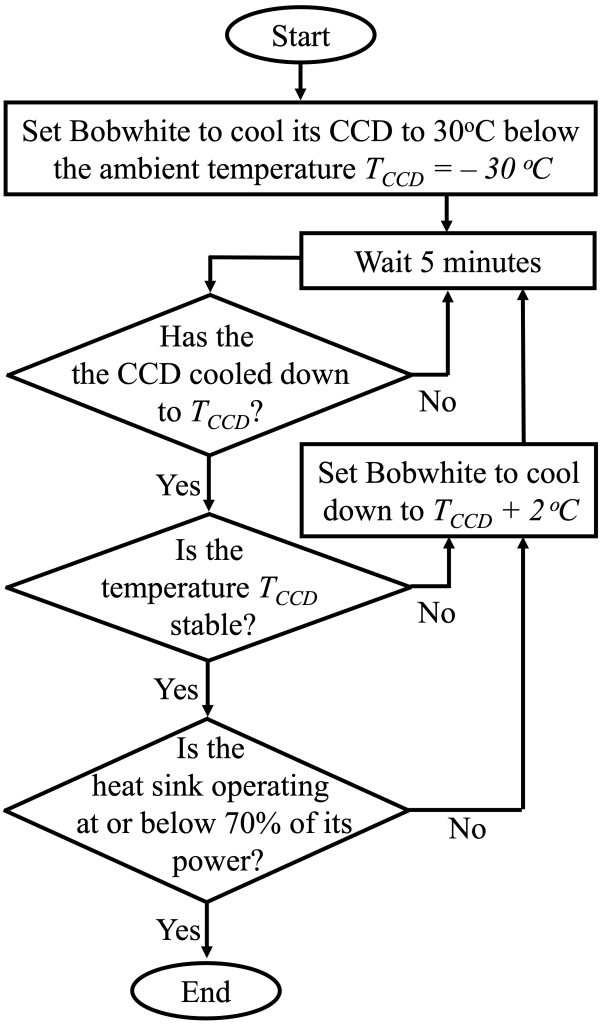

Figure 4.1: A flow chart of the process adopted to optimally cool Bobwhite's CCD.

Harlequin's CCD was always set to cool down to 30 °C below the ambient temperature at the beginning of the night, as its cooling system was functioning as expected. However, due to the inefficiency of Bobwhite's cooling system, a special procedure had to be followed to ensure that the CCD was cooled optimally. The procedure is outlined below and is supplemented with a decision-making tree that can be found in Figure 4.1. Usually, Bobwhite's CCD would be set to cool down to 30 °C below the starting ambient temperature, and the progress of its cooling would be monitored. If after five minutes it was found that Bobwhite either:

a) Failed to cool down to the specified temperature;

b) Cooled down to the specified temperature, but with the heat sink operating above 70% of its power;

c) Cooled down to the specified temperature, but failed to stabilize;

then, the requirement for Bobwhite would be relaxed, and it would be allowed to cool down to a new temperature setting $2\,^{\circ}\mathrm{C}$ higher than the previous one. If within the next five minutes Bobwhite wasn't able to stabilize satisfactorily at the new temperature setting, then the process would be repeated. Typically, acceptable performance was achieved at a temperature setting around $30\,^{\circ}\mathrm{C}$ below ambient.

4.2 Twilight: Taking Twilight Sky Flat-Field Images

Another important part of observing is taking good flat-field images. Dividing an image by a flat-field image will ideally remove artifacts such as pixel-to-pixel variations in response, vignetting and other optical or CCD artifacts.

In order to take a flat-field image, one must take a picture of a uniformly illuminated surface, such as an illuminated dome wall. If obtaining a flat-field image using a dome wall is not possible, one could take a picture of the sky at dawn or dusk when stars are either no longer visible or not visible yet. Despite the trickiness of taking twilight flats, they are superior to dome flats in the sense that the light illuminates the optics in the same way as the targets observed during the night. In other words, they give a more accurate measure of how detectors are illuminated across their full extent.

Originally, the intention was to obtain the flat-field images by taking pictures of a uniform white flat-fielding screen inside of the dome. This would

have been ideal, as these flats could be taken during the daylight, and would therefore offer the opportunity to obtain a substantial number of high quality flats. Unfortunately, getting dome flats was rendered impossible by QUAIL's wide field of view. The small flat-field screen did not fill the entirety of QUAIL's detectors. Because the illumination inside of the dome and the dome wall's colour and texture were not uniform, we were unable to use the dome wall or the screen to take flat-field images.

Since it was not possible to obtain flat-field images using the dome, it was decided to obtain them by taking the twilight flats. Despite the recommendations of Tyson & Gal (1993), the flat-field images could not be taken in the well-organized and systematic manner prescribed. Power fluctuations and interference from the dome motors caused frequent loss of connection to the telescope's handpaddle, the telescope itself, the CCD cameras and the Birger focusing rings. Consequently, attention shifted from obtaining a few very high quality flat-field images to simply taking as many flat-field images as possible with appropriate amount of counts, adjusting the exposure times on the fly.

The appropriate amount of signal on a CCD comes from two considerations. The first consideration is the signal-to-noise ratio (SNR). Flat-field images had to have a high SNR, as their purpose is to be used to correct for artifacts left by the optics, such as vignetting, or pixel-to-pixel sensitivity. If the SNR of the flat-field images is low, the optical artifacts can become distorted by other features, such as artifacts in the bias and/or dark frames. This can cause over-correction for the features in the bias and dark frames, as well as a lack of appropriate correction for artifacts in the optics. It is advantageous to take

the flat-field images when the apparatus is in focus, as the state of the optics will then be the same during the acquisition of flat-fields and the acquisition of data, and will allow for optimal flat-field correction.

The second consideration for the amount of signal present in the flat-field images is influenced by the non-linearity regime of the CCD. The CCD is comprised of pixels, which are potential wells separated by walls of insulators. As photons impinge on the CCD they are converted into electrons, which get deposited into the potential wells. The potential wells have a finite capacity of electrons it can hold, called the full-well capacity. During exposure, the potential wells fill up with electrons, creating a charge buildup and causing the efficiency of trapping electrons to decrease, which is one of the causes for the CCD to enter a non-linearity regime. Normally, in the linear regime, the electrons get converted to signal measured in counts using a specific ratio called gain. The gain is a property of the architecture of the CCD, and it governs the number of electrons it takes for the CCD to collect in order for the resultant image to register one count.

The second reason why a CCD camera can enter the non-linearity regime is due to the readout efficiency decreasing as the pixels reach their fill-well capacity. During the readout, the electrons deposited in the potential wells get shifted and read out by a voltage-to-digital converter. The closer the potential wells are to being full, the less precise the readout process becomes.

To prevent the CCD from entering the non-linearity regime, one must consider the optimal amount of signal on their flat-field image. It is possible to measure the CCD response by taking exposures of increasing duration of a

stable source of radiation (such as a lamp) and monitoring the change in the increase of signal. When the CCD enters the non-linearity regime the change in the amount of signal gathered per increase in the duration of exposure will diminish. Past this point taking longer flat-field exposures is inefficient at best, and dangerous at worst, as exposing the CCD to extreme amounts of radiation can permanently damage it.

Alternatively, if obtaining the measurement for when the CCD enters the non-linear regime is not possible, the gain and the full-well capacity provided by the manufacturer of the CCD camera can be used to approximate the optimal signal for flat-field images. For that purpose, the "rule of thumb" is to keep the signal such that the electron wells are on average at most 75% full. The gain of our CCDs was $\sim 0.4\ \mathrm{e}^{-}/\mathrm{count}$, which means that if the electron well was filled only up to $\sim 48\%$, the image would display as saturated, having maximum signal in counts. Hence, we aimed to acquire the signal of $\sim 30,000\ \mathrm{counts}$ during our flat-field exposure.

Ideally, a set of twilight sky flat-field images would be taken at dusk before beginning the observations, and another set would be taken at dawn when the observations are being concluded. However, the bulk of the observations had to be made remotely due to the pandemic, and frequent losses of connection due to power fluctuations would usually render QUAIL's apparatus inoperable several hours after a night of observing had started. Therefore, only dusk flats were taken, with Birger focus points of QUAIL's lenses being adopted to be those of the previous night.

4.3 Focusing: Finding the Right Birger Setpoints

Cessation of the flat acquisition procedure occurred when stars became visible on images. A standard star HD 217086 or a sufficiently bright star near an observing target was utilized to focus the lenses. The FWHM, flux and peak values were measured using `imexamine` over a range of focus settings to determine the optimal focus point. A sufficiently bright star was one bright enough to be clearly detected during short exposures with lengths of 3 to 9 seconds, but not so bright as to saturate the pixels. Using short exposures was necessary to ensure that the focusing was done expeditiously, so as to not waste the time that should be used for observations.

4.4 Observing Flux Calibration Targets

To relate the counts in a pixel to the flux (in energy units) from a target, one needs to observe a "standard" source whose energy flux as a function of wavelength has previously been calibrated. In combination with knowledge of the shape of the transmission curve of the filter through which the image was taken, the count rate in a pixel can be related to the total flux from the target transmitted through the filter. The count rate in a pixel obtained from observing an extended object can be related to the line flux per unit solid angle admitted through the filter in a similar manner.

We always strived towards obtaining several images of the standard star

whenever observing conditions were considered to be photometric. Precise details of the flux calibration and observation of the standard star are given in Section 6.6.

4.5 Target Observations

Each night, Bobwhite was equipped with the continuum filter, and Harlequin was equipped with one of the line filters. After adjusting the foci, observations of a research target would commence. An observation consisted of a series of short exposures through continuum and line filters taken simultaneously. Exposures in the continuum filter were taken at the same time as exposures in the line filter to make it possible to accurately remove the continuum contaminating line images regardless of sky conditions. To detect very faint emission, many exposures would be taken, sometimes over the course of several nights. Each exposure was four minutes in length, the maximum possible time before tracking errors would noticeably degrade the image quality.

Chapter 5
Observations

In this section, a brief observation log with dates and observing conditions is documented in table format for each target. The tables are supplemented with brief commentary on hardware and observatory conditions as well as other relevant notes.The images of the observation targets can be seen in Section 7 of this work.

All values for temperatures, such as the CCD temperatures (T_{CCD}) and the ambient temperature T_{amb} (as measured by the SensorPush device), are listed in degrees Celsius. Humidity is listed in $\%$. The dates on which the night of observation started are listed in the `Date` rows in `yyyy/mm/dd` format. The `Time` entries in the tables indicate the EST time at which the observations began in `hh:mm:ss` format. All exposures for listed observations of the Triangulum Galaxy (M33), And XVIII, The Dumbbell Nebula (M27), and The PacMan Nebula (NGC 281) are 240 s long. Table entries labeled as "Calibrated" contain the word "Yes" if the standard star HD 217086 was observed, and "No" if it wasn't. The entries labeled as "Took Sky Flats" indicate whether the twilight flat-field images were taken that night; if the entry contains "Yes" then the sky flats were taken, "No" otherwise. Any explanation for not taking twilight flat-field images is listed under "Observing Conditions".

The "Good Exposures" entry contains the number of continuum/line image pairs that met the following criteria:

1. Continuum and line images were taken within the same minute. Observ-

ing conditions could change rapidly during autumn evenings and hence the accuracy with which continuum could be subtracted from the line images would be impaired if there were a large time difference between the time at which the line and continuum images were taken. The specific details about the process of continuum subtraction can be found in Section 6.4.5.

2. Neither camera was exposed to light from the stadium or light inside the dome.

3. Neither image was compromised by obscuration by the dome.

4. Neither image suffered from the jolt of the optical system.

5. Neither image suffered from artifacts near the location of the target on the image.

6. Both images were reasonably focused, with the Moffat FWHM for unsaturated stars near the centre being ≤ 2.5 pixels or ≤ 12.25 arcseconds.

5.1 The PacMan Nebula NGC 281

The PacMan Nebula (NGC 281) turned out to be extremely bright in Hα, so it was only observed for twelve minutes using the Hα filter. However, its [OI] emission was extremely faint, so it was decided to observe the PacMan Nebula extensively with the [OI] filter. Although the PacMan Nebula was observed with the [OI] filter for over seven hours, the [OI] emission remained very faint, and it only became visible after the stars were removed from the [OI] image. Observing details are provided in Table 5.1.

PacMan Nebula NGC 281				
Date	2021/10/19	2021/10/27	2021/11/08	2021/11/07
Time	23:00:17	22:14:11	22:51:29	21:00:21
Harlequin Filter	[OI]			Hα
Bobwhite Filter	Continuum			
Harlequin T_{CCD}	-30.0	-30.0	-30.0	-30.0
Bobwhite T_{CCD}	-19.4	-20.0	-19.8	-23.0
T_{amb}	15.6	10.5	11.5	10.4
Humidity	58.5	66.2	64.4	72.5
Calibrated	Yes*	Yes	Yes	Yes
Took Sky Flats	Yes	Yes	Yes	Yes
Good Exposures	38	37	32	3
Observing Conditions	*Calibration attempt was made, but the images of HD 217086 have poor focus and star visibility.	Clear night, good observing conditions.	Perfectly clear, photometric night. Some clouds at and after 3:00 am.	Perfectly clear, photometric night.
Total Integration Time In [OI]: 7h 8m				
Total Integration Time In Hα: 12m				

Table 5.1: Observing Log for PacMan Nebula.

5.2 Triangulum Galaxy M33

The Triangulum Galaxy M33 was successfully observed in Hα and Continuum filters. Attempts to image it in the [OI] filter failed due to weather conditions and time constraints. However, the Hα images of the Triangulum Galaxy were of very high quality and the Hα signals from the HII regions of M33 were used to check and adjust the Hα fluxes calibrated by the standard star, as well as evaluate the overall performance of QUAIL. Observing details are provided in Table 5.2.

M33 Triangulum Galaxy		
Date	2021/11/08	2021/12/13
Time	01:11:46	23:07:00
Harlequin Filter	Hα	
Bobwhite Filter	Continuum	
Harlequin T_{CCD}	-30.0	-30.0
Bobwhite T_{CCD}	-23.2	-23.6
T_{amb}	8.49	4.55
Humidity	79.6	70.5
Calibrated	Yes	No
Took Sky Flats	Yes	Yes
Good Exposures	14	15
Observing Conditions	Perfectly clear, photometric night. Some clouds at and after 3:00 am.	Somewhat cloudy at the start, but cleared within 1h.
Total Integration Time: 1h 56m		

Table 5.2: Observing Log for M33.

5.3 The Dumbbell Nebula M27

The Dumbbell Nebula (M27) was clearly visible in each individual image in all filters, despite having a relatively short total integration time in each filter. Observing details are provided in Table 5.3.

5.4 Dwarf Spheroidal Galaxy And XVIII

The dwarf spheroidal galaxy And XVIII is the target that was observed the most. It was observed exclusively using the Hα and Continuum filters. Observing details are provided in Table 5.4.

Dumbbell Nebula M27				
Date	2021/10/18	2021/11/07	2021/10/19	2021/10/27
Time	19:07:35	18:11:33	19:37:19	19:11:36
Harlequin Filter	Hα		[OI]	
Bobwhite Filter	Continuum			
Harlequin T_{CCD}	-30.0	-30.0	-29.5	-30.0
Bobwhite T_{CCD}	-23.5	-20.5	-19.2	-19.9
T_{amb}	12.9	12.1	17.2	12.3
Humidity	55.9	65.1	52.7	57.2
Calibrated	No	Yes	Yes*	Yes
Took Sky Flats	Yes	Yes	Yes	Yes
Good Exposures	28	29	20	19
Observing Conditions	Clear night. Calibration not done due to constraints of time and pandemic.	Perfectly clear, photometric night	*Calibration attempt was made, but the images of HD 217086 have poor focus and star visibility.	Clear night, good observing conditions.
Total Integration Time In Hα: 3h 48m				
Total Integration Time In [OI]: 2h 36m				

Table 5.3: Observing Log for M27 Nebula.

And XVIII					
Date	2021/10/18	2021/11/05	2021/11/06	2021/11/07	2021/12/13
Time	22:59:02	23:07:01	22:58:31	21:18:36	21:47:10
Harlequin Filter	Hα				
Bobwhite Filter	Continuum				
Harlequin T_{CCD}	-30.0	-30.0	-30.0	-30.0	-30.0
Bobwhite T_{CCD}	-22.0	-28.0	-25.9	-23.1	-24.2
T_{amb}	9.43	4.55	6.37	10.19	4.35
Humidity	62.6	57.8	65.1	73.2	70.5
Calibrated	No	Yes	No	Yes	No
Took Sky Flats	Yes	Yes	No	Yes	Yes
Good Exposures	35	18	32	29	6
Observing Conditions	Clear night. Standard star not observed due to time and pandemic-related constraints.	Clear night. Some clouds towards the morning.	No sky flats or standard star observations due to time and pandemic-related constraints.	Perfectly clear, photometric night.	Standard star not observed due to clouds at start of night. The clouds cleared later.
Total Integration Time: 8h					

Table 5.4: Observing Log for And XVIII.

5.5 Standard Star HD 217086

While the nights on which the standard star HD 217086 was observed and the pertinent observing conditions were listed in Tables 5.2, 5.1, 5.4 and 5.3, this section will provide the finer details of observations of HD 217086 in Table 5.5. Unlike the other targets, the duration of each exposure varied from night to night. Table entries `Harlequin Exposure Lengths` and `Bobwhite Exposure Lengths` give $N \times T(s)$, where N is the number of images, and $T(s)$ is the integration time of each image.

Standard Star HD 217086				
Date	2021/11/05	2021/11/07	2021/11/08	2021/10/27
Time	22:48:58	20:44:28	22:42:13	21:54:00
Harlequin Filter	Hα			[OI]
Bobwhite Filter	Continuum			
Harlequin T_{CCD}	-30.0	-30.0	-30.0	-30.0
Bobwhite T_{CCD}	-27.0	-22.8	-19.8	-19.9
T_{amb}	4.55	10.2	11.5	10.5
Humidity	57.8	73.2	64.4	66.2
Took Sky Flats	Yes	Yes	Yes	Yes
Harlequin Exposures	13	5	6	12
Bobwhite Exposures	14	6	6	14
Harlequin Exposure Lengths	$6 \times 6(s)$ $7 \times 9(s)$	$5 \times 9(s)$	$6 \times 9(s)$	$12 \times 6(s)$
Bobwhite Exposure Lengths	$8 \times 3(s)$ $4 \times 6(s)$	$6 \times 2(s)$	$6 \times 2(s)$	$12 \times 3(s)$ $1 \times 5(s)$ $1 \times 10(s)$
Observing Conditions	Clear night, some clouds towards the morning.	Perfectly clear, photometric night.	Perfectly clear, photometric night. Some clouds at and after 3:00 am.	Clear night, good observing conditions.

Table 5.5: Observing Log for HD 217086.

Chapter 6
Reductions and Analysis

6.1 Dependence of The Bias on CCD Temperature

The dependency of the noise in the bias signal is dictated by the dependency of the readout noise on CCD temperature (henceforth, T_{CCD}). The nominal readout noise of KAF-3200 is $\pm 10\,\mathrm{e}^-$ at $T_{CCD} = 25\,^\circ\mathrm{C}$ when operated in low-noise readout mode (Semiconductor Components Industries, LLC, 2018). However, our CCDs were expected to operate at a variety of T_{CCD} values, so it is necessary to ascertain the amount of anticipated readout noise at a variety of T_{CCD}. Moreover, it is important to investigate the bias frames taken by our cameras for any consistent patterns, artifacts, and any potential dependency on the CCD temperature. Normally, the bias signal should not be dependent on T_{CCD}, and the noise in the bias frames should be directly proportional to T_{CCD}. However, it is imperative to investigate the bias frames prior to reducing the data, as failure to identify and ameliorate the defects in the bias frames may result in incorrect reduction of the data and negatively affect attempts to locate ionized gas.

To ensure that bias frames had no consistent patterns and artifacts, and to map out the dependency of the bias on the T_{CCD}, ten bias frames were taken at varying T_{CCD} with both cameras. It was found that for both cameras there is a linear relationship between the average signal in bias frames and the T_{CCD},

and a linear function was fit to the bias as a function of T_{CCD}.

It is extremely unusual for the bias signal to be dependent on the CCD Temperature. To further investigate the behaviour of the bias, the noise in the bias frames was plotted as a function of T_{CCD}. The resulting plots of the noise in the bias frames also yielded a linear relationship and can be seen in Figures 6.1 and 6.2 for Harlequin and Bobwhite respectively.

The linear fits to the relationships between the bias signal and its noise and T_{CCD} were computed in MatLab. They can be written as:

Harlequin:

$$bias_H(T) = (-0.349 \pm 0.024)T_{CCD} + (708.7 \pm 0.6) \tag{6.1}$$

$$\sigma_H(T) = (2.68 \pm 0.13) \times 10^{-2}\, T_{CCD} + (24.28 \pm 0.03) \tag{6.2}$$

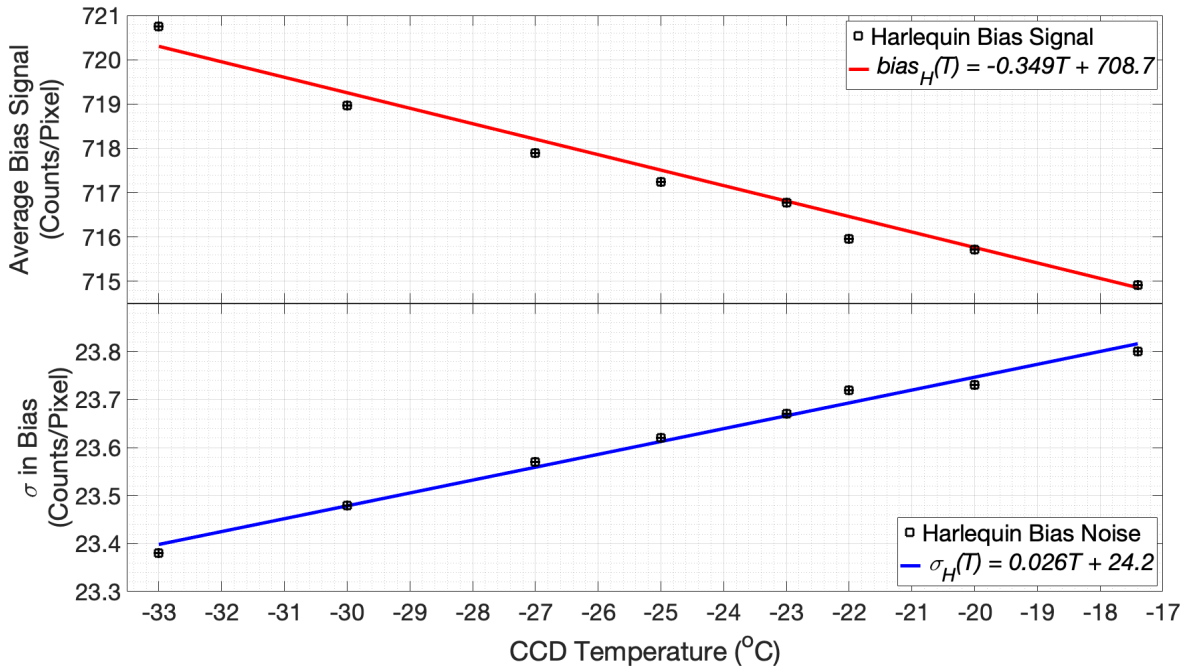

Figure 6.1: Harlequin's Bias vs T_{CCD}. The fit to the relationship is provided in Equation 6.1.

Bobwhite:

$$bias_B(T) = (-0.306 \pm 0.023)T_{CCD} + (1041.9 \pm 0.4) \tag{6.3}$$

$$\sigma_B(T) = (3.01 \pm 0.16) \times 10^{-2}\, T_{CCD} + (25.26 \pm 0.03) \tag{6.4}$$

where $bias_H(T)$, $\sigma_H(T)$, $bias_B(T)$ and $\sigma_B(T)$are measured in counts per pixel and T_{CCD} is in degrees Celsius.

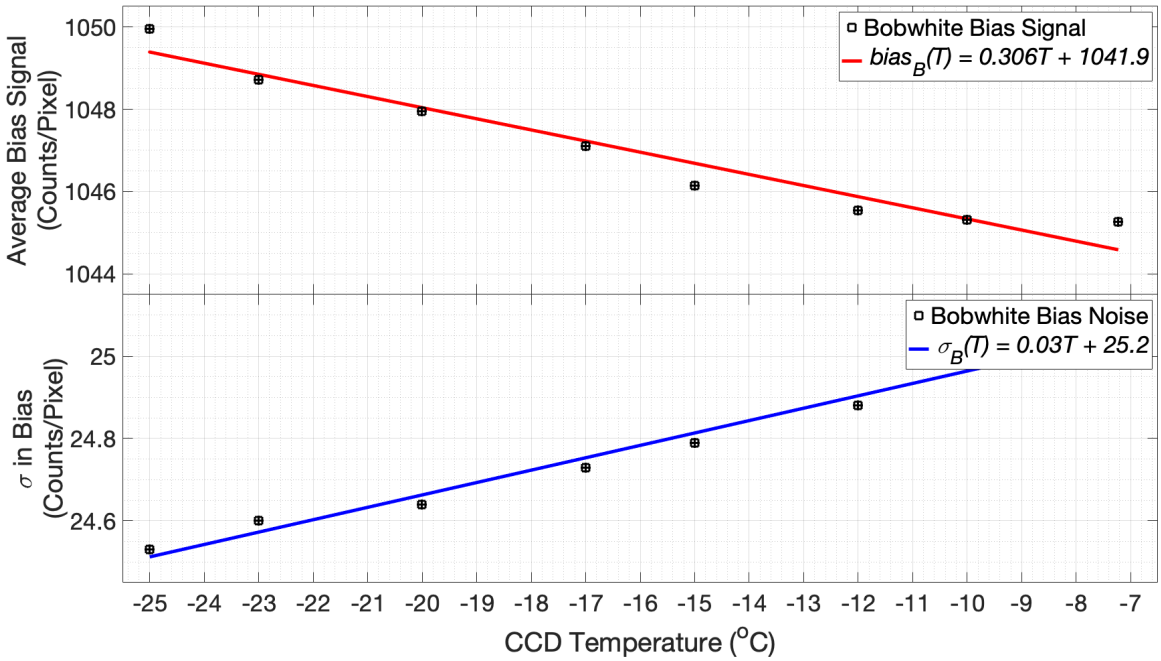

Figure 6.2: Bobwhite's Bias vs T_{CCD}. The fit to the relationship is provided in Equation 6.3.

The noise in the bias frames appears to behave in the anticipated manner – a decrease in T_{CCD} is accompanied by a decrease in the noise. The average signal in the bias frames, however, exhibits an unusual dependency on T_{CCD}. Normally, the bias signal is supposed to be independent of T_{CCD}, unless the minimal length of exposure is sufficient for the residual dark current to contribute to the bias signal. However, in that case the bias signal is expected to be directly proportional to T_{CCD}, which is not the behaviour exhibited by the

bias signal of our cameras. The observed increase in the bias signal cannot be attributed to the heating of the readout and/or data transfer electronics either, as this would be accompanied by a growth in the noise in the bias signal. A possible explanation to this behaviour of the bias signal is that the cameras increase the bias with the decrease in T_{CCD}. It is unknown whether this behaviour was implemented intentionally, or if it stems from an error in the configuration of the cameras. While the thorough investigation of the behaviour of the bias frames lies beyond the scope of this work, it was accounted for in the analysis.

The dependency of the bias signal on T_{CCD} necessitated investigating the bias frames for any lasting structures and/or artifacts. To do so, the bias frames from each temperature setting were combined using IRAF's `imcombine` and the resulting image was normalized by dividing by its mean. The normalized images were then binned in a variety of combinations to bring forth any features, and then plotted in MatLab. These images revealed that the biases had a parabolic shape when viewed from the x-axis (along rows) – the counts rise towards the ends of the long side of the CCD; the shape did not change with temperature. The difference in counts between the sides of the CCD and the centre of the CCD was constant to within a few percent. This behaviour is demonstrated in Figures 6.3 and 6.4 for the bias frames taken using Harlequin and Bobwhite respectively. In these figures, the bias frames are binned 24×23 and are shown from various vantage points.

To mitigate the behaviour found in the bias, Skeleton Bias Frames were synthesized for each camera. To do so, all bias images were normalized by the bias

levels prescribed by the pertinent equations for T_{CCD} at which they were taken. Then, for each camera, these normalized images were median-combined using IRAF's `imcombine` routine to create the Skeleton Bias Frames. The resulting images for Harlequin and Bobwhite were then saved as `Harlequin_Skeleton_Bias.fits` and `Bobwhite_Skeleton_Bias.fits`, respectively. Their plots can be seen in Figures 6.3 and 6.4 for Harlequin and Bobwhite respectively.

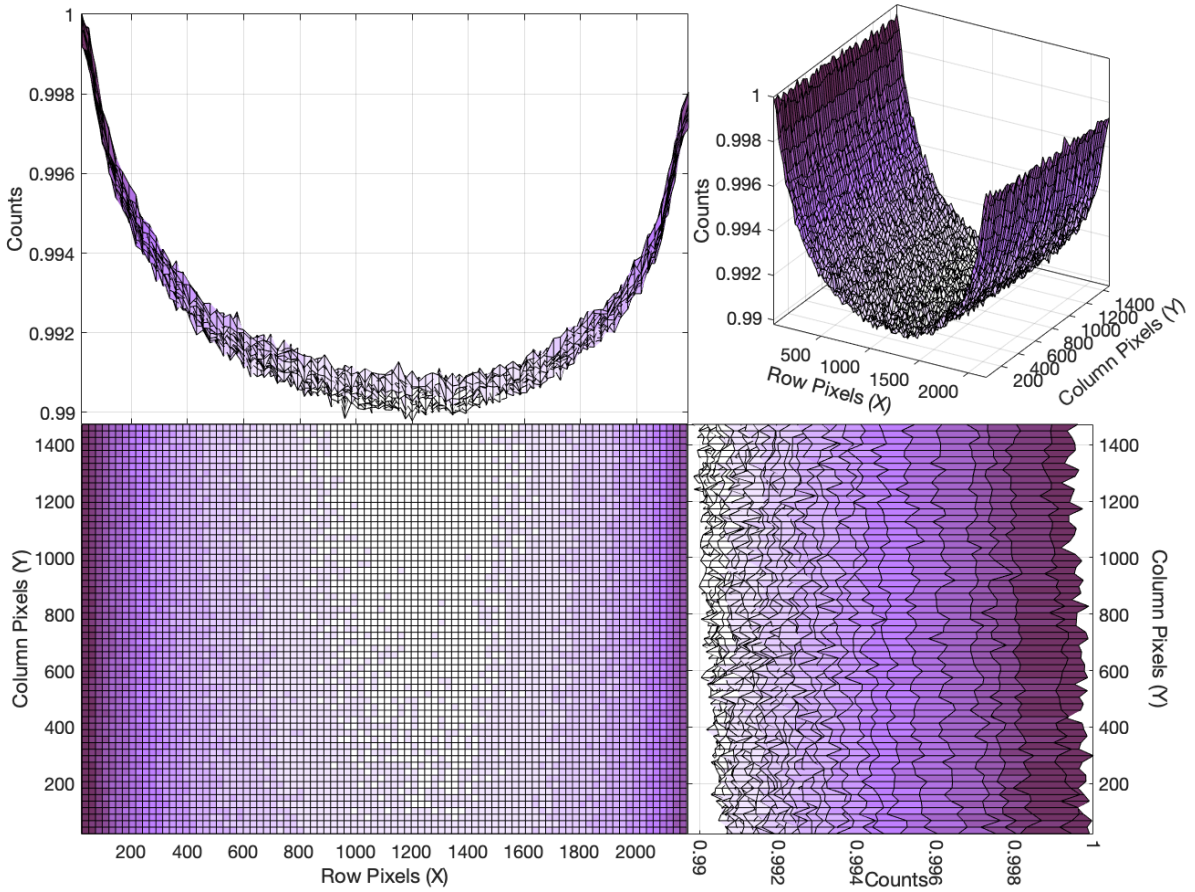

Figure 6.3: Plot of Harlequin Skeleton Bias, binned 24×23, with views from various angles. When viewed from the x-axis, the parabolic structure can be seen.

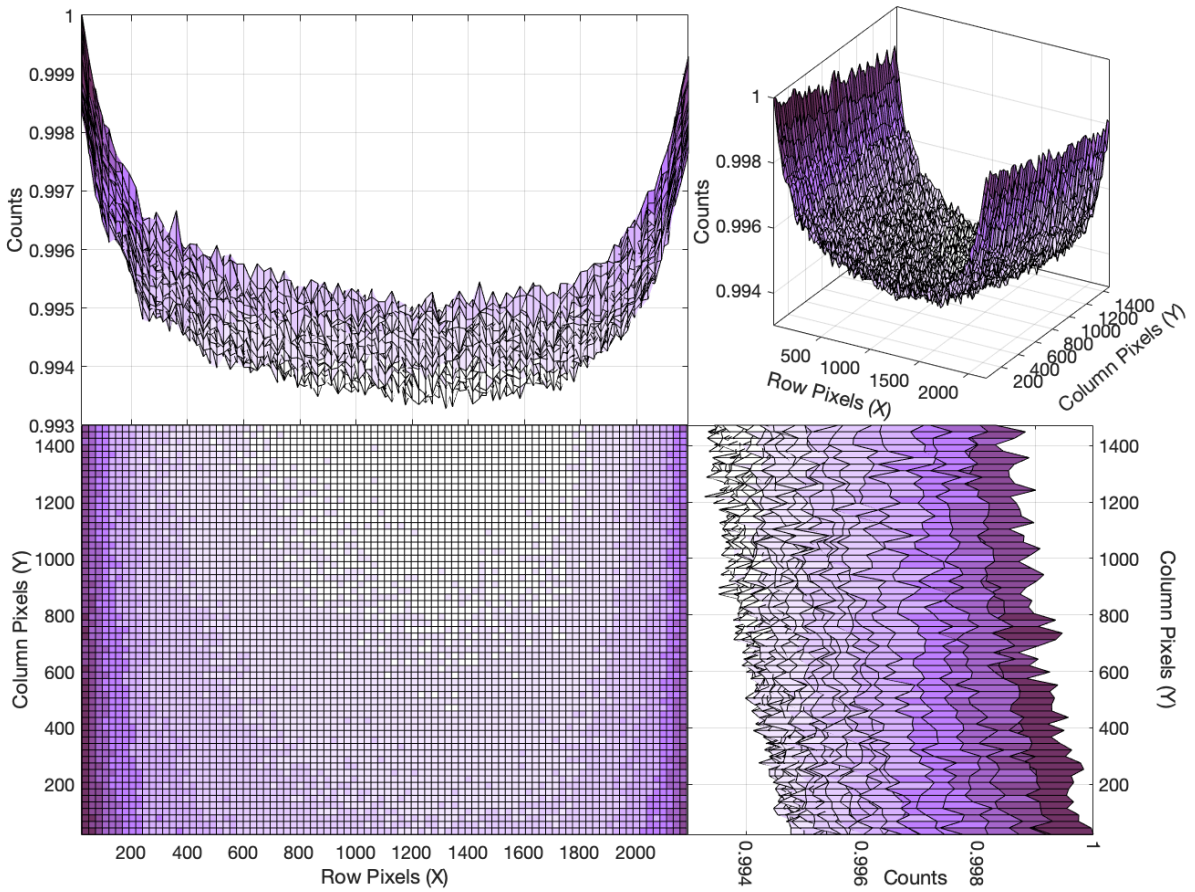

Figure 6.4: Plot of Bobwhite Skeleton Bias, binned 24×23, with views from various angles. When viewed from the x-axis, the parabolic structure can be seen.

6.2 Dependence of The Dark Current on CCD Temperature

Exposure times of our light frames were limited to 240 s due to imperfections in tracking and the need to frequently adjust the focus, hence the exposure times for our dark frames were selected to be the same to avoid the need to scale the dark current prior to its subtraction. Due to poor weather, frequent malfunctions of observatory electronics and software, and the constraints of the pandemic, our observing time was highly limited. Thus, to avoid having to measure the dark current nightly, it was decided to fit a function to the depen-

dency of the dark current on temperature and exposure length. To that end, sequences of dark frames were taken at varying CCD temperatures and exposure times. When the average dark frame signal/pixel at each temperature setting was plotted against length of exposure, it became evident that there was a dependency on temperature, as mentioned by the manufacturer Semiconductor Components Industries, LLC (2018). The plots of Harlequin's and Bobwhite's dark currents versus exposure length can be seen in Figures 6.5 and 6.6. In Figures 6.5 and 6.6 the errors associated with the exposure time stem from the errors associated with the total time required to take an image t_T which is discussed in Section 2.5; the errors associated with the signal are obtained from the standard deviation of the signal in the image.

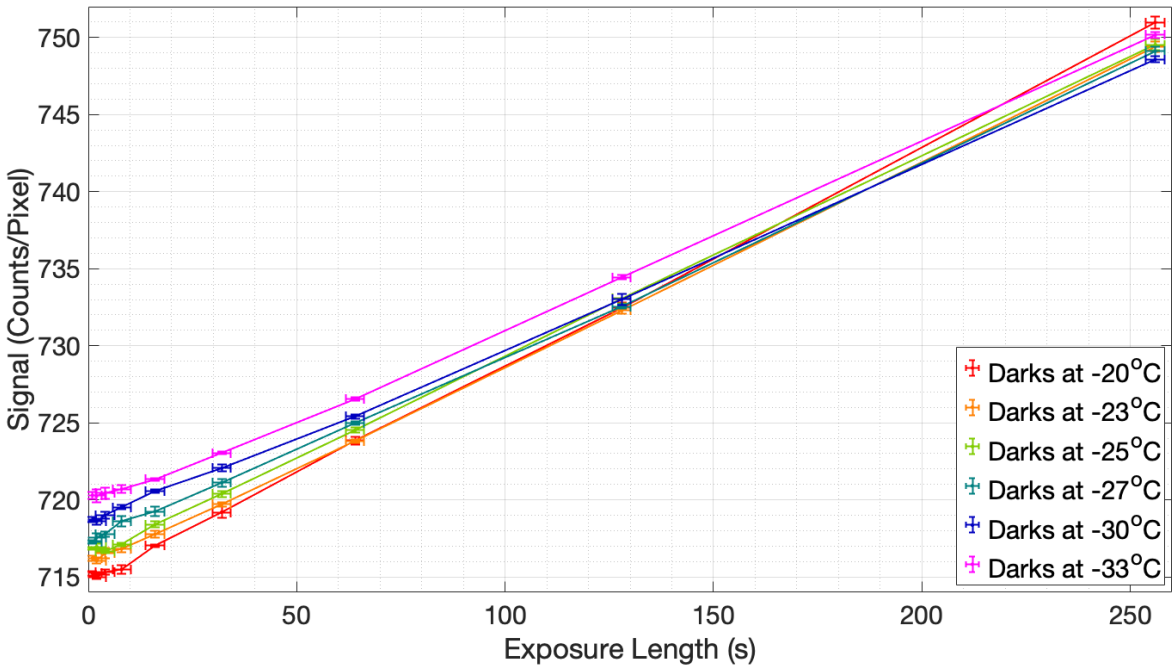

Figure 6.5: Harlequin's dark counts plotted against exposure time.

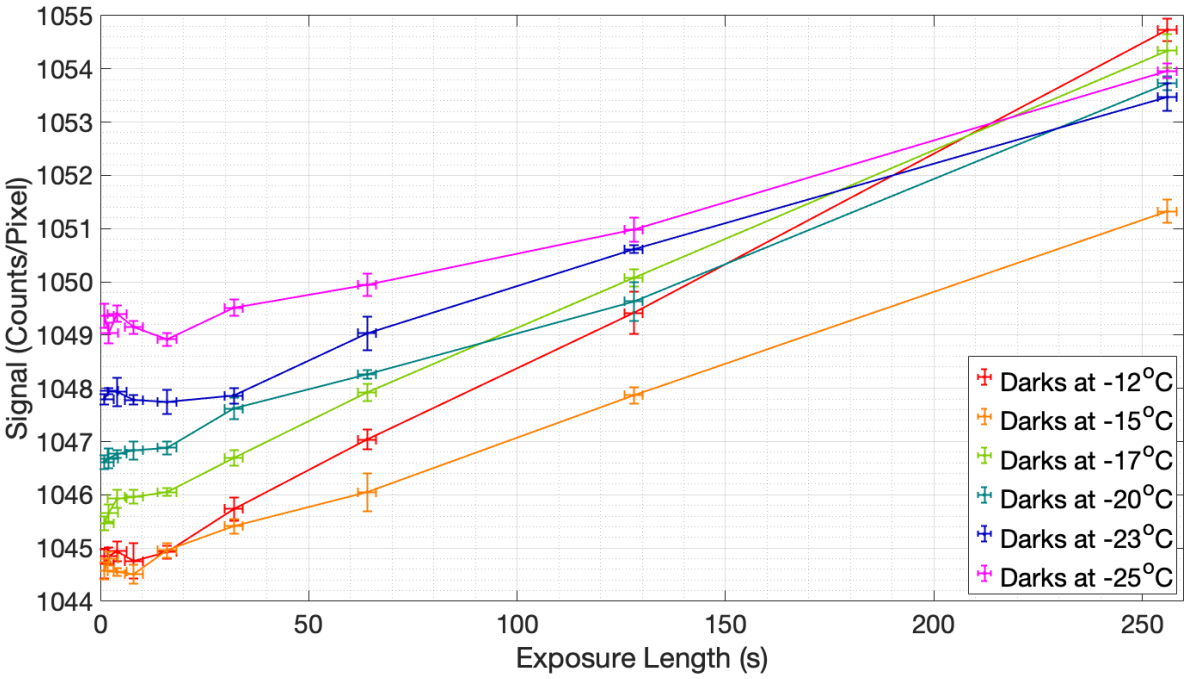

Figure 6.6: Bobwhite's dark counts plotted against exposure time.

At first, an attempt was made to fit a simple linear function of the form

$$DC(t, T_{CCD}) = a_T t + b_T \tag{6.5}$$

to the dark counts. Here $DC(t, T_{CCD})$ is the average dark counts, t is the exposure length in seconds, and T_{CCD} is the CCD temperature in degrees Celsius.

It is curious to note that at $t = 0$ s, the dark current is $DC(0, T_{CCD}) = b_T$, where b_T is the dark current taken over a 0 second exposure, also known as the bias. However, further investigation revealed that both the slope a_T (which is the dark current in counts/second) and the y-intercept b_T (which is the bias in counts) varied with T_{CCD}. The relationships between a_T and b_T and T_{CCD} were linear, which can be seen in Figures 6.7 for Harlequin, and 6.8 for Bobwhite.

For Harlequin the resulting fits to a_T and b_T can be written as:

$$a_{T,H}(T_{CCD}) = [(18.62 \pm 2.91)T_{CCD} + (1755 \pm 77)] \times 10^{-4} \tag{6.6}$$

$$b_{T,H}(T_{CCD}) = (-0.383 \pm 0.010)T_{CCD} + (706.9 \pm 0.3) \tag{6.7}$$

The value of $b_{T,H}(T_{CCD})$ is consistent with the bias signal calculated in Equation 6.1. Thus, the average dark current for Harlequin can be written as:

$$DC_H(t, T_{CCD}) = [(18.62 \pm 2.91)T_{CCD} + (1755 \pm 77)] \times 10^{-4}t + (-0.383 \pm 0.010)T_{CCD} + (706.9 \pm 0.3) \tag{6.8}$$

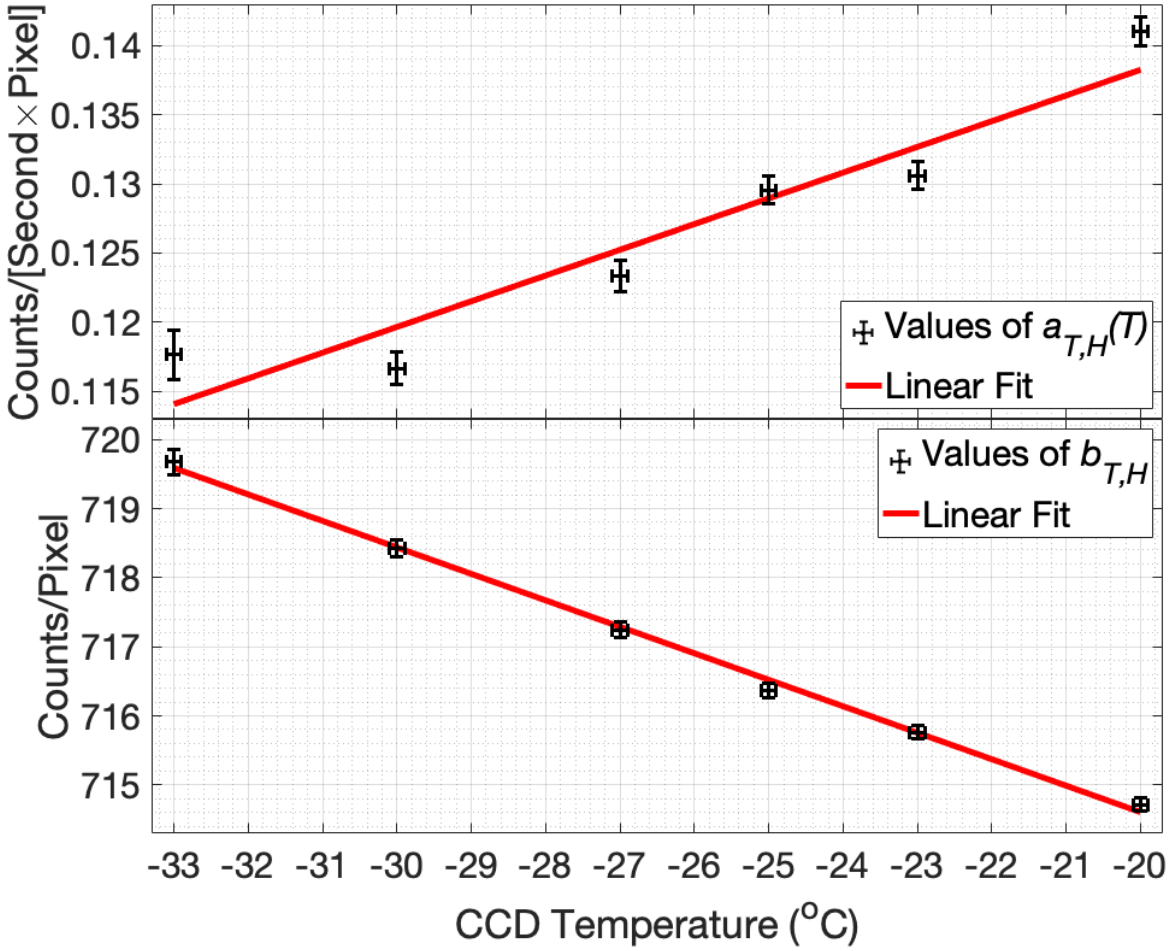

Figure 6.7: Data and fit to Harlequin dark current coefficients.

For Bobwhite, the fits to a_T and b_T can be written as:

$$a_{T,B}(T_{CCD}) = [(13.58 \pm 3.67)T_{CCD} + (534.1 \pm 70.5)] \times 10^{-4} \tag{6.9}$$

$$b_{T,B}(T_{CCD}) = (-0.349 \pm 0.043)T_{CCD} + (1039.8 \pm 0.8) \tag{6.10}$$

The value of $b_{T,B}(T)$ is consistent with the bias signal calculated in Equation 6.3. Thus, the average dark current for Bobwhite can be written as:

$$DC_B(t, T_{CCD}) = [(13.58 \pm 3.67)T_{CCD} + (534.1 \pm 70.5)] \times 10^{-4}t + (-0.349 \pm 0.043)T_{CCD} + (1039.8 \pm 0.8) \tag{6.11}$$

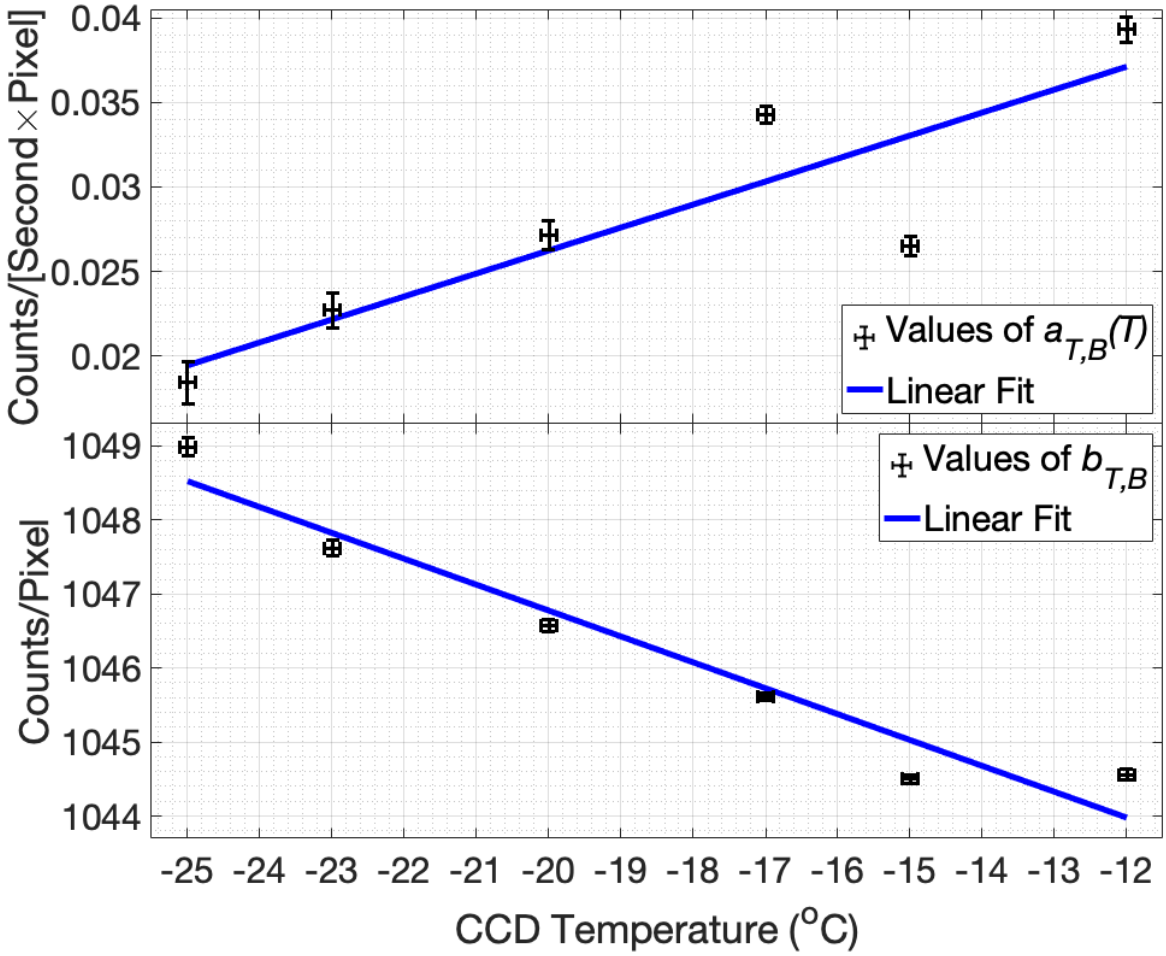

Figure 6.8: Data and fit to Bobwhite dark current coefficients.

6.3 Flat-Field Images

Over the course of all observing sessions, a total number of 825 flat-field images were acquired, of which 437 images were taken using the continuum filter, 193 using the Hα filter and 195 using the [OI] filter. Inspection revealed that only 313 images taken using the continuum filter, 133 images taken in Hα and 95 images taken in [OI] had an average number of counts ranging between 20,000 and 50,000. The rest of the images were either saturated or too dim to be considered good enough to use for flat-field corrections.

The number of viable flats was then further reduced by rejecting those for which clouds or stars were present, the dome was blocking the field of view, or short-lived artifacts appeared. Fortunately, the images that were rejected due to being compromised by environment and human error comprised a small fraction of the images. The bulk of further rejections arose from short-lived, large and unstable artifacts. These artifacts were present in nearly every image, and would change their shape from image to image, even in very short exposures (under $2\,\mathrm{s}$). An example of these artifacts can be seen in Figure 6.9. The artifacts are small, with peaks being only $\sim 7\%$ higher than the throughs.

However, the median-combined flat-field images created with the artifact-ridden flats yielded poor flat-field corrections. The median-combined flat-field image would retain some of the artifact shapes, which differed from night to night. Correcting using such flat-field images caused the sky background of targets to also show these artifacts.

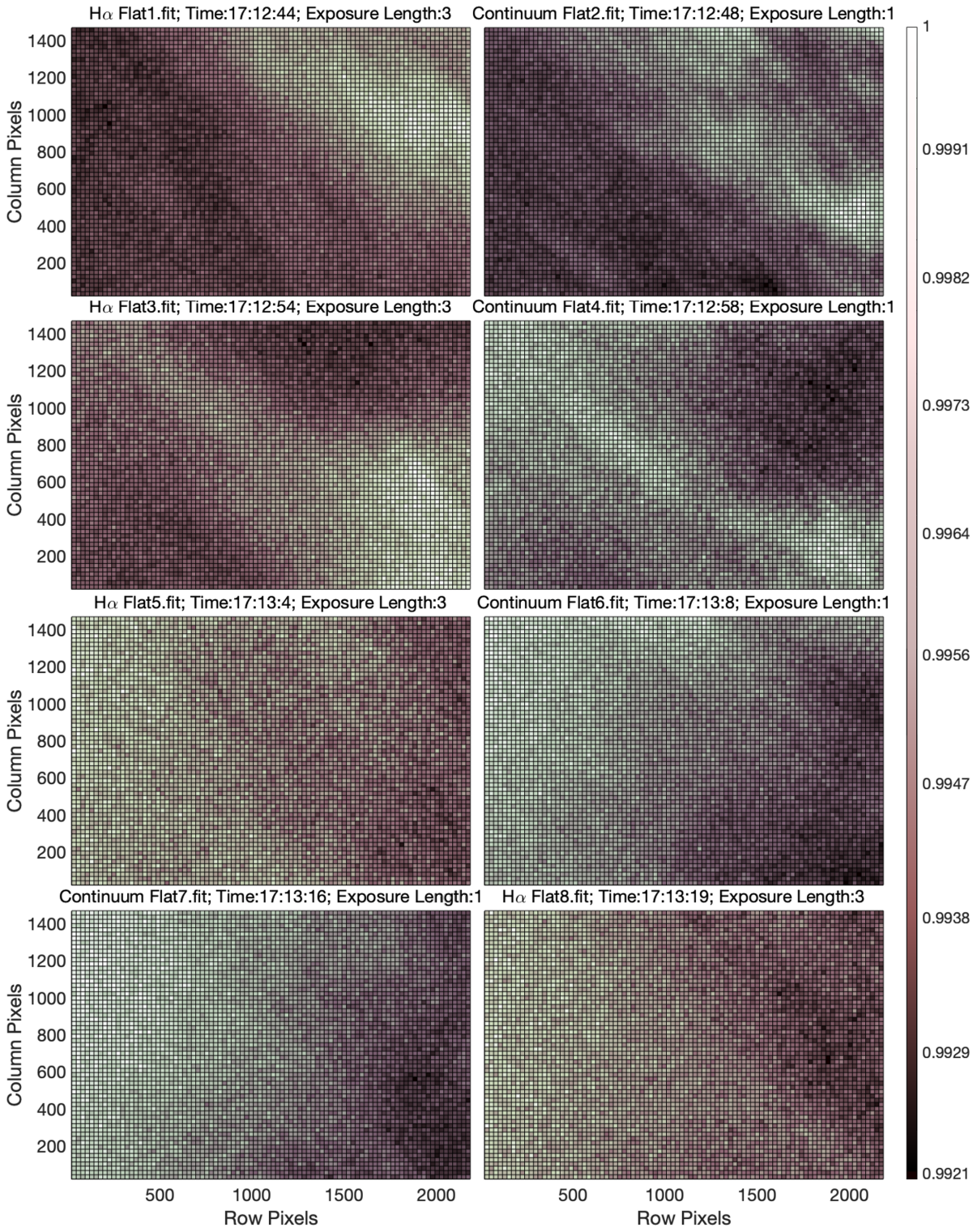

Figure 6.9: Colourmap plots of four continuum and four Hα flat-field images with artifacts. All images were taken on the photometric night of 2021/11/07. The maximum time difference between when the continuum and when the Hα images were taken is $4\,\mathrm{s}$. The counts/second in all images are normalized and the images are binned 24×23. The colourbar represents the normalized signal in counts/s.

Unfortunately, due to the scale of these artifacts and their fickle nature it was not possible to remove them from flat-field images. A possible explanation to the nature of these artifacts is the combination of the shimmering air due to temperature differences inside and outside of the dome, and airborne dust and vapour. Usually, the dome's shutter would be opened and the dome would be rotated to a new position immediately before taking the twilight flat-field images. The temperature difference between the inside and outside of the dome could create temporary condensation on QUAIL's optics, or/and possibly uneven brightness due to variations in the refractive index of air across the field of view. Both of these effects could potentially register on our flat-field images as the short-lived artifacts. This is further substantiated by the similarity and the behaviour in the shapes of the artifacts demonstrated in Figure 6.9.

During some observing nights, the flat-field images were so badly affected by the artifacts that no usable images were left after applying rejection criteria. To mitigate this, a master flat-field image was created by combining the bias and dark current subtracted selected flat-field images from every night using IRAF's `imcombine`. The master flats, called `H`α`_Master_Flat.fits`, `[OI]_Master_Flat.fits`, and `Continuum_Master_Flat.fits`, were used to reduce the images taken in Hα, [OI] and Continuum filters, respectively. A summary of the number of acceptable flat-field images that were used to create the combined flat-field image for each night can be seen in Table 6.1.

Number of Good Flats and Their Corresponding Filters and Dates					
Continuum					
Date of Observation (MM/DD)	10/18	11/15	11/23	11/7	11/8
Number of Good Flats	10	5	6	6	8
Hα					
Date of Observation (MM/DD)	10/19	11/18	11/5	11/7	12/13
Number of Good Flats	7	9	7	3	3
[OI]					
Date of Observation (MM/DD)	10/20	11/27	11/23		
Number of Good Flats	9	4	3		

Table 6.1: The final number of suitable flats taken through each filter that were deemed suitable for correcting target images.

6.4 Reduction of Images

6.4.1 Correcting for Bias, Dark, and Flat-Fields

The first steps in reducing the images were to subtract the bias and dark and to divide by the flat-field image. Due to a large number of images taken with two different cameras through three different filters, it was imperative to create a pipeline to process the images efficiently. To achieve that, a series of Python scripts were created.

To process images taken in Hα, script `Hα_Bias_Dark_Flat.py` was utilized. Similarly, the images taken in the [OI] filter were processed using `[OI]_Bias_Dark_Flat.py`, and `Continuum_Bias_Dark_Flat.py` was used to process the images taken using the Continuum filter.

The two scripts for processing the line images, which were acquired using Harlequin, followed identical paths up until flat-field correction. However, images taken in the Continuum filter needed to be processed separately as

they were taken using the Bobwhite's CCD, for which the bias and dark had to be evaluated using a different set of equations. The reduction procedures for images taken in different filters are outlined below, supplemented with a decision-making tree that can be seen in Figure 6.10.

To process the images, each script:

Step 1: Loaded the data from each image file `Image_N` into an array of values called `Image_Data_N`.

Step 2: Obtained the CCD temperature T_N from the image headers for each image.

Step 3: Calculated the average bias per pixel `Image_Bias_N` for each image using the CCD Temperature T_N and either:

(a) Equation 6.1 if the image was taken through the Hα or [OI] filter.

(b) Equation 6.3 if the image was taken through the Continuum filter.

Step 4: Created the `Bias_Frame_N` by multiplying the `Image_Bias_N` by either:

(a) `Harlequin_Skeleton_Bias.fits` if the image was taken through the Hα or [OI] filter.

(b) `Bobwhite_Skeleton_Bias.fits` if the image was taken through the Continuum filter.

Step 5: Calculated the Dark Current `Image_Dark_Current_N` using CCD Temperature T_N and either:

(a) Equation 6.8 if the image was taken using the Hα or the [OI] filter.

(b) Equation 6.11 if the image was taken using the Continuum filter.

Step 6: Compared `Image_Dark_Current_N` to the average dark current obtained from the overscan regions of the image `Image_N`. If the comparison of values yielded a satisfactory result, the script proceeded to the next step. Otherwise, it raised an alert about an anomaly in an image for manual inspection of the image.

Step 7: Subtracted the `Image_Bias_N` from the `Image_Dark_Current_N` to obtain `Bias_Corrected_Image_Dark_Current_N`.

Step 8: Subtracted the `Image_Bias_N` from the `Image_Data_N` resulting in `Bias_Corrected_Image_Data_N`.

Step 9: Subtracted the `Bias_Corrected_Image_Dark_Current_N` from the `Bias_Corrected_Image_Data_N` to obtain `Bias_And_Dark_Corrected_Image_Data_N`.

Step 10: Performed a flat-field correction on the `Bias_And_Dark_Corrected_Image_Data_N` by dividing it by either:

(a) `H`α`_Master_Flat.fits` if the image was taken using the Hα filter.

(b) `[OI]_Master_Flat.fits` if the image was taken using the [OI] filter.

(c) `Continuum_Master_Flat.fits` if the image was taken using the Continuum filter.

Step 11: Saved the resulting images as `Processed_Image_N.fits`

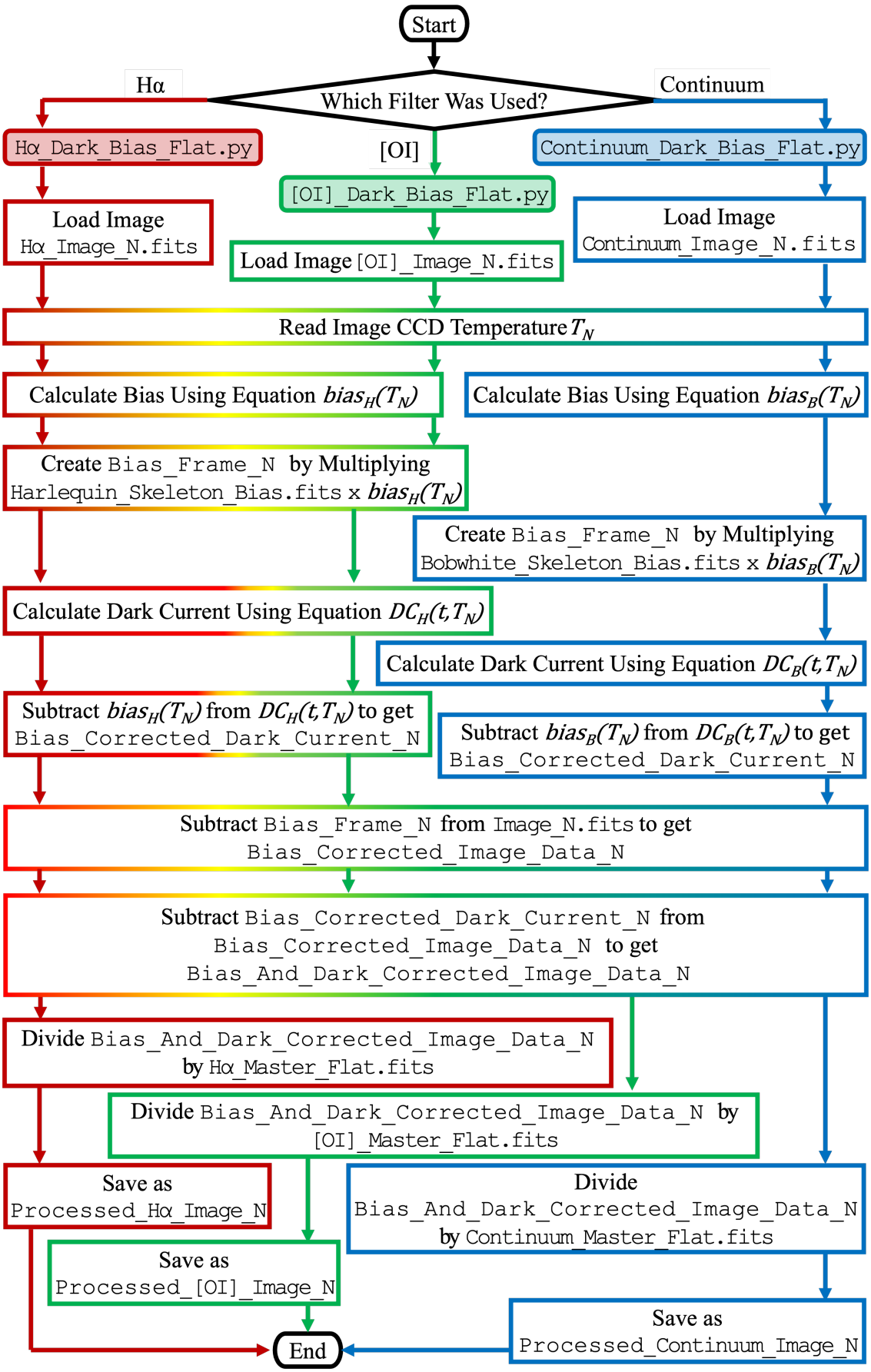

Figure 6.10: Decision Making Tree for the Reduction Procedure.

6.4.2 Image Registration

Because of imperfect tracking on any given night and/or imperfect pointing from one night to another, images acquired for any target were shifted with respect to one another. Thus, they had to be registered before being combined. In this section, the details of the algorithm for image registration are discussed in detail. The selection of a reference image was accomplished as follows:

6.4.2.1 Finding a Reference Image: Part 1

The process of image registration begins with finding a suitable reference image with respect to which all other line and continuum images will be registered.

The first step was to determine what kind of image should be used as a reference - a continuum or a line image – and if the reference image should be a line image, which line filter should be chosen as a reference.

If the target was imaged in [OI], then the reference image for image registration was chosen from one of the images of the target taken through the [OI] filter. If the target was only imaged in Hα, then the reference image was chosen from one of the images taken in Hα. These decisions were influenced by the anticipated faintness of the [OI] emission and the necessity to protect the signal in the [OI] images from potential distortions introduced by the registration.

Another consideration when selecting a reference image was the image quality. The reference image was chosen by finding an emission-line image with the smallest average Moffat FWHM of stars and highest average star signal enclosed by the Moffat FWHM. Usually, this meant that the image was acquired

at the smallest airmass.

To do so, a line image with the highest average signal was chosen as the Preliminary Reference Image. The Preliminary Reference Image was chosen after all images in emission-line and continuum alike were manually inspected for defects, and the defective images were rejected. The process of finding a reference image differed slightly depending on whether the target was imaged in one or both line filters. The different processes are described below and are supplemented with a decision-making tree that can be seen in Figure 6.11.

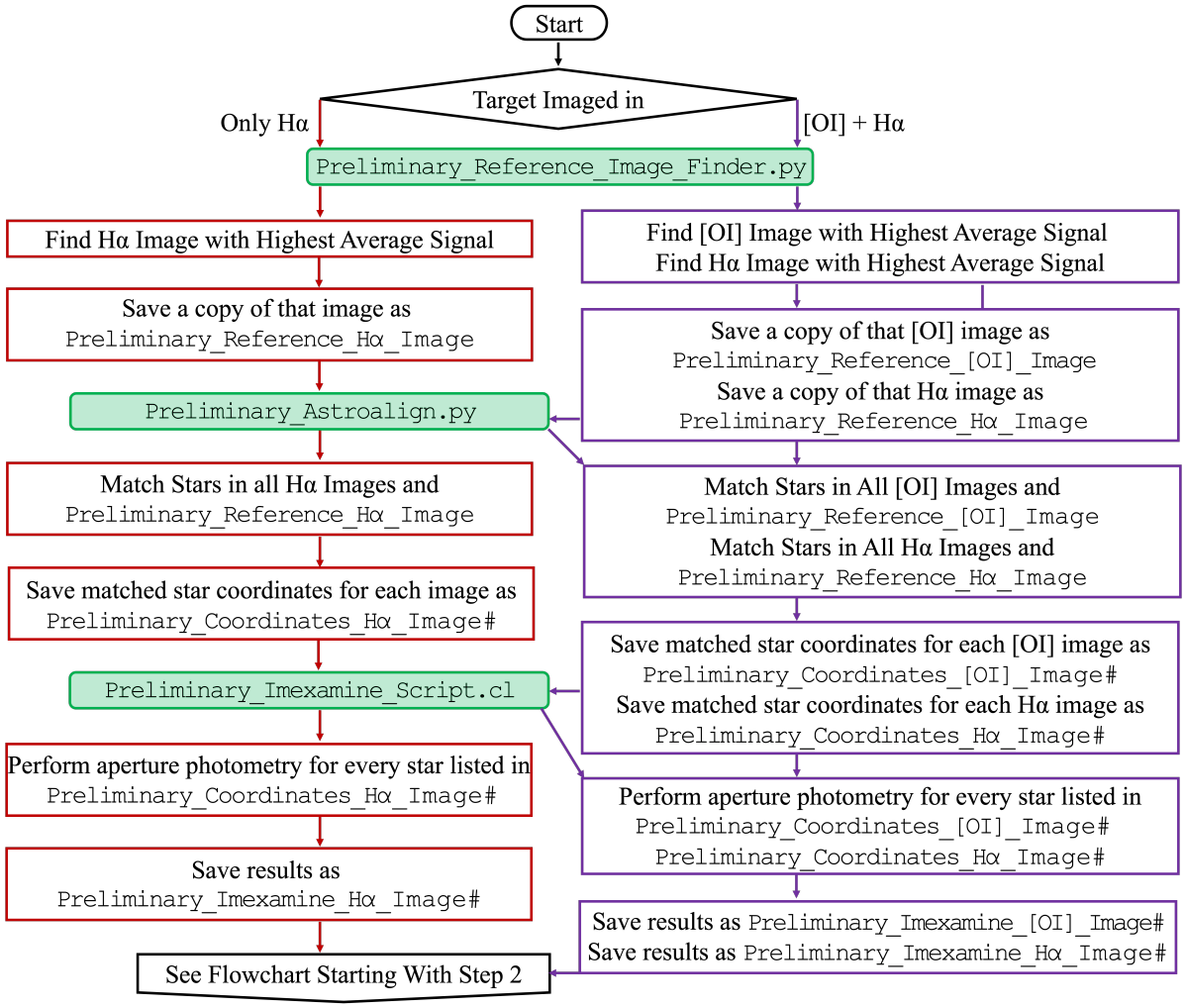

Figure 6.11: Image Registration Part 1: Finding A Reference Image Parts 1 and 2.

If the target was imaged in both line filters:

Step 1: Compute the average total signal for every [OI] image.

Step 2: Find [OI] image with the highest average signal.

Step 3: Save a copy as `Preliminary_Reference_[OI]_Image.fits`.

Step 4: Compute the average signal for every Hα image.

Step 5: Find Hα image with the highest average signal.

Step 6: Save a copy as `Preliminary_Reference_`Hα`_Image.fits`.

If the target was imaged only in Hα Steps 1 - 3 were omitted.

6.4.2.2 Finding a Reference Image: Part 2

Now it is time to inspect the chosen Preliminary Reference Image(s) for any defects. Slight defects, such as cosmic rays, elevate the average signal, while not contributing to the signal coming from the target. To do so, the Moffat FWHMs and the stellar signals they enclosed were computed for each line image.

This was accomplished by finding matching pairs of stars on each emission line image, and comparing the Moffat FWHMs of stars and the signals from stars enclosed within the Moffat profiles in these images. A candidate reference image would have the smallest Moffat FWHM and the highest enclosed stellar signal.

To identify this image, a Python script called `Preliminary_Astroalign.py` was developed. Using Python's `astroalign` package, it matched stars in an image with those on a Preliminary Reference Image. The `Preliminary_Astroalign.py` script saved the coordinates of matched stars into Preliminary Coordinates

files, which were used by `Preliminary_Imexamine_Script.cl` to perform aperture photometry on every star in every line image. Results of aperture photometry were saved on the hard disk. The procedure differed slightly depending on whether the target was imaged in one or both line filters. The decision-making tree for this algorithm can be found in Figure 6.11.

If the target was observed in both line filters, the script:

Step 1: Matched stars in the `Preliminary_Reference_[OI]_Image.fits` with stars in all [OI] images.

Step 2: Saved the stellar coordinates into a Preliminary Coordinate File `Preliminary_Coordinates_[OI]_Image#`.

Step 3: Use `Preliminary_Imexamine_Script.cl` to perform aperture photometry on stars in `Preliminary_Coordinates_[OI]_Image#`.

Step 4: Save results of aperture photometry into `Preliminary_Imaxamine_[OI]_-Image#`.

Step 5: Matched stars in the `Preliminary_Reference_H`α`_Image.fits` with stars in all Hα images.

Step 6: Saved the stellar coordinates into a Preliminary Coordinate File `Preliminary_Coordinates_H`α`_Image#`.

Step 7: Use `Preliminary_Imexamine_Script.cl` to perform aperture photometry on stars in `Preliminary_Coordinates_H`α`_Image#`.

Step 8: Save results of aperture photometry into `Preliminary_Imaxamine_H`α`_-Image#`.

If the target was only observed only in Hα Steps 1 - 4 were omitted.

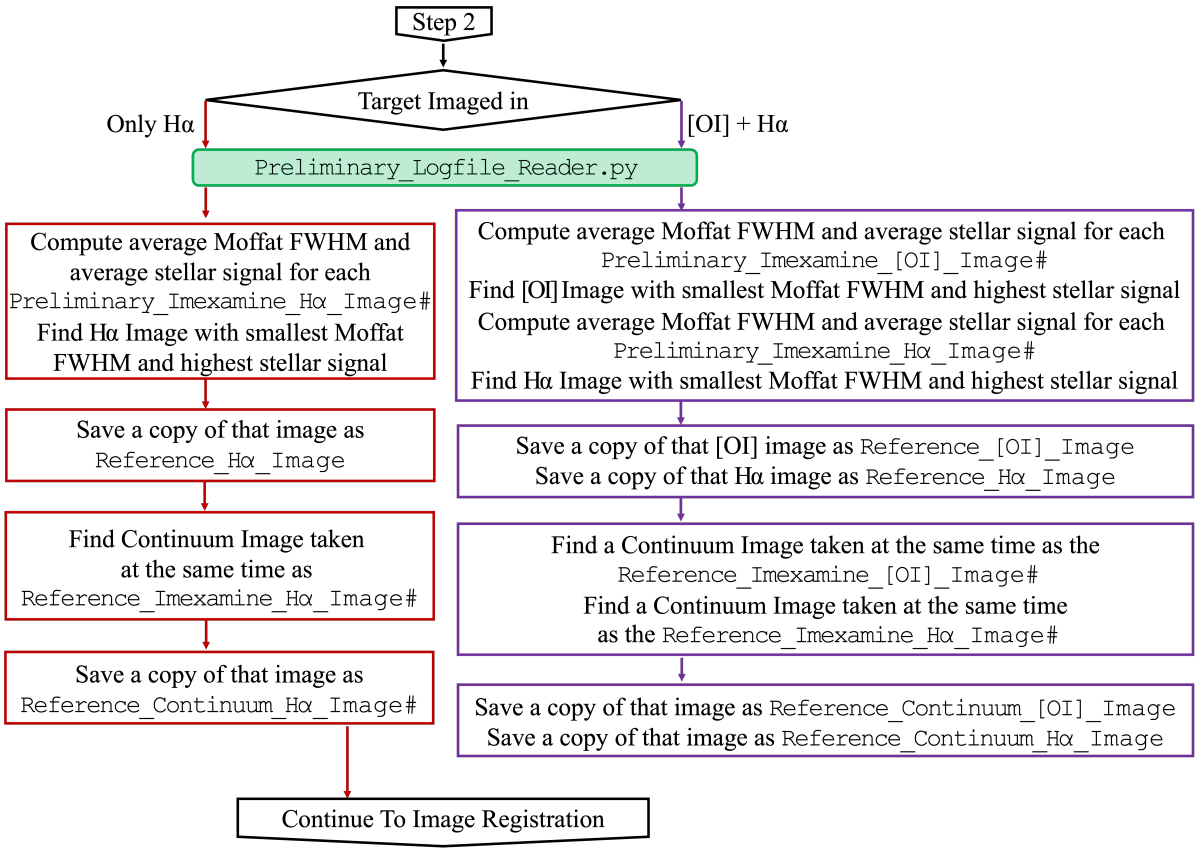

Figure 6.12: Image Registration Part 1: Finding A Reference Image Part 3.

6.4.2.3 Finding a Reference Image: Part 3

The results yielded by `Preliminary_Imexamine_Script.cl` were then used by another Python script called `Preliminary_Logfile_Reader.py` to compute the average Moffat FWHMs and enclosed signal for matched stars listed in the `Preliminary_Imexamine_[OI]_Image#` and `Preliminary_Imexamine_H`α`_Image#` files, depending on the line filters used.

This script then identified the reference line image by selecting a line image with the smallest average Moffat FWHM and the highest average total signal from stars enclosed by the Moffat FWHM. The reference continuum image was adopted to be the continuum image taken at the same time as the reference

line image. The continuum image taken at the same time as the [OI] image will be referred to as `Continuum_[OI]`; similarly, the continuum image taken at the same time as the Hα image will be referred to as `Continuum_H`α. The decision-making tree for this step can be seen in Figure 6.12. If the target was observed in both line filters:

Step 1: Average Moffat FWHMs and stellar signals were computed for each image using `Preliminary_Imaxamine_[OI]_Image`#. [OI] image with the smallest Moffat FWHM and the highest enclosed stellar signal was adopted as the reference image. A copy of the reference [OI] image was saved as `Reference_[OI]_Image.fits`.

Step 2: Continuum image taken at the same time as the `Reference_[OI]_Image.fits` was identified. A copy of that continuum image was saved as `Reference_Continuum_[OI]_Image.fits`.

Step 3: Average Moffat FWHMs and stellar signals were computed for each image using `Preliminary_Imaxamine_H`α`_Image`#. Hα image with the smallest Moffat FWHM and the highest enclosed stellar signal was adopted as the reference image. A copy of the reference Hα image was saved as `Reference_H`α`_Image.fits`.

Step 4: Continuum image taken at the same time as the `Reference_H`α`_Image.fits` was identified. A copy of that continuum image was saved as `Reference_Continuum_H`α`_Image.fits`.

If the target was only observed only in Hα Steps 1 and 2 were omitted.

6.4.2.4 Registering Images

Now that a reference image is identified, the images can be registered i.e., rotated, scaled, and shifted to match the reference image. If the target was imaged in [OI] then all images will be registered with respect to the `Reference_[OI]_Image.fits`. If the target was imaged in Hα only then all Hα and Continuum images will be registered with respect to `Reference_Hα_Image.fits`.

To register the images the stars on all images were matched with the stars on the reference image. The stellar coordinates were then used by IRAF's `geomap` routine to compute the transformations needed to register the images for each filter with its reference image. The transformations computed by IRAF's `geomap` were then passed to IRAF's `gregister` routine to register the images. This rotated, scaled and translated all continuum and line images according to the transformations computed by `geomap`. The registered images were then combined using IRAF's `imcombine` with the computed scales and weights to create the final [OI], Hα and Continuum images.

6.4.3 Alignment of Images

The two cameras were slightly rotated with respect to one another. To subtract continuum images from line images we needed to align the continuum images to their line image counterparts. To register a large number of images, a series of Python and IRAF scripts were developed.

The orientation of Bobwhite with respect to Harlequin was obtained by applying IRAF's `geomap` to images of a star field. The continuum images were

rotated with respect to the line images by $\theta = 4.09 \pm 0.12\ ^{\circ}$.

The continuum and line images could be considered to be of uniform scale, because `geomap` revealed no evidence of stretching or compressing in any direction. Their respective scales were computed to be

$$x_{mag} = \frac{x_{cont}}{x_{line}} = 0.9989 \pm 0.0004; \qquad y_{mag} = \frac{y_{cont}}{y_{line}} = 0.9988 \pm 0.0003$$

where x_{mag} and y_{mag} are the stretching/compressing factors, x_{cont} and y_{cont} are stellar coordinates in the registered continuum images, and x_{line} and y_{line} are stellar coordinates coordinates in the registered line images.

`geomap` revealed that on average the continuum images needed to be shifted by $\mathrm{x_{shift}} = -149 \pm 2$ pix horizontally (along the long side of the image) and by $\mathrm{y_{shift}} = 102 \pm 13$ pix vertically (along the short side of the images). The source of the large standard deviation in the shift along the y-axis is likely due to the variable focus across the field of view for Bobwhite. However it is possible the large spread of shifts could originate from the lens-camera system not being rigidly fastened to its hexagonal bucket, thereby moving slightly with changing orientation as its centre of mass shifted with telescope position.

6.4.4 Removing Stars

In order to see faint extended structures more clearly and measure their properties reliably, it helps to remove the stars. The presence of very bright stars in the field can eclipse the glow of a faint extended object. Removing the bright point sources makes it possible to adjust the image contrast and locate

any faint extended glow. Additionally, superimposed stars can contaminate the measurements of surface brightness of the object (Buta & McCall, 1999). Examples of this can be found in Section 7, which contains images of our targets with stars present and stars removed.

Theoretically, the stars on a line image should disappear after subtracting the corresponding flux-scaled continuum image, as stars emit continuum. However, due to slight focus differences between line and continuum images, we were unable to put that theory into practice. Simply subtracting the scaled and registered continuum images from the line images created an image ridden with artifacts of incomplete star subtraction, such as rings or spots. Moreover, all images that were taken using the Bobwhite CCD camera exhibited a focus that changed gradually from the centre of the image towards the North-East corner of the image. This corner will henceforth be referred to as The Corner of Dread, because the degradation of stellar profiles there caused a variety of problems during processing to remove stars.

Circumstances motivated us to remove stars using an IRAF script called `killall` developed by Buta & McCall (1999). In essence, the `killall` programmatically fits the PSF to a star or stars of choice, and uses it to remove all stars in the image that have a similar PSF. The detailed explanation of the functions and algorithms of `killall` can be found in Buta & McCall (1999). Although `killall` can mistake compact nebulae, such as HII regions in external galaxies, for stars and remove them, it is both improbable and inconsequential to our research, as the focus of our research is on extended objects. The star removal process generally followed that of Buta & McCall (1999), with the exception of

removing residual CCD response patterns. The steps that were taken to clean the images are enumerated below.

Step 1:

Locate the stars in an image by using IRAF's `daofind` routine. To run `daofind` effectively, it was provided with the minimum and maximum counts found in an image, the readout noise, the gain (electrons per ADU), an estimate for the FWHM of the PSF, and the standard deviation of the signal in a patch of sky (a starless and nebula-less patch of an image). This routine produced `picture.coo.1`, a file with coordinates and properties of found stars.

Step 2:

Obtain photometric measurements of stars using IRAF's `phot` routine. This routine used the image and `picture.coo.1` file to arrive at `picture.mag.1`, a file containing stellar positions, fluxes, magnitudes, and sky backgrounds along with their uncertainties.

Step 3:

Identify candidate PSF stars by using IRAF's `imexamine` on a few stars in the neighbourhood of the image centre. A good PSF candidate star was chosen to have $20,000$ to $35,000$ counts at peak, and with no neighbours in its immediate vicinity (within approximately 30 pixels).

Step 4:

Set up an analytical PSF by running IRAF's `psf` routine interactively. At this stage, the PSF was deemed to be invariant across the image, so parameter `daopars.varorder` was set to `-1`. The `psf` routine created an analytical profile

from the observed profiles of selected candidate PSF stars. The resulting mean PSF was stored in `picture.psf.1.fits`, which could subsequently be inspected by using the `seepsf` command.

Step 5:

Run `killall` for the first time, adopting `picture.psf.1.fits` as the PSF and `picture.mag.1` as the list of stars to be removed. During this run, `killall` iterated only once, producing the files `picture.allfits1` (the photometry file), `picture.nostr1`(an image with stars removed), and `picture.nogal1` (an image with background removed). This first run of `killall` typically removed the majority of the stars, albeit with imperfections due to using a fixed analytical PSF.

Step 6:

Choose a magnitude range for stars to define a variable PSF. The adopted range was within $\pm 1\,\mathrm{mag}$ of the original PSF candidates from Step 1. IRAF's `pselect` was used to create a list of PSF candidate stars from `picture.allfits1`. The output file was `picture.psfstars`.

Step 7:

Subtract all but PSF stars by using IRAF's `substar` on the original image. The output was `picture.sub.1.fits`.

Step 8:

Define a variable PSF using the candidate PSF stars. Now `daopars.varorder` needs to be changed to 1 or 2 depending on the severity of the variation of the PSF across the field of view. The best stars to use to define the PSF were

selected from `picture.sub.1.fits` on the basis of the radial plots of their profiles by the `psf` routine. The resulting PSF along with variability parameters was placed in `picture.psf.2`.

Step 9:

Run `killall` again using the variable PSF. All but oversaturated or severely unfocused stars were removed.

Step 10:

Manually remove stars with bad residuals by using IRAF's `imedit`.

Step 11:

Remove stars in The Corner of Dread if working with a continuum image. To do so, the values for minimum, maximum, FWHM and standard deviation of the sky were computed for the manually edited image from Step 10 and used with IRAF's `daofind` routine on that image to obtain the coordinates of the remaining stars. An attempt was then made to measure the Moffat FWHM of several of these stars using IRAF's `imexamine`; if the Moffat profile failed to converge for all remaining stars, the stars were inspected manually and their average radii were approximated. The stellar coordinates and the radii were used to run a custom `imedit_script` script, which utilized IRAF's `imedit` routine to remove the remaining stars.

Step 12:

Remove "salt & pepper" from the image. The "salt & pepper" refers to a form of noise in the image. It is created by the combination of dim stars much below the threshold for detection that did not get removed, cosmic rays, and

single white or black pixels left in the wake of partially successful star removal (Buta & McCall, 1999). Such pixels would stand out from the overall image background and make the image appear "grainy". Because these "grains" are much brighter or darker compared to their neighbours, the image starts to look like someone sprinkled salt and pepper on it. Removal of "salt & pepper" was accomplished by lowering the detection threshold for `daofind`'s parameters to obtain the coordinates of brighter pixels in the image. These coordinates were then used by `imedit_script` on the image from Step 11 to automatically replace the deviant pixels with the sky.

6.4.5 Subtracting Continuum

Because the line filters admit both line and continuum emission, the continuum needs to be removed from line images to reveal pure line emission and thereby gain an accurate depiction of its distribution and brightness. To subtract the continuum, the flux in the continuum images had to be scaled by the ratio of line and continuum filter transmissions.

The continuum filter is $8.6\,\mathrm{nm}$ wide, while the line filters are only $2.8\,\mathrm{nm}$ wide. It was expected that the continuum filter admitted about 3.1 times more flux than the line filters, as the peak transmissions were expected to be similar. Computing the integrals of the normalized filter transmission curves and taking the ratios yielded similar results. Integrating over the filter transmission curves using the trapezoid rule yielded

$$T_{Continuum} = \int_{\lambda_0}^{\lambda_f} t_{Continuum}\, d\lambda = 8.58\ \mathrm{nm};$$

$$T_{H\alpha} = \int_{\lambda_0}^{\lambda_f} t_{H\alpha}\, d\lambda = 2.81 \text{ nm}; \qquad \mathrm{T_{[OI]}} = \int_{\lambda_0}^{\lambda_\mathrm{f}} \mathrm{t_{[OI]}}\, \mathrm{d}\lambda = 2.60 \text{ nm}$$

computing the ratios of these integrals yields

$$\frac{T_{Continuum}}{T_{H\alpha}} = 3.05; \quad \frac{T_{Continuum}}{T_{[OI]}} = 3.30; \qquad \frac{T_{H\alpha}}{T_{[OI]}} = 1.08$$

Better estimates of the relative scales of fluxes were acquired by measuring the counts of matched stars on line and continuum images. Stellar counts were measured on bias and dark-subtracted, and flat-field corrected images. The stellar flux ratios were taken using the stellar fluxes from the line image and the associated continuum image. The associated continuum image is a continuum image obtained simultaneously with the line image, for the same target. The continuum image associated with some [OI] image `[OI]_#` will be referred to as `Continuum_[OI]_#`. The continuum image associated with some Hα image `Hα_#` will be referred to as `Continuum_Hα_#`.

Observations of the PacMan Nebula in Hα and observations of And XVIII on 2021-11-05 were omitted from the analysis. The Hα images of the PacMan Nebula and the images of And XVIII on 2021-11-05 were omitted due to the small number of images.

To obtain the fluxes of stars in images:

Step 1:

IRAF's `phot` procedure was used to perform photometry on the matched stars obtained during the Image Registration procedure (discussed in Section 6.4.2). The files contained the coordinates of stars matched in line and associated continuum images:

(a) Files `Final_Coordinates_[OI]#` and `Final_Coordinates_Continuum_[OI]#` were used for photometry. The results were saved into files `Initial_Photometry_[OI]_#` and `Initial_Photometry_Continuum_[OI]_#`.

(b) Files `Final_Coordinates_H`α`#` and `Final_Coordinates_Continuum_H`α`#` were used for photometry. The results were saved into files `Initial_Photometry_H`α`_#` and `Initial_Photometry_Continuum_H`α`_#`.

Step 2:

The stars in the photometry files obtained in Step 1 that were oversaturated or too dim were excluded from the sample using IRAF's `pselect` routine. This was done by selecting stars within $\pm 1\,\mathrm{mag}$ of our candidate PSF star discussed in Section 6.4.4. The stars located within $200\,\mathrm{pix}$ of the edge of the images were also excluded from the sample to alleviate issues of focus in The Corner of Dread in the continuum images.

Step 3:

Aperture photometry was performed again on each image for each star in the truncated star list obtained in Step 2 using `Preliminary_Imexamine_Script.cl` discussed in Section 6.4.2. For each image this created a file containing the Moffat FWHM and the total signal within the Moffat FWHM radius for each star in that image.

Step 4:

The stellar signal ratios listed in Column 7 in Tables 6.2 and 6.3 were computed as follows:

For [OI] Signals:

(a) The signal of each individual matched star $F_{C,N}$ in each `Continuum_[OI]` image was divided by its signal in [OI] $F_{[OI],N}$ in the the [OI] image, where the subscript N denotes the number of the individual star. This ratio can be written as $\frac{F_{C,N}}{F_{[OI],N}}$.

(b) An average of the stellar signal ratio $\langle\frac{F_{C,N}}{F_{[OI],N}}\rangle_{\#}$ was computed for all [OI] and `Continuum_[OI]` images. $\langle\frac{F_{C,N}}{F_{[OI],N}}\rangle_{\#}$ values were then inspected for outliers. If an outlier was found, the [OI] and `Continuum_[OI]` images were inspected for anomalies. If any anomalies in either the [OI] or the `Continuum_[OI]` images were found, these images were excluded from the analysis. The values of $\langle\frac{F_{C,N}}{F_{[OI],N}}\rangle_{\#}$ were then recomputed without the anomalous images and listed in Column 7 in Table 6.2.

For Hα Signals:

(a) The signal of each individual matched star $F_{C,N}$ in each `Continuum_`Hα image was divided by its signal in Hα $F_{H\alpha,N}$ in the the Hα image, where the subscript N denotes the number of the individual star. This ratio can be written as $\frac{F_{C,N}}{F_{H\alpha,N}}$.

(b) An average of the stellar signal ratio $\langle\frac{F_{C,N}}{F_{H\alpha,N}}\rangle_{\#}$ was computed for all Hα and `Continuum_`Hα images. $\langle\frac{F_{C,N}}{F_{H\alpha,N}}\rangle_{\#}$ values were then inspected for outliers. If an outlier was found the Hα and `Continuum_`Hα images were inspected for anomalies. If any anomalies in either the Hα or the `Continuum_`Hα images were found, these images were excluded from the analysis. The values of $\langle\frac{F_{C,N}}{F_{H\alpha,N}}\rangle_{\#}$ were then recomputed without the anomalous images and listed in Column 7 in Table 6.3.

Step 5:

The flux ratios listed in Columns 4, 5 and 6 in Tables 6.2 and 6.3 were computed using all images that were not excluded in Step 4c ([OI]) and Step 4c (Hα). The procedure can be described as follows:

(a) The average stellar signals $\langle F_{[OI]} \rangle$ for all stars in [OI] images were computed and listed in Column 5 in Table 6.2.

(b) The average stellar signals $\langle F_C \rangle$ for all stars in `Continuum_[OI]` images were computed and listed in Column 4 in Table 6.2.

(c) The average stellar signals $\langle F_{H\alpha} \rangle$ for all stars in Hα images were computed and listed in Column 5 in Table 6.3.

(d) The average stellar signals $\langle F_C \rangle$ for all stars in `Continuum_`Hα images were computed and listed in Column 4 in Table 6.3.

(e) The average continuum stellar fluxes $\langle F_C \rangle$ were divided by the average [OI] stellar fluxes $\langle F_{[OI]} \rangle$. These values are listed as $\frac{\langle F_C \rangle}{\langle F_{[OI]} \rangle}$ in Column 6 in Table 6.2.

(f) The average continuum stellar fluxes $\langle F_C \rangle$ were divided by average Hα stellar fluxes $\langle F_{H\alpha} \rangle$. These values are listed as $\frac{\langle F_C \rangle}{\langle F_{H\alpha} \rangle}$ in Column 6 in Table 6.3.

In Tables 6.2 and 6.3, Column 1 gives the name of the target. Column 2 provides the date on which the target was observed; all targets were observed in 2021, and the date is listed in mm/dd format. Column 3 provides the number of matched stars N_T between the continuum images and their listed line counterparts that were used to compute the values in Columns 4, 5, 6 and 7.

To subtract the continuum we chose to adopt the average ratios of individually matched stars listed at the bottom of Column 7 in Tables 6.2 and 6.3.

[OI Flux Ratios]						
1	2	3	4	5	6	7
Target	Date	N_T	$\langle F_C \rangle (\times 10^4)$	$\langle F_{[OI]} \rangle (\times 10^4)$	$\frac{\langle F_C \rangle}{\langle F_{[OI]} \rangle}$	$\left\langle \frac{F_C}{F_{[OI]}} \right\rangle$
PacMan	10/20	173	3.61 ± 1.10	1.23 ± 0.38	2.93 ± 1.27	2.95 ± 0.47
PacMan	10/27	195	3.27 ± 1.28	1.09 ± 0.42	3.00 ± 1.65	2.99 ± 0.57
PacMan	10/28	168	3.73 ± 1.13	1.20 ± 0.51	3.11 ± 1.62	3.21 ± 1.03
PacMan	11/08	184	3.56 ± 1.23	1.19 ± 0.43	2.99 ± 1.49	3.03 ± 0.73
PacMan	11/09	183	3.47 ± 1.20	1.18 ± 0.42	2.94 ± 1.46	2.97 ± 0.68
M27	10/19	244	3.83 ± 1.23	1.28 ± 0.42	2.99 ± 1.37	3.01 ± 1.35
M27	10/27	235	4.02 ± 1.22	1.31 ± 0.40	3.07 ± 1.32	3.07 ± 0.67
Average [OI] Signal Ratios					3.00 ± 1.45	3.03 ± 0.79

Table 6.2: Ratios of measured stellar signals in Continuum and [OI] filters.

Hα Flux Ratios						
1	2	3	4	5	6	7
Target	Date	N_T	$\langle F_C \rangle (\times 10^4)$	$\langle F_{H\alpha} \rangle (\times 10^4)$	$\frac{\langle F_C \rangle}{\langle F_{H\alpha} \rangle}$	$\left\langle \frac{F_C}{F_{H\alpha}} \right\rangle$
M33	$11-08$	74	3.16 ± 1.35	0.98 ± 0.42	3.23 ± 0.60	3.23 ± 0.25
M33	$12-13$	77	3.10 ± 1.28	0.99 ± 0.41	3.14 ± 0.59	3.15 ± 0.25
M33	$12-14$	81	3.06 ± 1.36	0.99 ± 0.43	3.09 ± 0.63	3.09 ± 0.29
M27	$10-18$	112	3.86 ± 1.18	1.08 ± 0.37	3.56 ± 0.46	3.64 ± 0.58
M27	$11-07$	405	3.09 ± 1.31	0.99 ± 0.40	3.10 ± 0.58	3.09 ± 0.38
And XVIII	$10-18$	256	2.94 ± 1.28	1.05 ± 0.48	2.80 ± 0.63	2.83 ± 0.45
And XVIII	$10-19$	252	3.14 ± 1.32	1.02 ± 0.44	3.08 ± 0.61	3.1 ± 0.33
And XVIII	$11-06$	249	3.12 ± 1.28	0.99 ± 0.40	3.16 ± 0.58	3.16 ± 0.27
And XVIII	$11-07$	250	3.10 ± 1.26	0.98 ± 0.40	3.16 ± 0.57	3.17 ± 0.26
And XVIII	$12-13$	245	3.10 ± 1.27	0.99 ± 0.40	3.14 ± 0.58	3.15 ± 0.3
Average Hα Signal Ratios					3.15 ± 1.82	3.16 ± 1.06

Table 6.3: Ratios of measured stellar signals in Continuum and Hα filters.

6.5 Airmass and Atmospheric Extinction

6.5.1 Local Mean Sidereal Time and Hour Angles of Targets.

The Hour Angle (H.A.) of a target is essential for calculating the airmass and hence correcting for atmospheric extinction. It is derived from the Right Ascension (α) and the Local Mean Sidereal Time (LMST) at the time of observation.

The LMST was calculated automatically by QUAIL's software, which re-used some of the original Dome Tracker code written by Matthew Cutone, Richard Bloch and Jesse Rogerson. Their code calculated the Greenwich Mean Sidereal Time (GMST) using

$$GMST = 6.63886 + (0.0657098244 * d) + (1.00273791 * t) \tag{6.12}$$

where d is the day number from the beginning of the calendar year and t is the current time in hours. Then, $LMST$ was calculated using

$$LMST = GMST + \frac{Longitude}{15} \tag{6.13}$$

For the York University Allan I. Carswell Astronomical Observatory, $Longitude = -79.5^o$. H.A. was calculated using the formula

$$H.A. = LMST - \alpha \tag{6.14}$$

The names of observation targets, their positions in α and δ, the times and dates at which their reference images were taken, and the corresponding LMST and H.A. are given in Table 6.4 in Section 6.5.2

6.5.2 Airmass

To determine the flux arriving at the Earth from a target, the observed count rate first must be corrected for atmospheric extinction. Since our targets are located at high altitudes, the curvature of the atmosphere does not have a significant effect, so the plane-parallel atmosphere approximation was be used to calculate the atmospheric extinction.

An object's airmass at the time of observation can be calculated using the following formula:

$$X = \left[\cos\left(\frac{(90 - H)\pi}{180}\right)\right]^{-1} \tag{6.15}$$

where H is the altitude of the target in degrees. H can be calculated using

$$H = \arcsin[\sin(l)\sin(\delta) + \cos(l)\cos(\delta)\cos(H.A.)] \tag{6.16}$$

where l is the latitude of York University, and δ and H.A. are the Declination and the Hour Angle of the object, respectively. The resulting airmasses can be seen in Table 6.4.

In Table 6.4 Column 1 contains the target name and the filter in which a reference line image was taken. Column 2 contains the target's α (J2000) in hh:mm:ss format. Column 3 contains the target's δ (J2000) in dd:mm:ss format. Column 4 contains the date at which the reference image for each tar-

get was taken in DD/MM format. All Hα images were obtained in November of 2021. Column 5 contains the time at which the reference image for each target was obtained in local time (EST) in hh:mm:ss format. Column 6 contains the LMST in hh:mm:ss format. Column 7 contains the H.A. in hh:mm:ss format. Column 8 contains the Altitude H of each target at the time of the reference image in degrees. Column 9 contains the Airmass X of each reference image.

Reference Line Image Information								
1	2	3	4	5	6	7	8	9
Target	α	δ	Date	Time	LMST	H.A.	H	X
HD 217086	$22^{h}56^{m}47^{s}$	$+62^{d}43^{m}37^{s}$	07/11	20:41:14	22:56:47	22:56:47	70.42	1.06
And XVIII	$00^{h}02^{m}14^{s}$	$+45^{d}05^{m}20^{s}$	07/11	22:15:16	00:02:14	00:02:14	78.88	1.02
M33	$01^{h}33^{m}50^{s}$	$+30^{d}39^{m}36^{s}$	08/11	01:15:59	01:33:50	01:33:50	57.35	1.19
M27 (OI)	$19^{h}59^{m}36^{s}$	$+22^{d}43^{m}16^{s}$	27/10	19:53:06	19:59:36	19:59:36	65.53	1.10
M27 (Hα)	$19^{h}59^{m}36^{s}$	$+22^{d}43^{m}16^{s}$	07/11	20:01:48	19:59:36	19:59:36	49.07	1.32
PacMan (OI)	$00^{h}52^{m}25^{s}$	$+56^{d}33^{m}54^{s}$	20/10	02:23:21	00:52:25	00:52:25	66.24	1.09
PacMan (Hα)	$00^{h}52^{m}25^{s}$	$+56^{d}33^{m}54^{s}$	07/11	21:08:40	00:52:25	00:52:25	74.50	1.04

Table 6.4: Hour Angles, LMST, Altitudes and Airmasses of the Reference Images. All reference images were obtained in the year 2021.

6.5.3 Atmospheric Extinction

Formally, the general formula for the atmospheric extinction coefficient is:

$$k(\lambda) = 2.5 \log(e) \int_0^z \alpha(\lambda)\, dx \tag{6.17}$$

where $k(\lambda)$ is the atmospheric extinction coefficient at wavelength λ of the target, $\alpha(\lambda)$ is the linear absorption coefficient, and z and 0 are the location of the target and the bottom of the atmosphere respectively.

The atmospheric extinction of a celestial target at wavelength λ can be cal-

culated from the object's airmass using the following formula:

$$m_{ext} - m_0 = k(\lambda)X \tag{6.18}$$

where m_{ext} is the magnitude observed through the atmosphere, m_0 is the magnitude of the object above the atmosphere, $k(\lambda)$ is the atmospheric extinction coefficient at wavelength λ in $\mathrm{mag/X}$, and X is the airmass. Equation 6.18 can be recast in terms of counts N:

$$-2.5\log(N_0) = -2.5\log(N_{ext}) - k(\lambda)X \tag{6.19}$$

where N_0 is the signal that would be received without the atmospheric extinction, and N_{ext} is the signal actually detected by the CCD at airmass X. Thus,

$$N_0 = N_{ext} * 10^{0.4k(\lambda)X} \tag{6.20}$$

For an emission line source, $k(\lambda)$ is the extinction coefficient at the redshifted wavelength.

In what will follow, the atmospheric extinction as a function of wavelength at York University will be derived. In Section 6.5.3.1 the general power-law fit for the extinction curve will be derived from extinction data retrieved from external observatories and York University. In Section 6.5.3.2 the ozone extinction component will be incorporated, and the synthetic extinction curve for York University will be derived.

6.5.3.1 Derivation of The General Atmospheric Extinction Curve

In this section the wavelength dependency of atmospheric extinction for the Allan I. Carswell Astronomical Observatory was estimated from the trends recorded at other observatories and values for extinction coefficients measured at York University for Johnson-Cousins $BVRI$ filters by Mundy (2018). Plots of $k(\lambda)$ versus λ for Kitt Peak, Mauna Kea, Paranal, Roque de Los Muchachos and Apache observatories together with the results of Mundy (2018) for York University are shown in Figure 6.13.

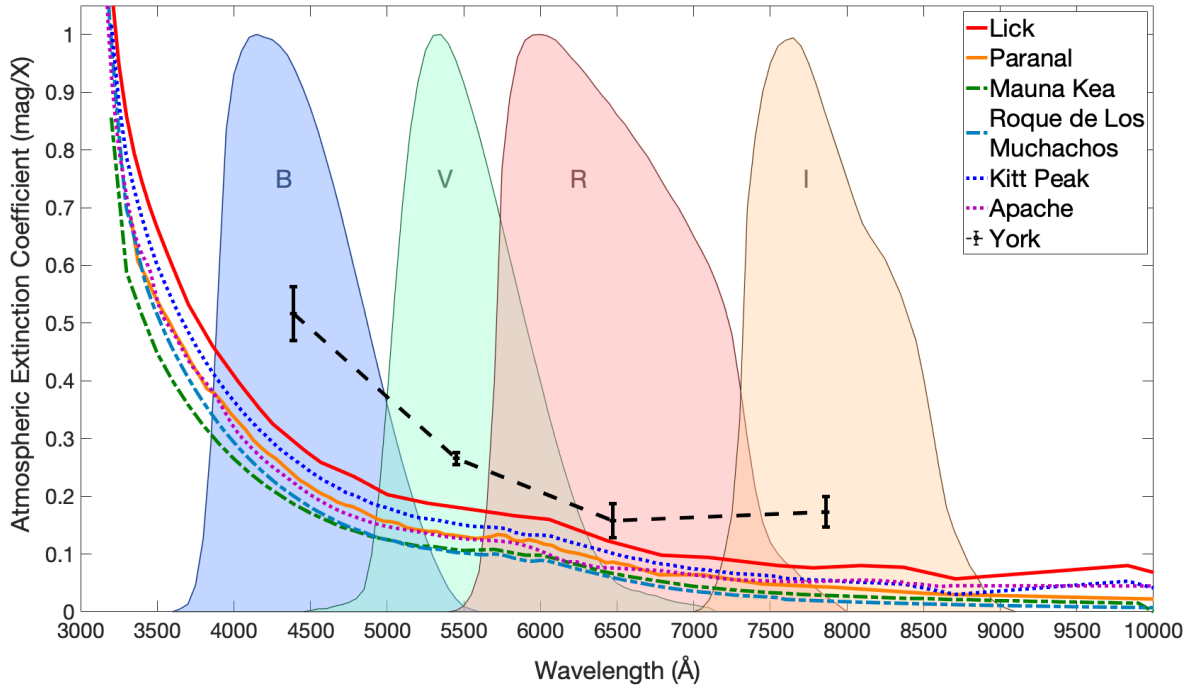

Figure 6.13: Atmospheric Extinction coefficient $k(\lambda)$ in mag/X versus wavelength λ in Å as measured at various observatories and York University. Also shown are the transmission curves for Johnson-Cousins $BVRI$ filters, which were used to define the extinction at York University (Mundy, 2018).

The overall shapes of the extinction curves for external observatories look similar since the atmospheric attenuation varies generally like λ^{-4}. Thus, $k(\lambda)$

can be represented by a power law

$$k(\lambda) = a_{ext}\,\lambda^{b_{ext}} + c_{ext} \tag{6.21}$$

where $k(\lambda)$ is the atmospheric extinction coefficient at wavelength λ, and a_{ext}, b_{ext} and c_{ext} are constants.

Figure 6.13 shows that there appears to be a trend in the shape of the extinction curve with the average extinction at any wavelength. The trend can be utilized to interpolate the extinction coefficients at the wavelengths of our filters. To do so, the curve for each external observatory was fitted with a power law. The resulting power law coefficients and the goodness of fits can be seen in Table 6.5 and the plots of the extinction coefficients for each observatory and their respective fits can be seen in Figure 6.14.

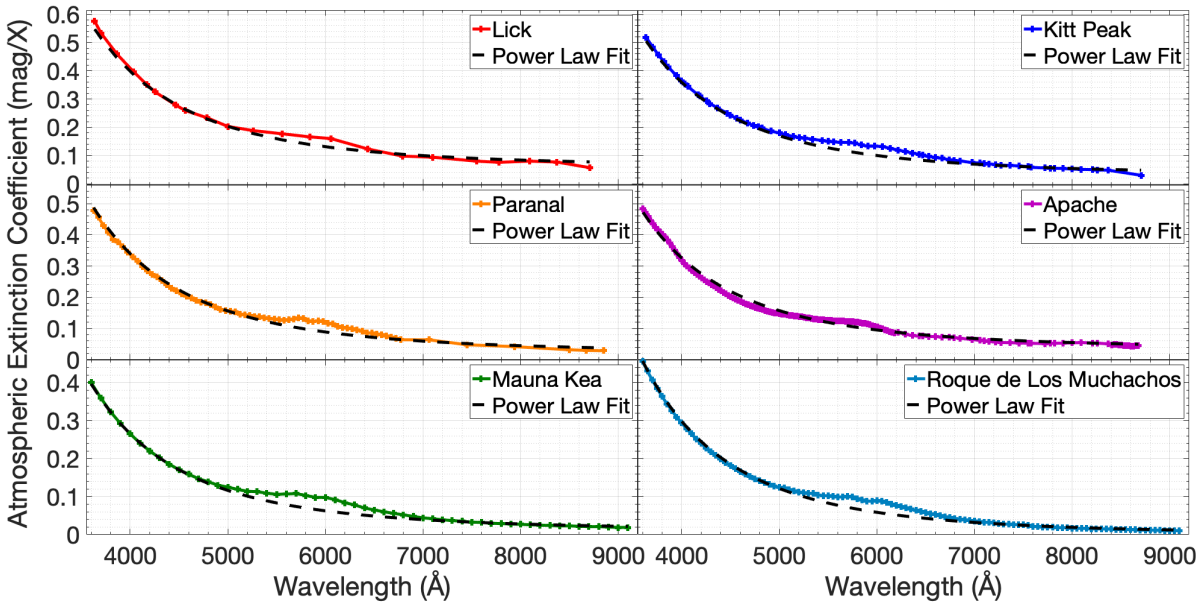

Figure 6.14: Plots of $k(\lambda)$ at external observatories and their respective power law fits.

Power Law Fit Coefficients to Atmospheric Extinction Curves				
Observatory	$a_{ext} \pm \delta a_{ext}$ $(\frac{mag}{X \cdot \lambda})$ $(\times 10^{14})$	$b_{ext} \pm \delta b_{ext}$	$c_{ext} \pm \delta c_{ext}$ $(\frac{mag}{X})$ $(\times 10^{-2})$	R^2
Lick	2.70 ± 1.94	-3.86 ± 0.09	6.07 ± 0.33	0.9934
Kitt Peak	2.85 ± 2.59	-3.87 ± 0.11	3.19 ± 0.38	0.9989
Paranal	3.25 ± 3.24	-3.89 ± 0.12	2.37 ± 0.54	0.9986
Apache	3.25 ± 3.06	-3.90 ± 0.11	3.56 ± 0.35	0.9944
Mauna Kea	5.05 ± 4.81	-3.97 ± 0.12	1.20 ± 0.25	0.9990
Roque de Los Muchachos	12.5 ± 6.10	-4.06 ± 0.06	0.15 ± 0.14	0.9994

Table 6.5: Coefficients of power-law fits and their respective errors to the atmospheric extinction curves of external observatories.

Having established the overall functional relationship between the extinction coefficients and wavelengths for each observatory, it is possible to investigate whether a_{ext}, b_{ext}, and c_{ext} correlate with the average extinction coefficient at any wavelength. The average extinction coefficient of each observatory was computed at the wavelengths of maximal transmission of the Johnson-Cousins $BVRI$ filters. The values of a_{ext}, b_{ext}, and c_{ext} for each observatory were then plotted against the average atmospheric extinction coefficient for each observatory. Plots are shown in Figure 6.15.

The plots of a_{ext}, b_{ext}, and c_{ext} in Figure 6.15 exhibit trends which we can utilize to derive the anticipated amount of atmospheric extinction at York University. To predict the atmospheric extinction curve for York, the trends for a_{ext}, b_{ext}, and c_{ext} with the average extinction coefficient $\langle k \rangle$ were fitted with Equations 6.22, 6.23 and 6.24. The resulting fits are plotted in Figure 6.15 .

$$\log(a_{ext,fit}) = [(-17.56 \pm 2.45) \times 10^{-2}] \log\left[\langle k \rangle - (95.24 \pm 0.02) \times 10^{-3}\right] + (13.23 \pm 0.23) \quad \textbf{(6.22)}$$

$b_{ext,fit}$ =

$$[(7.22 \pm 1.03) \times 10^{-2}] \log \left[\langle k \rangle - (9.51 \pm 0.01) \times 10^{-2}\right] + (-3.78 \pm 0.10) \quad (6.23)$$

$$c_{ext,fit} = [(68.97 \pm 36.10) \times 10^{-2}]\langle k \rangle + (-5.85 \pm 4.60) \times 10^{-2} \quad (6.24)$$

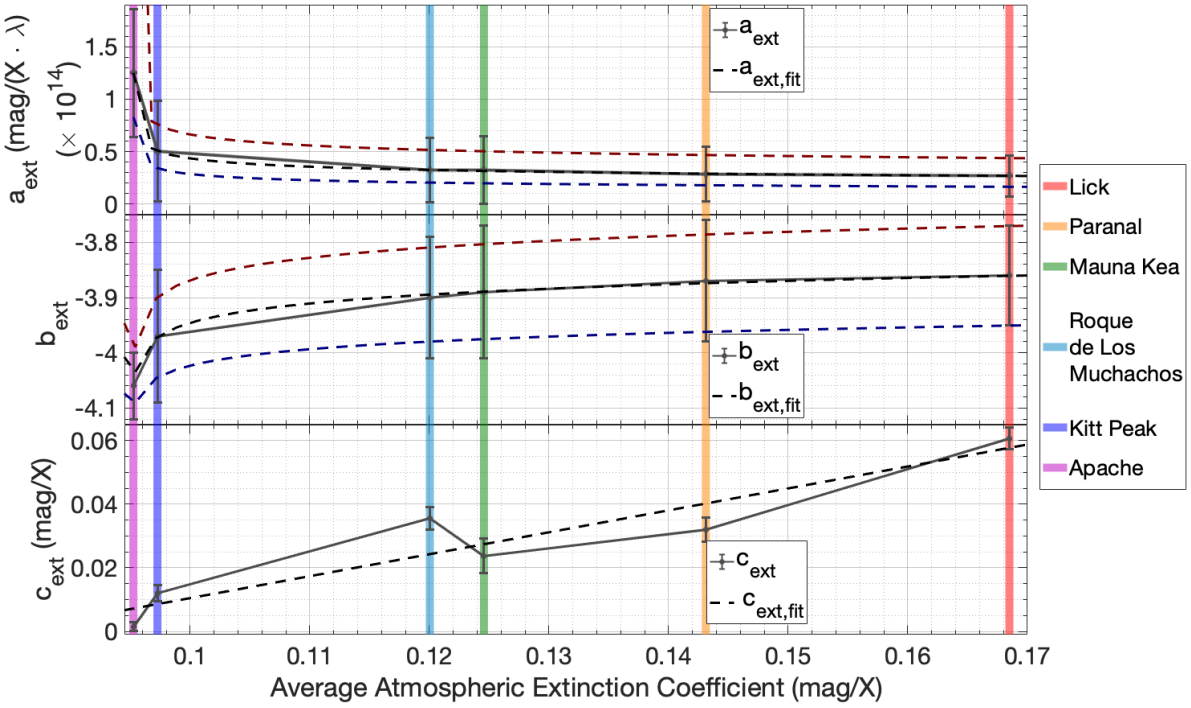

Figure 6.15: Plots of a_{ext}, b_{ext} and c_{ext} from power-law fits to $k(\lambda)$ are plotted against the average $k(\lambda)$ of each external observatory. The fits to the trends of a_{ext}, b_{ext} and c_{ext} are shown as dashed curves. The vertical coloured lines spanning the plot stand for the average $k(\lambda)$ computed for each observatory.

Substituting the average extinction coefficient $\langle k \rangle$ for York University into Equations 6.22, 6.23, and 6.24 yields

$$k(\lambda) = [(2.30 \pm 1.28) \times 10^{13}]\, \lambda^{-3.83 \pm 0.10} + (0.13 \pm 0.12) \quad \text{mag/X} \quad (6.25)$$

where λ is the wavelength in Å. These coefficients produce a curve that describes the wavelength dependency of the atmospheric extinction coefficients at York University reasonably well. It is represented as a dashed curve in Figure 6.16.

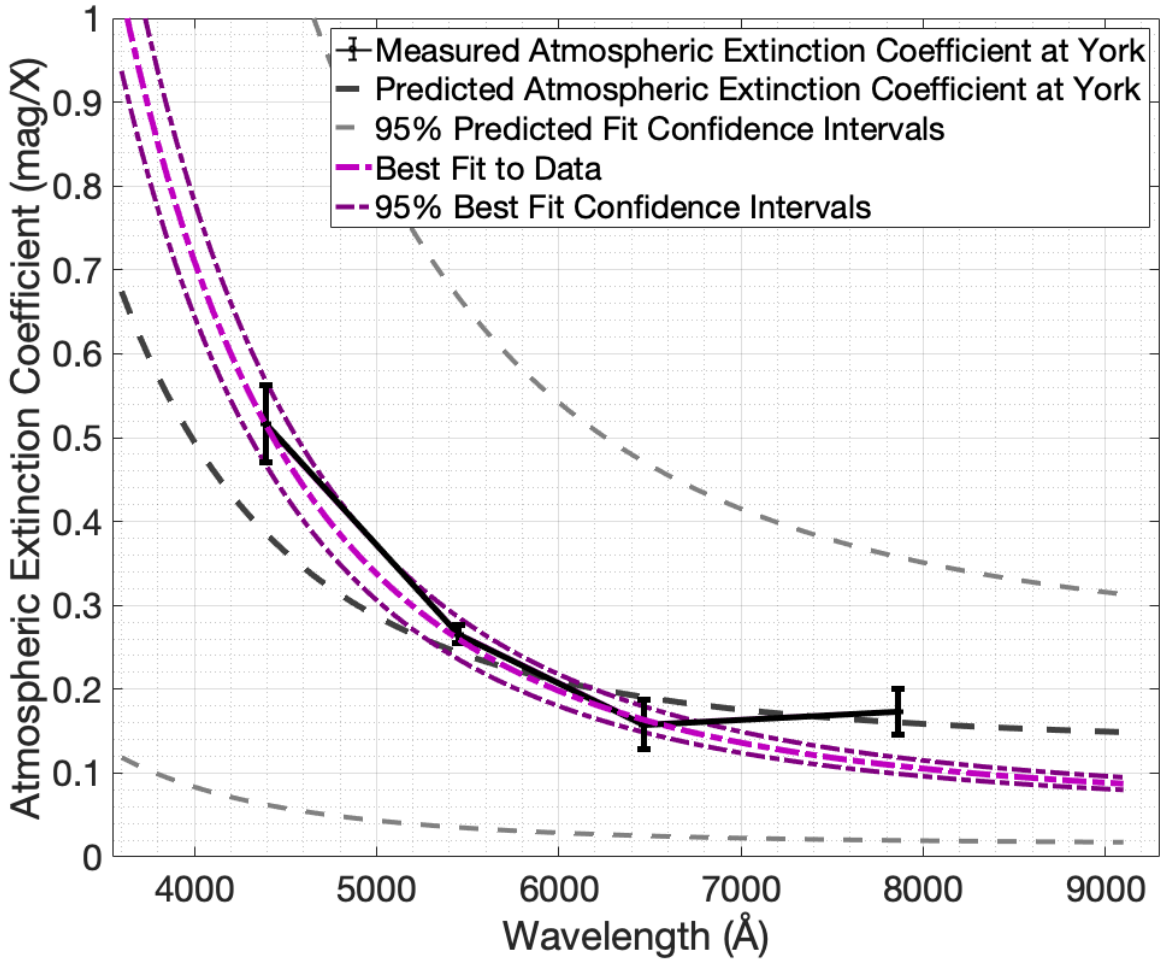

Figure 6.16: Plot of the $k(\lambda)$ versus λ. The $k(\lambda)$ values at York University as measured by Mundy (2018) is plotted in black. The predicted atmospheric extinction curve from Equation 6.25 and its 95% confidence intervals are shown in dark-grey and grey respectively. The best fit to $k(\lambda)$ at York University and its 95% confidence intervals are shown in pink and dark-pink.

This prediction and its error margins were used to narrow down the best fit for the atmospheric extinction curve at York University. To do so, the values of a_{ext}, b_{ext}, and c_{ext} for York University were varied within the allowed confidence intervals to find the curve that deviated least from the measurements by Mundy (2018). This process narrowed down the range of values of coefficients a_{ext}, b_{ext}, and c_{ext}.

The confidence interval for the York University extinction coefficient in the I-band was artificially inflated to twice its value. This was done to allow the fit to converge, because the extinction coefficient at this wavelength already

deviates significantly from the expected position on the extinction curve. The new range of power-law coefficients was then used to compute the best fit for York University and its confidence intervals by fitting a power-law function using MatLab. The best fit to York University's extinction coefficient data can be written as:

$$k(\lambda) = [(3.28 \pm 0.06) \times 10^{13}]\, \lambda^{-3.80 \pm 0.01} + [(5.88 \pm 0.44) \times 10^{-2}] \quad \mathrm{mag/X} \tag{6.26}$$

6.5.3.2 Derivation of The Ozone Extinction Feature and York University Extinction Curve

While the power-law fits describe the large-scale behaviour of the atmospheric extinction curves, there are also localized extinction features that have not been accommodated. In particular, this section will focus on the broadband absorption feature that spans from $450 \leq \lambda\,(\mathrm{nm}) \leq 760$. It is manifested on plots of the extinction curves as a broad but stunted bump. It arises from the absorption of light by ozone (O_3), which peaks at $\sim 600\,\mathrm{nm}$. Because the transmission bands of our filters are located within that bump, it is advantageous to introduce this feature to the atmospheric extinction fit for York University.

The ozone extinction bump can be isolated by dividing the atmospheric extinction coefficient data by their respective fitted curves. The results will be referred to as the residual curves. In the optical, all of the residual curves have a remarkably similar shape. Their plots can be seen in Figure 6.17.

Thus, to derive the most common ozone absorption feature, a median residual curve was obtained. The median was multiplied by the best fit power law for York to synthesize an improved atmospheric extinction curve appropriate

for all wavelength scales.

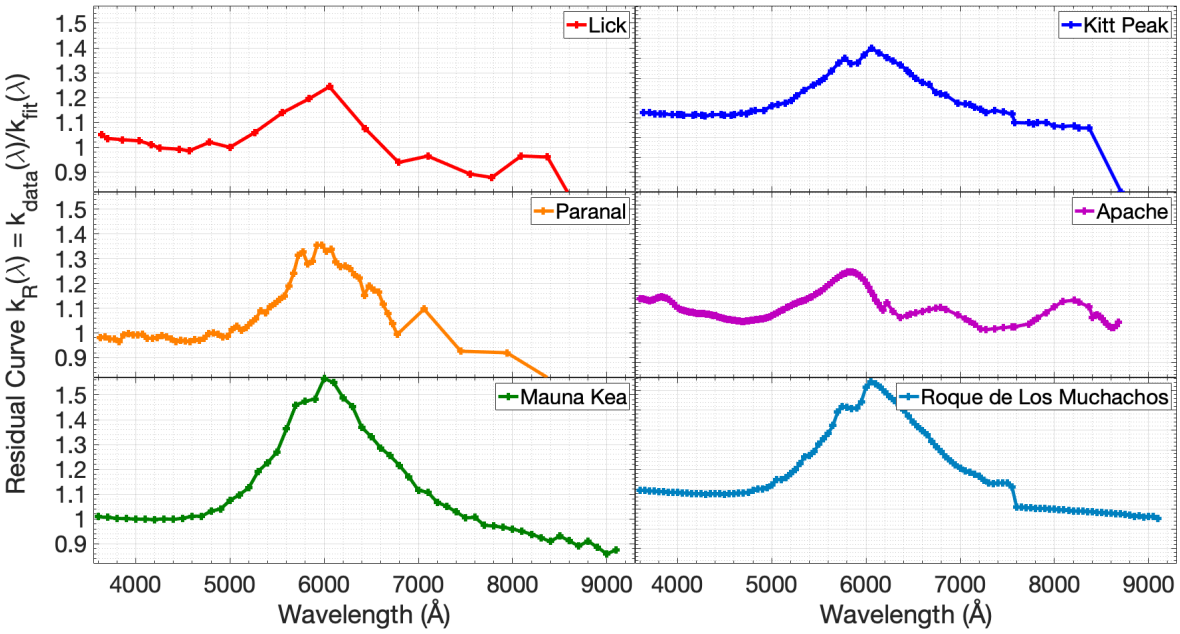

Figure 6.17: Plots of the atmospheric extinction coefficient curves divided by their respective fits. The "bump" in the plot is the atmospheric extinction feature due to ozone.

This synthetic atmospheric extinction curve which we adopted for correcting our measurements for atmospheric extinction can be seen in Figure 6.18.

Targets and Their Atmospheric Extinctions					
Object Name and Filter	λ (nm)	$k(\lambda)$ (mag X)	$k(\lambda)X$ (mag)	$\tau(\lambda)$ (mag)	$e^{\tau} = 10^{0.4k(\lambda)X}$
HD 217086	656.24	0.168 ± 0.073	0.178 ± 0.031	0.164 ± 0.071	1.178 ± 0.084
And XVIII	655.55	0.168 ± 0.073	0.171 ± 0.030	0.157 ± 0.068	1.170 ± 0.080
M33	656.28	0.167 ± 0.073	0.199 ± 0.035	0.184 ± 0.080	1.201 ± 0.096
M27 ([OI])	636.30	0.189 ± 0.082	0.208 ± 0.036	0.191 ± 0.083	1.211 ± 0.100
M27 (Hα)	656.28	0.167 ± 0.073	0.221 ± 0.038	0.204 ± 0.088	1.226 ± 0.108
PacMan ([OI])	636.30	0.189 ± 0.082	0.206 ± 0.036	0.189 ± 0.082	1.209 ± 0.099
PacMan (Hα)	656.28	0.167 ± 0.073	0.174 ± 0.030	0.160 ± 0.070	1.174 ± 0.082

Table 6.6: Airmasses and atmospheric extinctions of target reference images.

The synthesized fit for York University and the calculated values for target airmasses that can be found in Table 6.4. These values were used to calculate the extinctions of our targets. The values of atmospheric extinction particular to the reference images of targets can be found in Table 6.6.

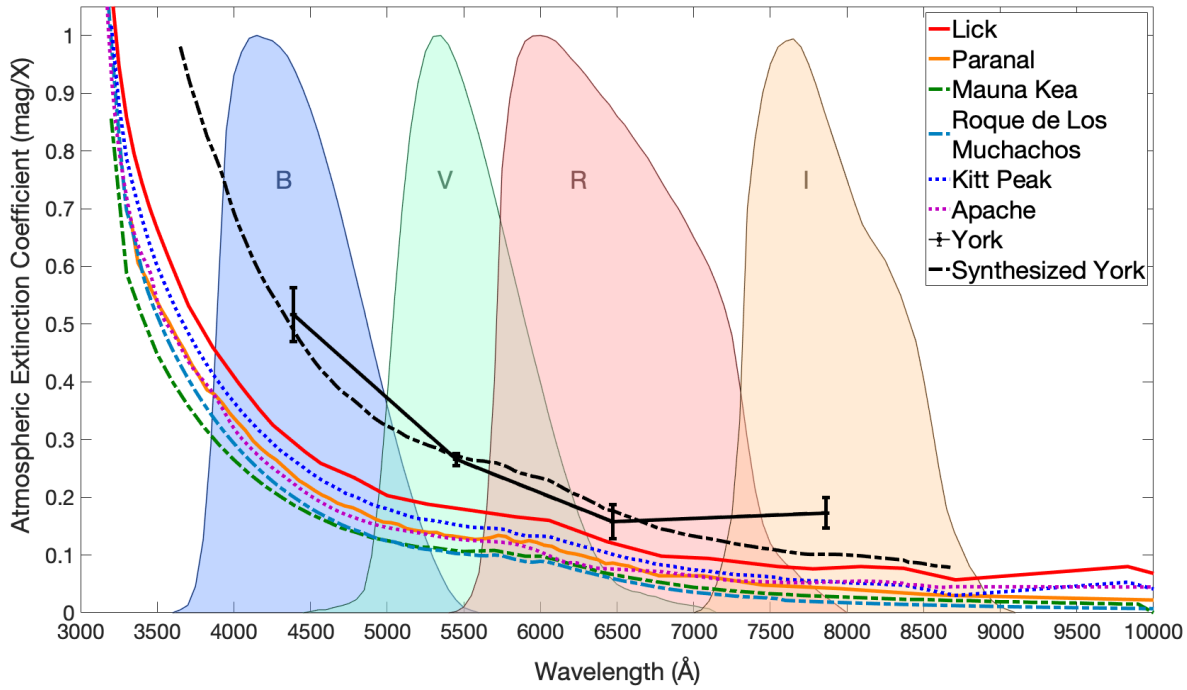

Figure 6.18: Plots of the atmospheric extinction curves for external observatories and York University. The adopted synthetic atmospheric extinction curve for York University is plotted atop of the Johnson-Cousins filter curves.

6.6 Calibration of Fluxes

6.6.1 Theory

6.6.1.1 System Constant β

The relationship between the count rate registered by the CCD by observing an object through a filter and the energy flux accruing above the Earth's atmosphere from that object at the wavelengths spanned by the filter can be written as

$$N = \beta \int F_\lambda(\lambda) e^{-\tau(\lambda)} t(\lambda) d\lambda \tag{6.27}$$

where N is the number of counts per second detected, $t(\lambda)$ is the filter transmission curve, $F_\lambda(\lambda)$ is the flux per unit wavelength from the object as a function

of wavelength λ (usually, in units of $\mathrm{erg\,s^{-1}\,cm^{-2}\,nm^{-1}}$, $\tau(\lambda)$ is the optical depth at wavelength λ of the atmosphere at the altitude of the object, and β is a constant. $\tau(\lambda)$ is related to the atmospheric extinction coefficient $k(\lambda)$ and the airmass X as follows

$$k(\lambda)X = 2.5\,\tau(\lambda)\log(e) \tag{6.28}$$

The system constant β is the factor that converts from counts per second to flux, and vice versa. This constant enables the measurement of magnitudes and surface brightness, and in turn gas densities and gas masses of nebulae. To find the constant β, a "standard" object with a known flux spectrum $F_s(\lambda)$, such as a spectroscopic standard star, should be observed through the same filter $t(\lambda)$ as the science targets. Rearranging Equation 6.27:

$$\beta = \frac{N_s}{\int F_{\lambda,s}(\lambda)e^{-\tau_s(\lambda)}t(\lambda)d\lambda} \tag{6.29}$$

where the subscript "s" refers to the flux standard.

6.6.1.2 Calibration of Continuum Sources

To calibrate the flux of a continuum source, we will make use of Equations 6.27 and 6.29, along with knowledge of the properties of a spectroscopic standard star. The count rate for a continuum source can be written as

$$N_C = \beta \int F_{\lambda,C}(\lambda)e^{-\tau_C(\lambda)}t(\lambda)d\lambda \tag{6.30}$$

where the subscript "C" refers to the continuum source. Using Equations 6.29 and 6.30 we can write

$$\frac{N_s}{\int F_{\lambda,s}(\lambda)e^{-\tau_s(\lambda)}t(\lambda)d\lambda} = \frac{N_C}{\int F_{\lambda,C}(\lambda)e^{-\tau_C(\lambda)}t(\lambda)d\lambda} \tag{6.31}$$

The quantities N_s, $\int F_{\lambda,s}(\lambda)e^{-\tau_s(\lambda)}t(\lambda)d\lambda$, and N_C are known. Moreover, because of the narrowness of our line filters, the optical depths $e^{-\tau_s(\lambda)}$ and $e^{-\tau_C(\lambda)}$ can be considered to be constant throughout the span of our filters, and will be referred to as $e^{-\tau_s}$ and $e^{-\tau_C}$ from now. Rearranging Equation 6.31 yields:

$$\int F_{\lambda,C}(\lambda)t(\lambda)d\lambda = \frac{N_C}{N_s}\frac{e^{-\tau_s}}{e^{-\tau_C}}\int F_{\lambda,s}(\lambda)t(\lambda)d\lambda \tag{6.32}$$

Considering the narrowness of our line filters, it is reasonable to assume that the continuum flux $F_{\lambda,C}(\lambda)$ admitted through the line filter is constant with wavelength, $F_{\lambda,C}(\lambda) = F_{\lambda,C}$. Rearranging Equation 6.32 yields

$$F_{\lambda,C} = \frac{N_C}{N_s}\frac{e^{-\tau_s}}{e^{-\tau_C}}\frac{\int F_{\lambda,s}(\lambda)t(\lambda)d\lambda}{\int t(\lambda)d\lambda} \tag{6.33}$$

A useful outcome of Equation 6.33 is that the absolute transmissions of the filters need not be known exactly. As long as the shape of the transmission curve is known, the transmission curve itself can have any scaling, and one will be able to obtain the calibrated flux. Assume that $t(\lambda)$ is the true transmission curve, and $A\,t(\lambda)$ is the normalized transmission curve, with A being some normalization constant. Substituting the normalized transmission curve into

Equation 6.33 yields:

$$F_{\lambda,C} = \frac{N_C}{N_s}\frac{e^{-\tau_s}}{e^{-\tau_C}}\frac{\int F_{\lambda,s}(\lambda) A\, t(\lambda) d\lambda}{\int A\, t(\lambda) d\lambda}$$
$$= \frac{N_C}{N_s}\frac{e^{-\tau_s}}{e^{-\tau_C}}\frac{A}{A}\frac{\int F_{\lambda,s}(\lambda) t(\lambda) d\lambda}{\int t(\lambda) d\lambda} = \frac{N_C}{N_s}\frac{e^{-\tau_s}}{e^{-\tau_C}}\frac{\int F_{\lambda,s}(\lambda) t(\lambda) d\lambda}{\int t(\lambda) d\lambda} \quad (6.34)$$

Rearranging Equation 6.33 yields

$$\frac{F_{\lambda,C}}{N_C} = \frac{e^{\tau_C}}{\beta \int t(\lambda)\, d\lambda} \quad (6.35)$$

Solving this equation for $F_{\lambda,C}$ yields the flux of the continuum source per unit wavelength. For an extended source of continuum, N_C and $F_{\lambda,C}$ would be quantified per unit solid angle.

In magnitude units, the surface brightness is given by

$$\mu_C = -2.5 \log(F_{\lambda,C}) - 21.1 - \zeta_\lambda \quad (6.36)$$

where μ_C is the surface brightness of a continuum source expressed as $\mathrm{mag/arcsec^2}$, $F_{\lambda,C}$ has units of $\mathrm{erg\,s^{-1}\,cm^{-2}\,\AA^{-1}\,arcsec^{-2}}$ and ζ_λ is a constant pertaining to our filter. For monochromatic fluxes, $\zeta_\lambda = 0$.

6.6.1.3 Calibration of Line Sources

We can calibrate the flux from a source of line emission in a similar way to calibrating the flux from a continuum source. For a line source observed through a line filter,

$$N_L = \beta \int F_L(\lambda) e^{-\tau_L(\lambda)} t(\lambda) d\lambda \quad (6.37)$$

where the subscript "L" refers to the line emission. As previously, β is defined by the observation of a standard source through the line filter, as given by Equation 6.29. Substituting into Equation 6.37, assuming as before that optical depths are constant over the passband,

$$\int F_L(\lambda)t(\lambda)d\lambda = \frac{N_L}{N_s}\frac{e^{-\tau_s(\lambda)}}{e^{-\tau_L(\lambda)}}\int F_{\lambda,s}(\lambda)t(\lambda)d\lambda \tag{6.38}$$

The line emission occupies a very narrow wavelength range, so the transmission of the filter can be approximated as $t(\lambda) = t_L$ and the line flux can be integrated over the passband. Rewriting Equation 6.38,

$$F_L = \frac{N_L}{N_s t_L}\frac{e^{-\tau_s}}{e^{-\tau_L}}\int F_s(\lambda)t(\lambda)d\lambda \tag{6.39}$$

Similarly to Equation 6.33, Equation 6.39 does not necessitate knowing the transmission curve exactly - only the shape of the transmission curve matters. The scaling of the transmission curve will cancel as follows:

$$\begin{aligned} F_L &= \frac{N_L}{N_s A\, t_L}\frac{e^{-\tau_s}}{e^{-\tau_L}}\int F_s(\lambda)A\,t(\lambda)d\lambda \\ &= \frac{N_L}{N_s t_L}\frac{A}{A}\frac{e^{-\tau_s}}{e^{-\tau_L}}\int F_s(\lambda)t(\lambda)d\lambda = \frac{N_L}{N_s t_L}\frac{e^{-\tau_s}}{e^{-\tau_L}}\int F_s(\lambda)t(\lambda)d\lambda \end{aligned} \tag{6.40}$$

where A is some scaling or normalization factor applied to the filter transmission curve. Equation 6.40 shows that one can calibrate the line flux admitted through the filter without having to know the exact values of the transmission curve.

Rearranging Equation 6.39 yields

$$\frac{F_L}{N_L} = \frac{e^{\tau_L}}{\beta t_L} \tag{6.41}$$

where F_L is the integrated flux of the emission line. The flux from an extended line source would be expressed as $\mathrm{erg\,cm^{-2}\,s^{-1}\,pixel^{-1}}$.

The surface brightness would be computed by dividing F_L by the number of square arcseconds in a pixel. To estimate a corresponding surface brightness, $F_{\lambda,C}$ at the effective wavelength of a broad-band filter, such as the Johnson-Cousins R filter, would be estimated by dividing F_L by the width of the broad-band filter.

6.6.2 Practice

In this section the theory developed in Section 6.6.1 will be applied to calibrate the fluxes obtained with QUAIL, by using the signal of the standard star HD 217086, its flux per unit wavelength obtained from publications, the transmission curves of our filters, and fluxes of HII regions of M33 obtained from QUAIL and published works.

6.6.2.1 The Standard Star: HD 217086

The signal obtained from the images of the standard star HD 217086 was used to calibrate our fluxes. The colour-inverted images of the standard star can be seen in Figure 6.19. The location of HD 217086 on these images is marked with a red star.

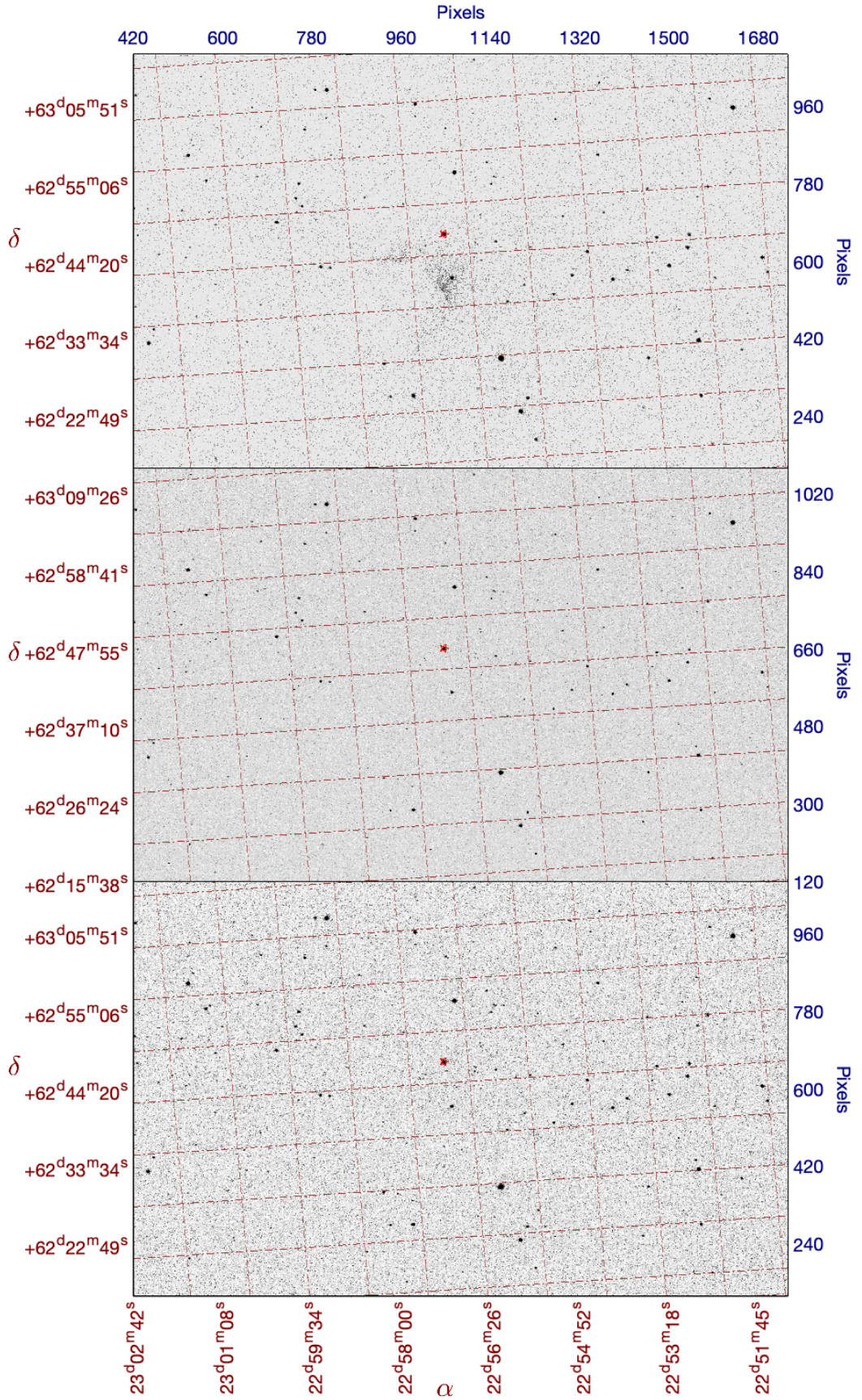

Figure 6.19: High-contrast colour-inverted image of HD 217086 in a): Hα; b): [OI]; c): Continuum.

Despite having been imaged for only 198 s in Hα we can see nebulosity (B[77] 44 Nebula) to the South - East of HD 217086 in the Hα image. The nebulosity is either too faint or not emitting in [OI] and Continuum.

6.6.2.2 Standard Star Counts

To calculate the calibration constant β, one needs to know the number of counts per second from the standard star N_s. For a reliable measurement, certain guidelines must be followed. First, it is advisable that the standard star be chosen such that it can be observed at a reasonable airmass, preferably as close as possible to the airmass of other targets. Second, the standard star must not be so bright as to saturate the CCD during short exposures, but also not so dim that it has to be observed for a prolonged period of time to obtain the number of counts that would be considered to represent a good signal-to-noise ratio. Third, the standard star must be observed on a photometric night to stabilize the interference of the atmosphere with the observed counts. Of course, the standard star should be observed well after dark. Also, sources of light pollution, such as LED strips in the dome, a nearby stadium, or building lights, should be mitigated where possible.

The standard star HD 217086 was observed under photometric conditions on November 11th, 2021. The resulting data were used to calibrate the fluxes of all other targets.

6.6.2.3 Integrated Values

To calculate the system constant β, the integral of the standard star's flux multiplied by the normalized transmission curve of the line filter $\int F_s(\lambda)t(\lambda)d\lambda$

must be known reliably. To achieve that, both the spectrum of the standard star and the filter's transmission curve need to have compatible resolutions. The resolution of neither curve should be so low as to require the other curve to be downsampled to absurdity. For the purposes of numerical integration, the resolution can be described as the precision with which some "digital function" $f(x_i)$ is defined. If the number of points is insufficient, then interpolating errors can degrade the accuracy of the integration. This is illustrated in Figure 6.20.

In Figure 6.20, the normalized filter transmission curve for our Hα filter as provided by the manufacturer is plotted in red, with black "diamonds" indicating the locations of the data points. The filter transmission curve is sampled every 1.0 Å . On the same plot, the spectrum of our standard star HD 217086 as provided by Carrasco et al. (2020) is plotted in blue, with datapoints indicated by stars ("*"). The resolution of this data is similar to that of our filter. The flux spectrum of HD 217086 as adapted from Massey et al. (1988) is plotted in yellow, with data points shown as black "diamonds". It is sampled every 6.85 Å.

To calibrate data acquired with the Hα filter, the spectrum of HD 217086 provided by Carrasco et al. (2020) was interpolated to match the resolution of the transmission curve of the Hα filter. The integral of the flux over the transmission curve was computed using the trapezoidal rule.

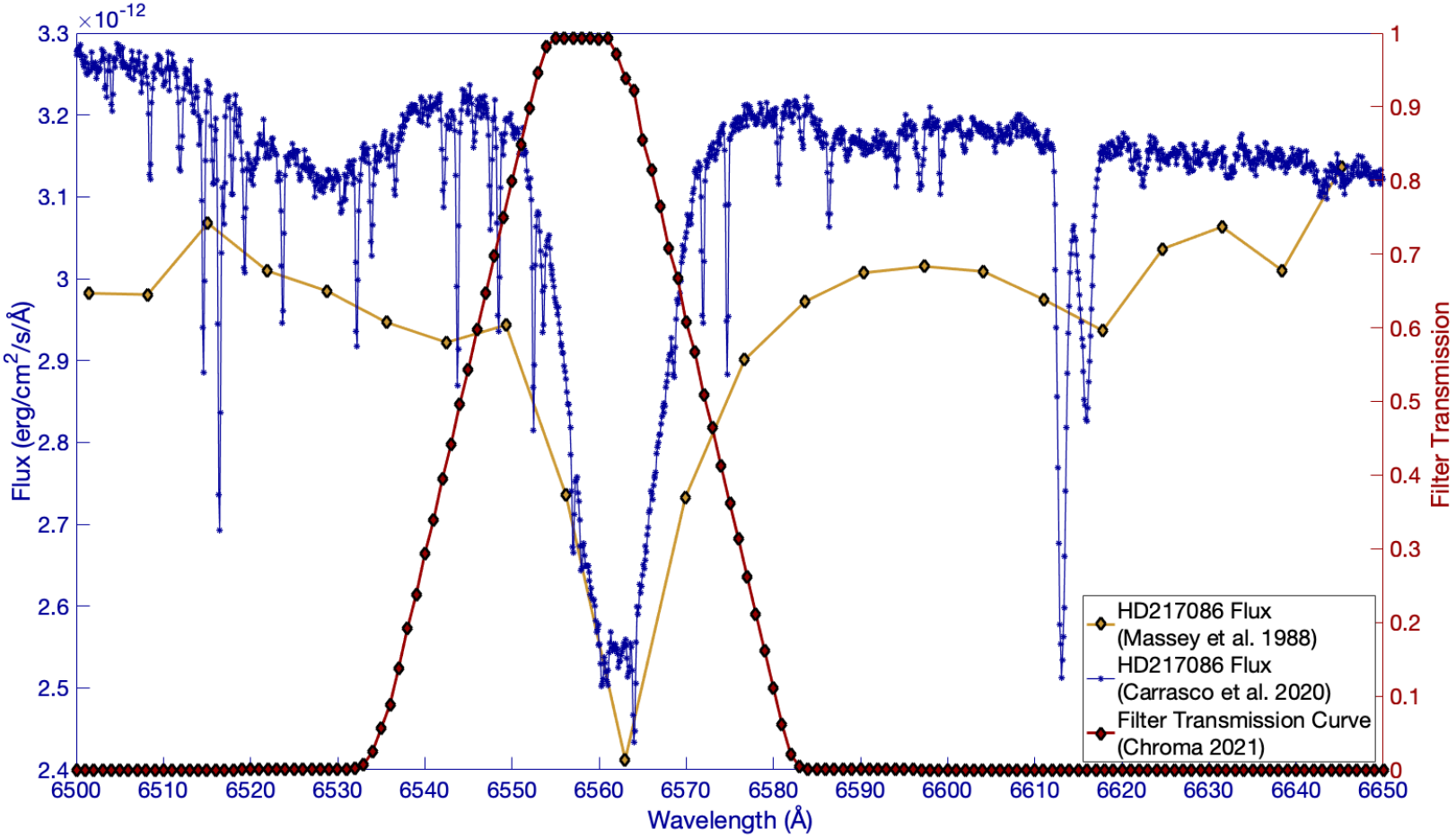

Figure 6.20: Plots of the normalized transmission curve versus wavelength of our Hα filter, and the flux of HD 217086 as provided by Carrasco et al. (2020) and Massey et al. (1988) at their original resolutions *.

The trapezoidal rule was chosen for integration because the shape of our transmission curve was simple and the transmission curve and the standard star's spectrum had good sampling - that is the transmission curve was defined with sufficiently high sampling which made it possible to interpolate it at the sampling rate of the standard's star flux.

6.6.2.4 System Constant β For The Hα Filter

We are now in a position to find the calibration constant β, which relates the count rate to flux. The count rate obtained for the standard star was measured using IRAF's `phot` routine. The count rate from the standard star HD 217086 is $N_s = 2200 \pm 30$ counts/s. Substituting N_s and the result of numerical integration into Equation 6.29 yields:

$$\beta = (31.49 \pm 0.44) \times 10^{12} \quad \text{counts}\,\text{cm}^2\,\text{erg}^{-1} \tag{6.42}$$

The flux for each target was calculated using the constant β, the optical depth (Table 6.6) and Equation 6.41, and is provided in Table 6.7.

The Flux-to-Count Ratios $\frac{F_L}{N_L}$ for Targets in Hα					
Target	λ	$\tau(\lambda) \pm \delta\tau(\lambda)$	$e^{-\tau}$	t_L	$\frac{F_L}{N_L}$
And XVIII	655.55	0.157 ± 0.068	0.855 ± 0.025	0.9571	3.15 ± 0.13
M33	656.28	0.184 ± 0.080	0.832 ± 0.029	0.9457	3.40 ± 0.16
M27 (Hα)	656.28	0.204 ± 0.088	0.816 ± 0.031	0.9456	3.47 ± 0.17
PacMan (Hα)	656.28	0.160 ± 0.070	0.852 ± 0.026	0.9456	3.32 ± 0.14

Table 6.7: Results and values used to obtain the flux per count/second in Hα ratio.

Chapter 7

Results

7.1 M33 - Triangulum Galaxy

The Triangulum Galaxy, also known as M33, was observed in Hα and Continuum filters. Despite being observed for only two hours and four minutes, the images produced a spectacular view. Images of M33 in Hα and Continuum can be seen in Figures 7.1 and 7.2 respectively.

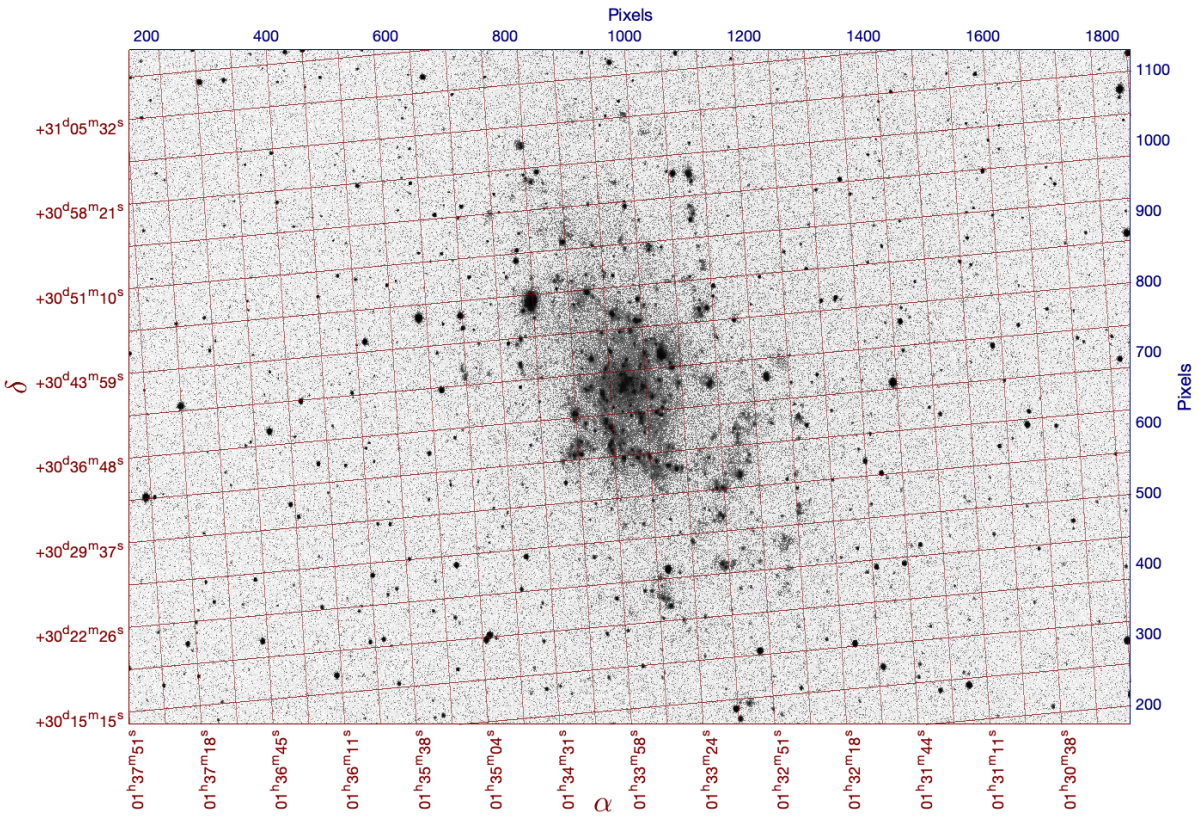

Figure 7.1: Colour-inverted image of M33 in the Hα filter.

The Hα image in Figure 7.1 shows that certain HII regions in M33 are visible and bright even with stars and continuum emission still present in the image. These regions include NGC 604, which is visible in the top-left corner of the galaxy, as well as NGC 588 and NGC 592, which are located to the right of

M33's core. These and other HII regions of M33 were subject to avid research and extensive observations in Hα, which makes them an ideal candidate for flux calibration of QUAIL. The details of the flux calibration can be found in Section 7.1.1.

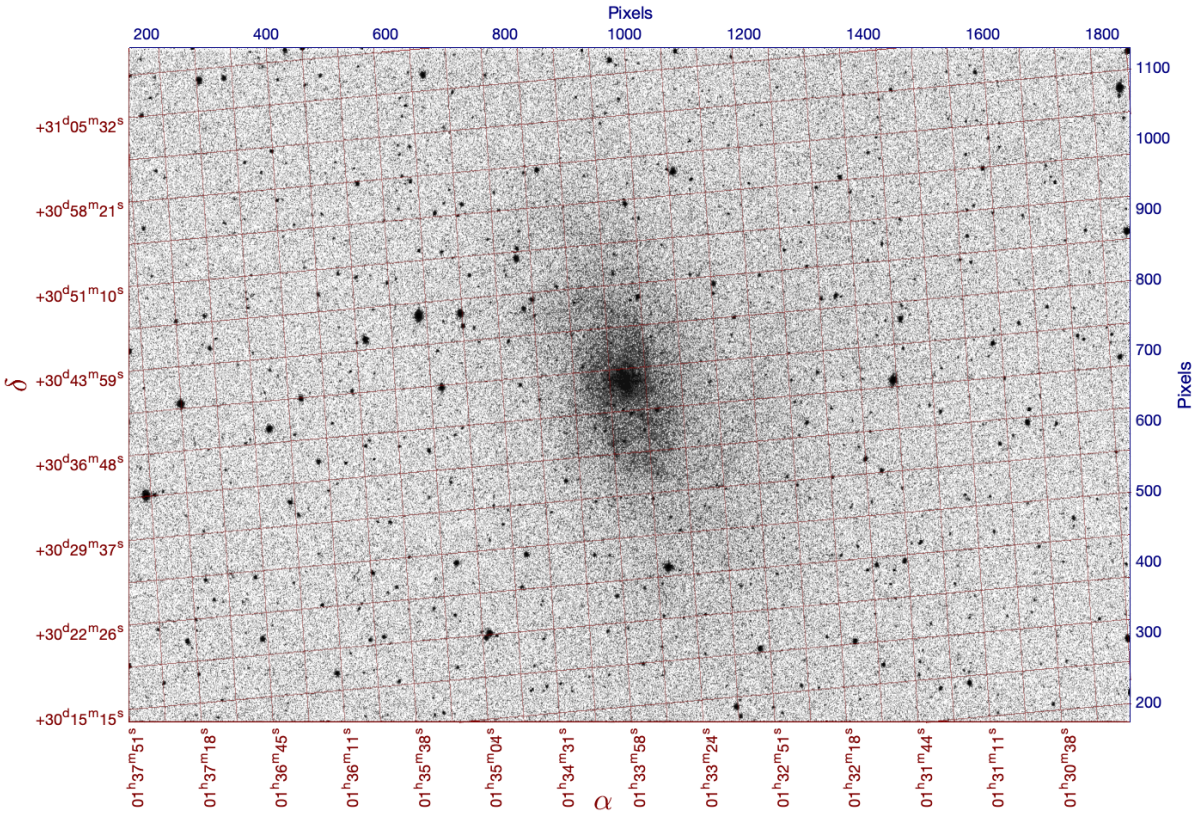

Figure 7.2: Colour-inverted image of M33 in the Continuum filter.

When the continuum is subtracted from the line image, as shown in Figure 7.3, one can clearly trace the Hα emission right into the core of M33. While the brighter HII regions were visible even on the starry and continuum-ridden image, the fainter HII regions in the core of M33 were severely obscured by the continuum emission. This shows that despite the narrowness of the Hα filter, a bright extended continuum source can severely degrade the visibility of faint nebular emission.

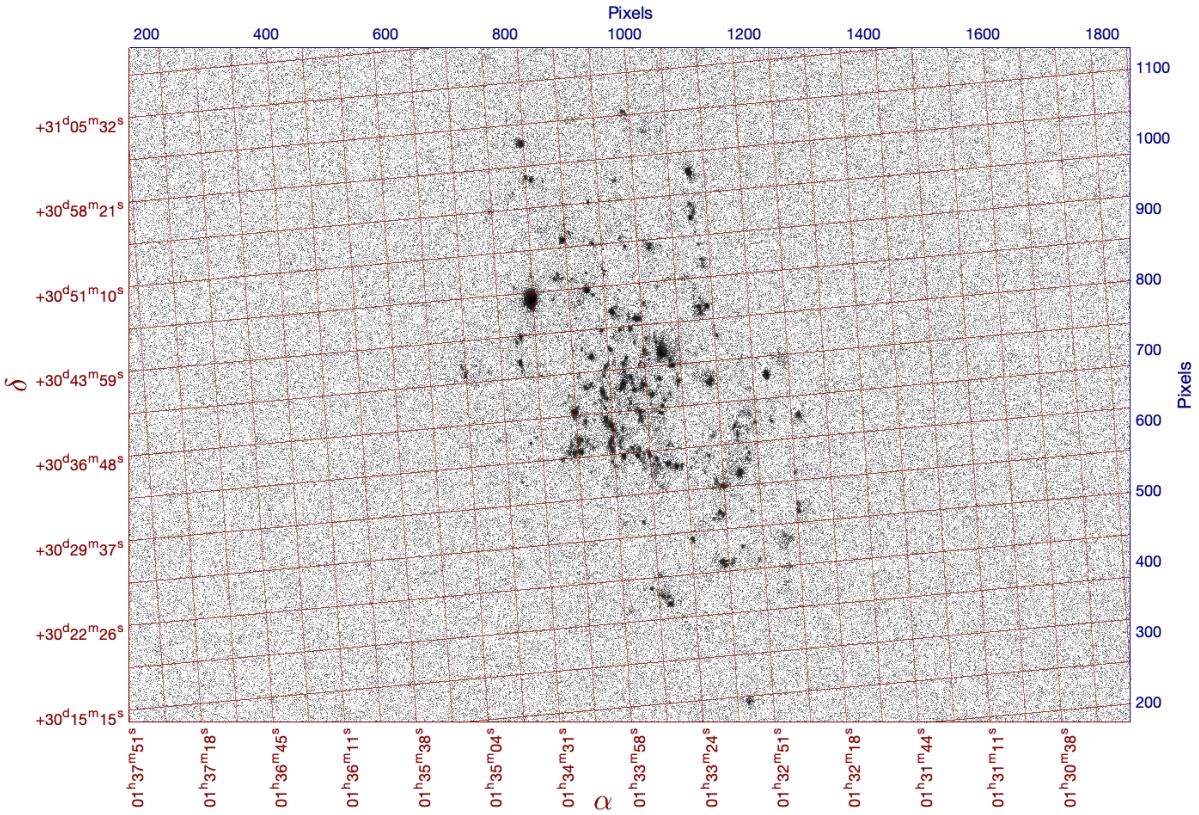

Figure 7.3: Colour-inverted starless and continuum-subtracted Image of M33 in Hα.

7.1.1 Calibration of Line Sources and Correction For The System Constant β

To convince ourselves of the reliability of the system constant β, we have measured the Hα fluxes of the HII regions in M33 (Triangulum Galaxy) for which there are published results. To measure the Hα flux from the HII regions detected by QUAIL, the HII regions listed in the works of Relaño & Kennicutt (2009), Lee & Lee (2014) and Hodge et al. (1999) needed to be located on our image of M33. To do so, transformation equations for mapping of the sky coordinates in α and δ were computed. This was done by matching the pixel positions of 120 stars on our M33 image to their sky coordinates obtained from Simbad. The pixel positions and sky coordinates of these stars were then used to compute the transformation equations using IRAF's `geomap` routine. The α and δ coordinates of the HII regions listed in Relaño & Kennicutt (2009), Lee

& Lee (2014) and Hodge et al. (1999) were transformed into pixel positions on the image. Some HII regions observed by Lee & Lee (2014) and Hodge et al. (1999) were not detected by QUAIL and were not used in the analysis. If an HII region was located too close to another nebulosity it was also excluded from this analysis. The patches of nebulosity that seemed to be blended together, or had a highly irregular shape were excluded from the analysis as well. The adopted nebulous regions plotted on top of a starless, continuum and background-subtracted image of M33 can be seen in Figure 7.4.

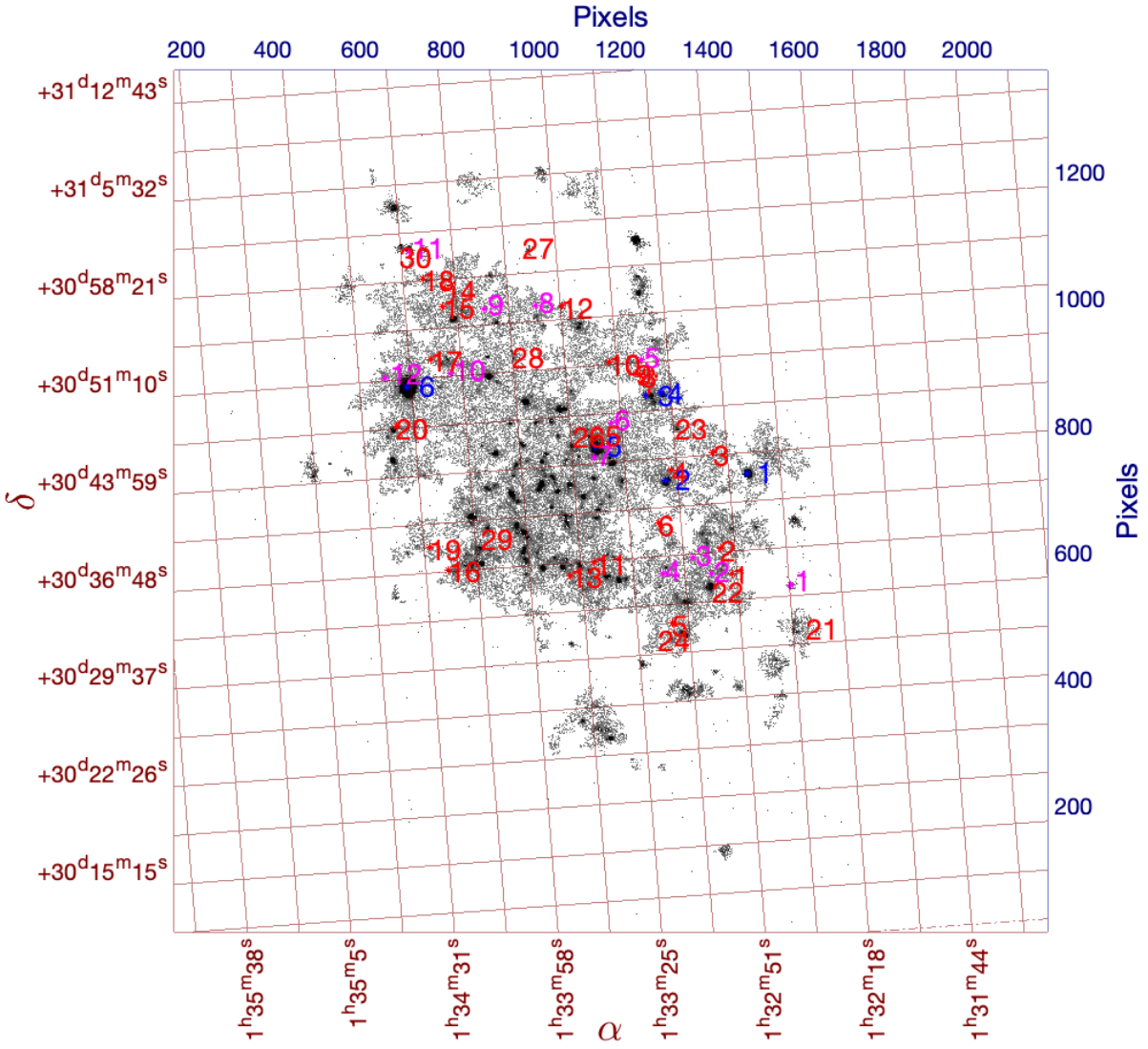

Figure 7.4: Colour-inverted, starless, continuum-subtracted and background-subtracted image of M33 in the Hα. The field of view was cropped to accentuate the features of M33. The HII regions listed in Relaño & Kennicutt (2009), Lee & Lee (2014) and Hodge et al. (1999) that were identified in our image are marked with blue, red and pink stars and numbers respectively.

The number of counts per second N_L from the adopted HII regions were obtained by summing over the image area equivalent to that in the published works. The Hα flux detected by QUAIL F_L was calculated using N_L and the pertinent ratio of flux to counts per second $\frac{F_L}{N_L}$, which can be found in Table 6.7. The aperture photometry provided by Hodge et al. (1999), Lee & Lee (2014) and Relaño & Kennicutt (2009) are compared with QUAIL's fluxes in Tables 7.1, 7.2 and 7.3 respectively.

In these tables, the publication to used to calibrate the Hα is listed in the header of the table. Column 1 lists the numbers corresponding to the identified HII regions as plotted in Figure 7.4. Column 2 lists the names of the HII regions in M33, if applicable. Columns 3 and 4 list coordinates α and δ (J2000) of the HII regions. Columns 5 and 6 list the fluxes obtained with QUAIL F_Q, and the fluxes obtained from the publication F_P, both in $\mathrm{erg/cm^2/s}(\times 10^{-14})$. Columns 7 and 8 list the logarithm of fluxes obtained with QUAIL $\log(F_Q)$, and publications $\log(F_P)$ respectively. Column 9 provides the flux ratio $F_R = F_Q/F_P$. Column 10 lists the logarithmic difference of fluxes measured from our images and fluxes provided in the publication $\log(F_R) = \log(F_Q) - \log(F_P)$ in $\mathrm{dex}(\times 10^{-2})$.

Relaño & Kennicutt (2009)									
1	2	3	4	5	6	7	8	9	10
Number	Name	α	δ	F_Q $(\times 10^2)$	F_P $(\times 10^2)$	$\log(F_Q)$	$\log(F_P)$	F_R	$\log(F_R)$
1	NGC 588	01:32:45	+30:38:56	5.76	5.93	-11.23	-11.22	0.97	-1.26
2	NGC 592	01:33:12	+30:38:48	4.02	3.04	-11.39	-11.51	1.32	12.2
3	IC131	01:33:16	+30:45:10	3.14	3.33	-11.50	-11.47	0.94	-2.55
4	IC131-West	01:33:11	+30:45:15	2.75	2.59	-11.56	-11.58	1.06	2.60
5	NGC 595	01:33:33	+30:40:40	17.1	14.9	-10.76	-10.82	1.15	6.07
6	NGC 604	01:34:33	+30:47:05	53.8	36.6	-10.26	-10.43	1.47	16.8

Table 7.1: Comparison of Hα fluxes of HII Regions of M33 obtained with QUAIL to those published by Relaño & Kennicutt (2009)

Lee & Lee (2014)									
1	2	3	4	5	6	7	8	9	10
Number	Name	α	δ	F_Q	F_P	$\log(F_Q)$	$\log(F_P)$	F_R	$\log(F_R)$
1	L10-6	01:32:40	+30:16:31	3.01	3.06	-13.52	-13.51	0.98	-0.61
2	L10-9	01:32:42	+30:36:20	5.04	2.60	-13.29	-13.58	1.93	28.7
3		01:32:44	+30:22:14	10.1	8.05	-12.99	-13.09	1.25	9.79
4		01:32:46	+30:34:38	12.0	12.2	-12.92	-12.91	0.98	-0.61
5	L10-25	01:32:52	+30:38:12	3.36	2.79	-13.47	-13.55	1.20	8.13
6		01:32:53	+30:37:57	0.14	1.16	-14.82	-13.93	0.12	-89.1
7		01:32:53	+30:48:24	5.23	5.56	-13.28	-13.25	0.94	-2.69
8	L10-27	01:32:54	+30:25:31	1.97	3.20	-13.70	-13.49	0.61	-20.9
9		01:32:56	+30:33:30	1.58	2.16	-13.80	-13.66	0.73	-13.6
10		01:33:01	+30:30:49	3.27	2.92	-13.48	-13.53	1.12	4.94
11	L10-45	01:33:08	+30:26:58	3.51	5.56	-13.45	-13.25	0.63	-20.0
12	L10-49	01:33:10	+30:42:22	4.45	1.60	-13.35	-13.79	2.77	44.3
13	L10-57	01:33:11	+30:34:21	11.6	9.90	-12.93	-13.00	1.17	6.96
14	L10-111	01:33:23	+30:26:13	1.28	1.56	-13.88	-13.80	0.82	-8.56
15	L10-113	01:33:24	+30:36:56	2.60	1.60	-13.58	-13.79	1.62	21.0
16	L10-116	01:33:24	+30:28:50	1.71	2.72	-13.76	-13.56	0.63	-20.0
17		01:33:27	+30:47:48	3.68	4.74	-13.43	-13.32	0.77	-10.9
18		01:33:27	+30:23:59	2.71	5.56	-13.56	-13.25	0.48	-31.2
19	L10-120	01:33:27	+30:18:17	1.99	1.46	-13.69	-13.83	1.36	13.5
20	L10-126	01:33:28	+30:16:01	5.28	4.32	-13.27	-13.36	1.22	8.76
21		01:32:30	+30:27:27	22.5	13.7	-12.64	-12.86	1.65	21.7
22		01:33:00	+30:30:30	27.7	40.3	-12.55	-12.39	0.68	-16.3
23		01:33:07	+30:42:42	11.7	5.96	-12.93	-13.22	1.95	29.2
24		01:33:18	+30:27:27	8.05	16.4	-13.09	-12.78	0.48	-31.0
25		01:33:29	+30:47:47	8.57	24.9	-13.06	-12.60	0.34	-46.3
26		01:33:35	+30:42:42	26.0	15.0	-12.58	-12.82	1.73	23.9
27		01:33:40	+30:42:42	10.7	11.1	-12.97	-12.95	0.96	-1.67
28		01:33:52	+30:56:56	7.77	18.0	-13.10	-12.74	0.43	-36.5
29		01:33:58	+30:48:48	1.63	5.31	-13.78	-13.27	0.30	-51.3
30		01:34:12	+30:35:35	11.3	11.4	-12.94	-12.94	0.99	-0.24

Table 7.2: Comparison of Hα fluxes of HII Regions of M33 obtained with QUAIL to those published by Lee & Lee (2014)

Hodge et al. (1999)									
1	2	3	4	5	6	7	8	9	10
Number	Name	α	δ	F_Q	F_P	$\log(F_Q)$	$\log(F_P)$	F_R	$\log(F_R)$
1	HBD 02	01:32:29	+30:30:51	32.4	37.0	-12.48	-12.43	0.87	-5.75
2	HBD 04	01:32:30	+30:26:58	5.80	4.39	-13.23	-13.35	1.31	12.0
3	HBD 05	01:32:30	+30:24:55	3.45	3.60	-13.46	-13.44	0.96	-1.76
4	HBD 06	01:32:31	+30:29:32	3.43	3.09	-13.46	-13.50	1.10	4.39
5	HBD 07	01:32:31	+30:35:54	3.59	2.50	-13.44	-13.60	1.43	15.8
6	HBD 08	01:32:31	+30:27:17	5.97	2.90	-13.22	-13.53	2.06	31.4
7	HBD 09	01:32:31	+30:37:16	11.3	7.00	-12.94	-13.15	1.61	20.7
8	HBD 11	01:32:31	+30:36:17	3.92	3.90	-13.40	-13.40	1.00	0.23
9	HBD 12	01:32:31	+30:26:50	6.82	3.80	-13.16	-13.42	1.79	25.4
10	HBD 15	01:32:32	+30:28:10	3.59	2.30	-13.44	-13.63	1.56	19.4
11	HBD 16	01:32:32	+30:23:33	46.7	6.40	-12.33	-13.19	7.29	86.3
12	HBD 18	01:32:32	+30:27:06	19.4	11.0	-12.71	-12.95	1.76	24.6

Table 7.3: Comparison of Hα fluxes of HII Regions of M33 obtained with QUAIL to those published by Hodge et al. (1999)

It was found that the fluxes measured from QUAIL are systemtically higher than those provided in the publications. On average, the ratio of fluxes $\langle F_R \rangle = \frac{F_Q}{F_P} = 1.26 \pm 1.03$. It is imperative to check the relationship between the published and detected fluxes. If the relationship is linear, with a slope of unity, the ratio of fluxes $\langle F_R \rangle$ calculated above can be used as a correction factor by which QUAIL's fluxes are scaled.

Plotting the logarithms of fluxes obtained with QUAIL against the logarithms of the fluxes retrieved from publications showed that the relationship is linear. The plot of the relationship can be seen in Figure 7.5. Fitting a function to the relationship yields

$$\log(F_Q) = (1.00 \pm 0.05)\log(F_P) + (0.07 \pm 0.65) \tag{7.1}$$

The slope of the fitted equation is unity, which means that the aforementioned

correction can be applied trivially - the Hα fluxes measured by QUAIL can be converted to the "standard" scale defined by the publications by calculating the mean ratio of QUAIL fluxes to published fluxes for HII regions in M33.

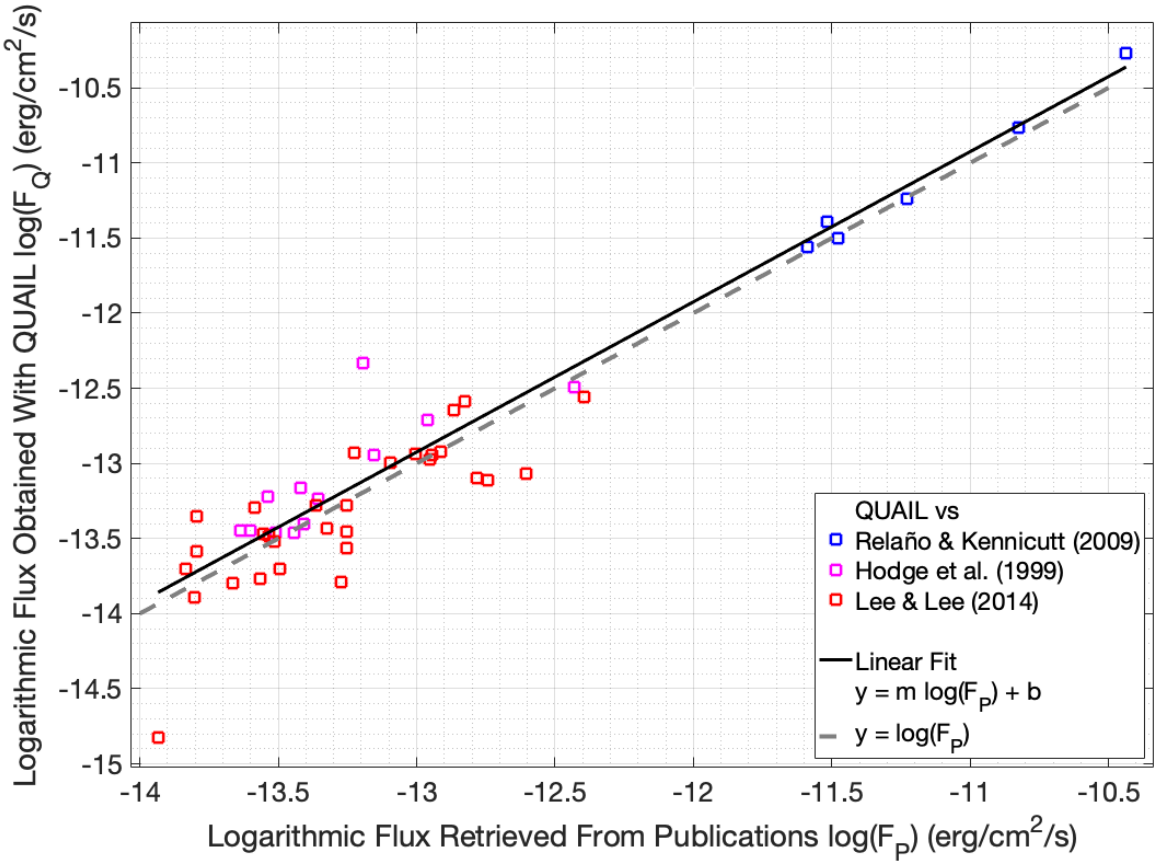

Figure 7.5: The logarithmic Hα fluxes measured from images taken with QUAIL are plotted against those isted in Relaño & Kennicutt (2009), Lee & Lee (2014) and Hodge et al. (1999). The values m and b in the legend pertain to the slope and the y-intercept of the fitted function written in Equation 7.1

The average logarithmic difference in fluxes can be found in two ways. One way is to simply subtract the logarithms of QUAIL's fluxes from published fluxes, which yields $\langle \log(F_{R_1}) \rangle = \langle \log(F_P) - \log(F_Q) \rangle = 0.0179 \pm 0.272$ dex. Another value was found by subtracting the function with the slope of 1, plotted in gray in Figure 7.1 from the fitted function in Equation 7.1 which yielded $\langle \log(F_{R_2}) \rangle = \langle \log(F_R) \rangle = (0.07 \pm 0.65)$ dex, which is the y-intercept of Equation 7.1.

Both values are consistent with the ratio of fluxes computed earlier, as $10^{\langle \log(F_{R_1}) \rangle} = 1.04 \pm 0.65$, and $10^{\langle \log(F_{R_2}) \rangle} = 1.19 \pm 1.78$.

The fluxes obtained from our targets will be corrected by dividing by the value of F_R to ameliorate the discrepancy between the measured and published Hα fluxes.

7.1.2 Visual Comparison of QUAIL's Images of M33 to Published Data

The purpose of QUAIL is to observe extended ultra-low surface brightness objects, such as HII regions in M33. To test how QUAIL fares compared to other optical systems it is necessary to compare an image with one acquired at a different facility. To do so, the starless, continuum-subtracted and background subtracted image of M33 in Hα taken with QUAIL was compared to the image of M33 taken with the Burrell Schmidt telescope at Kitt Peak National Observatory by Hoopes & Walterbos (2000).

To properly evaluate the data from the two instruments, it is imperative to evaluate the theoretical performance of each instrument. This can be done by employing Equation 1.25 and modifying it to take into account the exposure time:

$$\Phi = a \left(\frac{D}{L} \right)^2 (N \times T) \frac{e^{-\tau(\lambda) \sec(Z)}}{hc} \int E(\lambda) S_\lambda(\lambda) d\lambda \tag{7.2}$$

where N is the number of exposures, T is the duration of one exposure, a is the area of the pixel in m^2, D is the aperture diameter of the optical system in m, L is the focal length of the optical system in m, λ is the wavelength at which the observations are conducted in m, Z is the zenith angle in degrees,

$X = \sec(Z)$ is the airmass of the object, $S_\lambda(\lambda)$ is the intrinsic surface brightness of the object at wavelength of observation λ in $\mathrm{erg\,s^{-1}cm^{-2}nm^{-1}}$, and $E(\lambda)$ is the efficiency of the system. (Abraham & van Dokkum, 2014). The optical depth $\tau(\lambda)$ is defined as

$$k(\lambda) = -2.5\log(e)(-\tau(\lambda)) \tag{7.3}$$

where $k(\lambda)$ is the extinction coefficient of the atmosphere in $\mathrm{mag/X}$. Because the filters employed during observations are very narrow, and Equation 7.2 integrates over the filter width, the extinction term has been brought outside of the integral.

Hoopes & Walterbos (2000) used the $60\,\mathrm{cm}$ Burrell-Schmidt telescope at Kitt Peak National Observatory equipped with an Hα filter the width of $3.0\,\mathrm{nm}$ at half maximum transmission centered on $657.0\,\mathrm{nm}$. The system had a focal ratio of $f/3.5$, with a field of view of $1.15^o \times 1.15^o$. The image displayed in Figure 7.6 is a result of 20 exposures, each $900\,\mathrm{s}$ long. The image obtained from Hoopes & Walterbos (2000) had a scale of $2.028''/\mathrm{pixel}$. The details of the apparatus employed by Hoopes & Walterbos (2000) and QUAIL, as well as the total exposure times spent observing M33, can be found in Table 7.4.

The fact that the telescope used by Hoopes & Walterbos (2000) and the telescope that hosts QUAIL are both $60\,\mathrm{cm}$ in diameter gives rise to the question of why we did not image M33 through the $60\,\mathrm{cm}$ telescope at York University. The answer lies in the fact that the $60\,\mathrm{cm}$ telescope at York University has a far smaller field of view and a larger f-number than QUAIL, so it cannot be used to make a direct comparison of their respective performances. Moreover,

the $60\,\mathrm{cm}$ telescope at York University is not equipped with an Hα filter, which makes obtaining the necessary images of M33 in Hα impossible.

Parameters of the Burrell-Schmidt Telescope and QUAIL		
Instrument Parameter	QUAIL	Hoopes & Walterbos (2000)
Aperture Diameter D (cm)	14.3	61
$f/\# = \frac{L}{D}$	2.8	3.6
Focal Length L (cm)	40.04	219.6
Pixel Size a (μm)	6.8	21
CCD Quantum Efficiency	0.8	0.95
Readout Noise (e^-)	10	3
Gain (e^-/count)	0.42	1.5
FOV (N^o $\times$ M^o)	2.13×1.42	1.15×1.15
Filter FWHM (nm)	2.8	3
Filter Central Lambda (nm)	655.9	657.0
Latitude (^{o})	43.77	31.96
Longitude (^{o})	79.5019	111.5981
M33 Image LMST (hh:mm:ss)	04:06:00	22:10:44
M33 Altitude (^{o})	57.3511	47.0041
M33 Airmass sec(Z)	1.1877	1.3672
Extinction Coefficient $k(\lambda)$ (mag/X)	0.1675	0.0951
Exposure Duration T (s)	240	900
Number of Exposures N	29	20

Table 7.4: Parameters of QUAIL and the instrument used by Hoopes & Walterbos (2000).

Substituting the values for QUAIL and Hoopes & Walterbos (2000) into Equation 7.2 and taking the ratio yields:

$$\Phi_R = \frac{\Phi_S}{\Phi_Q} = 15.95 \frac{\int E_S(\lambda) S_\lambda(\lambda) d\lambda}{\int E_Q(\lambda) S_\lambda(\lambda) d\lambda} \tag{7.4}$$

where Φ_S and Φ_Q are the average photons per pixel collected by Hoopes & Walterbos (2000) and QUAIL respectively. Here the subscript S stands for "Schmidt" (telescope), the subscript Q stands for "QUAIL". This result means that the instrument used by Hoopes & Walterbos (2000) is ~ 16 times more

sensitive than QUAIL assuming that the optical efficiencies E_Q and E_S are the same.

To compare the performances of the instruments, the average number of photons detected per pixel in extended sources was obtained by measuring four HII regions visible on images taken with both instruments. The four regions in question are marked with red circles on M33 images taken with QUAIL (left) and Hoopes & Walterbos (2000) (right) in Figure 7.6.

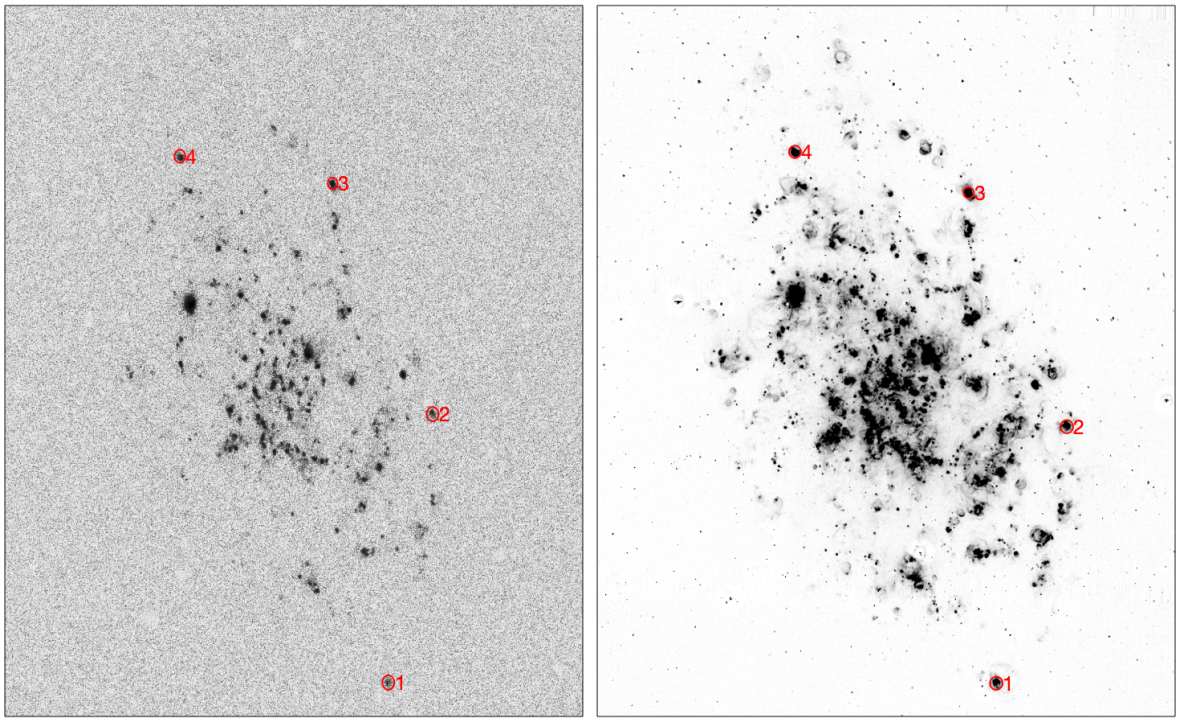

Figure 7.6: Comparison of Hα images of M33 taken by QUAIL to Hoopes & Walterbos (2000). The image of M33 taken by Hoopes & Walterbos (2000) is shown on the right.

Close-up images of the four HII regions can be seen in Figure 7.7 with images taken with QUAIL shown on the left and images taken by Hoopes & Walterbos (2000) on the right. The radii of the measurement regions in pixels were chosen such that the average signal per pixel would be computed over the same area in arcseconds.

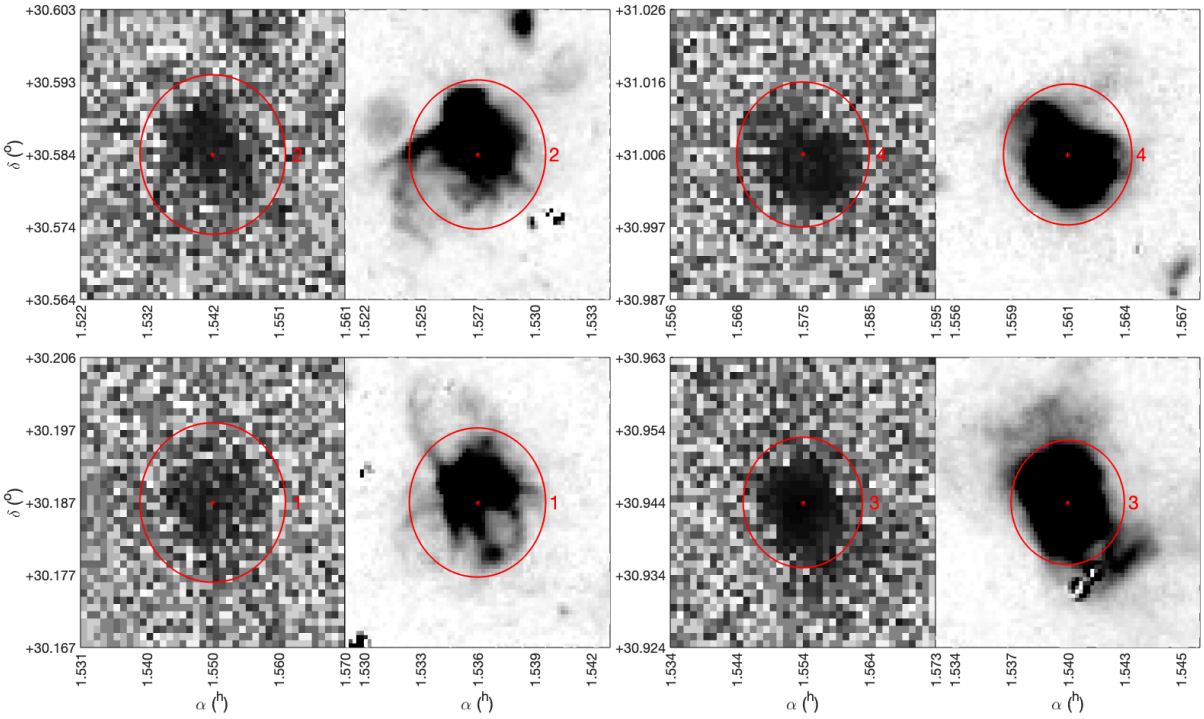

Figure 7.7: HII regions used to compare the performance of QUAIL to the instrument used by Hoopes & Walterbos (2000). The regions are over which the average photons per pixel were measured are enclosed by red circles. The numbers next to the red circles match those in Figure 7.7. QUAIL's images of the measurement regions are plotted on the left, Hoopes & Walterbos (2000) are plotted to the right of QUAIL's images.

The ratio of average photons per pixel measured from the HII regions is $\frac{F_S}{F_Q} = 14.08 \pm 3.21$, which is consistent with the theoretical prediction. The standard deviation of the sky in the Schmidt image is $\sigma_{S,m} = 5.95$ photons/pix, and the standard deviation of the sky in QUAIL's image is $\sigma_{Q,m} = 12.69$ photons/pix, with their ratio being $\frac{\sigma_{S,m}}{\sigma_{Q,m}} = 0.47$. This means that the image taken with QUAIL is almost twice as noisy as the image taken by Hoopes & Walterbos (2000). The ratio of the standard deviations is in a disagreement with the theory, because Poisson statistics predict that the standard deviation of the sky in the Schmidt image should be $\frac{\sigma_S}{\sigma_Q} = \sqrt{\Phi_R}$, which is 8.5 times larger than the measured ratio. This indicates that the sky at York University was ~ 70 times brighter than at Kitt Peak, which corresponds to a difference of 4.6 mag/arcsec^2. To match the

standard deviations of QUAIL and Hoopes & Walterbos (2000), an additional 217 exposures of 240 s must be taken with QUAIL.

7.2 NGC 281 - PacMan Nebula

To clarify a qualitative discussion of shapes and positions of emissions in the PacMan Nebula, it is helpful to anthropomorphize the morphology of the PacMan nebula's emissions in Hα. The PacMan nebula got its name from its resemblance to a popular video game character, but its Hα emission more closely resembles a flaming skull. Our picture of Hα emissions and a picture of a flaming skull taken from the Path of Exile Wiki (Summon Raging Spirit, 2023) can be seen in Figure 7.8. In what will follow, the discussion will often refer to the "chin" of the PacMan nebula as marked in Figure 7.8.

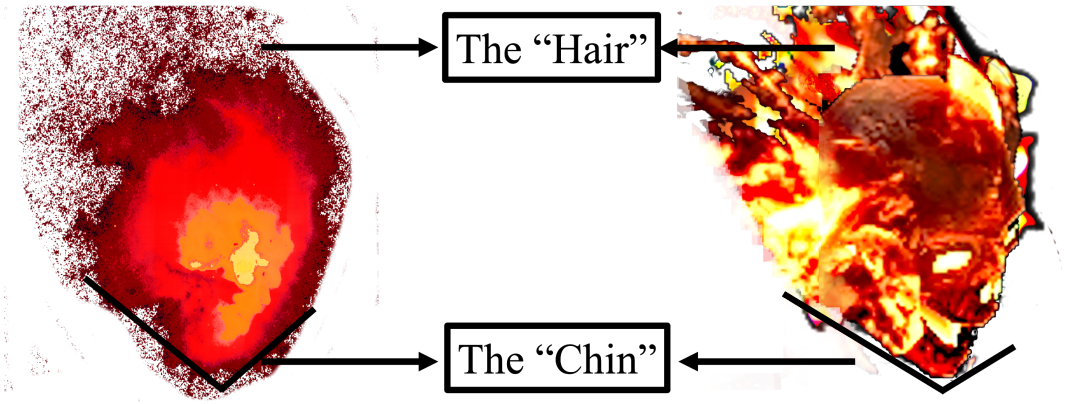

Figure 7.8: Colourmap of PacMan nebula's Hα emissions (left), and a picture of a flaming skull (right) for comparison.

Imaging the PacMan Nebula yielded a spectacular result that can be seen in Figure 7.9. In Figure 7.9, it is difficult to fully appreciate emission in [OI] and Continuum due to the density of stars in the field of view. Figure 7.11 shows the PacMan Nebula with stars removed.

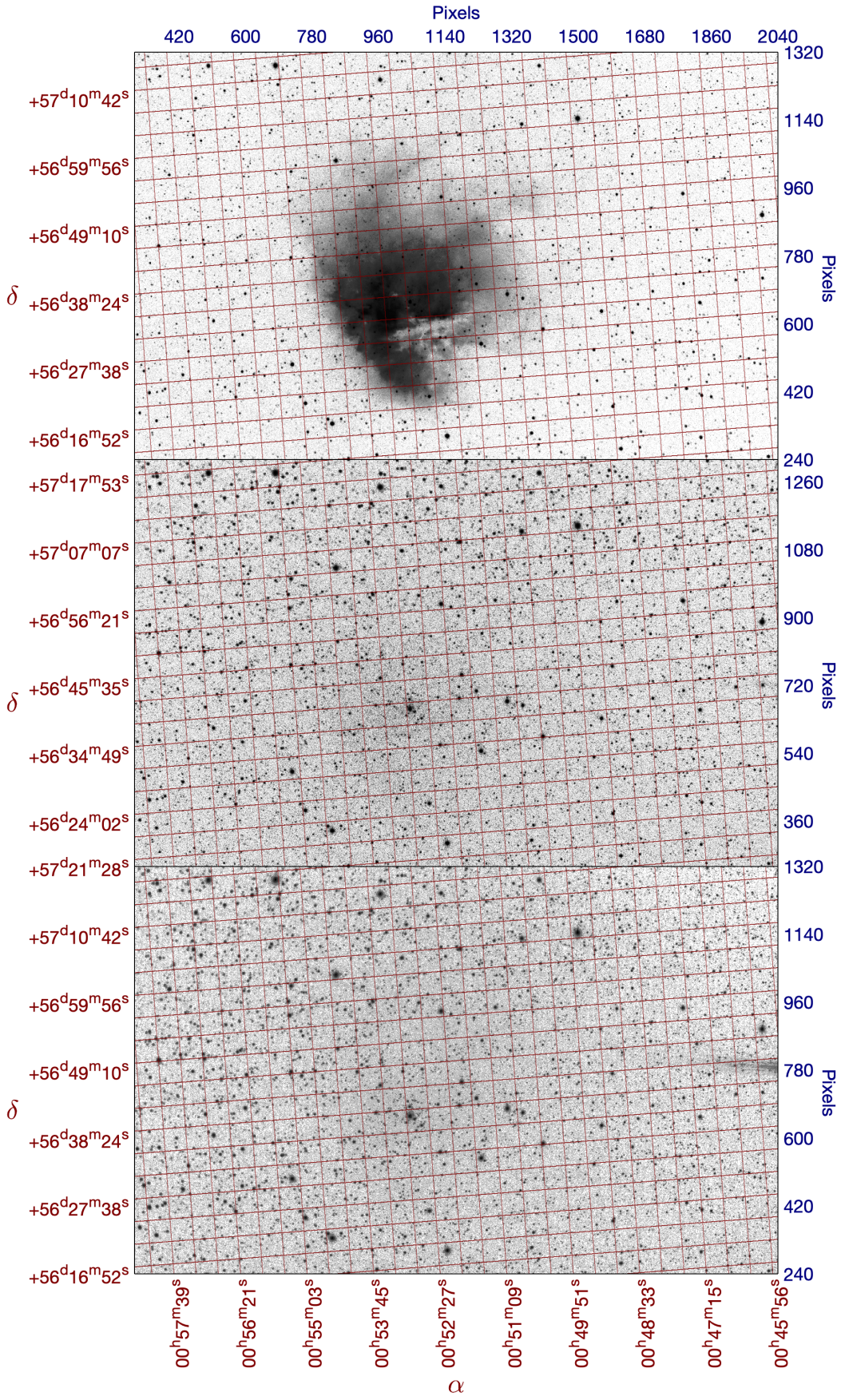

Figure 7.9: Colour-inverted images of the PacMan Nebula. Top image is in Hα. Middle image is in [OI]. Bottom image is in Continuum.

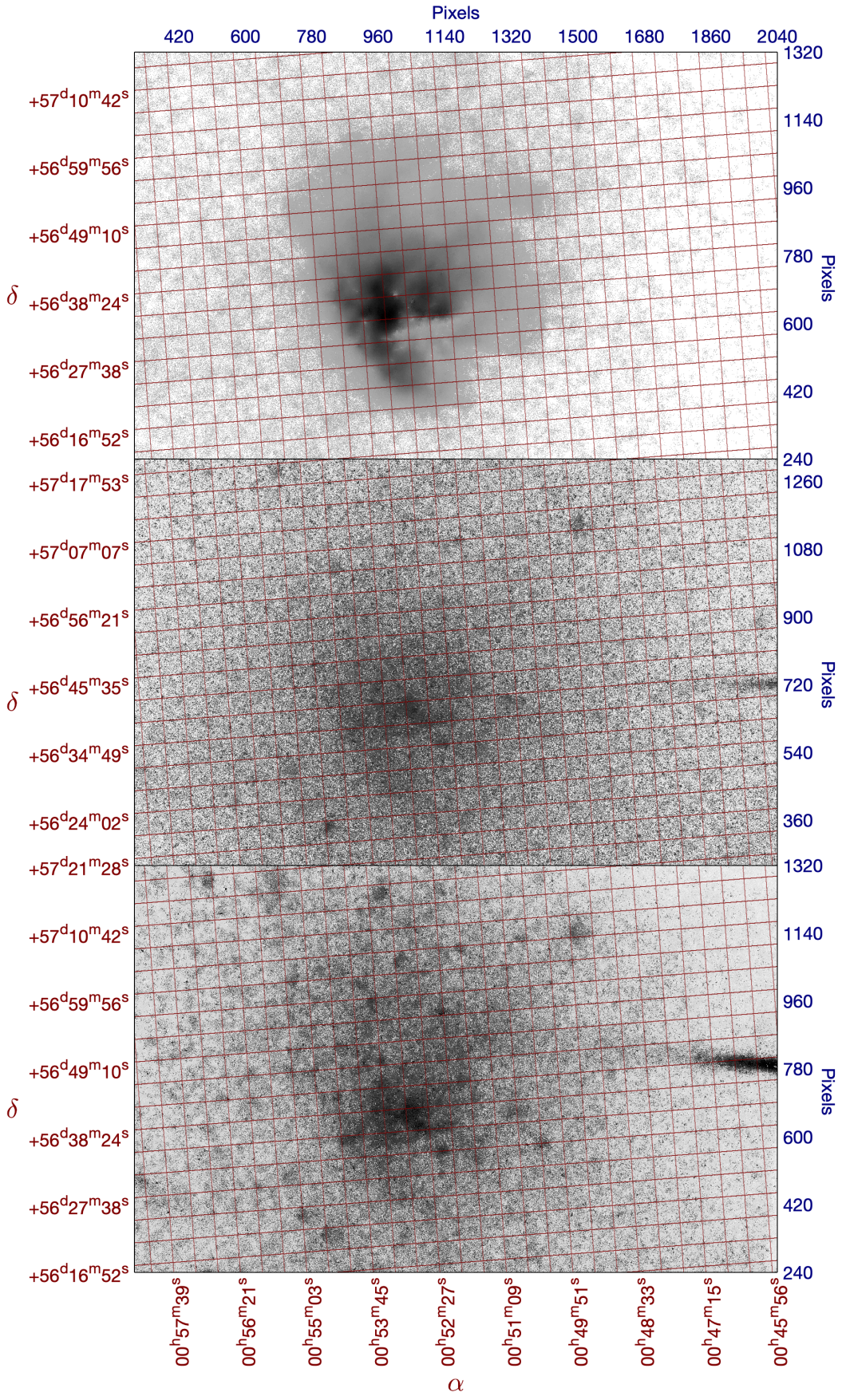

Figure 7.10: Colour-inverted starless images of the PacMan Nebula. Top image is in Hα. Middle image is in [OI]. Bottom image is in Continuum.

Upon removing stars, a faint nebular glow seems to emerge around the area of the "chin" of the nebula in [OI]. Subtracting the continuum from the line images and binning 3×3 yielded a bright emission in Hα and some dim and diffuse emission in [OI] which can be seen in Figure 7.11.

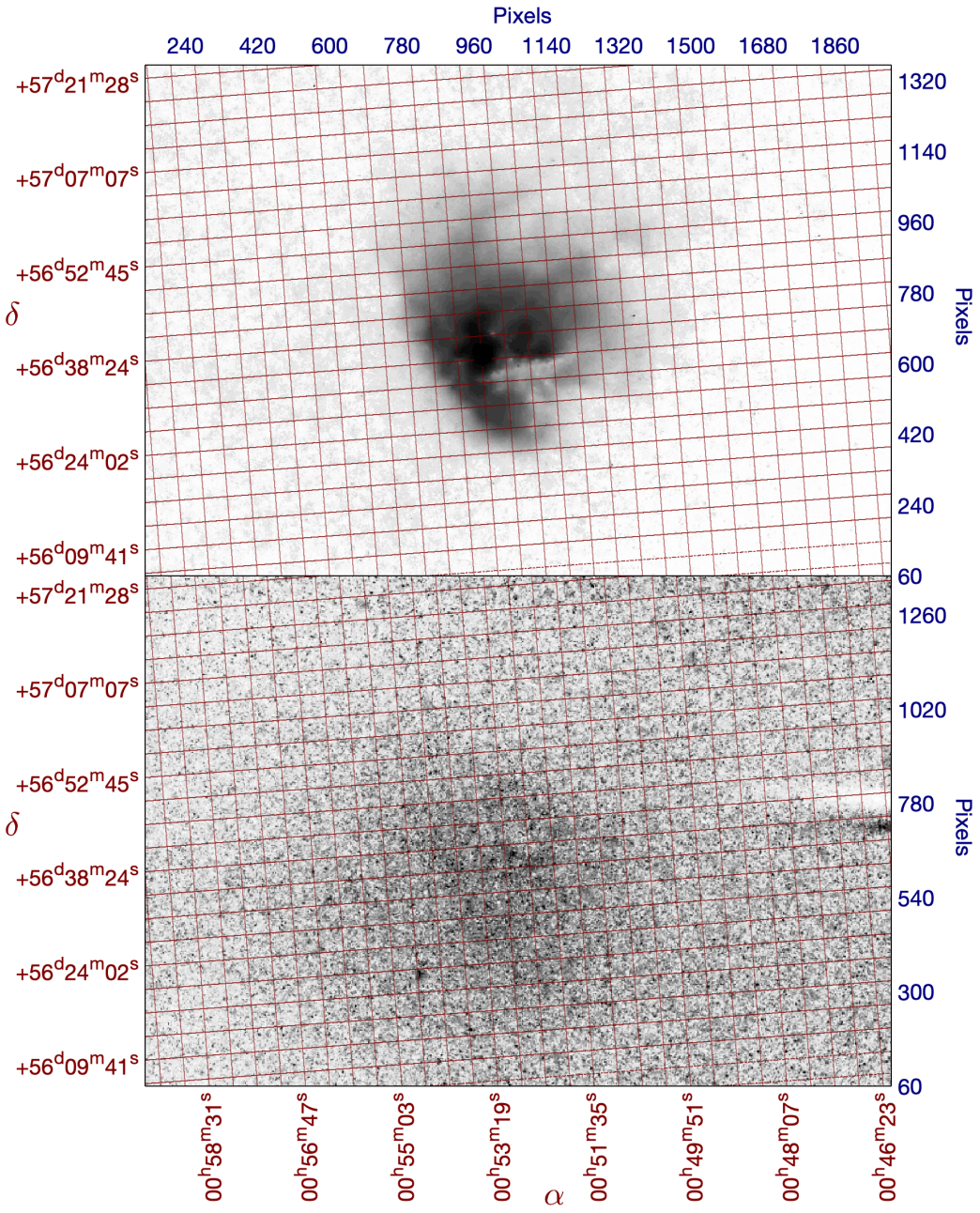

Figure 7.11: Colour-inverted starless, continuum subtracted, images of the Pac-Man Nebula. Top image is in Hα. Bottom image is in [OI]. Both images are binned 3×3.

Colourmaps of the binned images can be seen in Figure 7.12. It should be

noted that the peak count rate for the emission in [OI] is 40 times fainter than that in Hα. The nebular glow in [OI] seems to mimic the shape of the PacMan's "skull", as seen in Hα.

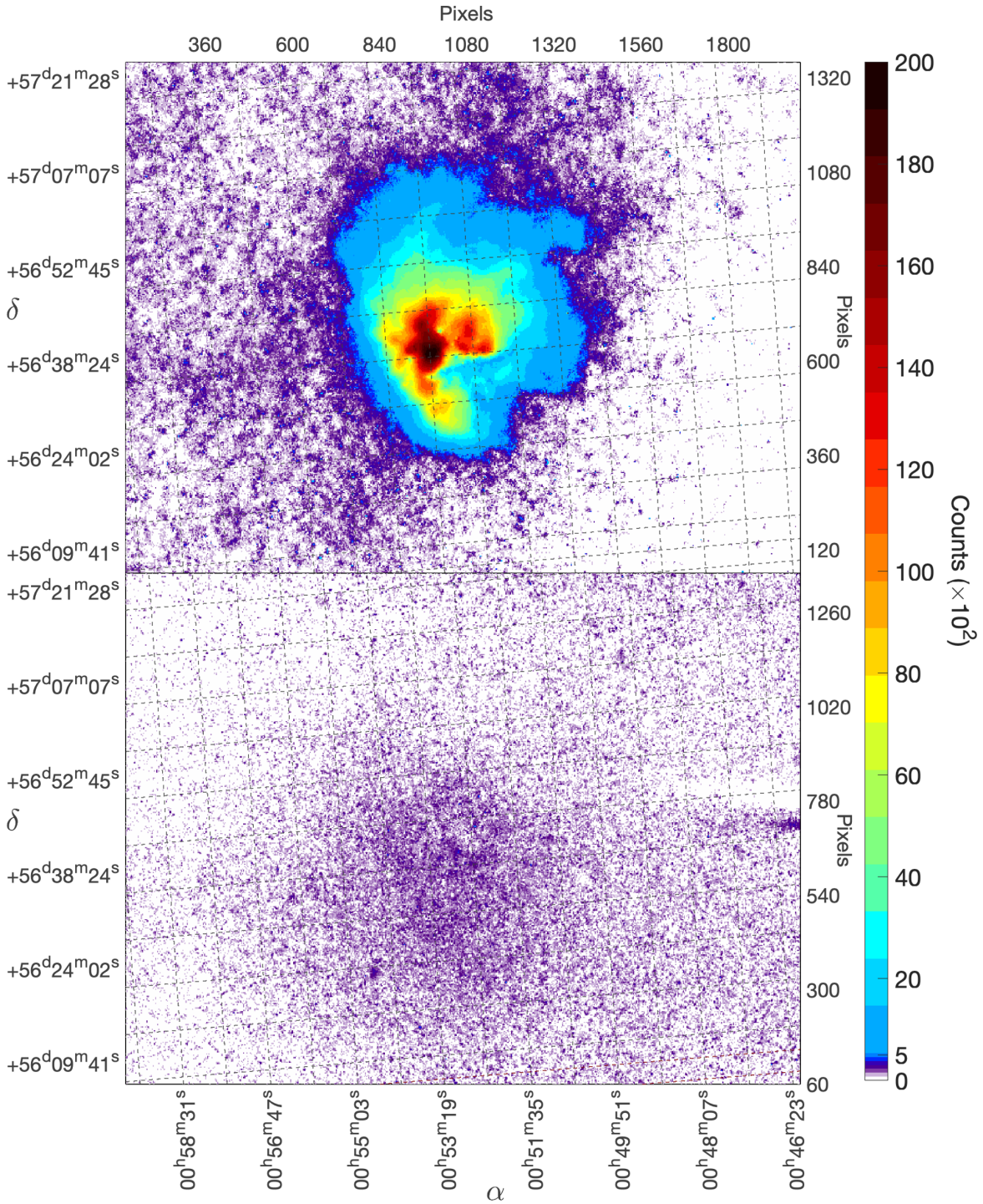

Figure 7.12: Colourmap of the colour-inverted starless starless, continuum subtracted, images of the PacMan Nebula which were binned 3×3. Top image is in Hα. Bottom image is in [OI]. The colour bar values represent the logarithmic counts.

It is worthwhile to investigate the ratio of emissions through the two filters to judge where [OI] is enhanced relative to Hα and thereby locate the transition zones. With 3×3 binning, the ratio of [OI] to Hα yields the image in Figure 7.13, represented as a colourmap. In Figure 7.13 the ratio of signals where the ray of a nearby bright star enters the field of view of the image are manually set to zero, as the ratio there is not representative of emissions in [OI] or Hα. The colourmap makes it evident that the ratio of count rates within the location of the Hα emissions lies within $0.001 \leq N_{[OI]}/N_{H\alpha} \leq 1$. The ratio $N_{[OI]}/N_{H\alpha}$ is the highest towards the right-hand-side of the image primarily due to the near-absense of the Hα emissions in that location, and is not indicative of density enhancements.

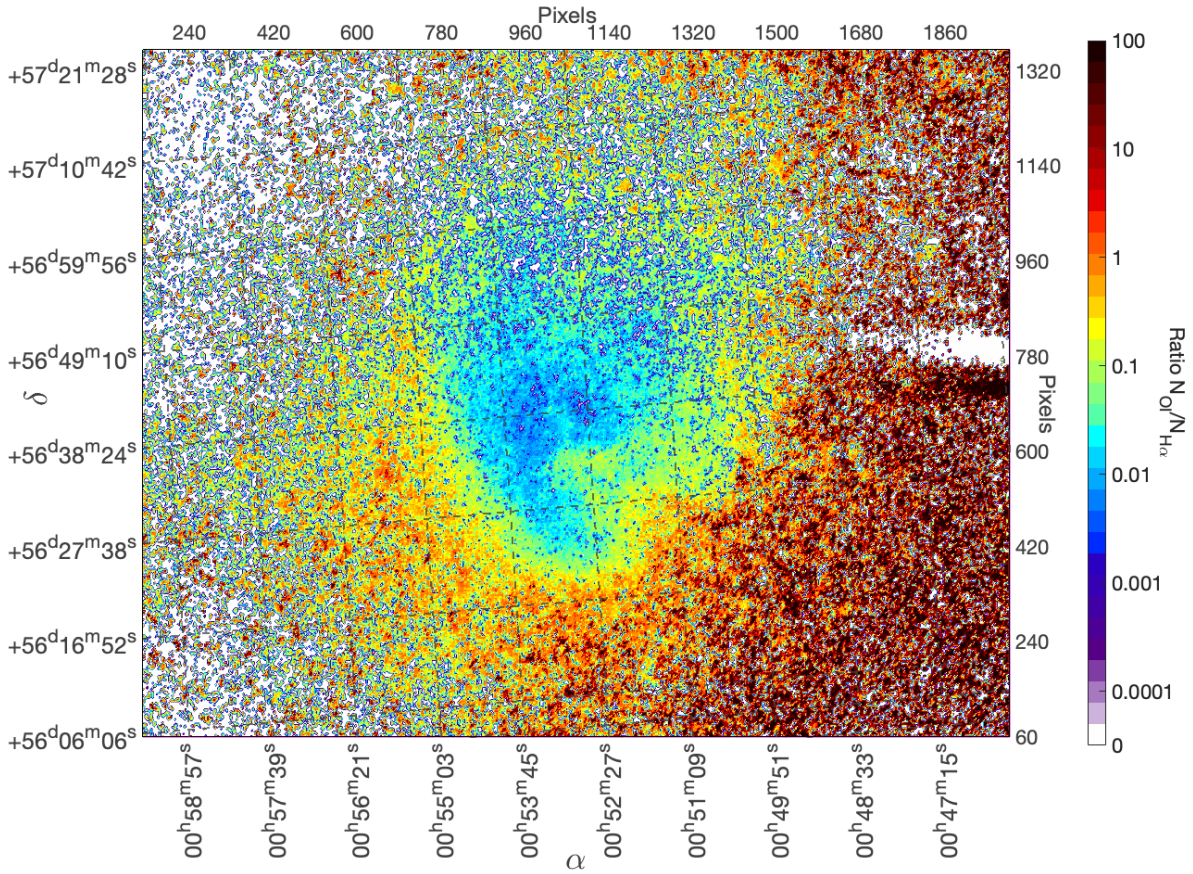

Figure 7.13: Colourmap of Ratio of [OI] to Hα, binned 3×3.

Neutral oxygen emission is enhanced relative to Hα primarily on the "lower face" - the chin and the mouth area - of the PacMan nebula, and weakens towards the nebula's "hairline". The areas where the neutral oxygen emissions are enhanced are plotted in orange on the colourmap image in Figure 7.13. The morphology indicates that the nebula is ionization bounded on the South-East side of the nebula, and density-bounded on the North-East. This suggests that the PacMan nebula is Orion-like with UV radiation creating a cavity in a molecular cloud to the South-East and creating a champagne flow to the North-West.

7.3 M27 - Dumbbell Nebula

The Dumbbell Nebula, also known as Messier 27, provided some of our most striking observational results. It is clearly visible in all three of our filters even before the stars are removed. Colour-inverted and cropped images of M27 can be seen in Figure 7.14. The field of view in all images of M27 was cropped to accentuate the features of the nebula.

The Z-shape present in the [OI] images in Figures 7.14 and 7.15 is also present in the Hα image. The continuum emission is very diffuse and underwhelming when compared to its line counterparts. However it generally mimics the overall shape of the emissions in Hα and [OI]. Figure 7.15 contains the star-free images of M27. The removal of stars was accomplished using IRAF as described in Section 6.4.4. The blotches around the central nebulosity in the continuum are artifacts of the stellar removal process.

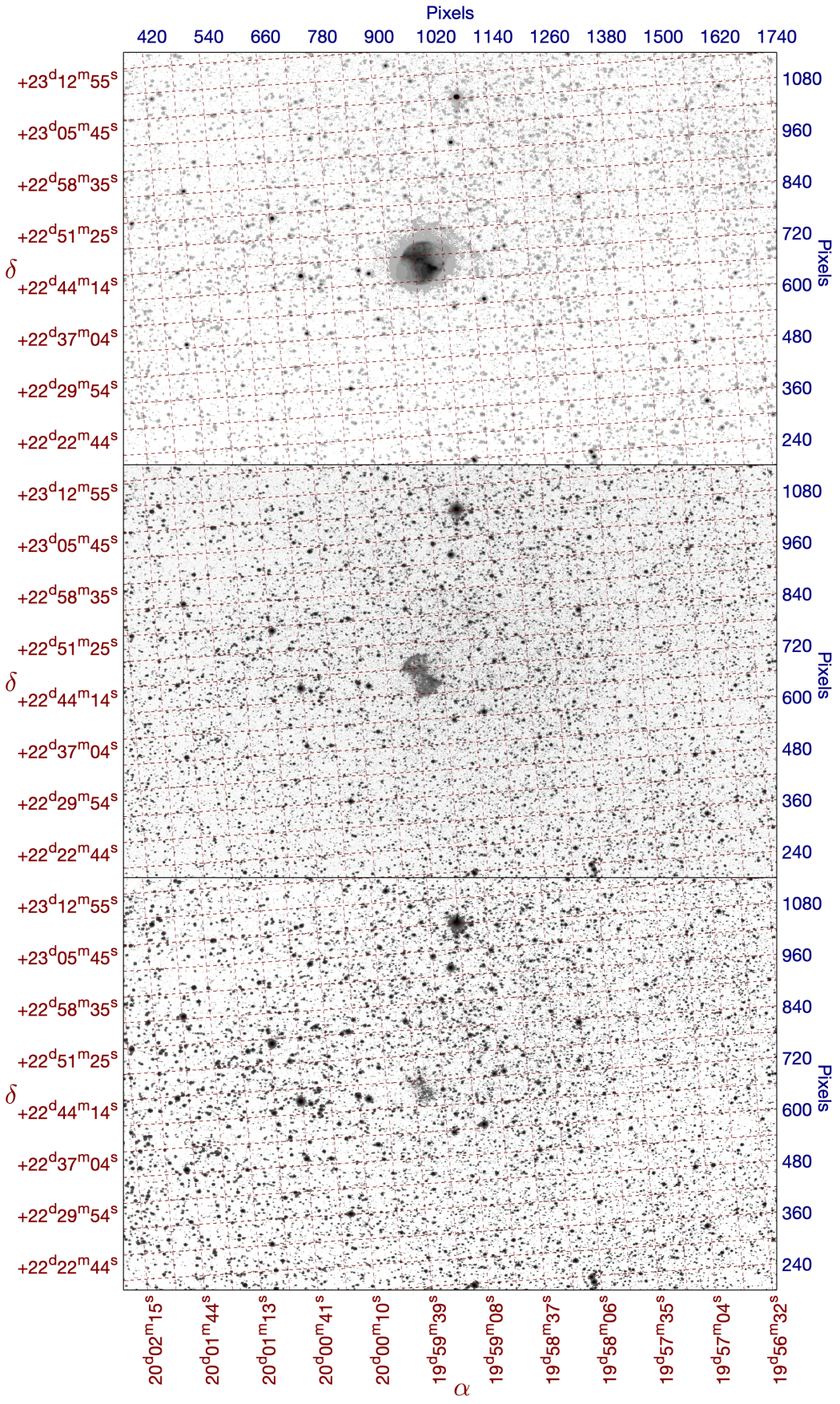

Figure 7.14: Colour-inverted images of M27. Top image is in Hα. Middle image is in [OI]. Bottom image is in Continuum.

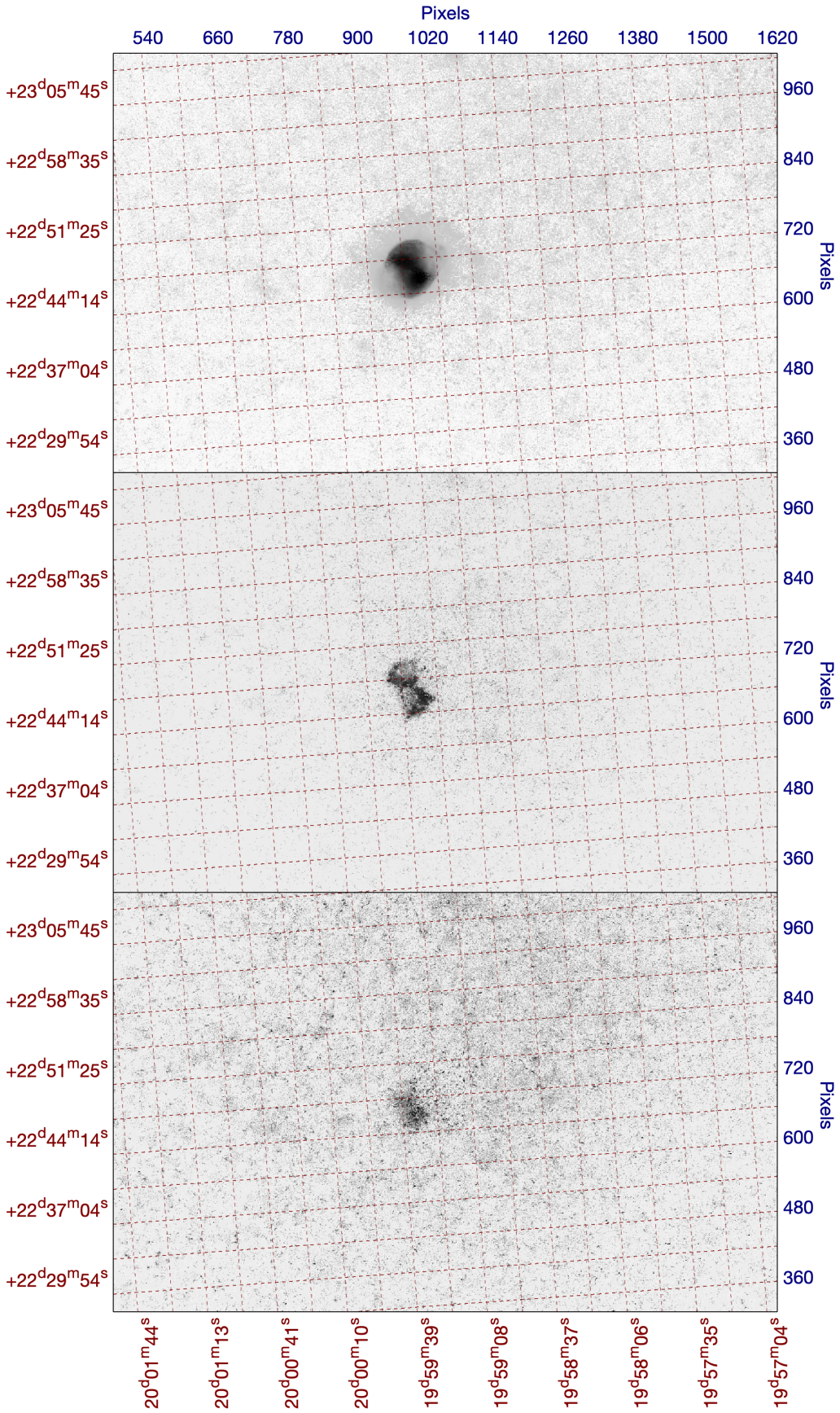

Figure 7.15: Colour-inverted starless images of M27. Left image is in Hα. Middle image is in [OI]. Right image is in Continuum.

To isolate the line emission, the continuum admitted by the line filters needs to be subtracted. Star-free and continuum subtracted images of M27 in Hα and [OI] can be seen in Figure 7.16.

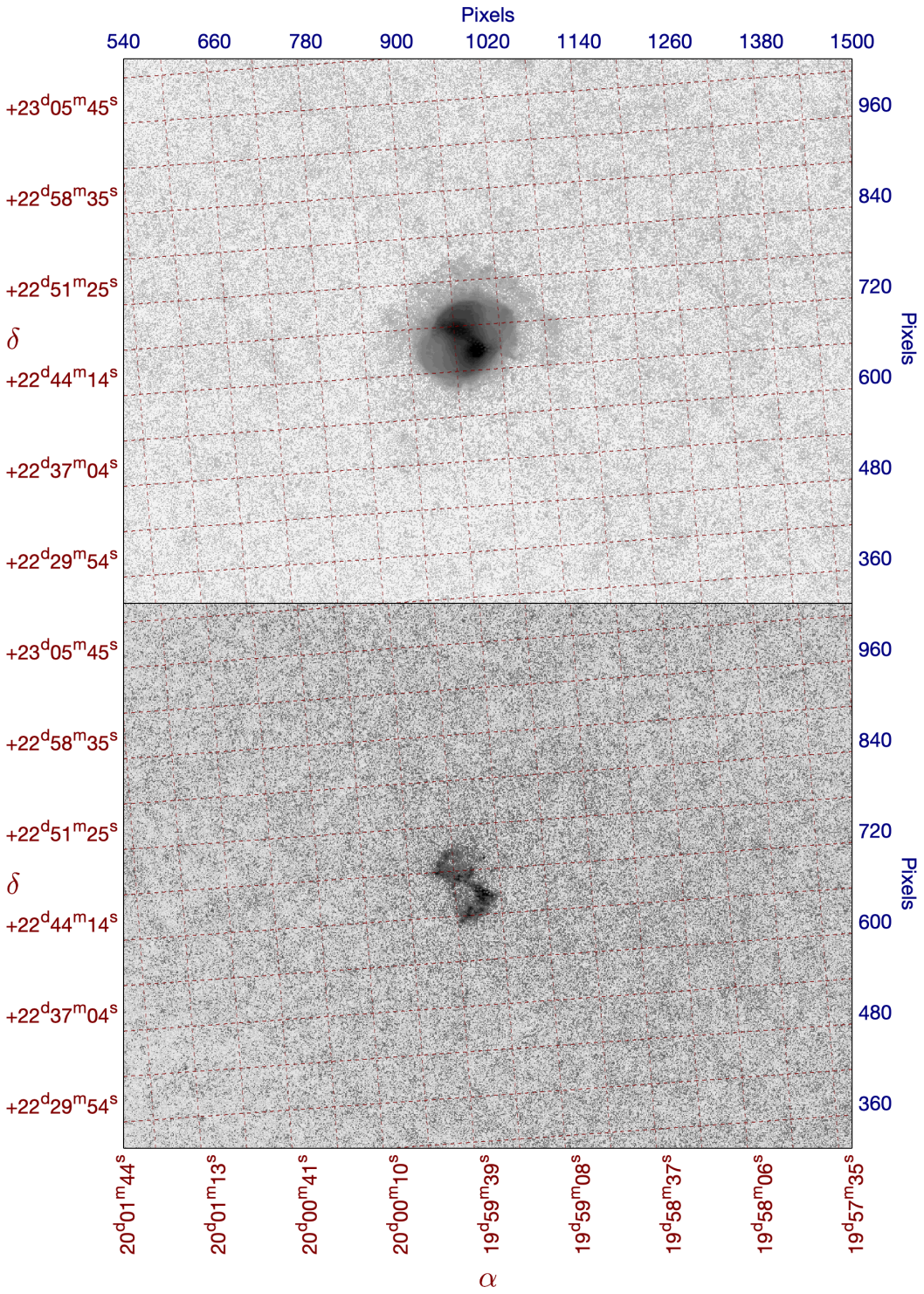

Figure 7.16: Starless, continuum-subtracted and sky-background subtracted images of M27. The top image is in Hα. The bottom image is in [OI].

It is interesting to compare the signals from the nebula in Hα and [OI]. The signals obtained over four minute exposures from M27 in Hα and [OI] can be seen in Figure 7.17.

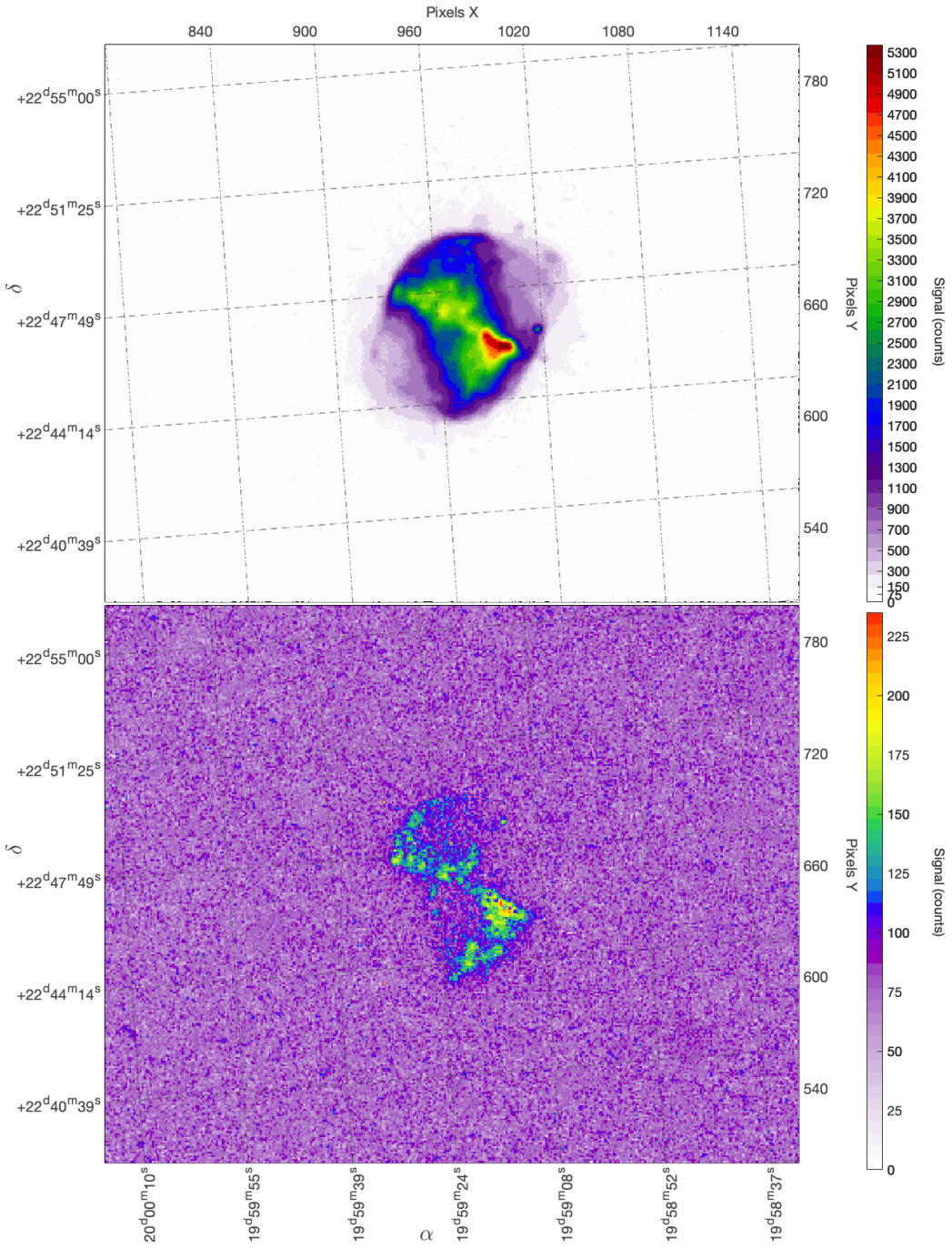

Figure 7.17: Colourmap of starless, continuum-subtracted and sky-background subtracted images of M27 in Hα and [OI] with full dynamic colour ranges shown.

By dividing the two continuum and sky-subtracted line images by each

other one can locate the transition zones as the ratio of [OI] to Hα signal will be enhanced where [OI] is enhanced. Prior to taking the ratio it is advantageous to visualize the signals in [OI] and Hα using a common colourmap, which can be seen in Figure 7.18.

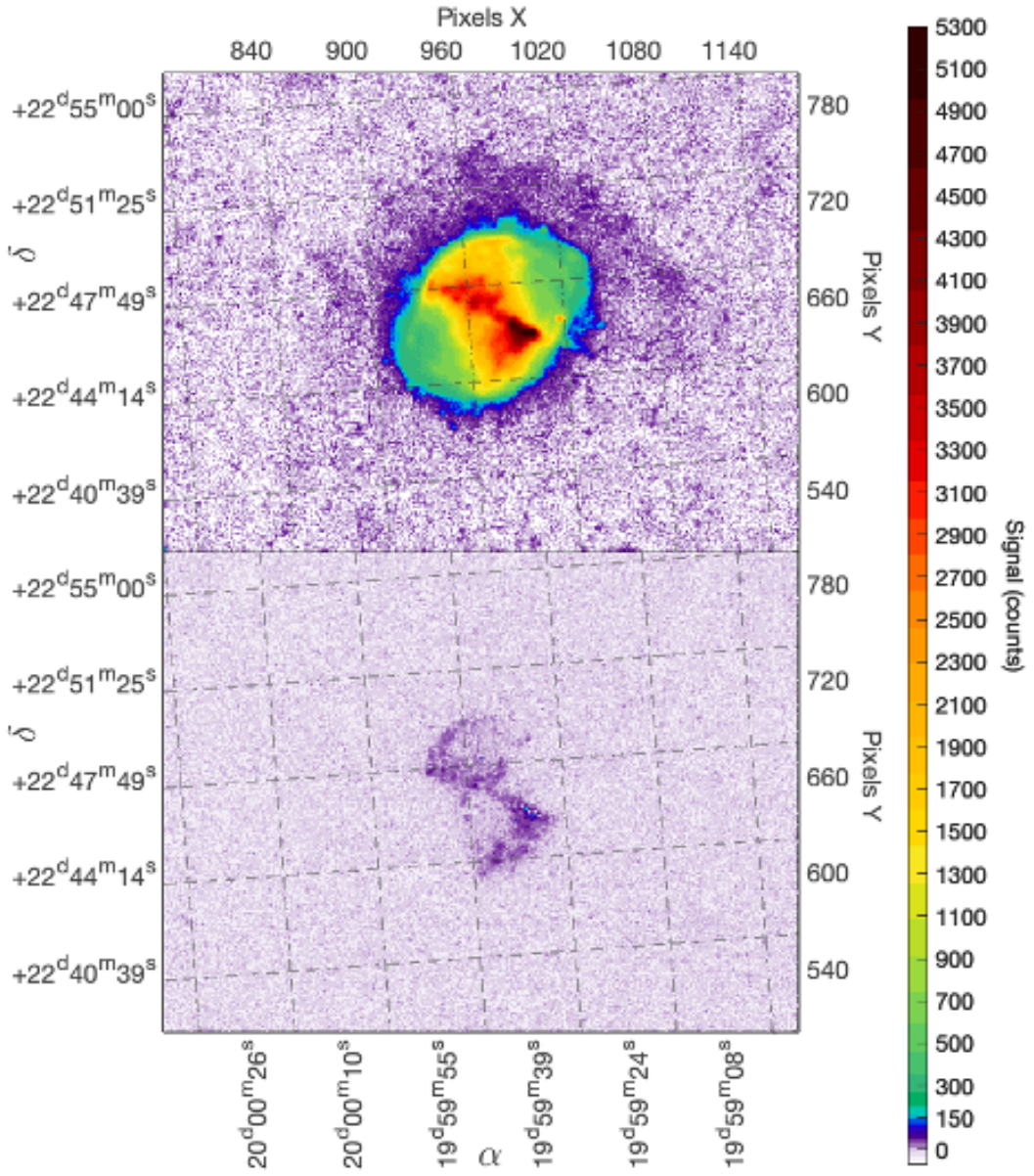

Figure 7.18: Colourmap of starless, continuum-subtracted and sky-background subtracted images of M27. The top image is in Hα. The bottom image is in [OI].

Figure 7.18 shows that the signal in [OI] only reaches a value of ~ 235 counts and is generally much lower than the signal in Hα, which reaches as high as

5300 counts.

However, the visual comparison of fluxes provided in Figure 7.18 does not provide the specific details about the transition zones and density enhancements of M27. To obtain the specific details about the transition zones and density enhancements it is useful to compute the ratio of [OI] to Hα signals, and see where the signal in [OI] is enhanced relative to the signal in Hα.

Prior to computing the signal ratio of [OI] to Hα it is useful to first isolate the Hα and [OI] emissions from the unrelated pixel background around the nebula. This can be done by selecting the pixels pertinent to the nebula and saving them into a so-called mask. The unrelated pixels can be dealt with in a variety of ways, depending on the type of data being processed, the software used, and the end-goal of creating a mask. In some cases, it makes sense to separate the pixels of interest and the unrelated pixels into two separate images. In other cases, simply setting the unrelated pixels to zero or some other value might be a better option.

To create the Hα and [OI] emission masks for our purposes the background pixels were set to zero, while the pixels containing the nebular emissions were kept with their original values. The resulting images containing only the line emission were plotted as colourmaps and can be seen in Figure 7.19. The colourmaps revealed that the Hα signal is typically much higher than the [OI] signal found in the same region of the nebulosity.

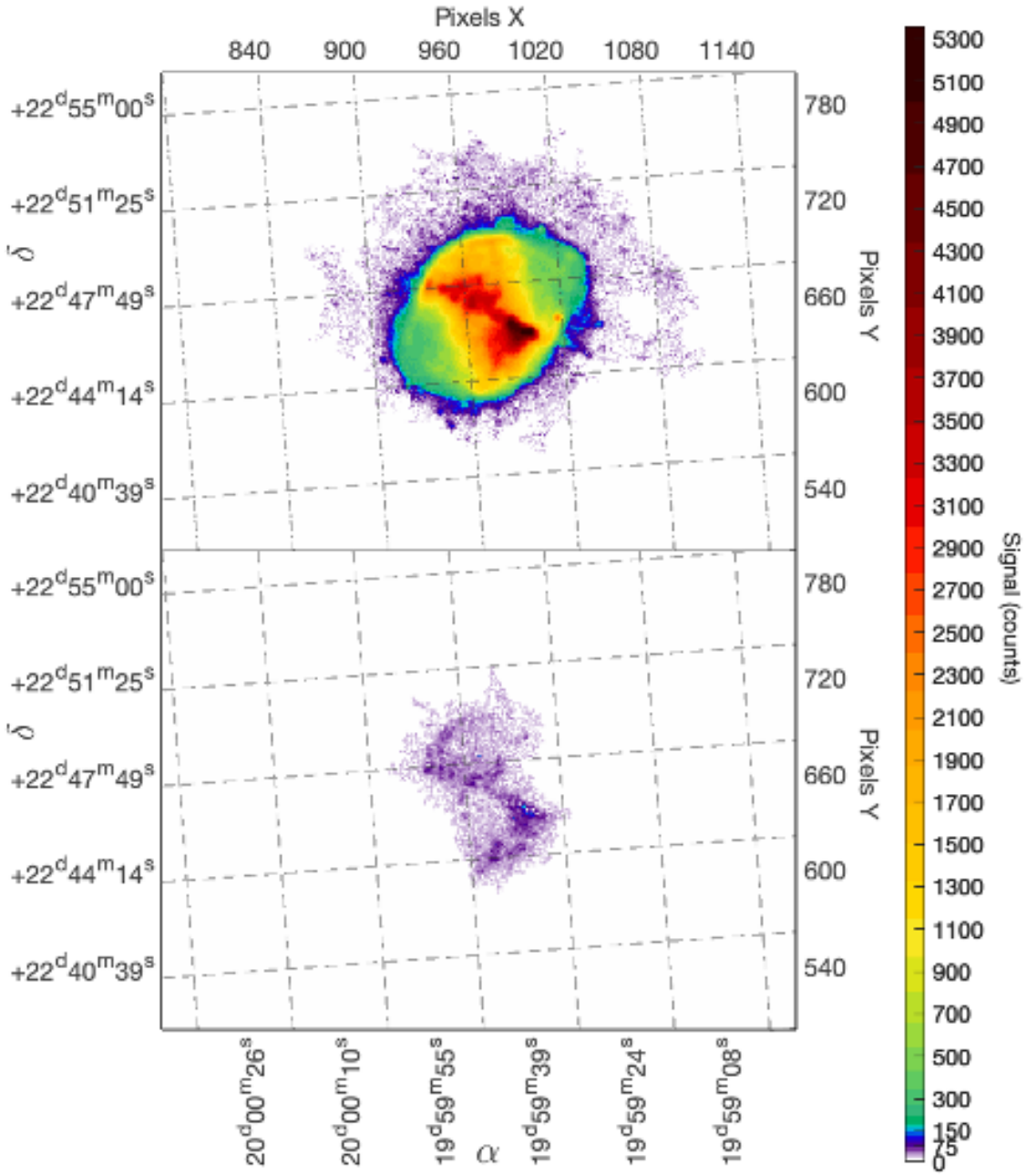

Figure 7.19: Colourmap of emissions in Hα and [OI] from M27. The top image is in Hα. The bottom image is in [OI].

The ratio of the continuum and background-subtracted image in [OI] relative to that of Hα was then computed. The visual representation of the flux ratio can be seen in Figure 7.20. Only pixels where the ratio of fluxes is greater than or equal to zero are displayed.

The image shows that there are density enhancements of [OI] in the nebula

(shown in red), tracing where transition zones are located. There is a gradient of signal density, where the signal ratio of [OI] to Hα increases towards the top and bottom parts of the Z-shape. This proves that the nebula is ionization bounded in some directions, assuming that the radiation field is isotropic.

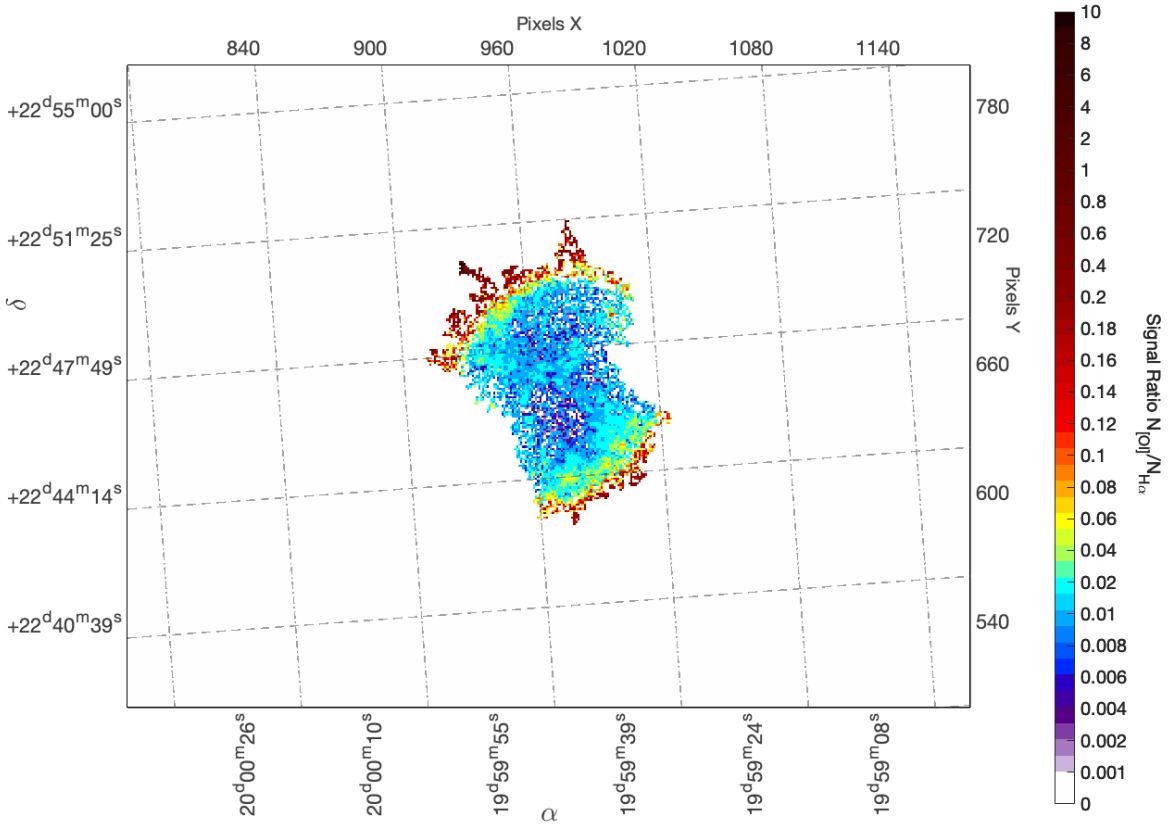

Figure 7.20: Colourmap of the signal ratio of emissions in [OI] to Hα from M27.

7.4 And XVIII

7.4.1 Images of And XVIII

The high-contrast colour-inverted combined median images of And XVIII in Continuum and Hα can be seen in Figure 7.21. Faint hints of nebulosity can be seen in both the Continuum and the Hα images. The location of And XVIII on our images is marked with a red star.

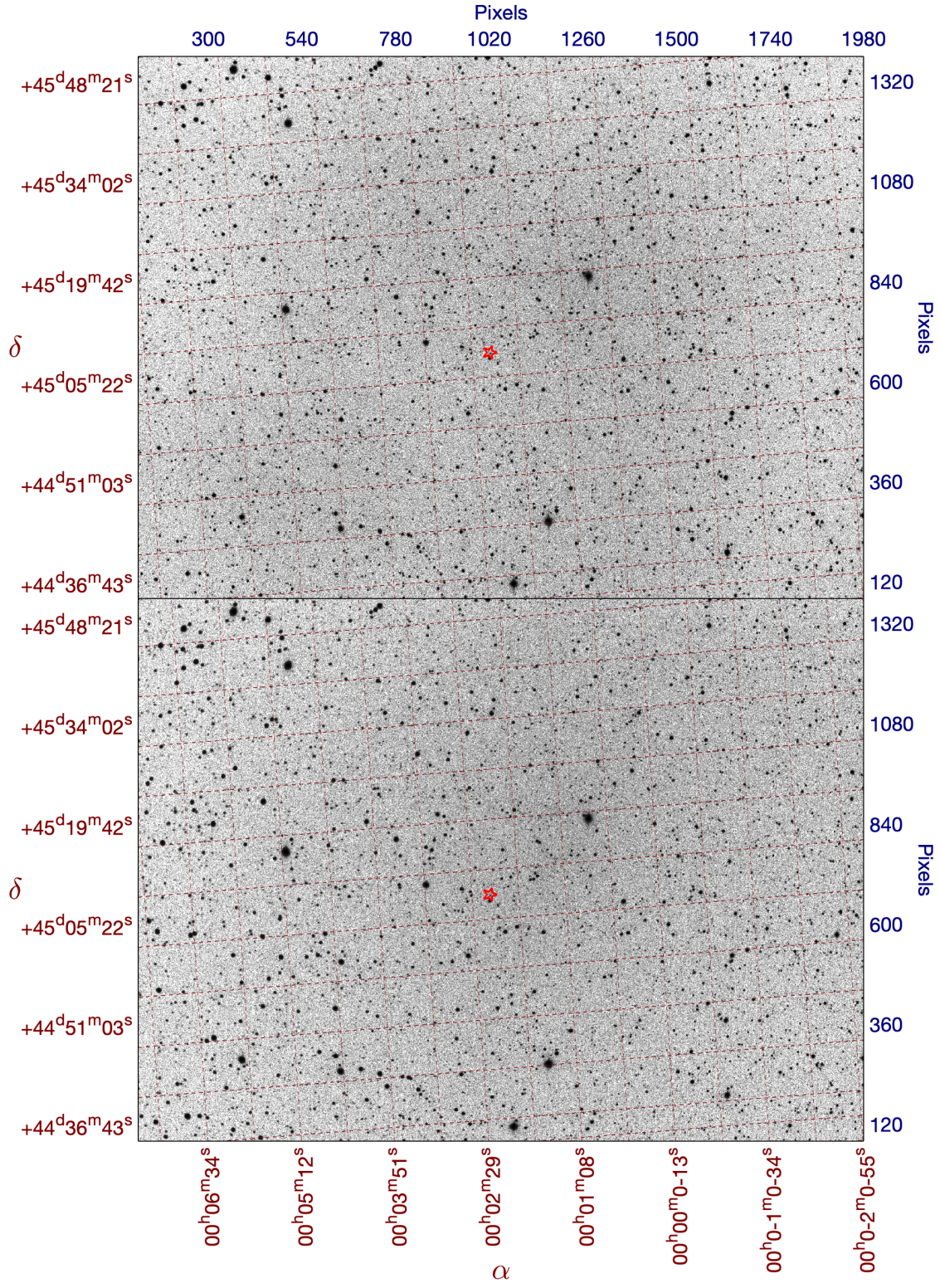

Figure 7.21: Colour-inverted images of And XVIII. The top image is in Hα. The bottom image is in Continuum.

The removal of stars made it possible to see the faint extended structure in

the vicinity of And XVIII more clearly. It can be seen in in Figure 7.22.

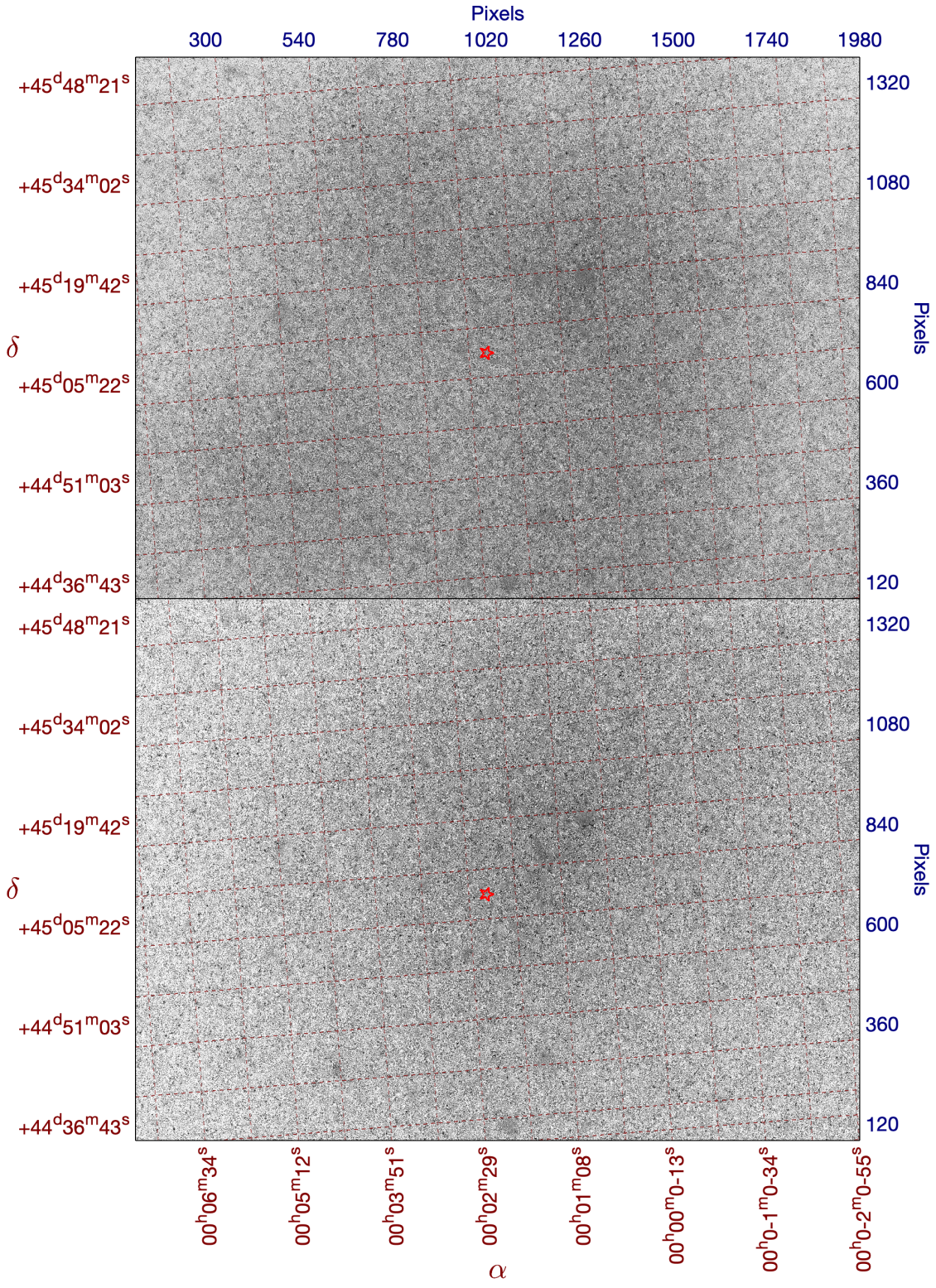

Figure 7.22: Colour-inverted, starless images of And XVIII. . The top image is in Hα. The bottom image is in Continuum.

In both images displayed in Figure 7.22 a patch of nebulosity is located slightly North-West of the centre of the image. The Hα exhibits three additional nebulous patches to the South and North-East of the dSph.

Subtraction of the continuum from the line image revealed a new pattern of nebulosity roughly symmetrical about the position of And XVIII. The continuum-subtracted line image can be seen in Figure 7.23.

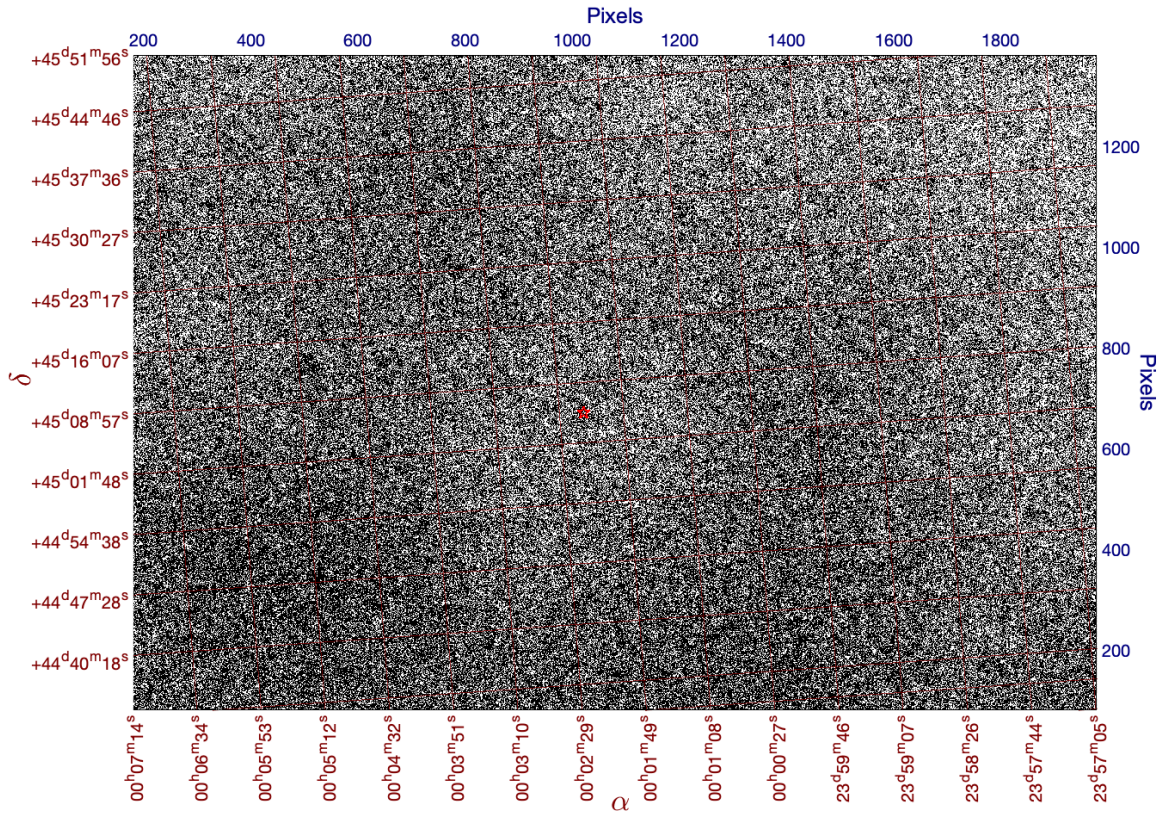

Figure 7.23: Colour-inverted, starless and continuum-subtracted Image of And XVIII in Hα.

The nebular emission extends outward from the galaxy starting at a radius of $\sim 9'$, and extending to $\sim 40'$. This is much smaller than expected, as the gas would have travelled out to $54 \leq \theta(') \leq 1260$ assuming the last burst of star formation was $1.5 - 8\,\mathrm{Gyr}$ ago, as discussed in Section 3.4.4.

7.4.2 Surface Brightness of And XVIII

We are now in a position to compute the flux and surface brightness of the nebulosity surrounding And XVIII. The flux was measured using SAOImage DS9 within the circular regions which can be seen in Figure 7.24. The corners of the image were not included in this analysis, as the darkening of the image in the corners could be attributed to vignetting.

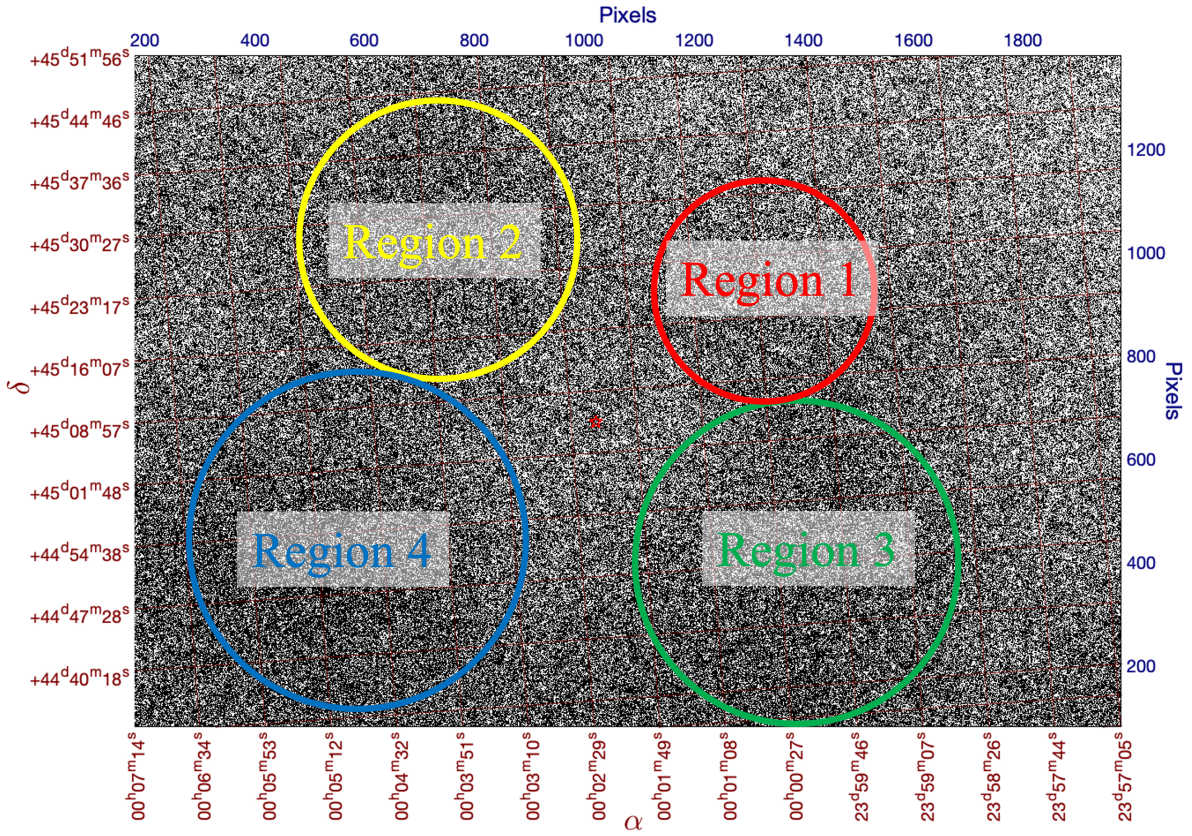

Figure 7.24: Colour-inverted, starless, continuum-subtracted, sky-subtracted image of And XVIII in Hα with the four regions where the measurement of the flux was taken drawn and labeled.

The measurements of counts and surface brightness are given in Table 7.5. The surface brightness I_L in Table 7.5 is calculated using

$$I_L = \frac{N_{L,T}}{A \langle F_R \rangle} \frac{e^{\tau_L}}{\beta t_L} \tag{7.5}$$

where $\langle F_R \rangle = 1.26 \pm 1.03$ is the flux correction factor determined in Section 6.6.2.4, and $e^{\tau_L}(\beta\, t_L)^{-1} = (3.15 \pm 0.13) \times 10^{-14}$ erg/count/cm^2 comes from Equation 6.41 and can be found in Table 6.7, A is the area of the nebulous region of the image in arcsec^2, and $N_{L,T}$ is the sum of all counts per second in that region.

To relate the surface brightness in the band of our filter to the surface brightness in the Bessel R filter or equivalent, we need to scale the flux we obtained with QUAIL to the flux from a continuum source transmitted through that filter. Benn & Ellison (1998) measured the sky brightness at La Palma observatory through the William Herschel Telescope in the Bessel R to be $\mu_{sky_{LP}} = 21.0$ mag/arcsec^2. To do so, we calculate the monochromatic surface brightness of an extended continuum source that would yield the same integrated surface brightness as the Hα line emission after being filtered by the Bessel R filter. The equivalent width of the Bessel R filter is $W_R = 1561.86$ Å. The corresponding surface brightness in magnitude units of the continuum source would be given by:

$$\mu_R = -2.5 \log \left(\frac{I_L}{W_R} \right) - 21.1 - \zeta_\lambda \tag{7.6}$$

where $\zeta_\lambda = 0.549$ is the magnitude zero-point for flux of the Bessel R filter (McCall, 2004). The regions and their surface brightnesses can be were calculated using Equations 7.5 and 7.6 and are listed in Table 7.5. The error in R surface brightness μ_R is dominated by the error in the correction factor $\langle F_R \rangle$.

Region	Region Center (x, y) (pix)	Radius R_R $(arcsec)$	Area A (arcsec^2) $(\times 10^6)$	Total Counts $N_{L,T} \pm \delta N_{L,T}$ $(\frac{\text{counts}}{\text{s}})$	Surface Brightness I_L $(\times 10^{-20})$ (erg/cm^2/s/arcsec^2)	R Surface Brightness μ_R (mag/arcsec^2/Å)
1	$(1444, 910)$	945	2.80	2716 ± 33	1.55 ± 1.27	27.88 ± 0.89
2	$(720, 1020)$	1102	3.82	5122 ± 39	2.15 ± 1.76	27.52 ± 0.89
3	$(1394, 330)$	1085	3.70	8003 ± 39	3.46 ± 2.83	27.00 ± 0.89
4	$(504, 380)$	1190	4.45	10580 ± 43	3.81 ± 3.11	26.90 ± 0.89

Table 7.5: Measured Hα surface brightnesses and pertinent measurement regions of the image of And XVIII

7.4.3 Mass Of Gas Around And XVIII

We can use the total flux measured over the four regions described in Section 7.4.2 to obtain the mass of nebulous matter found around And XVIII. Summing the counts per second yields $N_L = 26000 \pm 78$ counts/s. We can calculate the total flux in these regions using equation:

$$F_L = \frac{N_L}{\langle F_R \rangle} \frac{e^{\tau_L}}{\beta t_L} \tag{7.7}$$

Calculating the total Hα flux in the image yields:

$$F_L = (6.61 \pm 5.41) \times 10^{-10} \quad \text{erg cm}^{-2}\,\text{s}^{-1} \tag{7.8}$$

To find the number of photons emitted per second, we divide the total flux F_L by the energy of the Hα photon. The energy of the Hα photon is

$$E_{H\alpha} = h\,c/\lambda_{H\alpha} = 3.03 \times 10^{-12} \quad \text{erg} \tag{7.9}$$

where h is Planck's constant, and c is the speed of light in vacuum. The photon rate R is then

$$R = F_L/E_{H\alpha} = 218 \pm 178 \quad \text{cm}^{-2}\,\text{s}^{-1} \tag{7.10}$$

The rate at which photons are emitted should be proportional to the rate of recombinations of hydrogen ions. Thus,

$$R = \frac{\alpha_{eff,H\alpha}(T) N^2 V}{4\pi d^2} \tag{7.11}$$

where N is the particle density of hydrogen ions, V is the volume of the region, d is the distance to And XVIII, and $\alpha_{eff,H\alpha}(T)$ is the recombination coefficient pertaining to recombinations that lead to the transitions from the third to second energy level of hydrogen:

$$\alpha_{eff,H\alpha}(T) = (7.7 \times 10^{-14}) \left(\frac{T}{10^4}\right)^{-1.0} \quad (\mathrm{cm^3\,s^{-1}}) \tag{7.12}$$

where T is the temperature of the gas (Osterbrock, Donald E., 1989). Using the temperature $T = 13,000 \pm 4,000$ K, which is the temperature at which it is claimed that the gas photo-evaporates from dSphs, (Ivkovich & McCall, 2019), the recombination coefficient is

$$\alpha_{eff,H\alpha}(T) = (5.92 \pm 1.82) \times 10^{-14} \quad \mathrm{cm^3\,s^{-1}}$$

Despite seeing emission in the four circular areas only, to simplify the calculations the volume of the nebulosity was assumed to be a spherical shell with inner radius of $R_{s_I,pix} = 250$ pix and an outer radius of $R_{s_O,pix} = 850$ pix. All values related to calculating distances and geometries can be found in Table 7.6. The diagram of this shell can be seen in Figure 7.25.

The distance to And XVIII is provided by Makarova et al. (2017) as $d_{A18,Mpc} = 1.33^{+0.06}_{-0.09}$ Mpc and is given in Table 3.5. Using the volume of the two spheres provided in Table 7.6, the volume of the shell is:

$$V_{Shell} = V_{S_{Out},cm} - V_{S_{In},cm} = 8.47^{+1.18}_{-1.76} \times 10^{68} \quad \mathrm{cm^3} \tag{7.13}$$

where $V_{S_{Out},cm}$ is the volume of the outer sphere, and $V_{S_{In},cm}$ is the volume of the inner sphere. The subscripts S_{Out} and S_{In} stand for Sphere Outer and Sphere Inner respectively, and the dimenstions that were used to calculate their volumes can be found in Table 7.6.

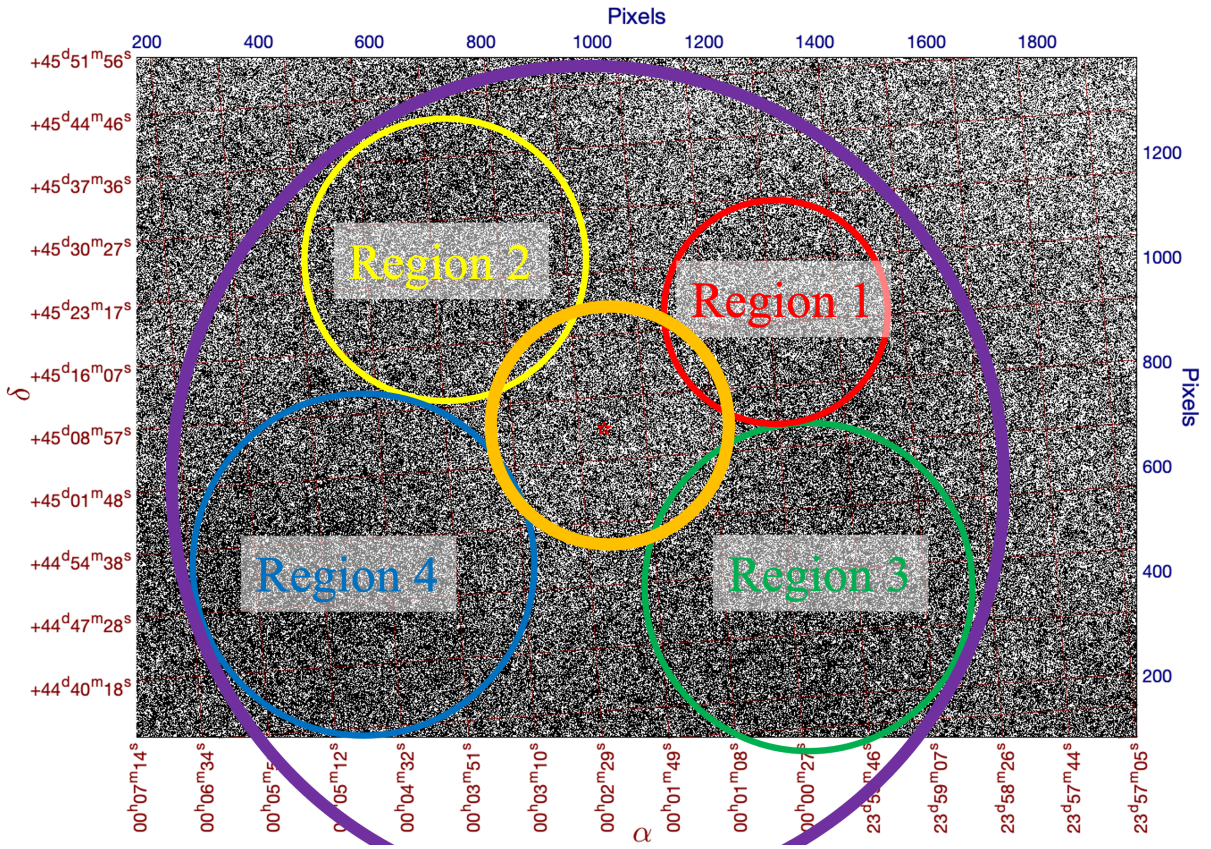

Figure 7.25: Colour-inverted, starless, continuum-subtracted, sky-subtracted image of And XVIII in Hα with the four regions where the measurement of the flux was taken drawn and labeled. The cross-section of the shell with which the volume of gas is approximated is bounded by the orange and purple circles.

Using the calculated volume, solving Equation 7.11 for the density of hydrogen yields

$$N = \sqrt{\frac{4\,\pi\,d_{A18,cm}^2\,R}{\alpha_{eff,H\alpha}(T)\,V_{Shell}}} = 3.03^{+1.37}_{-1.36} \times 10^{-2} \quad \mathrm{cm}^{-3} \tag{7.14}$$

The mass of gas in solar masses can be calculated using

$$M_{Gas} = \frac{M_H}{M_{\odot,kg}}\sqrt{\frac{4\pi R\,V_{Shell}\,d_{A18,cm}^2}{\alpha_{eff,H\alpha}(T)}} = (2.16)^{+0.96}_{-0.98} \times 10^{10} \quad \mathrm{M}_\odot \tag{7.15}$$

where M_H is the mass of a hydrogen atom in kilograms and $M_\odot$ is the mass of the Sun in kilograms.

In reality, the emitting volume V may be smaller. How much smaller can be quantified geometrically by introducing the filling factor $f = f_M f_m$, where f_M and f_m are the macroscopic and microscopic volume filling factors respectively. The mass of gas is dependent on the filling factors as

$$M_{Gas,f} = M_{Gas,\odot}\sqrt{f_M f_m} \tag{7.16}$$

where $M_{gas,f}$ is the mass of gas calculated with the consideration of the filling factor, and M_{gas} is the mass of gas calculated in Equation 7.15.

7.4.3.1 Macroscopic Filling Factor f_M

The macroscopic filling factor describes the gas distribution on macroscopic scales. The upper and lower limits on the macroscopic filling factor f_M can be estimated by assuming different geometric shapes in which the gas can arrange itself. All dimensions and geometries that were used to calculate the macroscopic filling factor can be found in Table 7.6.

The lower limit of the macroscopic filling factor can be obtained by dividing the sum of the volumes of spheres with radii equivalent to those of the four measurement regions by the volume of the spherical shell calculated in Equation 7.13. The lower limit of f_M is then

$$f_{M,l} = \frac{\sum_{i=1}^{4} V_{r_i,pix}}{V_{S_{Out},pix} - V_{S_{In},pix}} = 0.20 \tag{7.17}$$

The upper limit to the macroscopic filling factor is calculated from the ratio of the volumes of two tori shown in Figure 7.26. The volume of a torus can be

calculated using the following formula:

$$V_{t_i,pix} = 2\pi^2 R^2_{t_i,pix} R_{tr_i,pix} \tag{7.18}$$

where $R^2_{t_i,pix}$ is the radius of the tube and $R_{tr_i,pix}$ is the radius of revolution. Torus 1, drawn in orange, has the tube radius $R_{t_1,pix}$ equal to the average of the radii of Regions 1 and 2:

$$R_{t_1,pix} = \frac{R_{r_1,pix} + R_{r_2,pix}}{2} \tag{7.19}$$

Similarly, the tube radius for Torus 2 is adopted to be the average of the radii of Regions 3 and 4:

$$R_{t_2,pix} = \frac{R_{r_3,pix} + R_{r_4,pix}}{2} \tag{7.20}$$

The radius of revolution of Torus 1 in pixels $R_{tr_1,pix}$ is adopted to be the average of distances between the location of And XVIII to the centres of Regions 1 and 2:

$$R_{tr_1,pix} = \frac{d_{r_1,pix} + d_{r_2,pix}}{2} \tag{7.21}$$

Similarly, the radius of revolution of Torus 2 in pixels $R_{tr_2,pix}$ is adopted to be the average of distances between the location of And XVIII to the centres of Regions 3 and 4.

$$R_{tr_2,pix} = \frac{d_{r_3,pix} + d_{r_4,pix}}{2} \tag{7.22}$$

The position of And XVIII on the image is

$$(x_{And18}, y_{And18}) = (1023, 668) \quad \text{pix} \tag{7.23}$$

The upper limit of the macroscopic filling factor is then

$$f_{M,u} = \frac{\sum_{i=1}^{2} V_{t_i,pix}}{V_{S_{Out},pix} - V_{S_{In},pix}} = 0.77 \tag{7.24}$$

The macroscopic filling factor is then $0.20 \leq f_M \leq 0.77$.

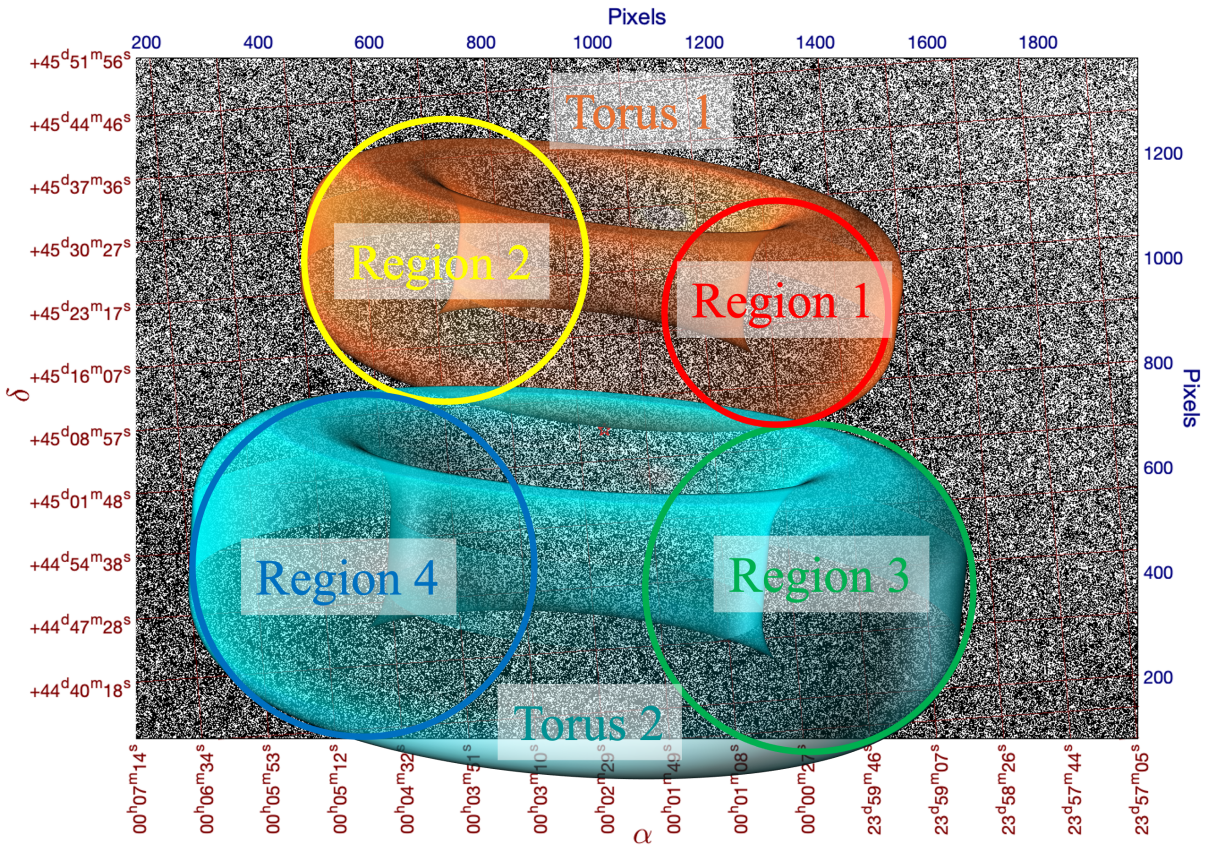

Figure 7.26: Two tori comprising the lower limit of the volume of gas drawn on top of the starless, continuum-subtracted, sky background subtracted image of And XVIII in Hα with the four measurement regions.

7.4.3.2 Microscopic Filling Factor f_m

The microscopic filling factor describes how clumpy or varying in density the gas is on small scales.

The upper and lower limits of the microscopic filling factor are taken from Cedrés et al. (2013). Cedrés et al. (2013) show that the microscopic filling factor for HII regions in the galaxy NGC 6946 can be as low as $f_{m,l} = 10^{-4}$. They also show that the highest value for the filling factor in the HII regions is $f_{m,u} = 10^{-1.8}$. Thus, the microscopic filling factor is $10^{-4} \leq f_m \leq 10^{-1.8}$.

Region Number	Region Center	Region Radius			Region Area			Distance to And XVIII			Volume	
i	(x, y) (pix)	$R_{r_i,pix}$ (pix)	$R_{r_i,arc}$ ($''$)	$R_{r_i,cm}$ (cm) ($\times 10^{22}$)	$A_{r_i,pix}$ (pix^2) ($\times 10^5$)	$A_{r_i,arc}$ ($''^2$) ($\times 10^6$)	$A_{r_i,cm}$ (cm^2) ($\times 10^{45}$)	$d_{r_i,pix}$ (pix)	$d_{r_i,arc}$ ($''$)	$d_{r_i,cm}$ (cm) ($\times 10^{22}$)	$V_{r_i,pix}$ (pix^3) ($\times 10^8$)	$V_{r_i,cm}$ (cm^3) ($\times 10^{67}$)
1	$(1444, 910)$	270	945	1.88	2.29	2.80	1.11	486	1701	3.38	0.82	2.78
2	$(720, 1020)$	315	1102	2.19	3.12	3.82	1.51	464	1624	3.23	1.31	4.42
3	$(1394, 330)$	310	1085	2.16	3.02	3.70	1.46	502	1757	3.50	1.25	4.21
4	$(504, 380)$	340	1190	2.37	3.63	4.45	1.76	594	2079	4.14	1.65	5.56

Sphere	Sphere Center	Sphere Radius			Sphere Area			Distance to And XVIII			Volume	
S	(x, y) (pix)	$R_{S_S,pix}$ (pix)	$R_{S_S,arc}$ ($''$)	$R_{S_S,cm}$ (cm) ($\times 10^{22}$)	$A_{S_S,pix}$ (pix^2) ($\times 10^5$)	$A_{S_S,arc}$ ($''^2$) ($\times 10^6$)	$A_{S_S,cm}$ (cm^2) ($\times 10^{45}$)	$d_{S_S,pix}$ (pix)	$d_{S_S,arc}$ ($''$)	$d_{S_S,cm}$ (cm) ($\times 10^{22}$)	$V_{S_S,pix}$ (pix^3) ($\times 10^8$)	$V_{S_S,cm}$ (cm^3) ($\times 10^{67}$)
Inner $S = In$	$(1024, 669)$	250	875	1.74	1.96	2.40	0.95	0	0	0	0.65	2.21
Outer $S = Out$	$(1025, 670)$	850	2975	5.92	22.7	27.8	11.0	0	0	0	25.7	86.9

Torus Number	Torus Center	Torus Radius			Torus Area			Radius of Revolution			Volume	
i	(x, y) (pix)	$R_{t_i,pix}$ (pix)	$R_{t_i,arc}$ ($''$)	$R_{t_i,cm}$ (cm) ($\times 10^{22}$)	$A_{t_i,pix}$ (pix^2) ($\times 10^5$)	$A_{t_i,arc}$ ($''^2$) ($\times 10^6$)	$A_{t_i,cm}$ (cm^2) ($\times 10^{45}$)	$R_{tr_i,pix}$ (pix)	$R_{tr_i,arc}$ ($''$)	$R_{tr_i,cm}$ (cm) ($\times 10^{22}$)	$V_{t_i,pix}$ (pix^3) ($\times 10^8$)	$V_{t_i,cm}$ (cm^3) ($\times 10^{67}$)
1	$(1023, 668)$	293	1025	2.04	2.70	3.30	1.31	475	1662.5	3.31	8.05	27.2
2	$(1023, 668)$	325	1137	2.26	3.32	4.06	1.61	548	1918	3.82	11.4	38.6

Table 7.6: Regions and geometries that were used to calculate the macroscopic filling factor of the nebulous regions of And XVIII.

7.4.3.3 Mass Of Gas Around And XVIII With Filling Factors

With macroscopic filling factor $0.20 \leq f_M \leq 0.77$, and microscopic filling factor $10^{-4} \leq f_m \leq 10^{-1.8}$ we can estimate the lower and upper bounds of the gas mass. The overall filling factor is obtained using $f = f_M f_m$:

$$2.00 \times 10^{-5} \leq f \leq 1.23 \times 10^{-2} \tag{7.25}$$

where the lower and upper bounds of the overall filling factor have been calculated using $f_l = f_{M,l} f_{m,l}$ and $f_u = f_{M,u} f_{m,u}$ respectively. Using results for the overall filling factor and Equation 7.16, the lower and upper bounds for the mass of gas around And XVIII is

$$7.99 \leq \log(M_{Gas,f}) \leq 9.38 \tag{7.26}$$

The amount of gas lost as predicted by theory in Section 3.4.3 is $\log(M_{gas}) = 7.12^{+1.79}_{-0.35}\ \mathrm{M}_\odot$. This means that the lower limit of the detected gas mass is located withing the error margin of the predicted value. Possible explanations for any conflict between the observed and the predicted gas masses can be found in found in Section 7.4.6.

The mass of gas is only one of the two theoretically predicted quantities related to the missing gas of And XVIII. The discussion of the location of the missing gas can be found in Section 7.4.4.

7.4.4 Location Of Gas Around And XVIII

The theoretical distance that any photo-evaporated gas has traveled from And XVIII was calculated in Section 3.4.4. The distance that the gas would have traveled if it was evacuated during the latest star formation event is $22.36 \leq d_t\ (\mathrm{kpc}) \leq 87.49$, which corresponds to $0.9 \leq \theta_t\ (^\circ) \leq 4.1$.

The nebulosity in the image spans approximately $0.24 \leq \theta\,(^{\circ}) \leq 0.83$ from And XVIII. The upper bound of the location of the gas on the image is smaller than the lower bound on the theoretical distance traveled.

This could mean that either the theoretical value for the distance traveled by the photo-evaporated gas is incorrect, possibly due to the expansion velocity is too high. Alternatively, the nebulosity in our image is not the photo-evaporated gas. A detailed discussion of the possible sources of this discrepancy can be found in Section 7.4.6.

Regardless of the source of the discrepancy, it would prove advantageous to take a mosaic image of And XVIII, especially with improved cooling and better flat-field images. If the nebulosity is real, then we will see it on our images again. The mosaic image will also allow us to see whether the gas traveled farther out, as predicted by theory.

7.4.5 Recombination Timescale Of Gas Around And XVIII

To finally convince ourselves that what we see in the image is not And XVIII's missing gas, we can calculate the the recombination timescale and check whether the gas would have recombined by now. The recombination timescale is defined as

$$\tau_R = \frac{1}{\alpha_A(T) N} \tag{7.27}$$

where $\alpha_A(T)$ is the Case A recombination coefficient that governs the recombinations to all energy levels:

$$\alpha_A(T) = 4.18 \times 10^{-13} \left(\frac{T}{10^4}\right)^{-0.7} \quad \mathrm{cm^3\,s^{-1}} \tag{7.28}$$

Substituting the temperature $T = 13,000 \pm 4,000$ K into Equation 7.28 yields

$$\alpha_A(T) = (3.48 \pm 0.75) \times 10^{-14} \quad \mathrm{cm^3\,s^{-1}}$$

Using the value for the recombination coefficient $\alpha_A(T)$ and the density of hydrogen atoms N found earlier we can solve Equation 7.27:

$$\tau_R = 1.11^{+0.33}_{-0.34} \times 10^{15}\ \mathrm{s} = 3.52^{+1.05}_{-1.08} \times 10^{7} \quad \mathrm{yr}$$

Considering that the most recent burst of star formation was $1.5 - 8$ Gyr ago (Makarova et al., 2017), then all of the photoevaporated gas would now be neutral. This further drives the conclusion that the nebulosity around And XVIII is unlikely to be the sought for photoionized gas. Section 7.4.6 contains a discussion of possible sources of discrepancies between the predicted and observed values, as well as a discussion of the source of the detected nebulosity on our image.

7.4.6 Conclusions and Deliberations

In Sections 7.4.3, 7.4.4 and 7.4.5 it was shown that there are large discrepancies between the predicted and observed properties. These discrepancies can be explained via several scenarios.

7.4.6.1 First Scenario: Theory Needs Revisions

In the first scenario, the discrepancies between the observations and predictions can be explained if the theory behind the predictions is flawed. The veracity of the theoretical values can be ascertained by continuing the research into dSphs, including And XVIII. Continuing observations of dSphs will ensure that their orbits, luminosities, baryonic and dark matter content, and other qualities will be known to a high degree of precision. This will facilitate the

improvements to the theory of formation of all dSphs and their relationship with the Potential Plane, as well as ascertaining the causes for gas loss for each individual dSph. In particular, continuing observations of And XVIII can facilitate the exploration of other potential mechanisms of gas loss, since additional data could reveal morphology changes, or trails of baryonic matter left in And XVIII's wake that could indicate the loss of gas due to external processes. Lastly, it could reveal that And XVIII is just a strange dSph that does not follow the photo-evaporation theory and needs to be studied as a special case.

7.4.6.2 Second Scenario: Gas Cloud in Line Of Sight

In the second scenario what we have detected is a cloud of hydrogen gas along the line of sight to And XVIII.

Golden (2022) ensured that there would be no Hα emissions from ionized gas in the Milky Way at the same wavelength as produced by any emitting gas associated with And XVIII. This rules out the possibility that what we are seeing are emissions of gas within the Milky Way.

The recombination timescales of gas suggest that there could neutral hydrogen gas located in the vicinity of And XVIII. Of course, we wouldn't be able to detect it, as HI emits at the wavelength $21\,\mathrm{cm}$. If the gas got photo-evaporated during the last event of star formation, it would be found in neutral form in the vicinity of And XVIII. However, no such gas has been detected around other dSphs (Grcevich & Putman, 2009). Additionally, Spekkens et al. (2014) found that the upper limit on the mass of HI gas within 0.3^o of And XVIII is $4.8 \times 10^6\ \mathrm{M}_\odot$. The upper limit computed by Spekkens et al. (2014) is smaller than the lower limit of the theoretically predicted mass of gas, and is found much closer to And XVIII than predicted by theory.

The question remains whether it is possible for the photo-evaporated gas to remain ionized due to being maintained by an independent source of ultravi-

olet photons. Given the short recombination timescale for the observed gas, there must be a source of ultraviolet photons that maintains the ionization of the gas. It cannot be ionized by And XVIII, as its last episode of star formation ended 1.5 Gyr ago, and all the O and B type stars have died by now.

Could M31 be the source of radiation that is responsible for maintaining the ionization of the photo-evaporated gas? Lets introduce a back-of-the-envelope calculation that can give us a ballpark estimate of M31's ionizing capabilities. The distance between And XVIII and M31 is $d_{M31,A18} = 579 \pm 87$ kpc $= (1.79 \pm 0.27) \times 10^{24}$ cm. At that distance, it is feasible to approximate that M31 is a point source of radiation, and that the gas around And XVIII is a rectangular slab. The slab has the dimensions of $x_{slab} = y_{slab} = 6.09^{+0.27}_{-0.41} \times 10^{22}$ cm and $z_{slab} = 2.49 \times 10^{23}$ cm. The back face of the slab is located at a distance $d_{M31,A18} + r_{out,cm} - z_{slab} = 1.59 \times 10^{24}$ cm It is possible to employ the "back-of-the-envelope" approach to calculating ionization in a slab of gas at ionization equilibrium yields the minimum photon flux that M31 must emit to ionize that slab of gas (Muzzin, Adam and Hall, Patrick B. and McCall, Marshall L. , 2020). The equation pertinent to this approach is:

$$\frac{Q(H^0)}{4\pi d^2_{M31,A18}} = \alpha_A(T) N^2 z_{slab} \tag{7.29}$$

where $Q(H^0)$ is the total luminosity by number of ionizing photons emitted by M31. This presumes M31 to be a point-source whose entire flux is used up in maintaining the ionization of the slab of gas. The flux of photons emitted by M31 needed to ionize the gas around And XVIII is then

$$\frac{Q(H^0)}{4\pi d^2_{M31,A18}} = 6.97 \times 10^7 \quad \text{photons}\,\text{cm}^{-2}\,\text{s}^{-1} \tag{7.30}$$

The energy of photons at the ionization limit for hydrogen is

$$E_i = 13.6 \text{ eV}) = 2.18 \times 10^{-11} \quad \text{erg} \tag{7.31}$$

The luminous energy emitted by M31 that is needed to ionize the gas around And XVIII is then

$$E_T = E_i \frac{Q(H^0)}{4\pi d^2_{M31,A18}} = 1.52 \times 10^{-3} \quad \text{erg}\,\text{cm}^{-2}\,\text{s}^{-1} \tag{7.32}$$

The logarithmic FUV and NUV luminosities of M31 retrieved from Gil de Paz et al. (2009) are

$$\log(L_{FUV}) = 35.38 \quad \text{W}; \qquad \log(\text{L}_{\text{NUV}}) = 35.54 \quad \text{W} \tag{7.33}$$

The FUV and NUV bands of GALEX only cover the wavelength ranges $124.7 \leq \lambda_{FUV}\,(\text{nm}) \leq 178.8$ and $165.1 \leq \lambda_{NUV}\,(\text{nm}) \leq 228.3$ respectively, which are redder than the wavelength pertinent to ionizing radiation $\lambda_{H^0} = 91.2$ nm. However, FUV and NUV luminosities provide an upper limit to the luminosity of ionizing radiation escaping M31. Most of the ionizing photons emitted by O and B type stars inside of M31 remain within the galaxy, as they are used in ionizing the gas in M31. Converting from logarithmic luminosity yields

$$L_{FUV} = 2.40 \times 10^{42} \quad \text{erg}\,\text{s}^{-1}; \qquad \text{L}_{\text{NUV}} = 3.47 \times 10^{42} \quad \text{erg}\,\text{s}^{-1} \tag{7.34}$$

An upper limit to the total UV luminosity of M31 is then

$$L_{UV} = L_{FUV} + L_{NUV} = 5.87 \times 10^{42} \quad \text{erg}\,\text{s}^{-1} \tag{7.35}$$

Accommodating for the effect of geometrical dilution at the distance to the slab of gas yields:

$$L_{UV,And18} = \frac{L_{UV}}{4\pi d^2_{M31,A18}} = 1.83 \times 10^{-7} \quad \mathrm{erg\,cm^{-2}\,s^{-1}} \tag{7.36}$$

This back-of-the-envelope approach indicates that the UV flux of M31 ifalls at least 4 orders of magnitude short of being able to ionize the gas around And XVIII.

7.4.6.3 Third Scenario: Instrumental Artifacts

In the third scenario, there is no gas around And XVIII, and what we think we are detecting is, in fact, an artifact of instrumentation or image processing. To convince ourselves that we are not calculating the flux of an artifact, the background signals of M27 and M33 were binned after masking out M27 itself and HII regions in M33. The choice of binning was influenced by the differences between the total exposure times of M33, M27 and And XVIII. And XVIII was imaged in Hα for eight hours; M33 was imaged in Hα for one hour and fifty-six minutes; M27 was imaged in Hα for three hours and forty-eight minutes.

To match the background signal for M33 to that which would be obtained over eight hours, the star-free continuum-subtracted image of M33 was binned 4×4. Similarly, the background signal of the star-free continuum-subtracted image of M27 was binned 2×2. The resultant images can be seen in Figures 7.27 and 7.28. These images reveal that there is no pattern that resembles the nebulosity around And XVIII. The colormap of a starless, continuum-subtracted image of And XVIII can be seen in Figure 7.29. The colour bar to the right of the figures displays the signal levels in the images.

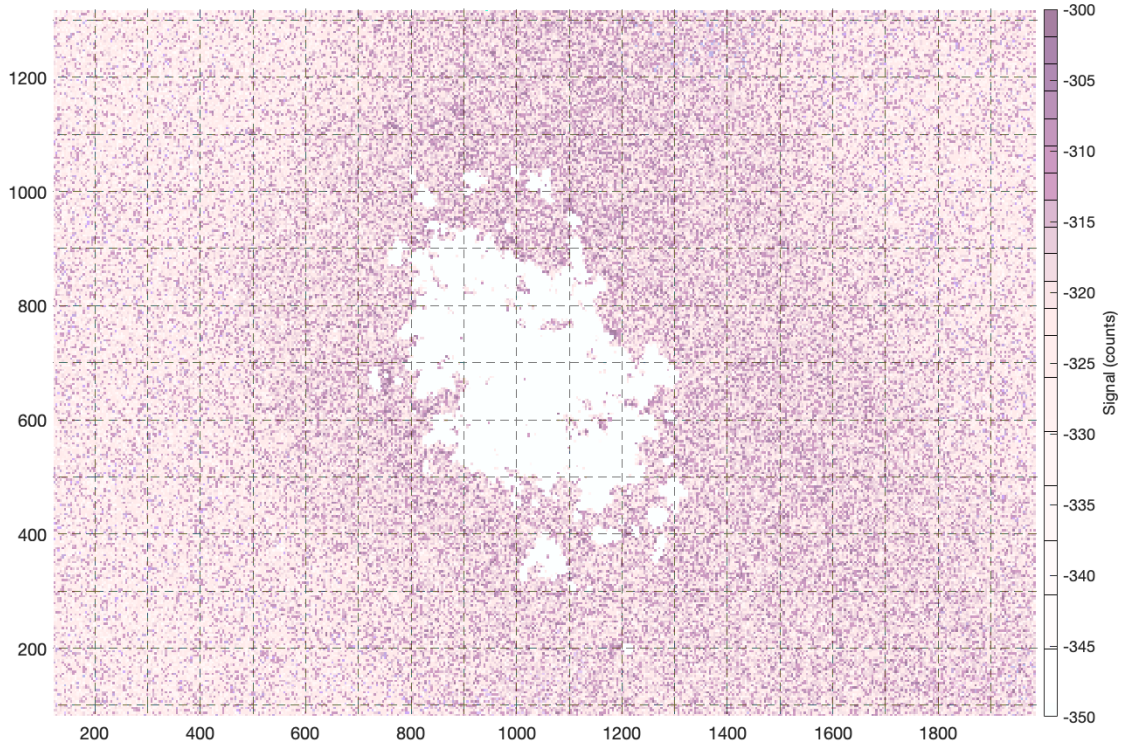

Figure 7.27: Colour-inverted, starless and continuum subtracted image of background of M33 in the Hα filter, binned 4×4.

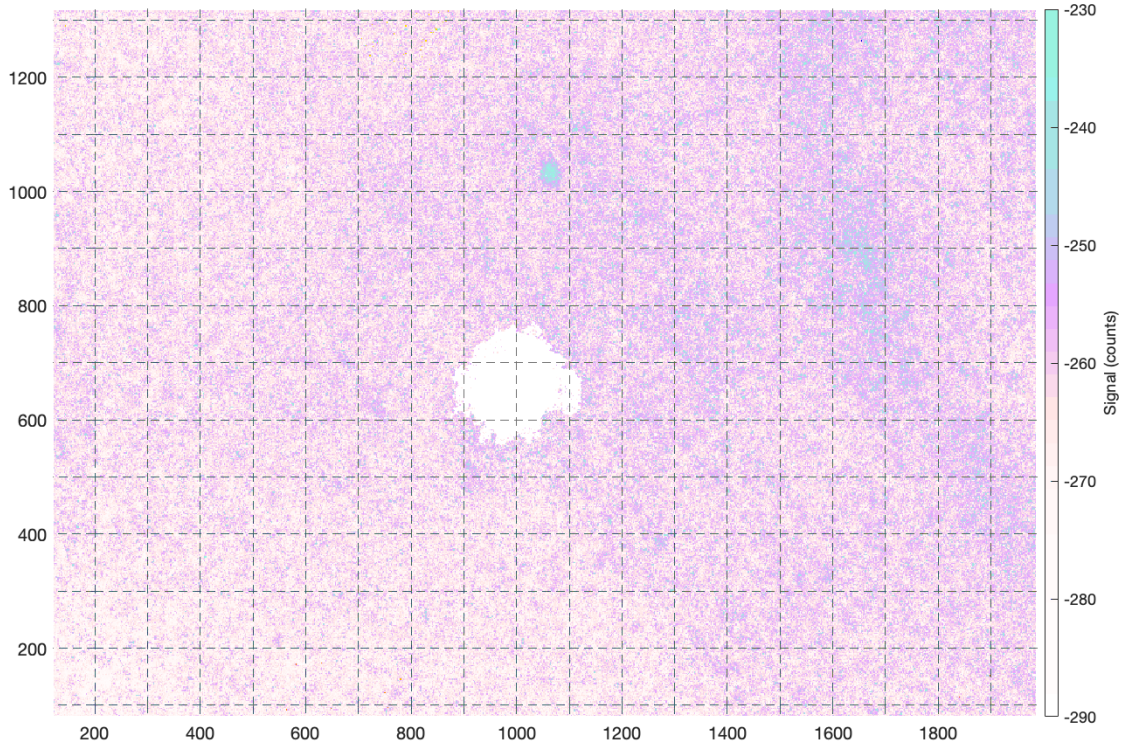

Figure 7.28: Colour-inverted, starless and continuum subtracted image of background of M27 in the Hα filter, binned 2×2.

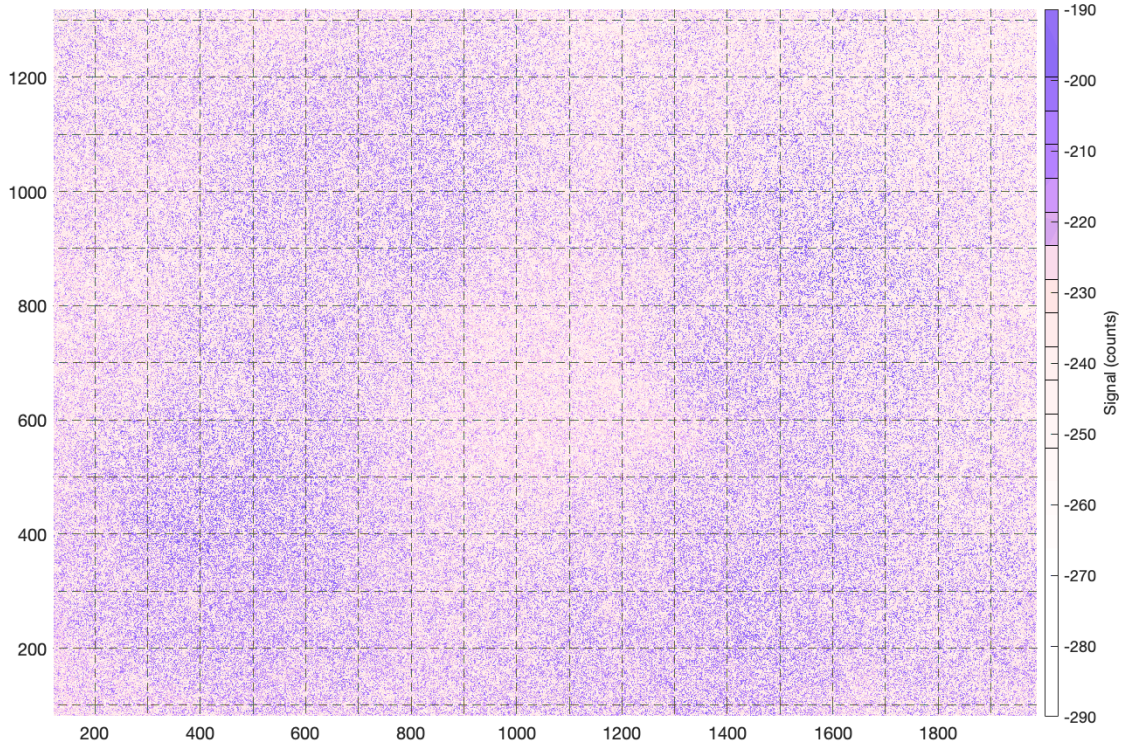

Figure 7.29: Colour-inverted, starless and continuum subtracted image of And XVIII in Hα filter

The brightest features in the binned backgrounds of M33 and M27 measure at $N_{M33} = -313.95$ counts, and $N_{M27} = -259.96$ counts respectively. Meanwhile, the signal from the four regions from a starless image of And XVIII is $N_{A18} = -232.37$ counts. The sky background measure at $N_{M33,sky} = -324.02$ counts, $N_{M27,sky} = -267.27$ counts, and $N_{A18,sky} = -240.03$ counts for M33, M27 and And XVIII respectively. The standard deviations of the sky background measure at $\sigma_{M33} = 7.32$ counts, $\sigma_{M27} = 6.32$ counts, and $\sigma_{A18} = 14.86$ counts for M33, M27 and And XVIII respectively. The features in M33 and M27 stand as high as $1.38\sigma_{M33}$ and $1.15\sigma_{M33}$ standard deviations above the sky background respectively. The features, enclosed by the four measurement regions on images of And XVIII stand $1.64\sigma_{A18}$ standard deviations above the background of its sky.

However, if the features found in images of M33 and M27 are caused by artifacts of data processing, they will not be visible on images of And XVIII. To become visible the features in these images need to be higher than the stan-

dard deviation of the sky of And XVIII. Because σ_{A18} is higher than σ_{M33} and σ_{M27}, the features in images of M33 and M27 will only be as high as $0.68\sigma_{A18}$ and $0.49\sigma_{A18}$, so they wouldn't be visible on the image of And XVIII.

Chapter 8
Conclusions

The purpose of this thesis was to determine whether ultra-low surface brightness extended emission-line objects can be observed using the Quick Array of Isolated Lenses (QUAIL) from skies typical of contemporary population centres, such as at York University in Toronto. The premise was to be tested by attempting to locate transition zones of nebulae and detect the possible gas missing from the dwarf spheroidal galaxy And XVIII. We successfully observed nebulae of the Triangulum Galaxy M33, and the transition zones of the Dumbbell Nebula M27 and the PacMan Nebula NGC 281.

A comparison of images of M33 acquired with the Burrell Schmidt telescope at Kitt Peak National Observatory revealed QUAIL was just as efficient at collecting line emission from extended courses during Fall 2021, when the data was collected. However, it also revealed that the data collected at York University Allan I. Carswell Astronomical Observatory is compromised by the sky that is 70 times brighter than a dark site, such as Kitt Peak.

Unfortunately, the attempt to locate the putative missing gas of the dwarf galaxy And XVIII was inconclusive.

On the one hand, there appears to be some gas that emits Hα around And XVIII, as it is visible before star removal. However, the discrepancies between the observed and the predicted properties of the gas suggest that what we detected is not the photo-evaporated gas from And XVIII. The mass of observed gas is higher than predicted by theory, with the lower limit of the observed gas mass being within the upper limit of the predicted gas mass. The size of the observed nebulosity is much smaller than predicted by theory. Most importantly, the density of the detected gas suggests that if the photoionization occurred around the time of the last episode of star formation, this gas should

have already become neutral. Additionally, it does not appear that the ionization of the gas can be maintained by ultraviolet radiation escaping from M31. Although it is possible that the nebulosity is an artifact of image processing, no similar features were found in images of other targets that would substantiate this possibility.

Observations were plagued by bad weather (which drastically limited the observation time), hardware failings, and limitations in the data reduction process. There is a reason to believe that future users of QUAIL will be able to obtain better data, because the CCD cameras have been refurbished and the failings of the $60\,\mathrm{cm}$ telescope and its domes have now been fixed. The pandemic and the complications that it brought are now over, too. Observational data can be greatly improved by simply increasing the observation time.

In conclusion, I deem this project to be successful, as an apparatus that is capable of observing ultra-low surface brightness emission-line sources from a bright site has been successfully developed, implemented and tested.

Bibliography

Abraham, R. G. & van Dokkum, P. G. 2014, 126, 55

Anna Skrinnik. 2024, Quail_Software, urlhttps://github.com/QuailObserver/QUAIL_-Software, accessed: 2024-01-08

Apple Inc. 2024, Apple Inc.: Identify your Mac mini model, urlhttps://support.apple.com/en-ca/102852, accessed: 2023-08-08

Bender, R., Burstein, D., & Faber, S. M. 1992, 399, 462

Benn, C. R. & Ellison, S. L. 1998, 42, 503

Blitz, L. & Robishaw, T. 2000, The Astrophysical Journal, 541, 675

Buta, R. & McCall, M. L. 1999, APJ, 124, 33

Carrasco, E., Mollá, M., García-Vargas, M. L., Gil de Paz, A., Cardiel, N., Gómez-Alvarez, P., & Berlanas, S. R. 2020, Monthly Notices of the Royal Astronomical Society, 501, 3568

Cedrés, B., Beckman, J. E., Bongiovanni, Á., Cepa, J., Asensio Ramos, A., Giammanco, C., Cabrera-Lavers, A., & Alfaro, E. J. 2013, 765, L24

Cheeku Technologies. 2024, Fedus: FEDUS USB Extension Cable, urlhttps://www.fedus.in/products/usb-extension-cable-for-pc, accessed: 2023-08-08

Dekel, A. & Silk, J. 1986, APJ, 303, 39

Diffraction Limited. 2024a, Diffraction Limited: SBIG Aluma 3200, urlhttps://diffractionlimited.com/product/aluma-3200/, accessed: 2023-08-08

—. 2024b, SBIG Cameras, urlhttps://diffractionlimited.com/diffraction-cameras/, accessed: 2024-13-05

Djorgovski, S. & Davis, M. 1987, APJ, 313, 59

Eaton. 2024, EATON: Tripp-Lite by EATON, urlhttps://assets.tripplite.com/product-pdfs/en/u360004slim.pdf, accessed: 2023-08-08

Ferrara, A. & Tolstoy, E. 2000, MNRAS, 313, 291

Future Technology Devices International Limited. 2024, FTDI Chip: UC232R-10N, urlhttps://ftdichip.com/products/uc232r-10/, accessed: 2023-08-08

Gil de Paz, A., Boissier, S., Madore, B. F., Seibert, M., Joe, Y. H., Boselli, A., Wyder, T. K., Thilker, D., Bianchi, L., Rey, S. C., Rich, R. M., Barlow, T. A., Conrow, T., Forster, K., Friedman, P. G., Martin, D. C., Morrissey, P., Neff, S. G., Schiminovich, D., Small, T., Donas, J., Heckman, T. M., Lee, Y. W., Milliard, B., Szalay, A. S., & Yi, S. 2009, VizieR Online Data Catalog: GALEX ultraviolet atlas of nearby galaxies (Gil de Paz+, 2007), VizieR On-line Data Catalog: J/ApJS/173/185. Originally published in: 2007ApJS..173..185G

Gnedin, N. Y. & Kravtsov, A. V. 2006, APJ, 645, 1054

Golden, K. 2022, Foundations of the Quad Array of Isolating Lenses (QuAIL) Project

Grcevich, J. & Putman, M. E. 2009, APJ, 696, 385

Hodge, P. W., Balsley, J., Wyder, T. K., & Skelton, B. P. 1999, VizieR Online Data Catalog, J/PASP/111/685

Hoopes, C. G. & Walterbos, R. A. M. 2000, 541, 597

Ivkovich, N. & McCall, M. L. 2019, Monthly Notices of the Royal Astronomical Society, 486, 1964

Karachentsev, I. D. & Kaisina, E. I. 2013, AJ, 146, 46

Karachentsev, I. D., Makarov, D. I., & Kaisina, E. I. 2013, AJ, 145, 101

Kormendy, J. 2014, Springer International Publishing, "Lessons from the Local Group:A Conference in honor of David Block and Bruce Elmegreen", 323

Learn the Sky LLC. 2022, The Blog: HR Diagram Explained, urlhttps://www.learnthesky.com/blog/HR-Diagram, accessed: 2023-08-08

Lee, J. H. & Lee, M. G. 2014, APJ, 793, 134

Lin, D. N. C. & Faber, S. M. 1983, apj, 266, L21

Lux, H., Read, J. I., & Lake, G. 2010, mnras, 406, 2312

Makarova, L. N., Makarov, D. I., Karachentsev, I. D., Tully, R. B., & Rizzi, L. 2017, MNRAS, 464, 2281

Massey, P., Strobel, K., Barnes, J. V., & Anderson, E. 1988, APJ, 328, 315

McCall, Vaduvescu, O., Pozo Nunez, F., Barr Dominguez, A., Fingerhut, R., Unda-Sanzana, E., Li, B., & Albrecht, M. 2012, A&A, 540, A49

McCall, M. L. 2004, 128, 2144

McGaugh, S. S., Schombert, J. M., Bothun, G. D., & de Blok, W. J. G. 2000, APJL, 533, L99

Mundy. 2018, Calculating the Atmospheric Extinction Coefficients of the Allan I. Carswell Observatory

Muzzin, Adam and Hall, Patrick B. and McCall, Marshall L. . 2020, PHYS 4070/5090 Stars and Nebulae (York University)

Osterbrock, Donald E. 1989, Astrophysics of Gaseous Nebulae and Active Galactic Nuclei (University Science Books)

Relaño, M. & Kennicutt, Robert C., J. 2009, APJ, 699, 1125

Ricotti, M. & Gnedin, N. Y. 2005, APJ, 629, 259

Roberto Abraham. 2012, Birger_Software, urlhttps://github.com/robertoabraham/ProjectDragonfly, accessed: 2024-01-08

Semiconductor Components Industries, LLC. 2018, Datasheet, Semiconductor Components Industries, LLC, Vienna, Austria

SensorPush. 2024, SensorPush: HTP.xw Extreme Accuracy Water-Resistant Temperature / Humidity / Barometric Pressure Smart Sensor, urlhttps://www.sensorpush.com/products/p/htp-xw, accessed: 2023-08-08

Sohn, S. T., Besla, G., van der Marel, R. P., Boylan-Kolchin, M., Majewski, S. R., & Bullock, J. S. 2013, apj, 768, 139

Spekkens, K., Urbancic, N., Mason, B. S., Willman, B., & Aguirre, J. E. 2014, 795, L5

Swinburne University of Technology. 2022, Dwarf Galaxy, urlhttps://astronomy.swin.edu.au/cosmos/D/dwarf+galaxy, accessed: 2023-14-08

The Digital Picture. 2024, The Digital Picture: Canon EF 400mm f/2.8L IS II USM Lens Review, urlhttps://www.the-digital-picture.com/Reviews/Canon-EF-400mm-f-2.8-L-IS-II-USM-Lens-Review.aspx, accessed: 2023-08-08

Tollerud, E. J., Beaton, R. L., Geha, M. C., Bullock, J. S., Guhathakurta, P., Kalirai, J. S., Majewski, S. R., Kirby, E. N., Gilbert, K. M., Yniguez, B., Patterson, R. J., Ostheimer, J. C., Cooke, J., Dorman, C. E., Choudhury, A., & Cooper, M. C. 2012, APJ, 752, 45

Tully, R. B. & Fisher, J. R. 1977, 54, 661

Tyson, N. D. & Gal, R. R. 1993, AJ, 105, 1206

Vaduvescu, O. & McCall, M. L. 2006, AJ, 131, 1318

Vaduvescu, O., McCall, M. L., Richer, M. G., & Fingerhut, R. L. 2005, The American Astronomical Society, 130, 1593

van den Bergh, S. 1994, apj, 428, 617

Wikipedia contributors. 2023, USB, urlhttps://en.wikipedia.org/wiki/USB, accessed: 2023-14-08

—. 2024, Thunderbolt (interface), urlhttps://en.wikipedia.org/wiki/Thunderbolt_-(interface), accessed: 2023-06-05

Wildcard Innovations. 2019, Argo Navis Digital Telescope Computer, urlhttps://wildcard-innovations.com.au/product//argo_describe.html, accessed: 2024-12-07

Zaritsky, D., Gonzalez, A. H., & Zabludoff, A. I. 2006, The American Astronomical Society, 638, 725

Appendix A
Full-Sized Images

A.1 Standard Star HD 217086

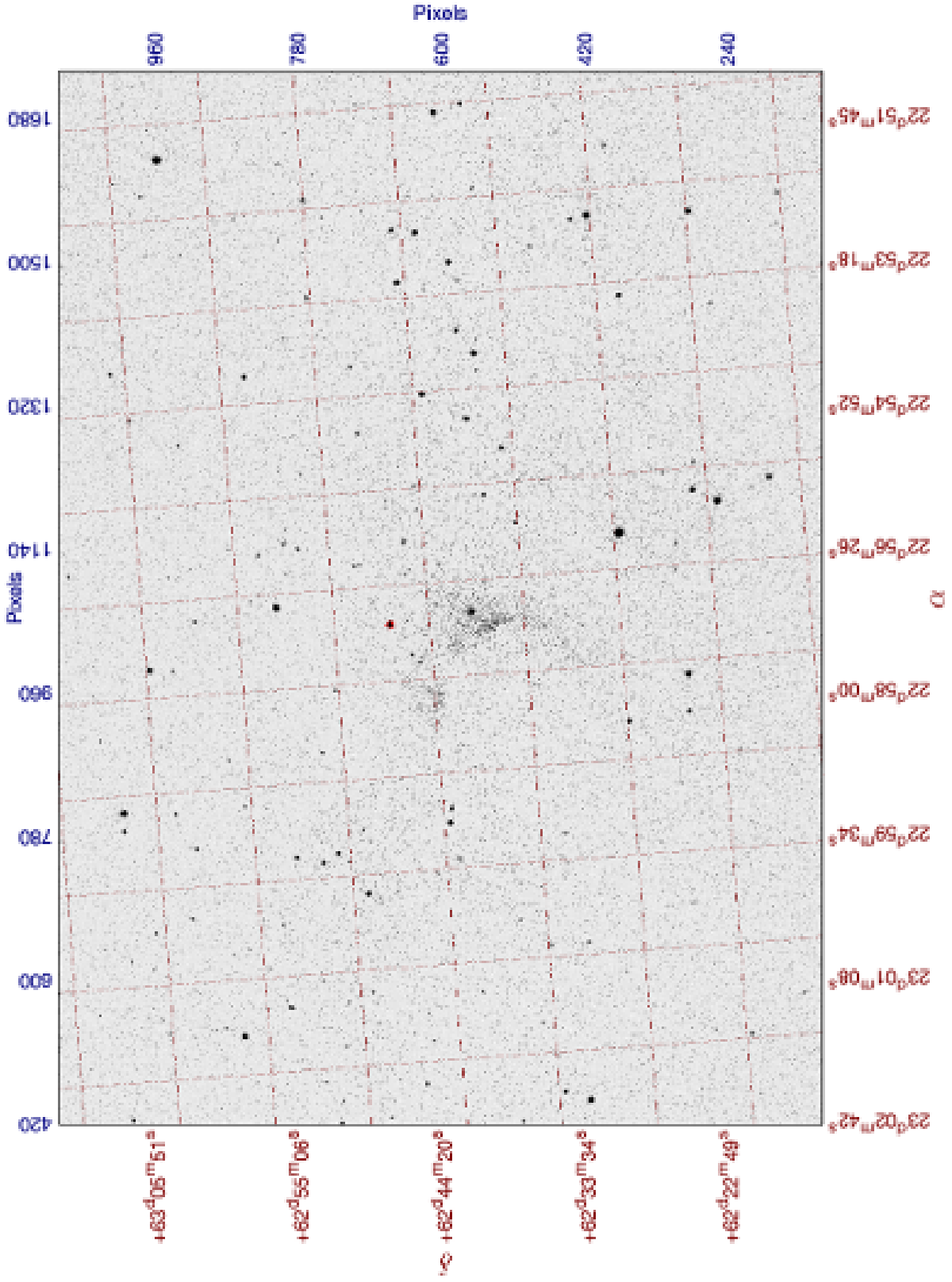

Figure A.1: Full-size Image of HD 217086 in Hα.

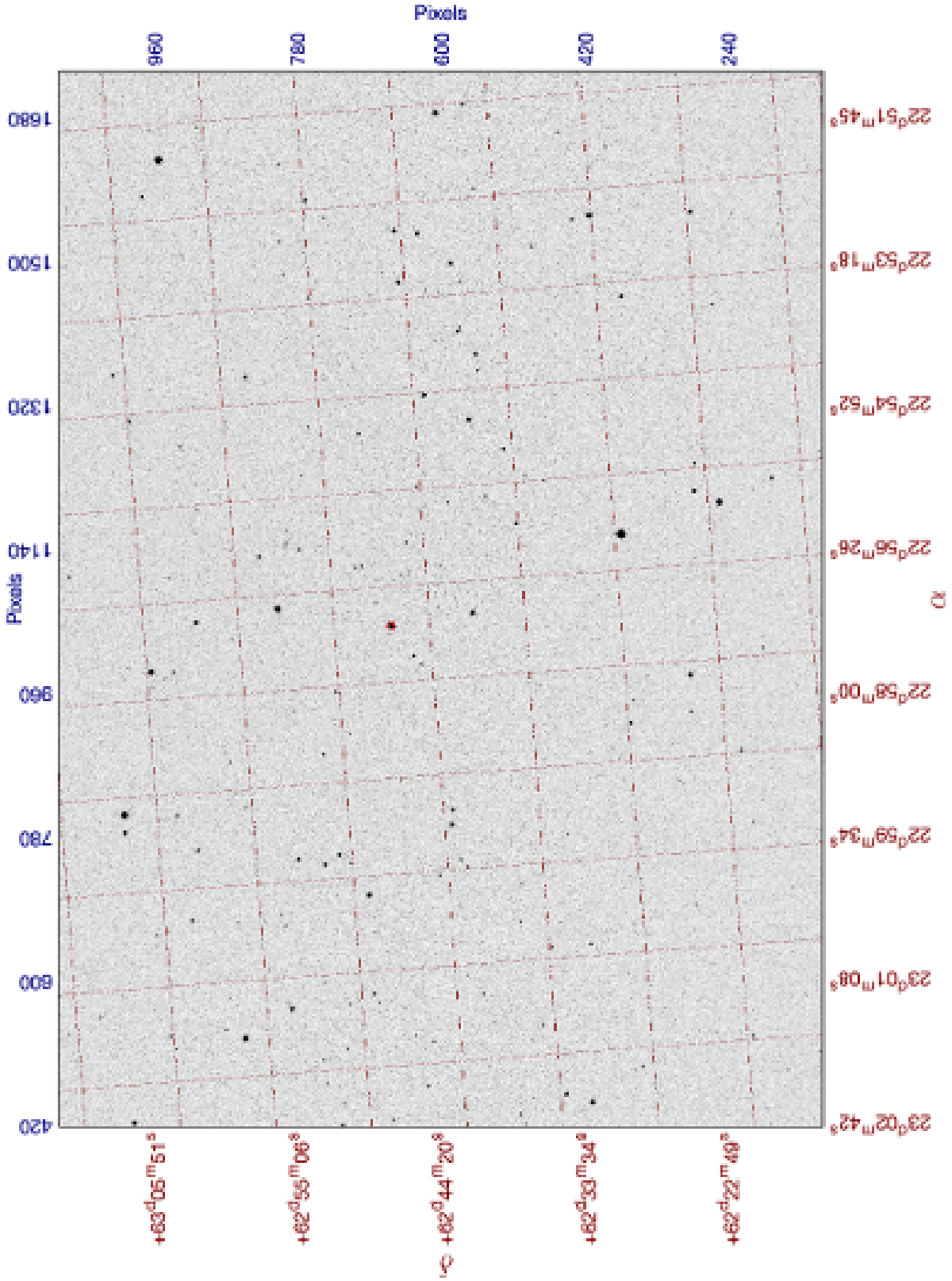

Figure A.2: Full-size Image of HD 217086 in [OI].

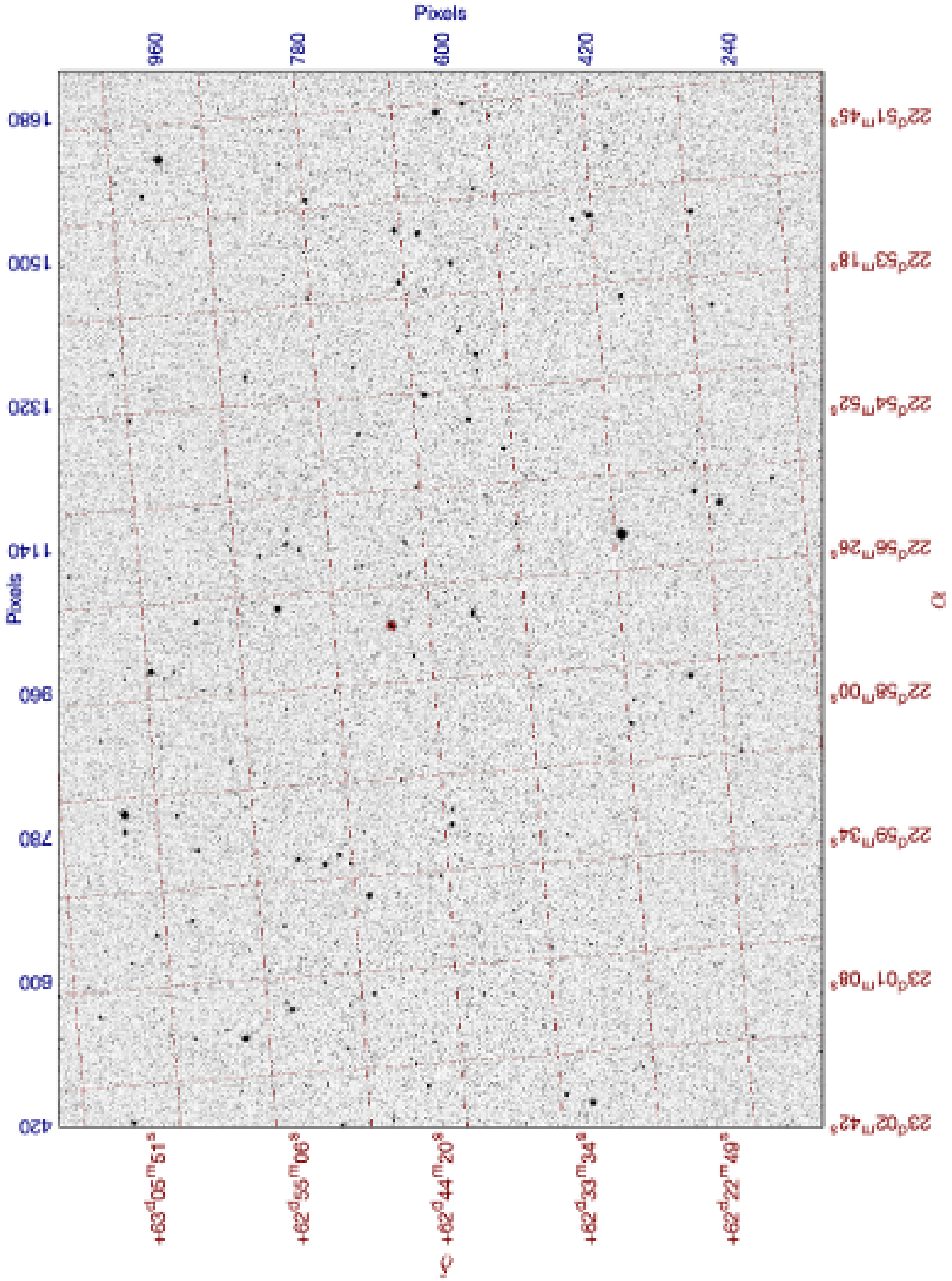

Figure A.3: Full-size Image of HD 217086 in Continuum.

A.2 M33 - Triangulum Galaxy

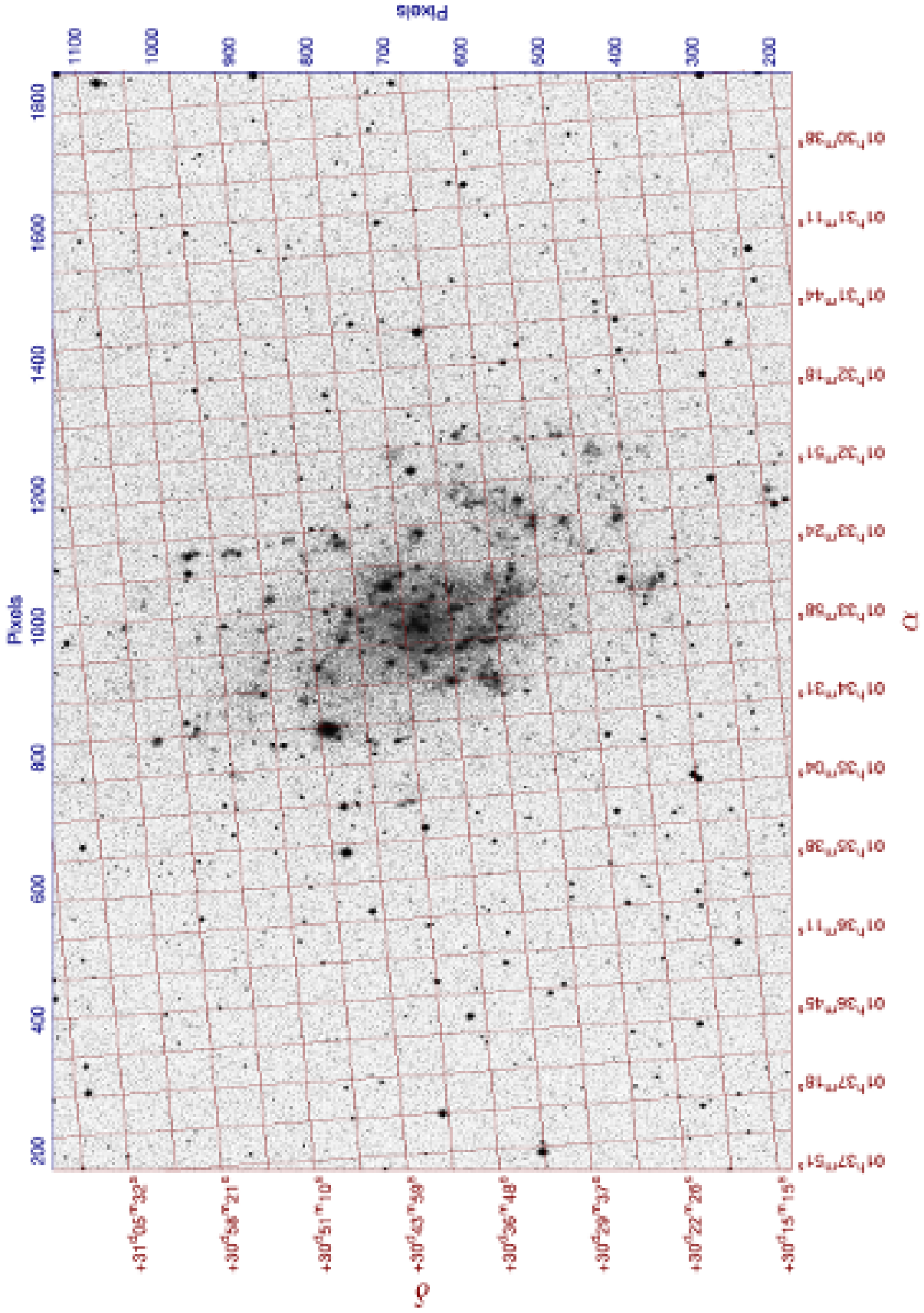

Figure A.4: Full-size image of M33 in Hα.

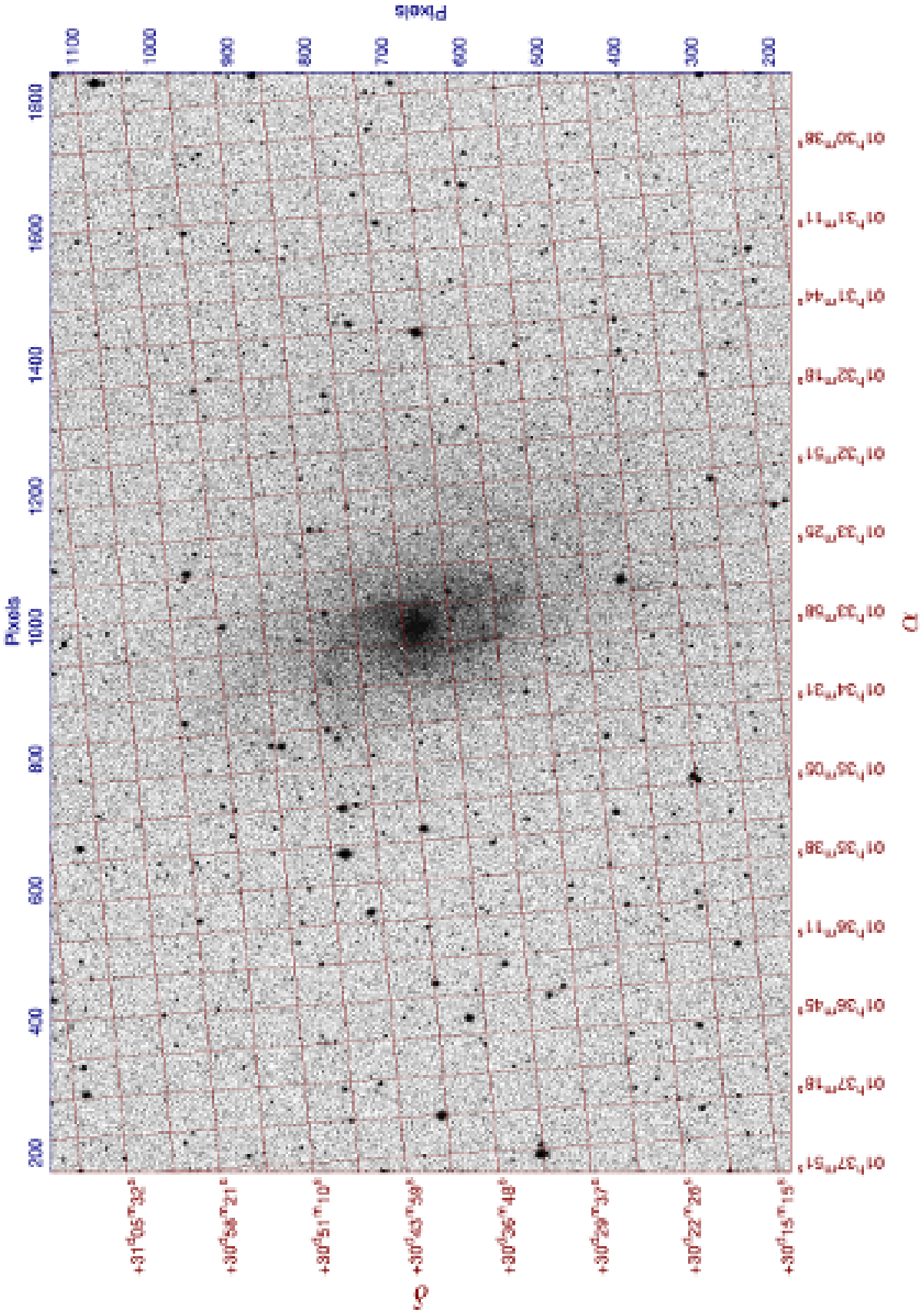

Figure A.5: Full-size image of M33 in Continuum.

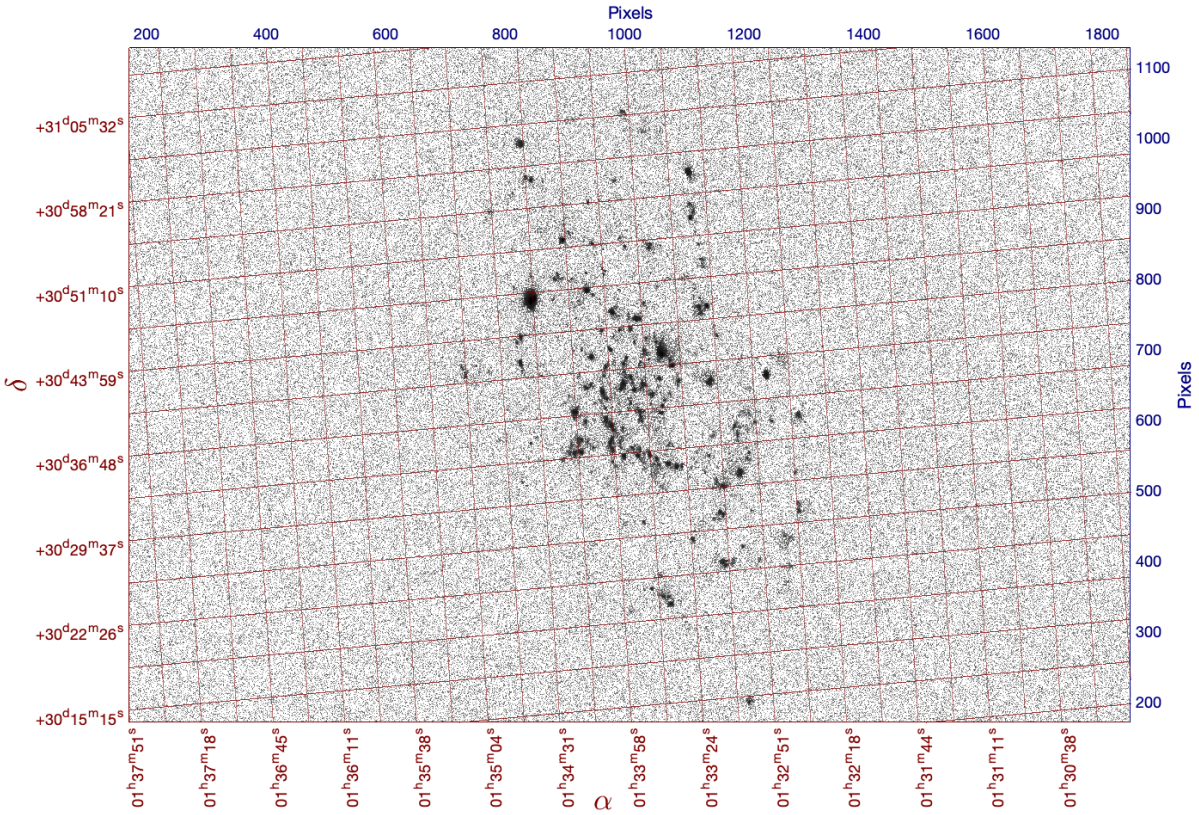

Figure A.6: Full-size starless and continuum-subtracted image of M33 in Hα.

A.3 M27 - The Dumbbell Nebula

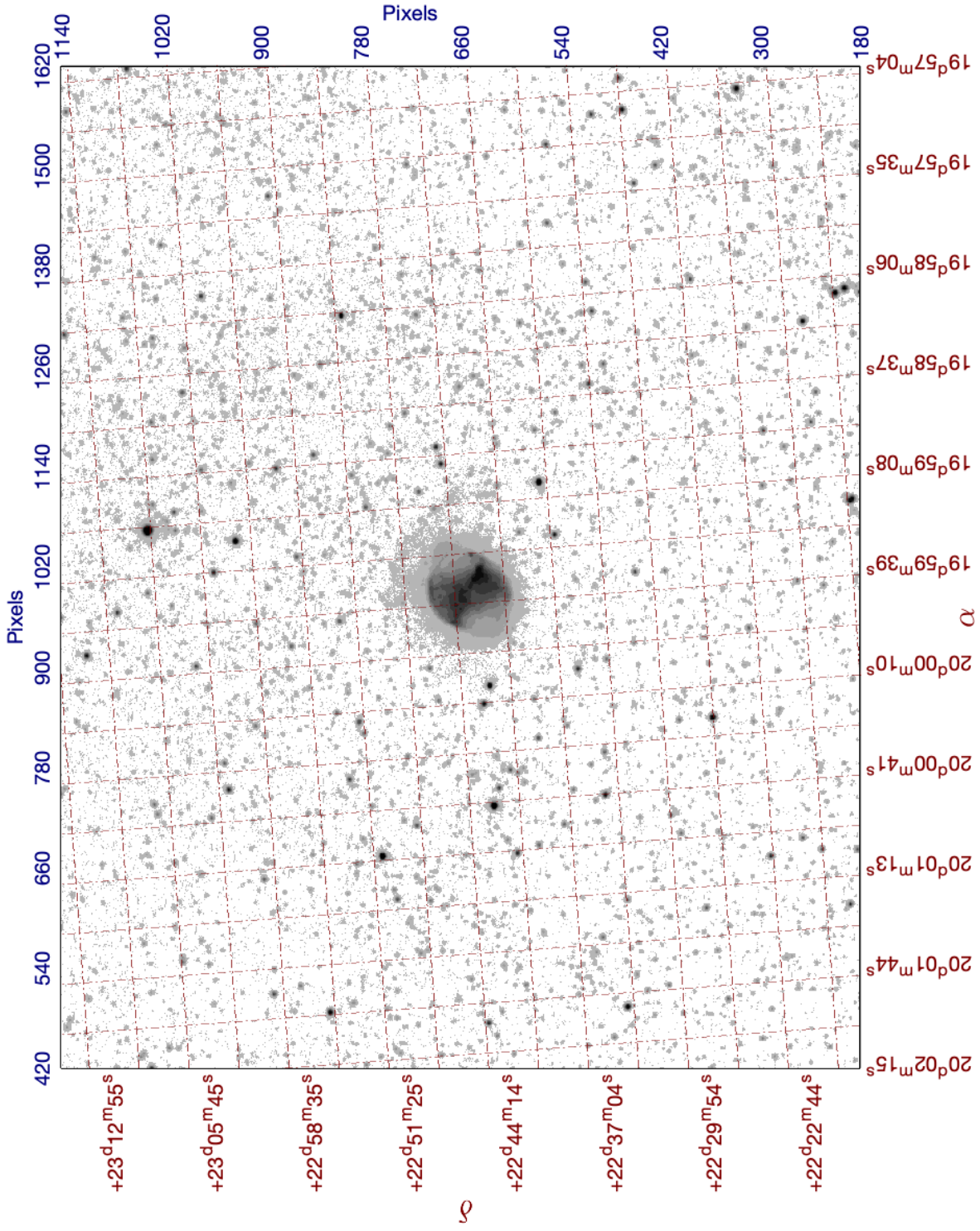

Figure A.7: Full-size image of The Dumbbell Nebula in Hα.

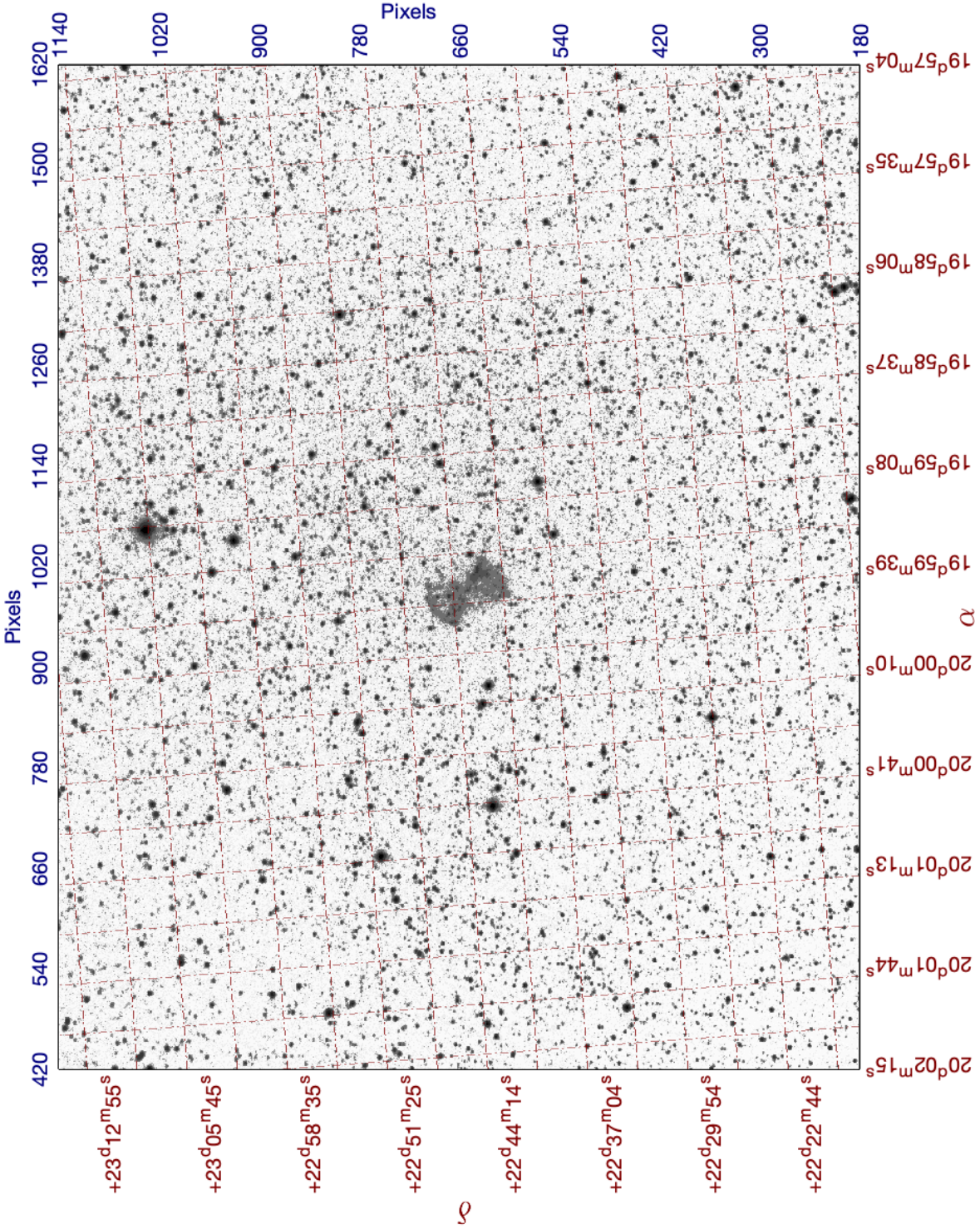

Figure A.8: Full-size Image of The Dumbbell Nebula in [OI].

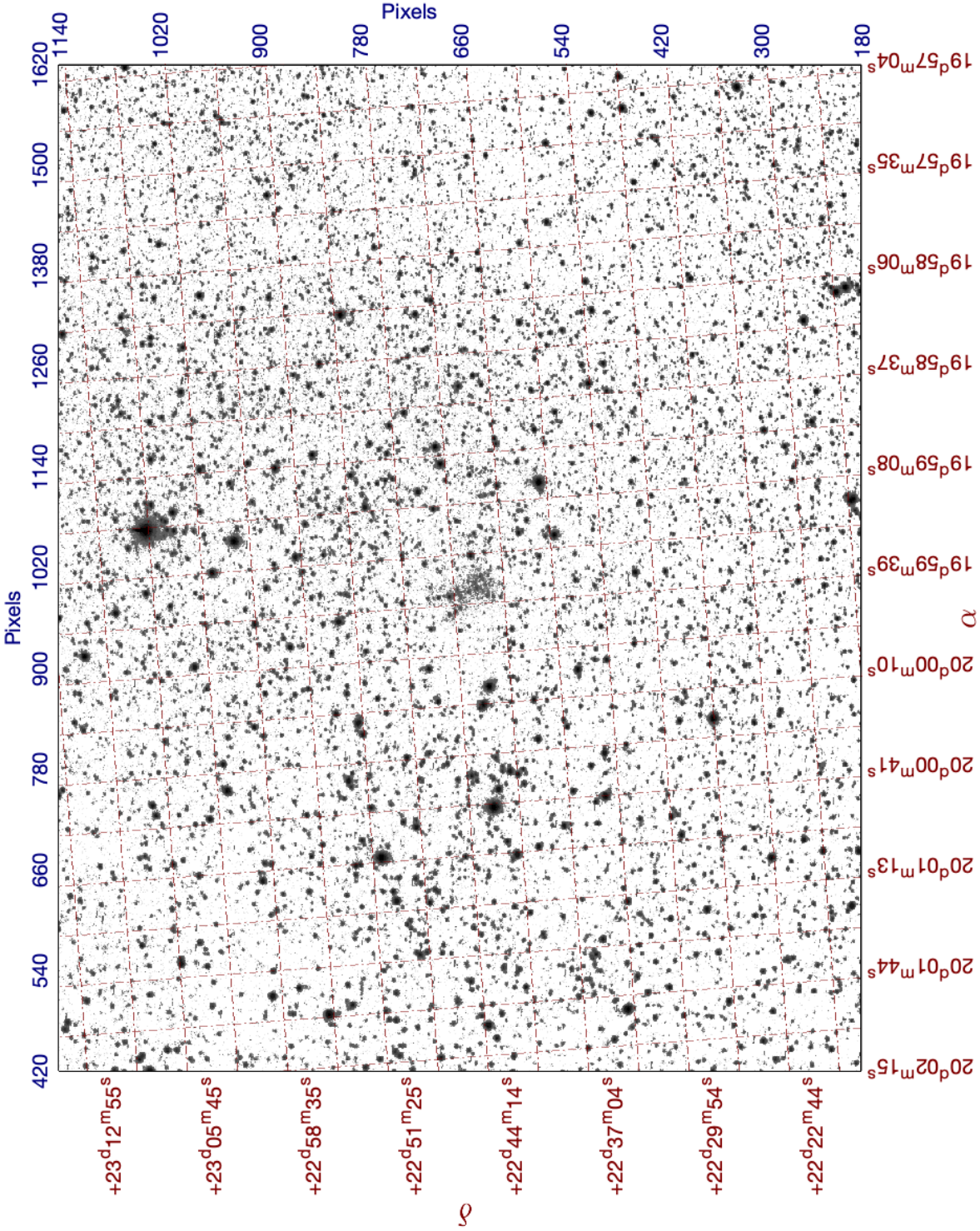

Figure A.9: Full-size Image of The Dumbbell Nebula in Continuum.

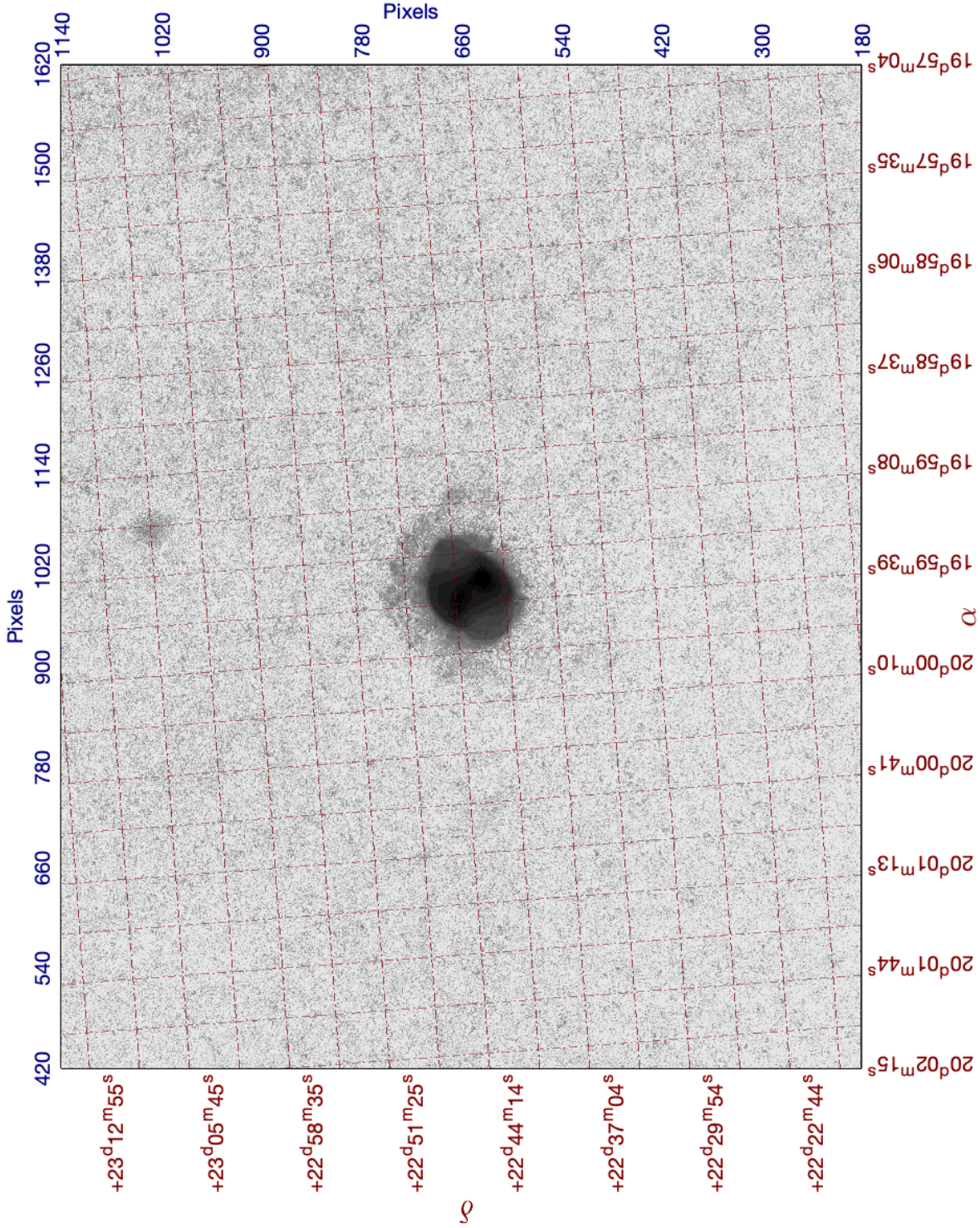

Figure A.10: Full-size starless image of The Dumbbell Nebula in Hα.

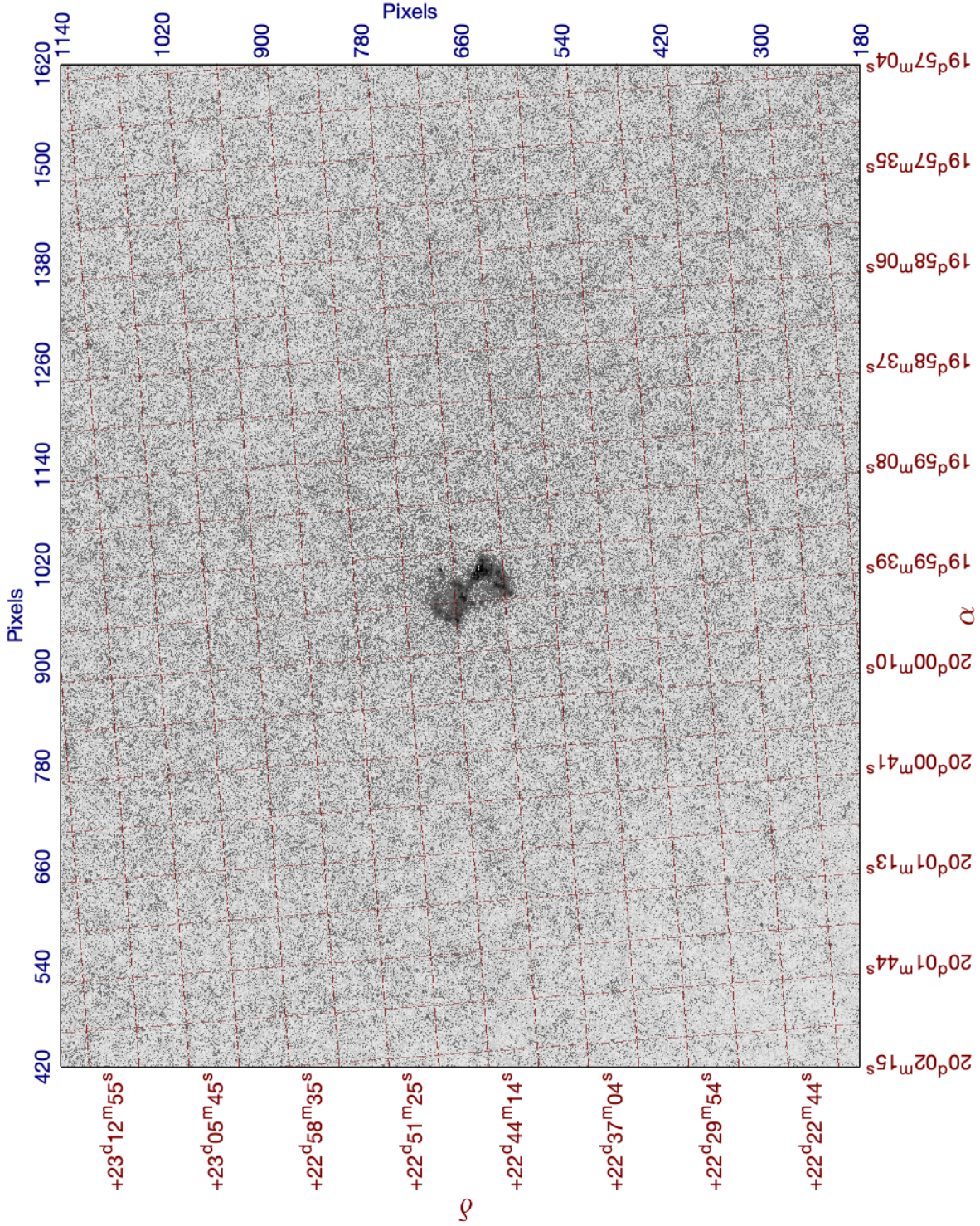

Figure A.11: Full-size starless image of The Dumbbell Nebula in [OI].

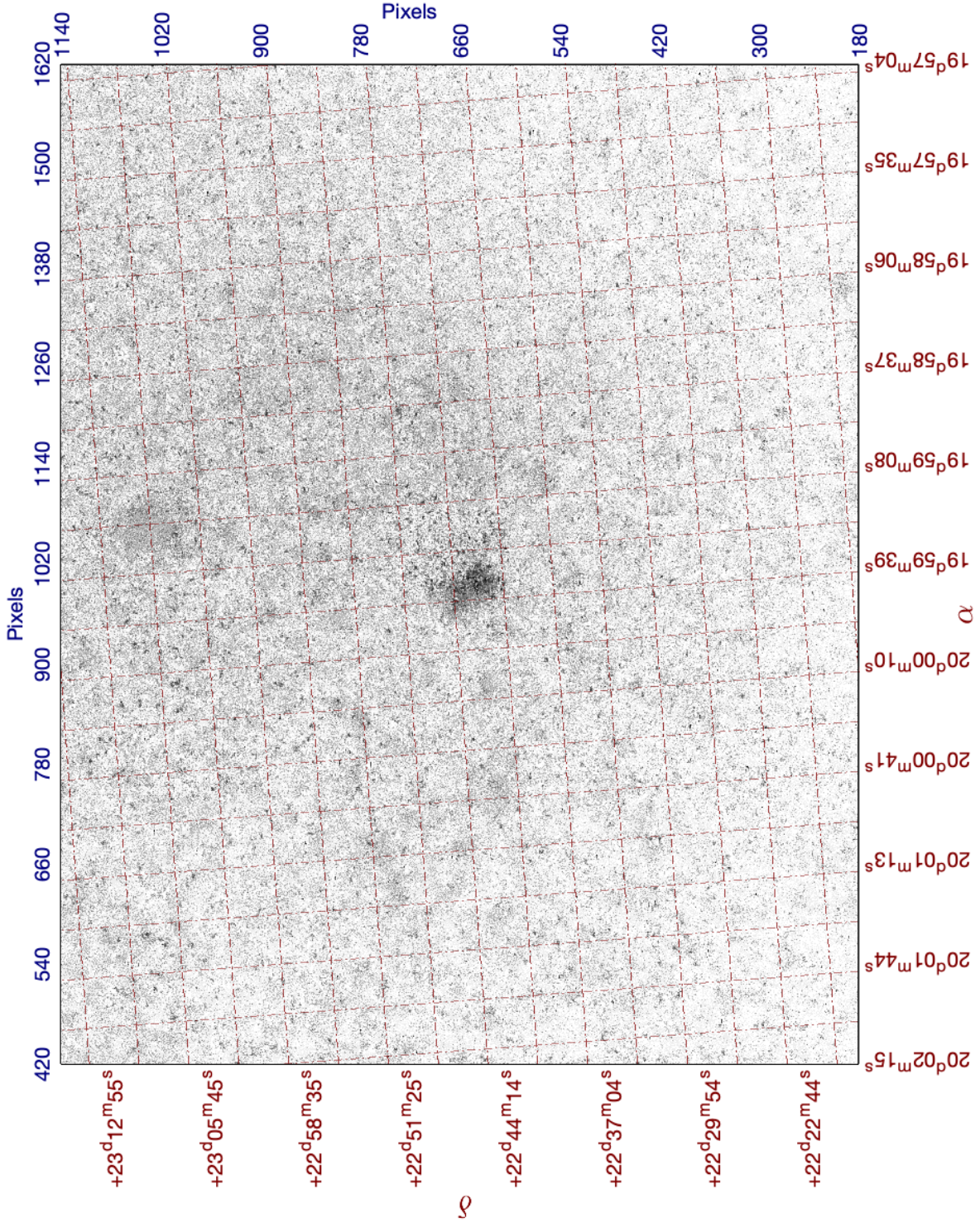

Figure A.12: Full-size starless image of The Dumbbell Nebula in Continuum.

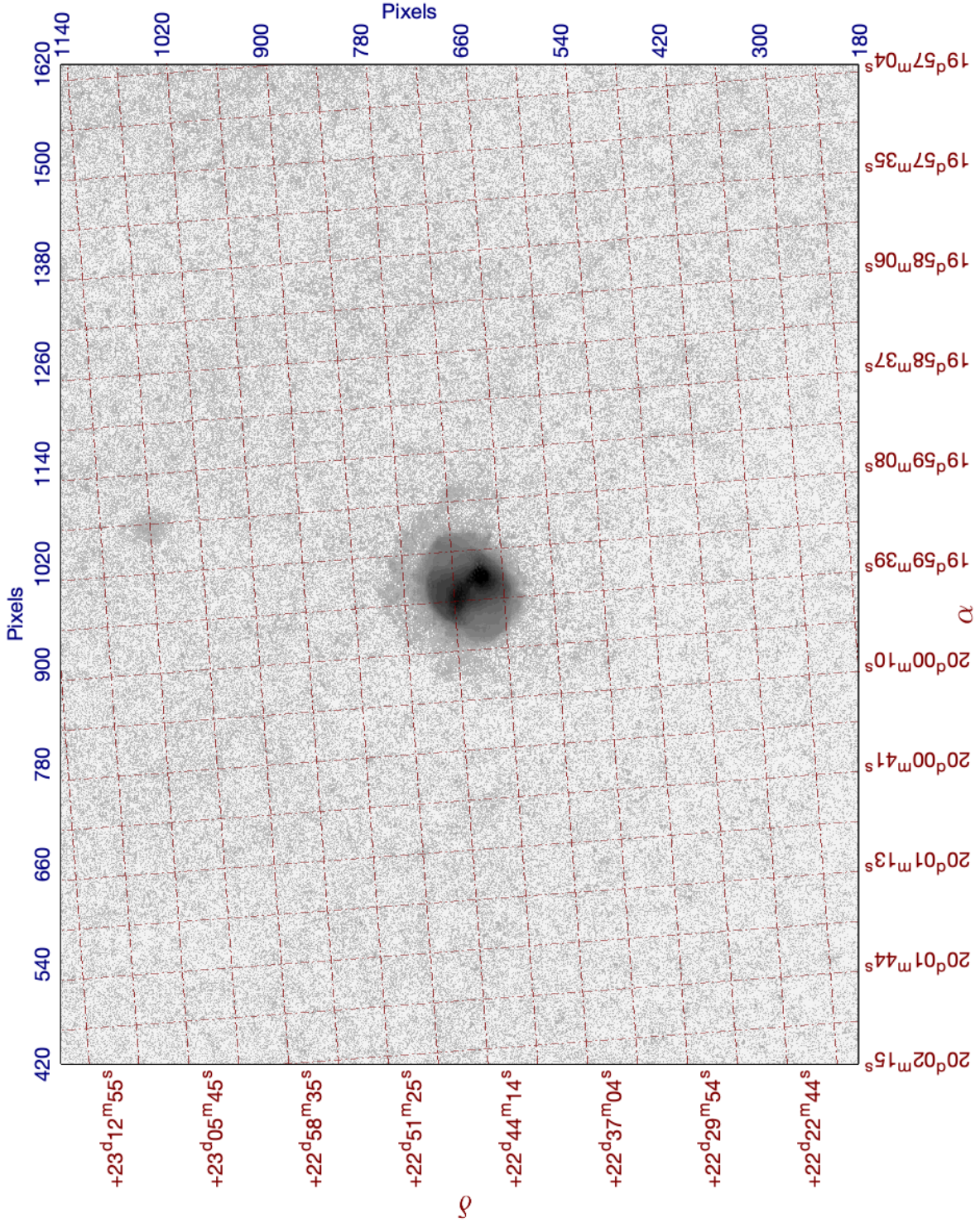

Figure A.13: Full-size starless and continuum-subtracted image of The Dumbbell Nebula in Hα.

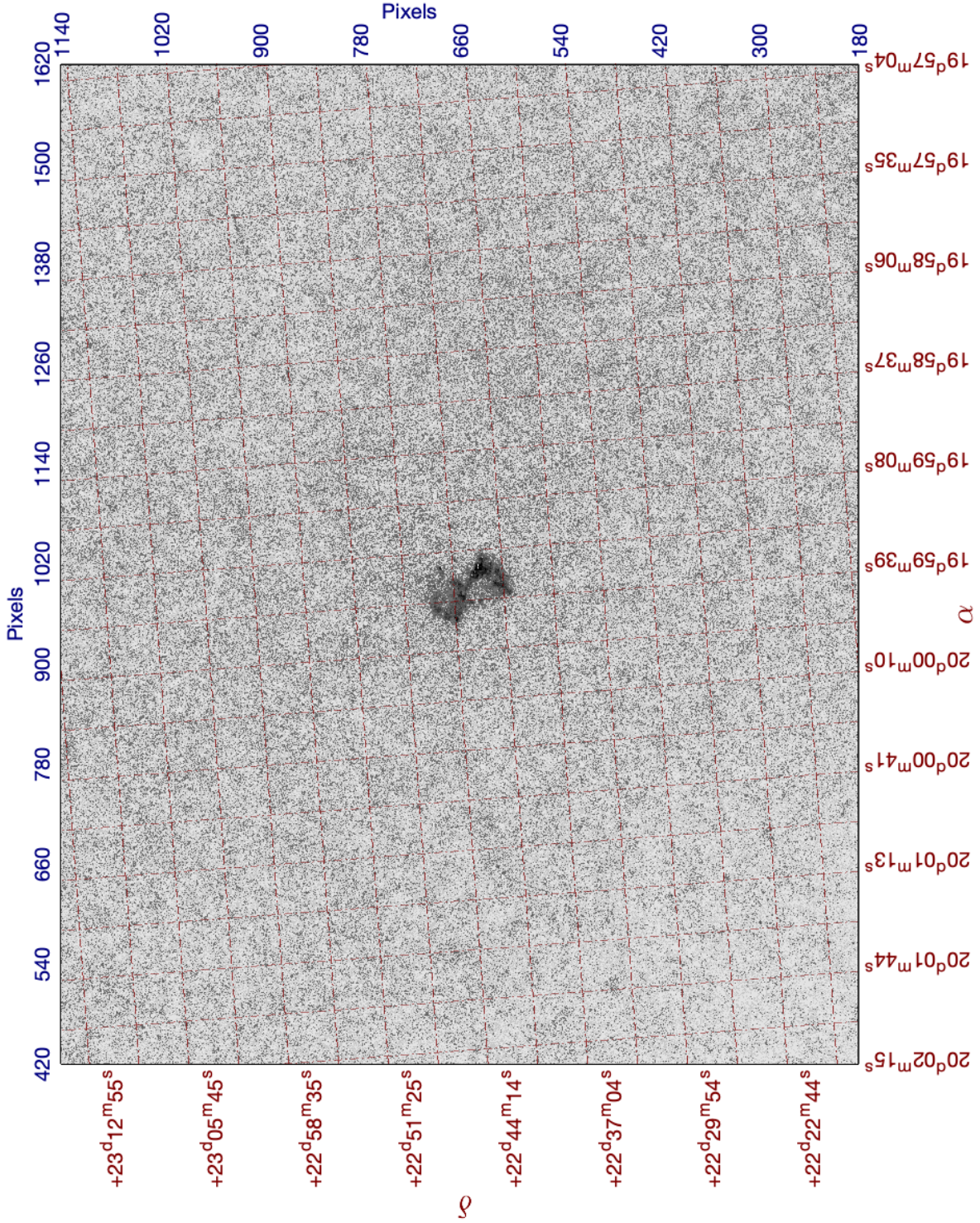

Figure A.14: Full-size starless and continuum-subtracted image of The Dumbbell Nebula in [OI].

A.4 The PacMan Nebula

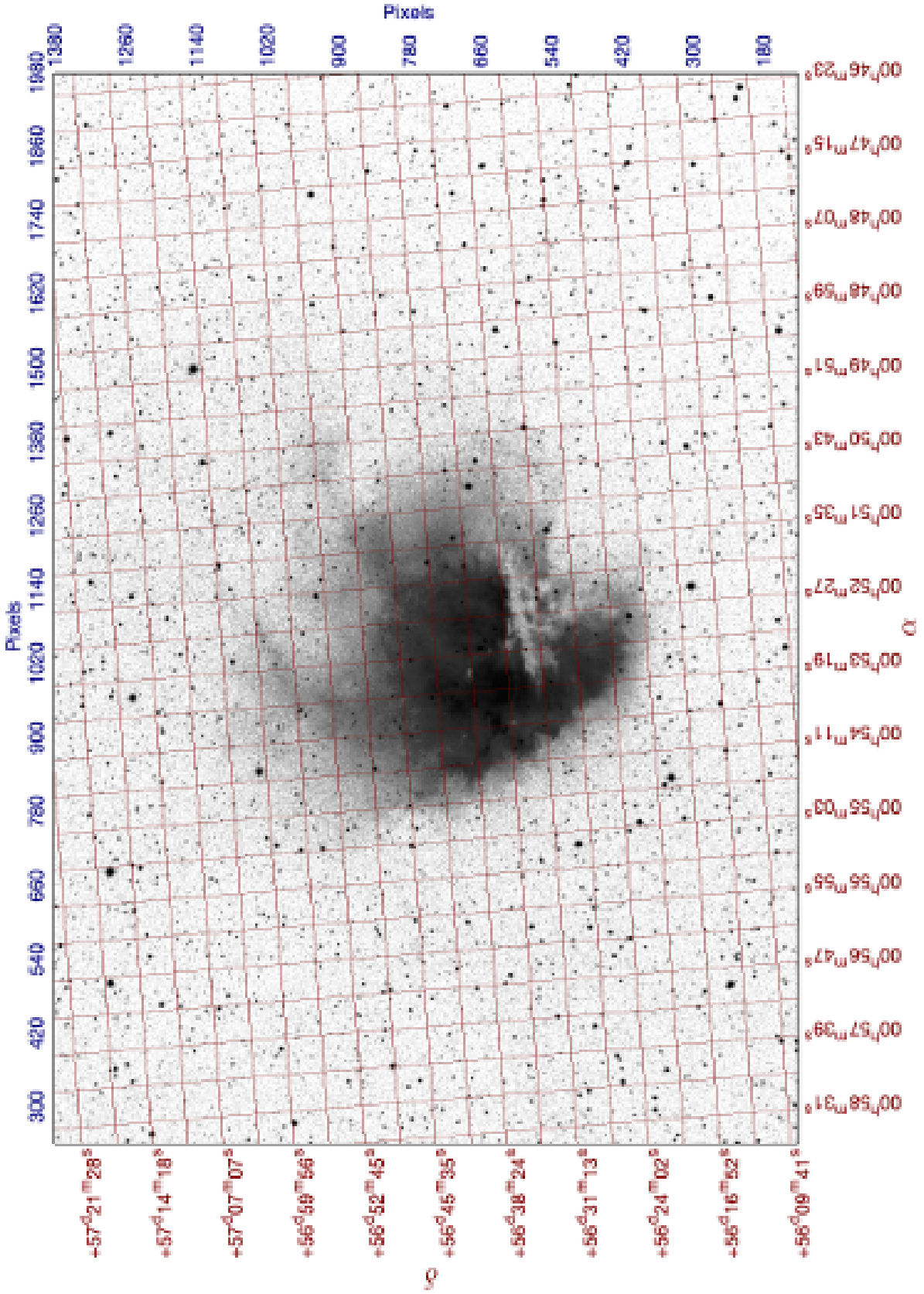

Figure A.15: Full-size Image of The PacMan Nebula in Hα.

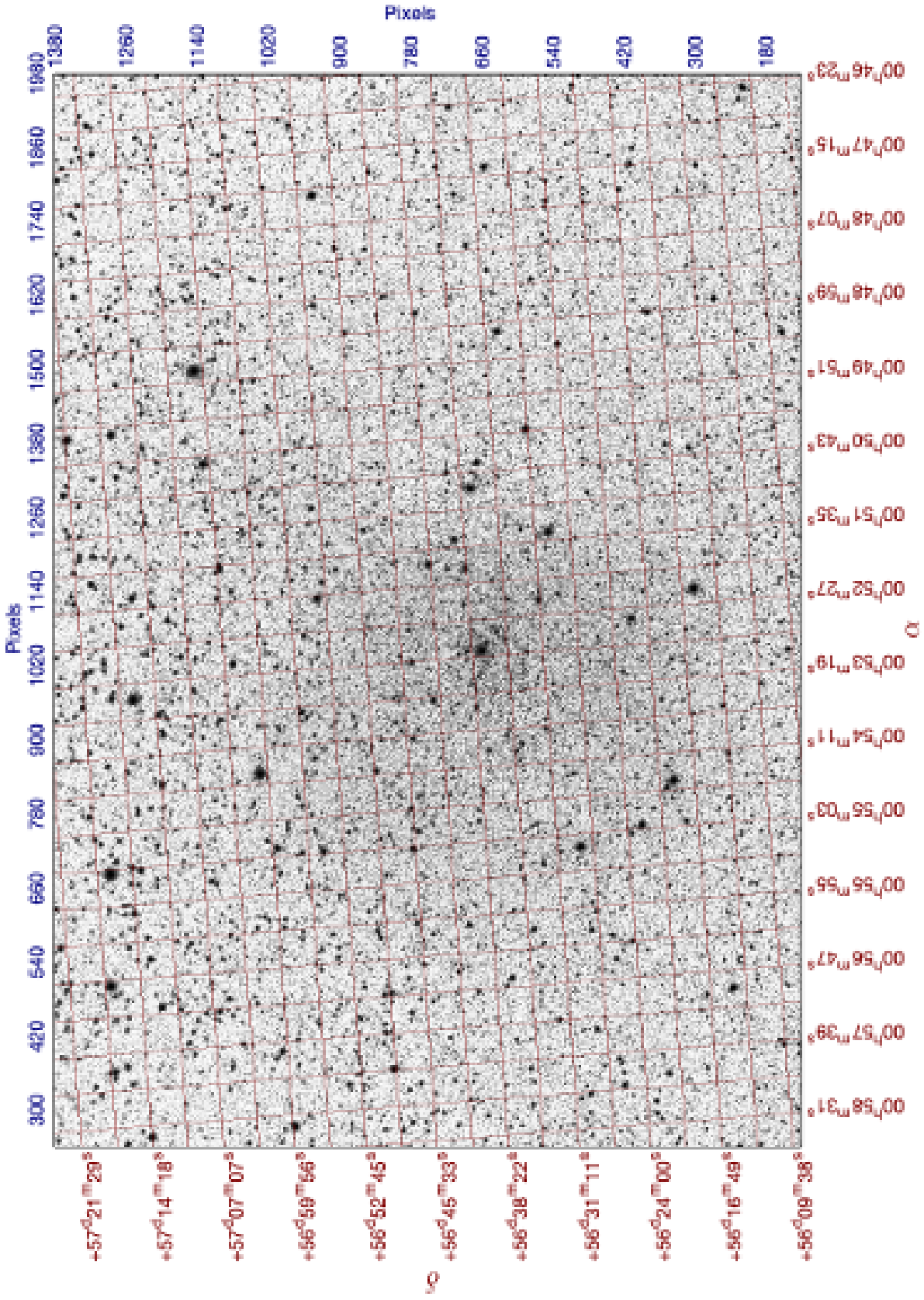

Figure A.16: Full-size Image of The PacMan Nebula in [OI].

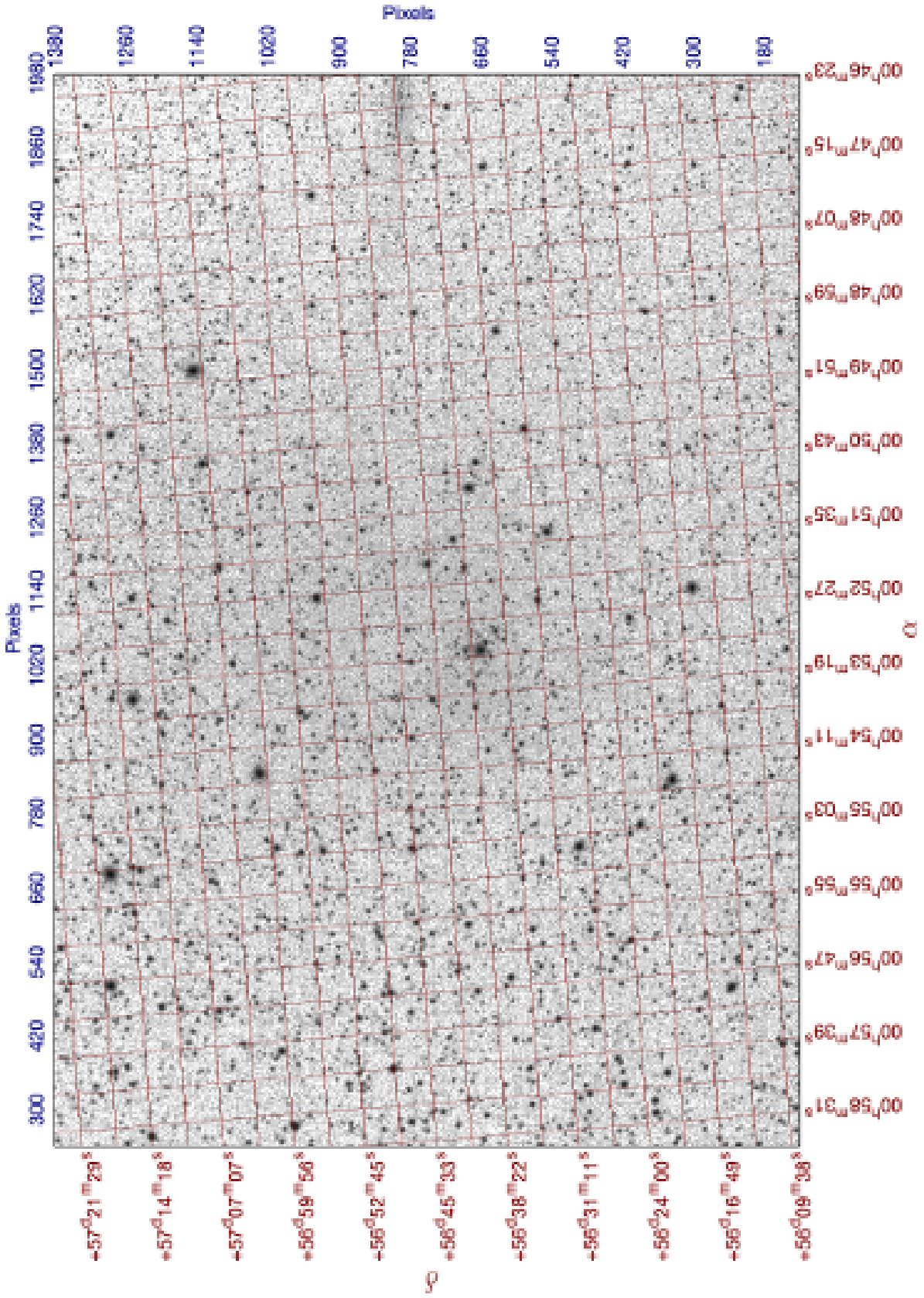

Figure A.17: Full-size Image of The PacMan Nebula in Continuum.

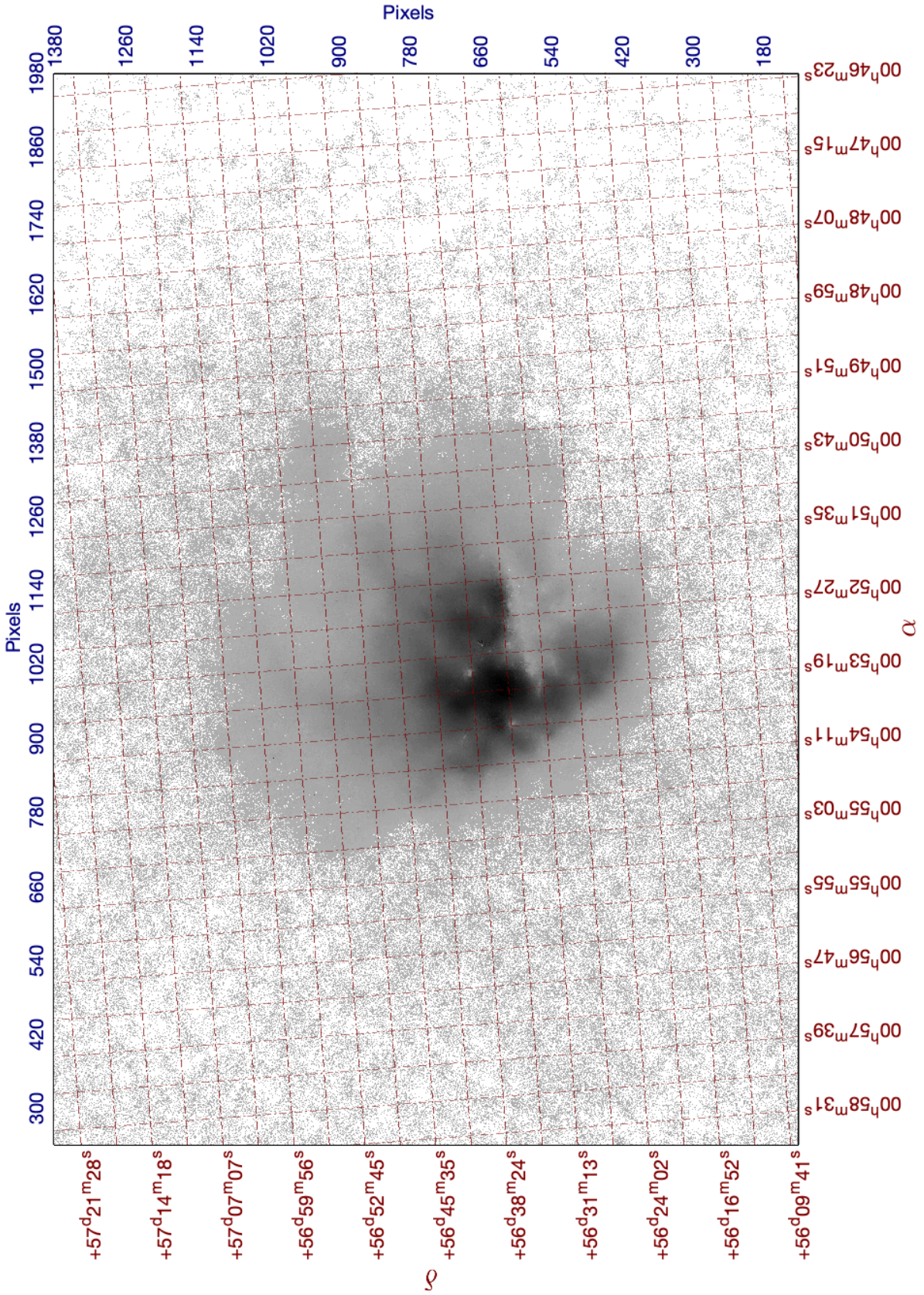

Figure A.18: Full-Size starless image of The PacMan Nebula in Hα.

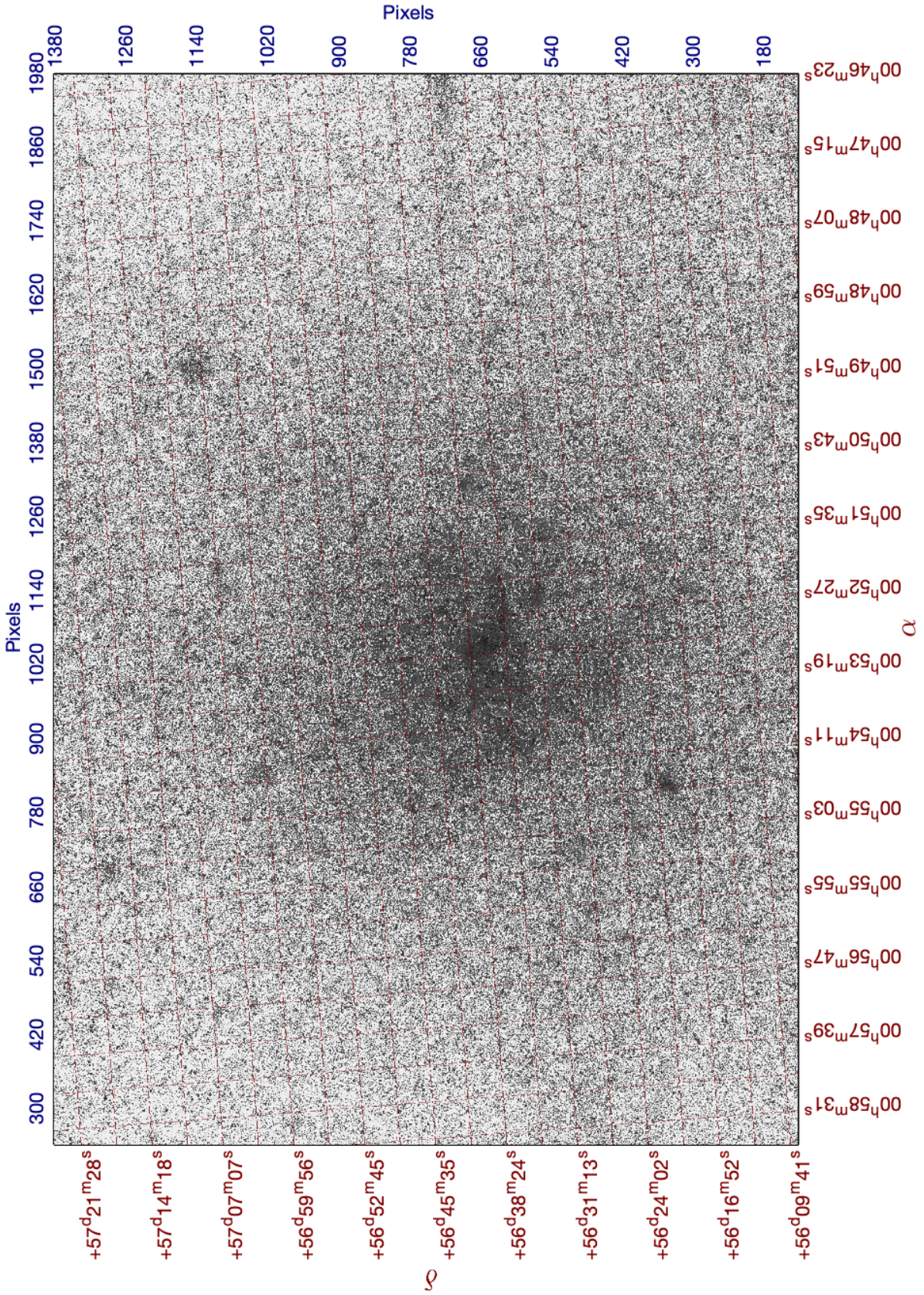

Figure A.19: Full-size starless image of The PacMan Nebula in [OI].

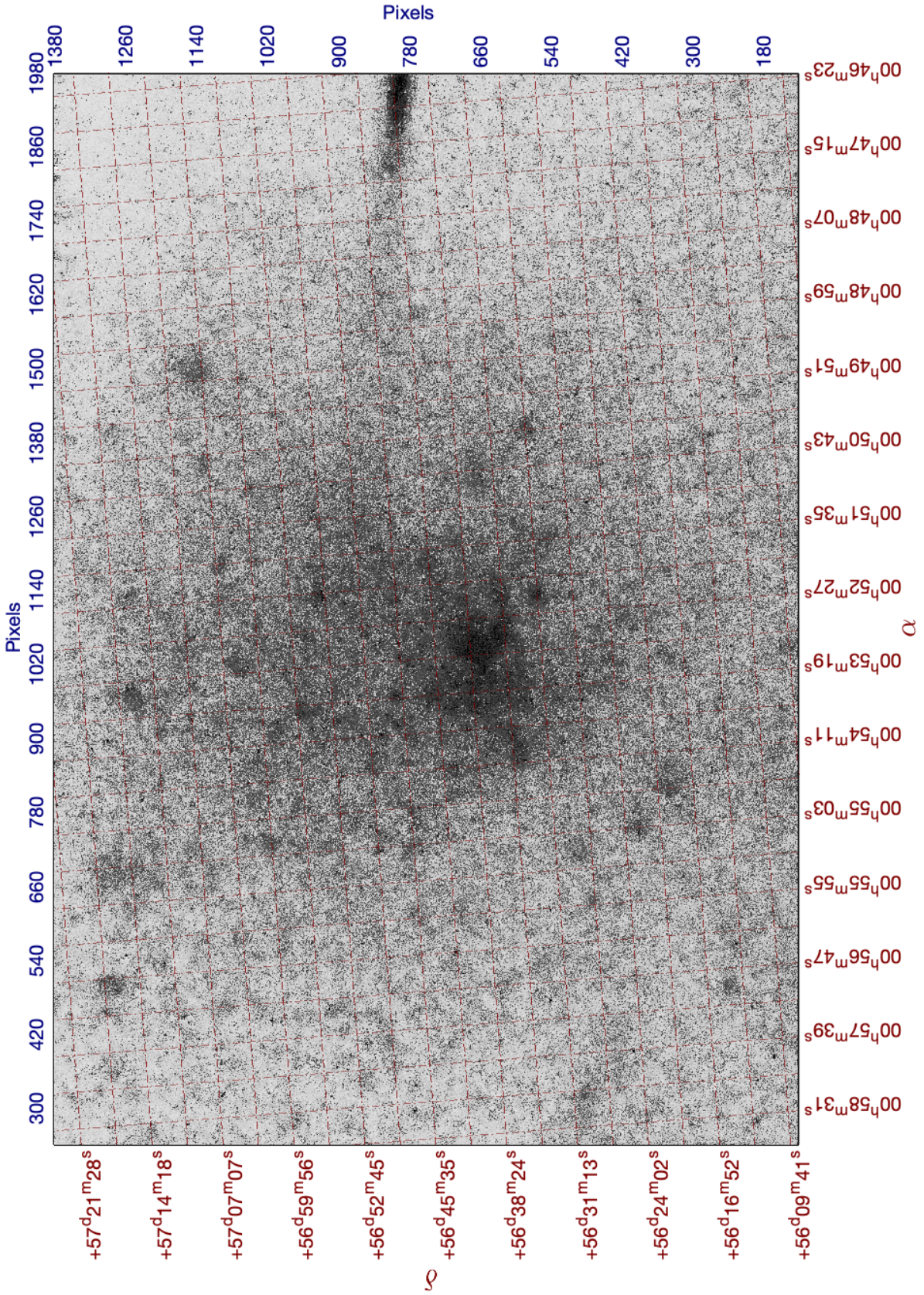

Figure A.20: Full-size starless image of The PacMan Nebula in Continuum.

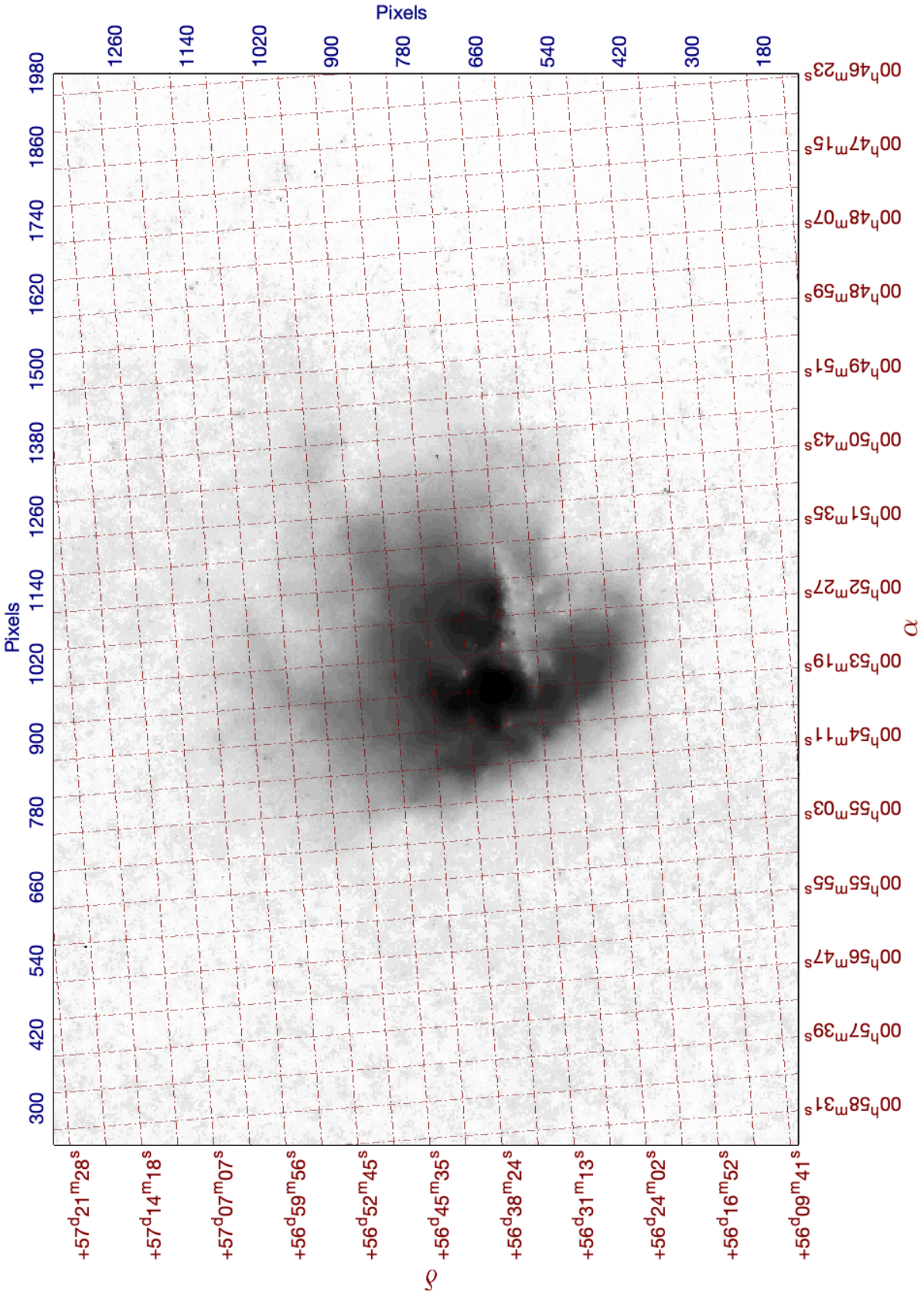

Figure A.21: Full-Size starless and continuum-subtracted image of The PacMan Nebula in Hα binned 3×3.

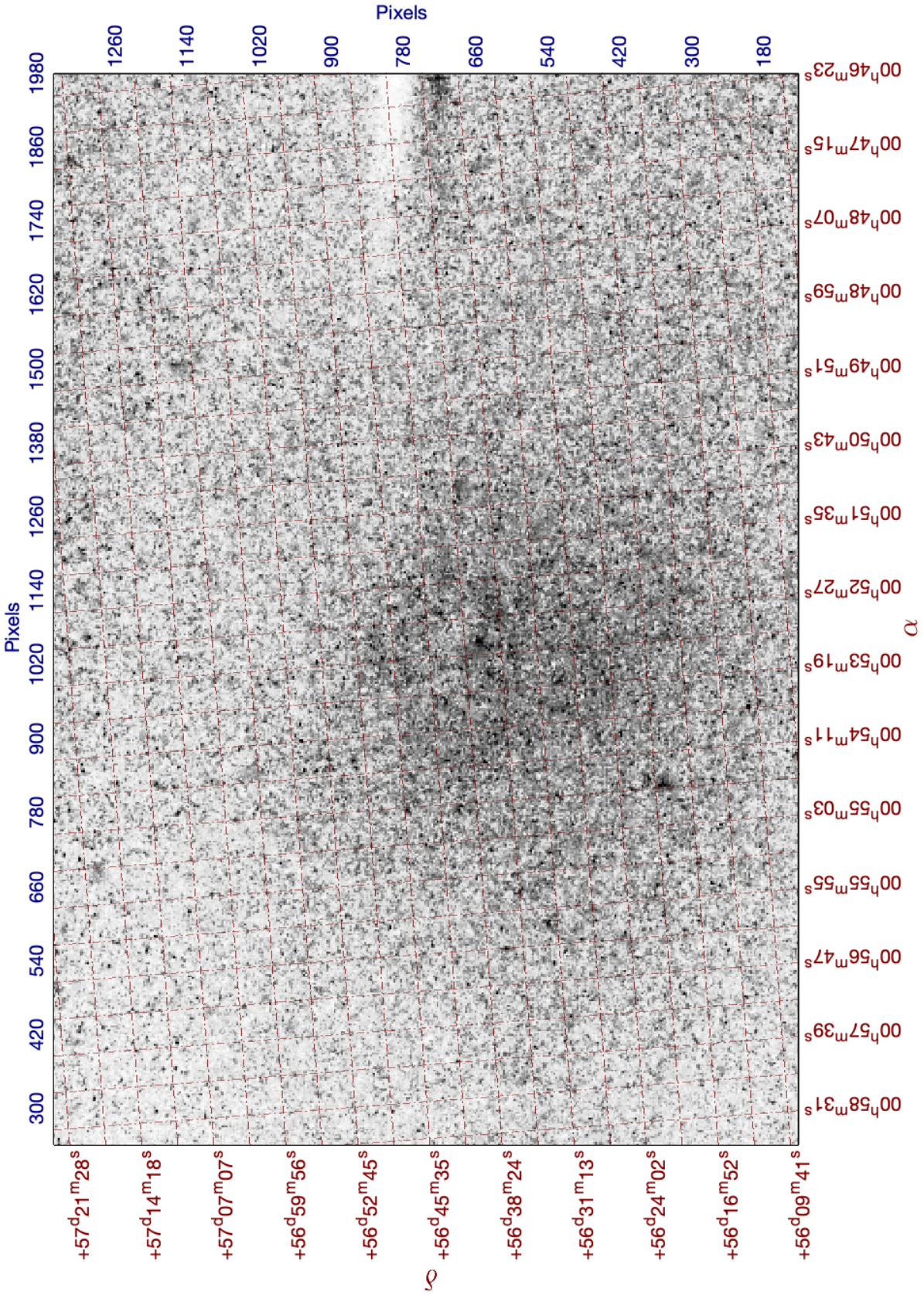

Figure A.22: Full-size starless and continuum-subtracted image of The PacMan Nebula in [OI] binned 3×3.

A.5 And XVIII

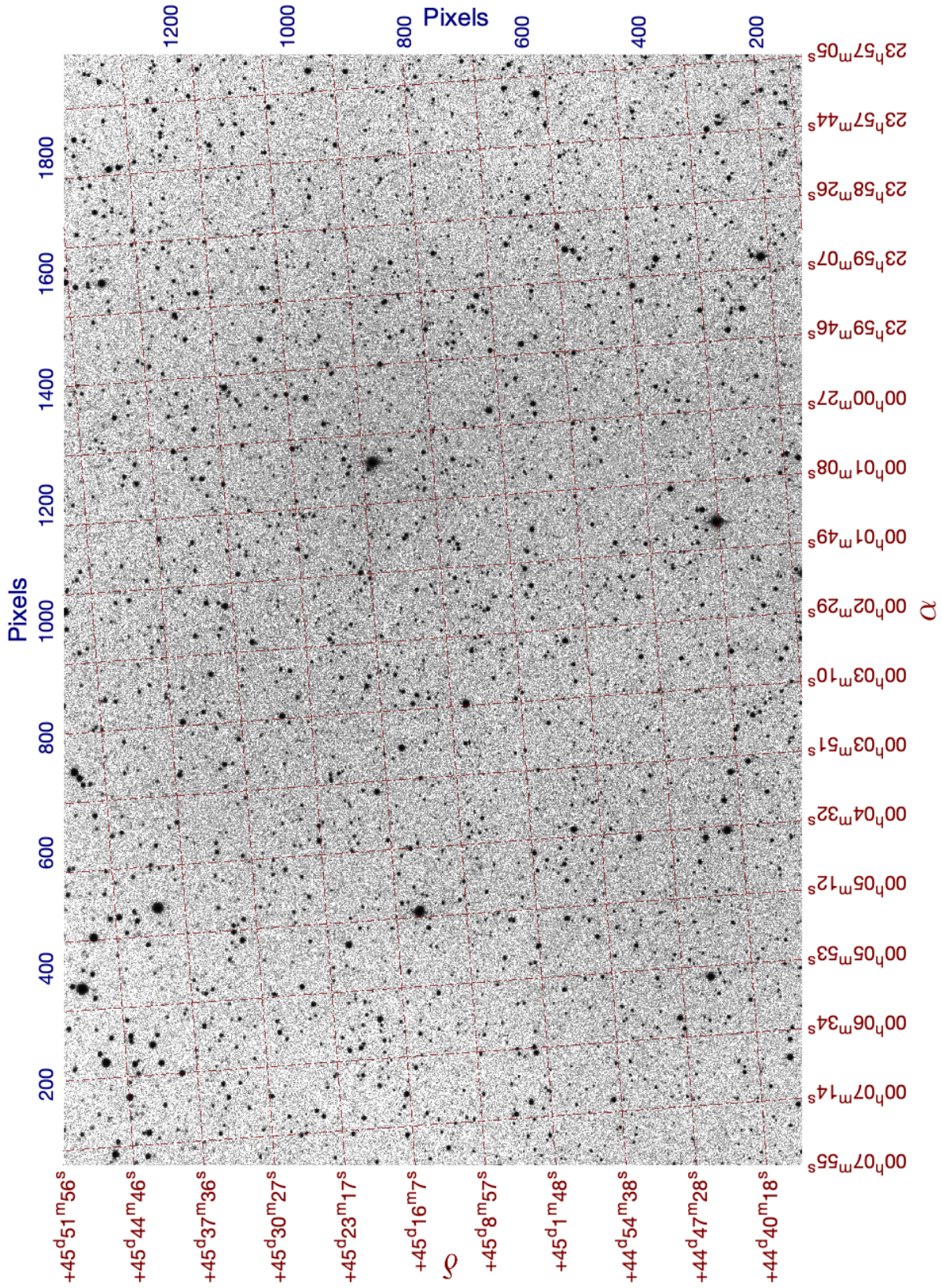

Figure A.23: Full-size image of And XVIII in Hα.

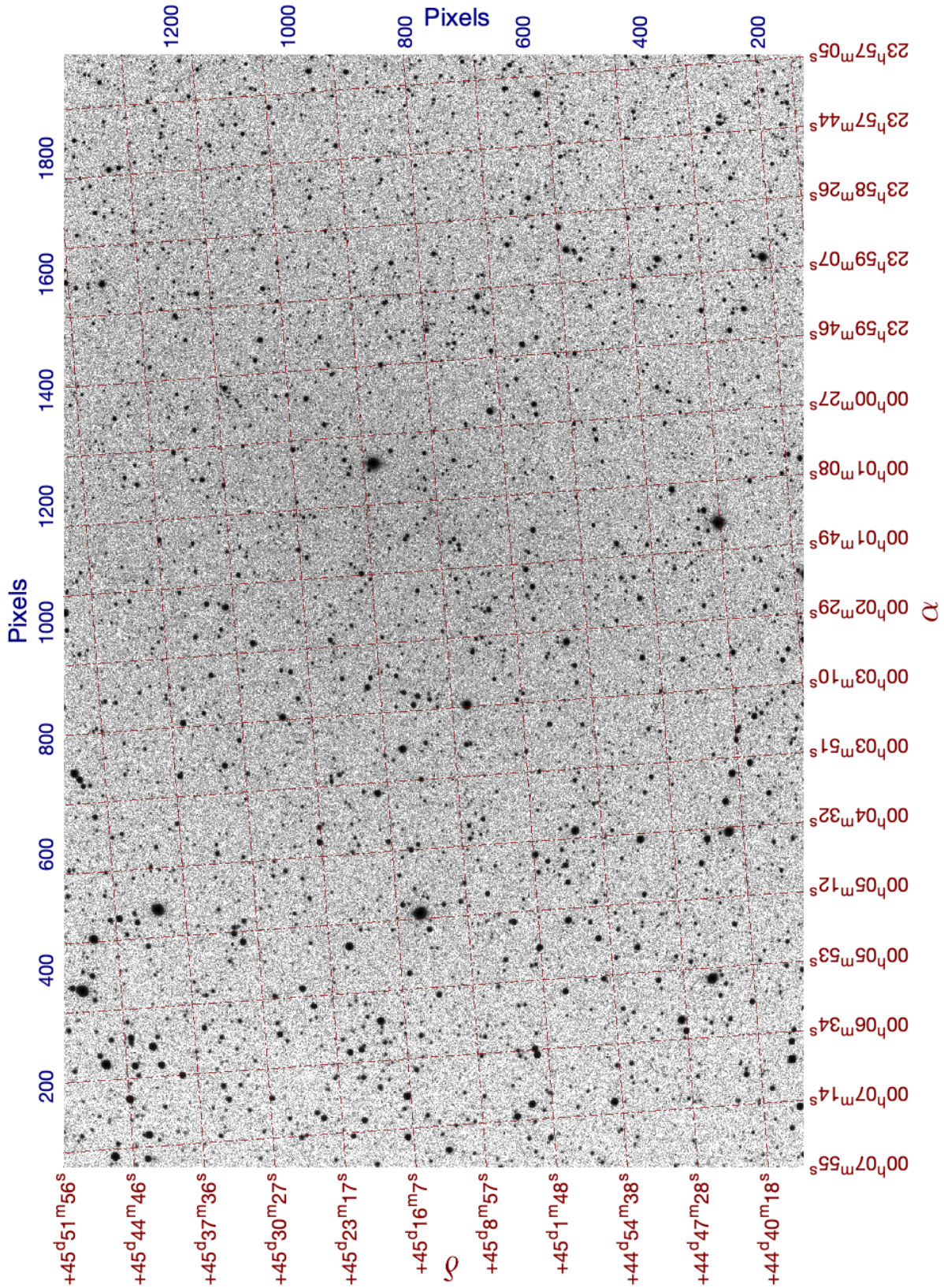

Figure A.24: Full-size image of And XVIII in Continuum.

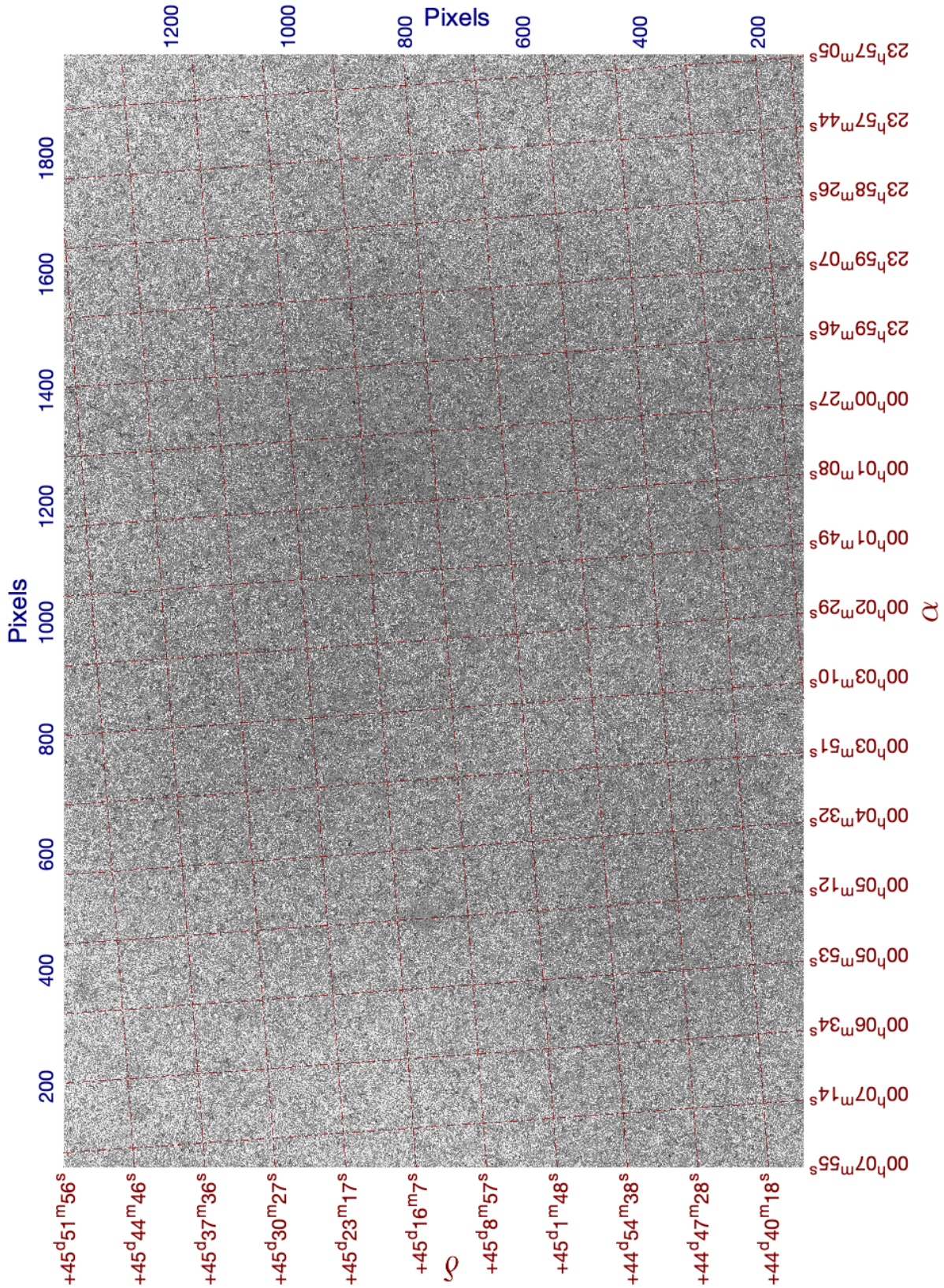

Figure A.25: Full-size starless image of And XVIII in Hα.

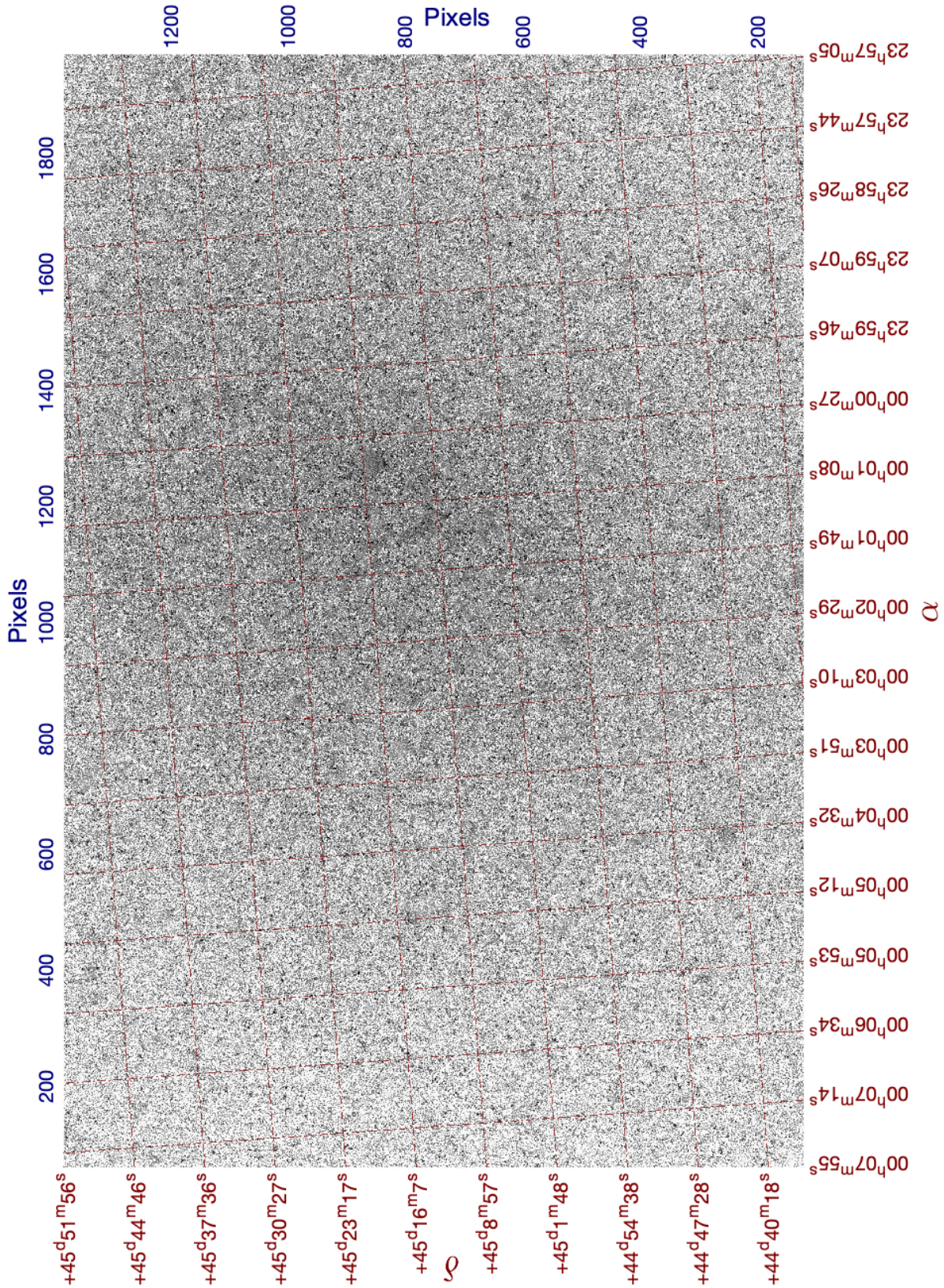

Figure A.26: Full-size starless image of And XVIII in Continuum.

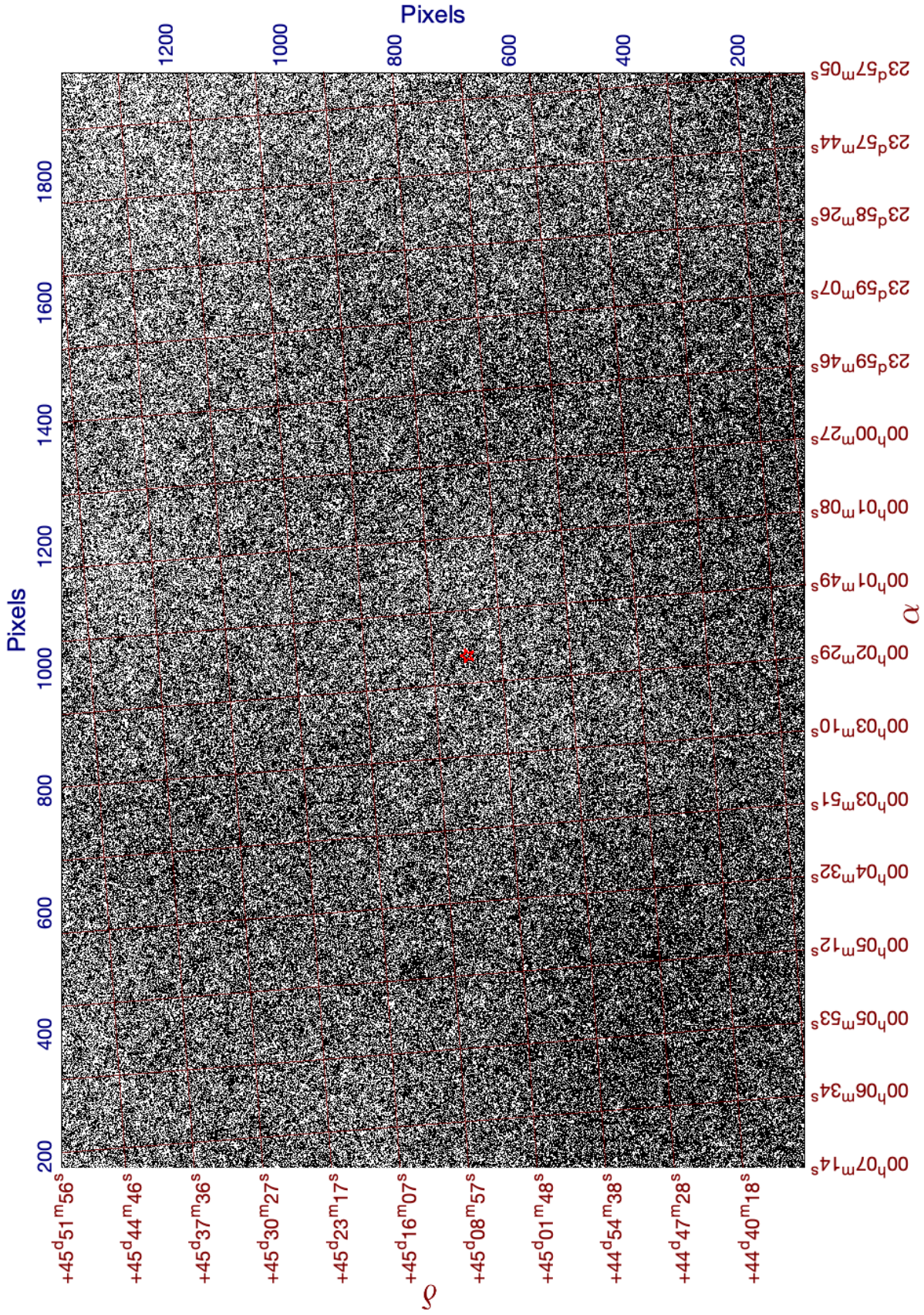

Figure A.27: Full-size starless and continuum-subtracted image of And XVIII in Continuum.